ESRF

European Synchrotron Radiation Facility

Highlights 2005

Contents

Introduction

One of our major preoccupations during 2005 has been the development of a long-term strategy for the ESRF. The ESRF looks forward regularly with a five year horizon via the Medium-Term Scientific Plan with, for example, the on-going programme of beamline reviews that result in the refurbishment of several beamlines each year. After well over a decade of User operation, the time had come for a serious appraisal of the scientific and technical challenges facing the ESRF on a time-scale of ten to twenty years. With a large number of new national medium-energy (third generation) sources operating or in construction, the present synchrotron radiation landscape in Europe is very different from that at the time of the ESRF's inauguration. The preparation of a preliminary document, *New Scientific Opportunities at the European Synchrotron Radiation Facility* [1], has involved discussion with a very large number of interested parties both within and external to the ESRF. This document was received with enthusiasm by the ESRF Science Advisory Committee (SAC) and Council in November 2005.

The basic aim of the Long-Term Strategy is to maintain the ESRF as Europe's principal provider of "hard" X-rays (that is between about 8 and 500 keV) with specialised beamlines allowing internationally-leading innovative science. The scientific case for a renewed and upgraded ESRF emphasises the speciality of the ESRF for "cutting-edge" research, complementary to the new national sources. Five broad scientific areas are considered, namely:

- nano-science and nano-technology
- pump-probe experiments and time-resolved diffraction
- science at extreme conditions
- structural and functional biology and soft matter
- X-ray imaging

It is clear that one of the most rapidly-expanding and dynamic research areas is that of nanoscience and nanotechnology. Synchrotron radiation in general, and the ESRF in particular, has a crucial role to play in these fields, with the provision of fine focus X-ray beams (down to less than 50 nm) with very high intensity. The high stability and reliable operation of the ESRF's X-ray source will be essential prerequisites for applications that push back the nanoscience frontiers. Many pioneering experiments have been carried out at the ESRF using novel time-resolved diffraction techniques to study chemical bonding and biological systems. These studies are expected to expand enormously with the development of the new X-ray free-electron laser sources, but in the interim period optimised ESRF beamlines will permit exciting science on the picosecond timescale. Science at extremes of temperature and pressure has become another speciality of the ESRF and we wish to develop these capabilities to ever more extreme values. Very high magnetic fields, combined with extreme temperature and pressure, will open up new scientific horizons.

The continuing revolution in biology is leading to the need for highly-automated nanofocus beamlines to handle membrane proteins and macromolecular assemblies for which even micrometre-size crystals cannot be grown. We foresee a rapid growth in the use of advanced small-angle scattering techniques applied to interdisciplinary science at the soft-condensed matter/life science border. This is a field where the many variants of X-ray imaging are developing rapidly. The ESRF has always been at the forefront in X-ray imaging and we see these techniques becoming of increasing importance in new areas of medicine, environmental sciences and the human heritage sciences.

The main elements of the upgrade and renewal programme to allow the new science introduced briefly above are:

- the reconstruction of about one third of the beamlines to give improved performance and routine nanofocus capabilities
- the extension of about one third of the Experimental Hall so that long (~ 120 m) beamlines can be constructed with nanometre focused spots
- the upgrade of the accelerator complex, with higher beam current and a continuing effort to enhance the very high brilliance and reliability of the X-ray source
- the design of a new higher brightness lattice, working towards the "ultimate" third generation storage ring X-ray source
- the development of advanced synchrotron

radiation instrumentation, underpinning the beamline and source improvements
• the development of science-driven partnerships to enable new science and applications

Many of these upgrades are natural extensions of the on-going development programmes at the ESRF. For example, the beamlines ID11 and ID13 are being extended for micro- and nanofocus applications, with experimental hutches external to the main experimental Hall (see **Figure 1** inset: photo of the ID13 extension). The new Multilayer Laboratory (see **Figure 1**: photo of Multilayer Lab) with its state of the art fabrication and characterisation facilities reflects the in-house commitment to provide improved focussing multilayer mirrors.

The next steps in the further refinement of the ESRF Long-Term Strategy are detailed discussions at the forthcoming Users' Meeting in February 2006, followed by the preparation of an updated paper to be presented to the SAC and Council in May and June respectively. With Council's approval we can then work on a fully-costed upgrade programme for the ESRF to start in 2007 or 2008.

Returning to the year that has just ended, you will see that the *Highlights 2005* summarises a year of general success and progress for the ESRF. Despite some serious water leak problems with the Machine, availability remained at a very high level (97.6% compared to 98.0% in 2004); we have initiated a programme to replace faulty elements, notably the "crotch" absorbers. Once again, our Users demonstrated their support of and interest in the ESRF with a record number of proposals; in 2005 there were 1881 proposals for beamtime. Publication levels remain very high; a total of more than 1200 refereed papers on work at the ESRF were published in 2004. A large number of these papers appeared in the most prestigious scientific journals, demonstrating the quality of the science that is carried out at the ESRF.

We hope that you find the *Highlights 2005* interesting and informative and we look forward to an important renewal of the ESRF over the next few years through the Long-Term Strategy programme.

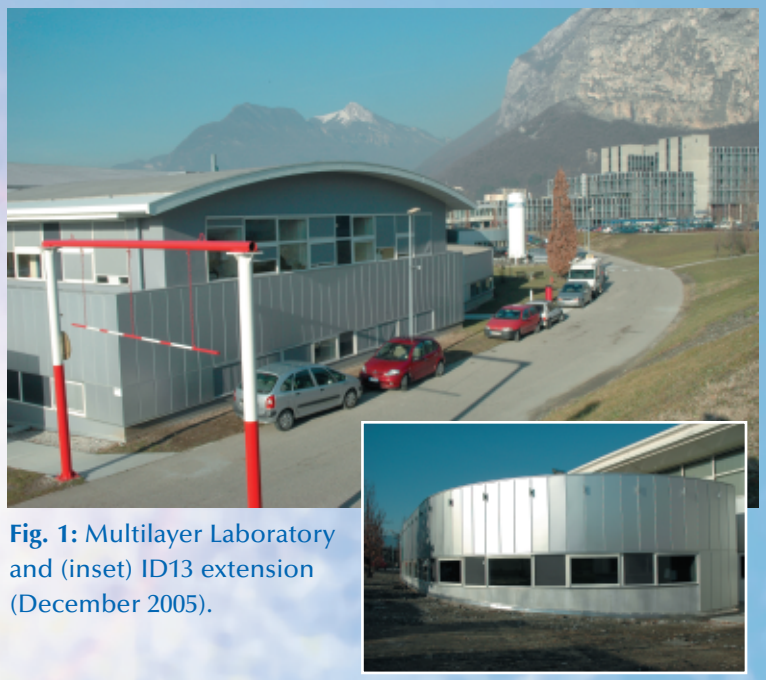

Fig. 1: Multilayer Laboratory and (inset) ID13 extension (December 2005).

This volume of the *Highlights* is dedicated to our friend and colleague Paolo Carra, who died in October. Paolo was a distinguished and innovative scientist who is very sadly missed.

W.G. Stirling, P. Elleaume, R. Dimper, H. Krech, S. Larsen, M. Rodriguez Castellano, F. Sette, P. Thiry, K. Witte

(January 2006)

Reference

[1] Obtainable at http://www.esrf.fr/UsersAndScience/Publications

ESRF

Highlights 2005

scientific Highlights

High Resolution and Resonance Scattering

Introduction

This year's contribution presents a rich bouquet of distinct applications and developments reflecting the scientific and technical breadth of the beamlines. The chapter is organised into four parts: surface science and magnetism at high pressure, both representative of studies under extreme conditions, and then new applications and further experiments.

Investigations under extreme conditions continue to play a major role in our group. Examples given this year are on low dimensional systems and high pressure applications with emphasis on magnetic properties. Among them, three contributions deal with surface science. A pioneering inelastic X-ray scattering experiment in surface-sensitive geometry has been conducted on the charge-density wave system $NbSe_2$, and further activity in this area should be forthcoming. In other areas such as surface applications to magnetic properties and fast and slow dynamics, nuclear resonance techniques already show their maturity. Investigations of magnetic properties under high pressure and at low temperature are a domain of nuclear resonance scattering especially nuclear forward scattering. Results are presented for samarium and europium chalcogenides, which have quite different behaviours. In the case of samarium emphasis was put on strongly-correlated electron systems and in the case of europium it was on model systems for pure Heisenberg magnetism.

Without new applications and developments something would be missing from our report. Three contributions from very different fields take this into account. Hard X-ray photoemission spectroscopy, developed in the framework of the European project VOLPE, allows one to extend the powerful technique of photoemission spectroscopy to the hard X-ray regime in order to achieve bulk sensitivity. The application of a position sensitive detector in conjunction with an inelastic X-ray scattering spectrometer allowed dispersion contributions to the energy resolution to be overcome and demonstrated the potential for a compact instrument with an energy resolution down to 10 meV. The final contribution shows that inelastic X-ray scattering also has the capability to directly measure the density of phonon states thus complementing inelastic neutron and nuclear inelastic scattering.

In the last section we present a cross-section of a variety of applications. They range from glass physics to the understanding of thermoelectric materials – why they are electric

conductors and thermal insulators, then geophysical and biological topics, and finally to fundamental questions in physics.

Besides the scientific activities, the year 2005 had a great influence on the instrumentation as well. The beamlines continued to increase the effective available flux on the sample by various means. Undulators with two different magnetic structures can be optimised for different energy regimes. The first segments of this kind have been installed at ID16, ID18, and ID28. In their final configuration, this will increase the flux between a factor of two and five. Furthermore, the focusing capabilities have been improved at the inelastic scattering beamlines allowing both an optimised and variable setup especially for investigations under extreme conditions.

A major impact is expected from the refurbishment program at ID26, which has just begun. After re-opening of the beamline in summer 2006, two dedicated stations will become available: one for absorption and one for emission spectroscopy. Dedicated spectrometers and focusing devices will also be implemented. The most challenging part will aim at fast time resolved studies (pump-and-probe) and is envisaged at a later stage.

Last but not least external review committees have very positively evaluated ID16 and the nuclear resonance stations (ID18 and ID22N). Their recommendations are currently being analysed and possible implementations discussed.

R. Rüffer

Surface Science

Dynamics at the Surface and Beyond

The quasi-two-dimensional $NbSe_2$ is a van der Waals layered material and a member of the remarkable transition metal dichalcogenide family. A metal at room temperature, $NbSe_2$ undergoes a charge density wave (CDW) transition at about 33 K and a superconducting transition at about 5 K. This CDW transition is interesting on many fronts, not least as it is an incommensurate, continuous phase transition and the CDW phase remains incommensurate right down to the formation of the superconducting phase [1].

In the study of dynamics, a variety of techniques, including inelastic neutron scattering and He scattering, have either concentrated on the surface or the bulk properties. Inelastic X-ray scattering offers the unique possibility to study surface and bulk dynamics in a single experiment. This is achieved by setting the sample in grazing-incidence condition thus holding the incoming X-rays below the critical angle of total external reflection. In this case, the incident electromagnetic field displays an exponential decay in the sample bulk. In this geometry the scattering depth is about 4 nm [2], and the topmost four atomic layers contribute 50% to the scattered signal. By increasing the incidence angle beyond the critical angle one can penetrate deep into the sample bulk. This surface sensitive setup was realised on **ID28** by inserting a deflector mirror in front of the sample. Thanks to the small vertical beam size at the sample position, the experiment could be conducted

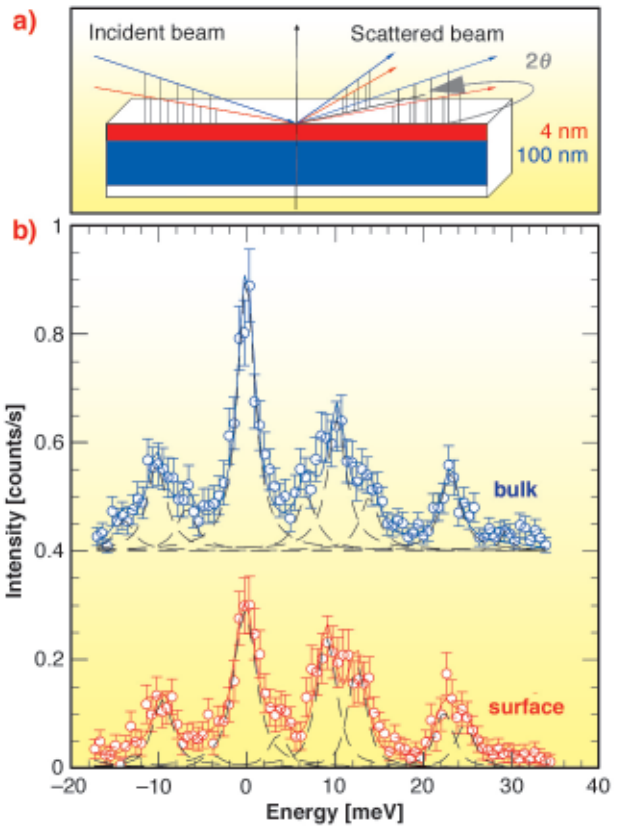

Fig. 2: (a) The scattering geometry for grazing-incidence inelastic scattering. (b) Spectra of $NbSe_2$ collected in surface and bulk geometry at 2/3 of the Brillouin zone along the [ξ00] direction. (Raw data: open circles with error bars. Dashed lines: individual elastic and inelastic contributions. Solid line: overall best fit result.

with an overall energy resolution of 3 meV, even in this flux-demanding geometry.

By varying the angle of incidence above and below the critical angle of total external reflection we have measured surface and bulk $NbSe_2$ energy transfer spectra, from -20 to 35 meV, at a number of points in momentum space (see **Figure 2**). The predominantly longitudinal Σ_1 ω_1 and Σ_1 ω_2 modes are intense. In addition, small contributions from some of the Σ_3 branches, predominantly of transverse nature, are also visible. We use a damped harmonic oscillator (DHO) model function to extract peak positions and so determine surface and bulk phonon dispersion curves shown in **Figure 3**. In both configurations the longitudinal Σ_1 ω_2 mode displays significant softening in energy at 2/3 of the reduced Brillouin zone. This points to a strong interaction between the phonons and the conduction electrons. The increased anomaly at the surface is evidence that some change is occurring in the topmost layers. One possibility is that the surface electronic state cuts the Fermi surface at a different position from that of the bulk Fermi wave vector, as predicted by Benedek *et al*. [3]. Another possibility would involve an increased electron-phonon interaction, which is consistent with the change of symmetry and coordination of the upper atomic layers with respect to that of the bulk.

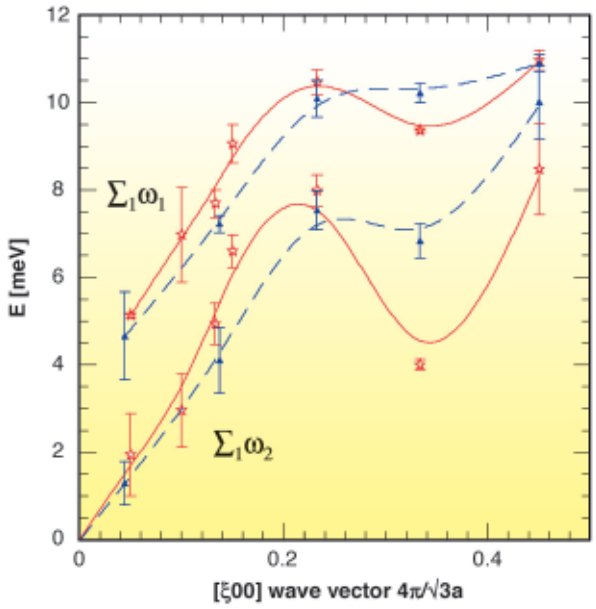

Fig. 3: Room temperature surface (☆) and bulk (▲) phonon dispersion curve of 2H-$NbSe_2$ here $\xi = 2 - h$ is in reciprocal space units. The Σ_1 ω_1, Σ_1 ω_2 modes are shown. A shift to lower energy is seen in the surface data at $\xi = 0.33$ (lines are a guide to the eye).

In summary, we have measured the bulk and surface phonon dispersion relations for 2H-$NbSe_2$ at 300 K, by selecting between surface- and bulk- sensitive geometry by means of grazing-incidence inelastic X-ray scattering, and varying depth sensitivity from 4 nm to 100 nm. Our results indicate that the anomaly for the surface mode occurs at a lower energy than that measured in bulk sensitive geometry in the same experiment, showing evidence of a modified behaviour in the uppermost layers. We demonstrate that inelastic X-ray scattering in grazing-incidence conditions provides a unique tool to selectively study either surface or bulk lattice dynamics in a single experiment.

References

[1] D. E. Moncton, J. D. Axe, and F. J. DiSalvo, *Phys. Rev. B* **16**, 801 (1977).
[2] H. Dosch, *Phys. Rev. B* **35**, 2137 (1987).
[3] G. Benedek, L. Miglio, and G. Seriani, in *Helium Atom Scattering from surfaces*, edited by E. Hulpke, Springer Series in Surface Science, **27**, 208 (1992).

Principal Publication and Authors

B.M. Murphy (a, b), H. Requardt (c), J. Stettner (a), J. Serrano (c), M. Krisch (c), M. Müller (a), W. Press (a,d), *Phys. Rev. Lett.* **95**, 256104 (2005).
(a) Institut für Experimentelle und Angewandte Physik, Christian-Albrechts-Universität, Kiel (Germany)
(b) CCLRC Daresbury Laboratory, Warrington (UK)
(c) ESRF
(d) ILL

Resonant Atoms in a Cavity: A Boost for Coherent X-ray Scattering

Remarkable effects occur upon the resonant interaction of light with matter, if the radiating atoms themselves are embedded in resonant structures like cavities or waveguides: When the incident radiation couples to a resonant mode of the cavity, one can observe a substantial decrease in the radiative lifetime, if the atoms are located in an antinode of the standing wave. This is caused by a strong modification of the photonic density of states in the vicinity of reflecting boundaries. As already discussed by Purcell in 1946 [1], this leads to an enhancement of the spontaneous emission rate of the radiating atoms. The fundamental interest in this phenomenon and the potential applications in optical information technology have led to intense research activities, constituting the field of cavity quantum electrodynamics. Experiments in this field are typically performed in the microwave or optical regime of the electromagnetic spectrum. Due to a growing interest in the study of ultrafast processes using pulsed X-ray sources, it is appealing to study the effect of confining environments on the spontaneous emission of X-rays as well. With decreasing wavelength of the radiation, however, the coupling efficiency of the spontaneous radiation into the cavity modes drastically decreases, so that the effect on the spontaneous emission rate is negligibly small. This situation improves significantly if the emission is highly directional with a wavevector k_0 that coincides with a wavevector of a cavity mode. In general, such a situation

occurs when an ensemble of resonant emitters, rather than a single atom, is excited coherently by a directional radiation pulse with wavevector k_0. Due to the collective nature of the excitation, the subsequent radiative decay of this state proceeds into the direction of the incident wavevector k_0. The excitation of Mössbauer nuclei by pulses of synchrotron radiation allows one to prepare such a collectively excited state with a well-defined wavevector k_0 in the X-ray regime. This provides a very efficient mechanism to funnel the spontaneous (re)emission of X-rays into a selected photonic mode of a waveguide or cavity where the resonant nuclei are located.

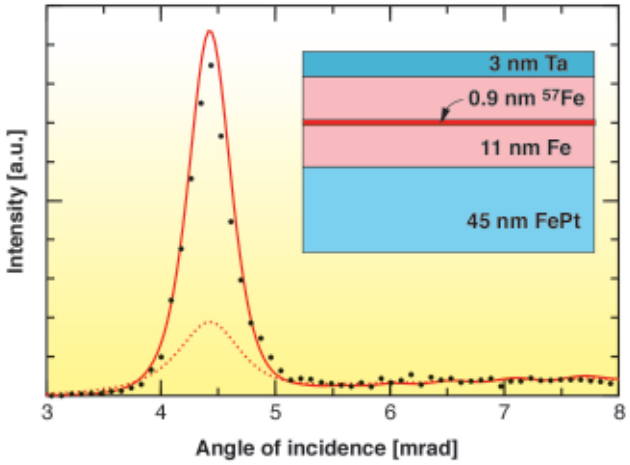

Fig. 4: Coherent enhancement of the specular reflectivity from a ^{57}Fe probe layer that is embedded in a waveguide [2], as sketched in the inset. At 4.4 mrad the first-order guided mode is excited. The solid red line is a theoretical simulation. For comparison, the dashed red line displays the angular dependence of any incoherent signal from the ^{57}Fe nuclei, *e.g.*, fluorescence radiation.

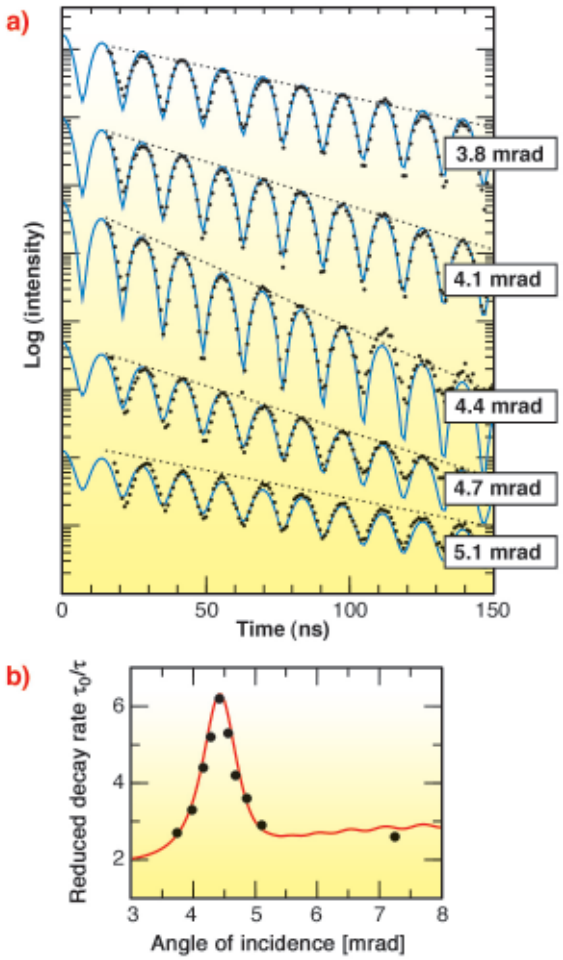

Fig. 5: (a) Time spectra of the specular reflection recorded at different angular positions around the peak in **Figure 4**; (b) The angular dependence of the nuclear decay rate (normalised to the natural decay rate) as derived from the time spectra, together with a theoretical simulation (solid red line).

In this experiment we have studied the influence of a planar single-mode waveguide on the radiative decay of an ensemble of ^{57}Fe nuclei. These nuclei are located as an ultrathin layer in the centre of the guiding layer. The sample used here is sketched in the inset of **Figure 4**. The guided mode is excited at an incidence angle of of φ_m = 4.4 mrad, where a strong boost of the radiation resonantly reflected from the ^{57}Fe nuclei is observed. This is a result of the strong enhancement of the photonic density of states in the waveguide [2]. To investigate the effect of the cavity resonance on the nuclear lifetime, time spectra at different angular positions around the guided mode were recorded. A selection of these spectra is shown in **Figure 5a** where a drastic variation of the decay constant on the angle of incidence is visible. (The oscillation period reflects the energetic separation of the hyperfine transitions that results from a magnetic hyperfine field of B = 33.1 T at the nucleus.) **Figure 5b** shows the dependence of the nuclear decay rate on the angle of incidence. The 6-fold acceleration of the decay at the peak position and the overall shape of the curve is well described by the simulation shown in **Figure 4** (solid line).

The phenomena described here rely on the mode structure of the vacuum field as it is modified by the medium that surrounds the radiating atoms. The corresponding temporal alteration of the photon-matter interaction might be particularly relevant for time-resolved studies of dynamics in nanoscale structures using short-pulsed X-ray sources with pulse durations in the range of ps to fs. Since these phenomena are final state effects of the scattered photon field, they do not require a high number of photons per mode in the incident beam.

References

[1] E. M. Purcell, *Phys. Rev.* **69**, 681 (1946).
[2] R. Röhlsberger, T. Klein, K. Schlage, O. Leupold, and R. Rüffer, *Phys. Rev.* B **69**, 235412 (2004).

Principal Publication and Authors

R. Röhlsberger (a), K. Schlage (b), T. Klein (b), O. Leupold (a), *Phys. Rev. Lett.* **95**, 097601 (2005).
(a) DESY, Hamburg (Germany)
(b) Universität Rostock, Institut für Physik (Germany)

Iron Self-diffusion in Amorphous and Nanocrystalline Alloys using Nuclear Resonance Reflectivity

Atomic diffusion in amorphous and nanocrystalline alloys has been a subject of great interest, as it governs the structural relaxation and associated changes in the physical properties in these alloys. Depth profiling techniques like radioactive tracer and secondary ion mass spectrometry are most widely used for such studies, however, these techniques are limited by their depth resolution which is of the order of a few tens of nanometres. This is a severe limitation in the study of metastable systems like amorphous and nanocrystalline phases, where diffusion lengths of more than a few nanometres may be difficult to achieve, as annealing temperatures have to be kept low in order to avoid structural changes. Dynamic techniques like Mössbauer spectroscopy or nuclear forward scattering on the other hand are limited by the time window over which they are sensitive to atomic diffusion. For example, diffusivities accessible using ^{57}Fe Mössbauer spectroscopy lie in the range 10^{-12} to 10^{-13} m^2/s.

In the present work we demonstrate the possibility of using nuclear resonance scattering from isotopic multilayers for studying self-diffusion of Mössbauer isotopes over a wide range of diffusivity. For a reasonable range of annealing times, a diffusivity range of 10^{-26} m^{2}s^{-1} to 10^{-18} m^{2}s^{-1} could be made accessible. At the same time, this technique is sensitive enough to measure diffusion lengths as small as 0.1 nm, which is more than an order of magnitude larger than the sensitivity of conventional depth profiling techniques. The systems selected for present studies are amorphous and nanocrystalline alloys of iron.

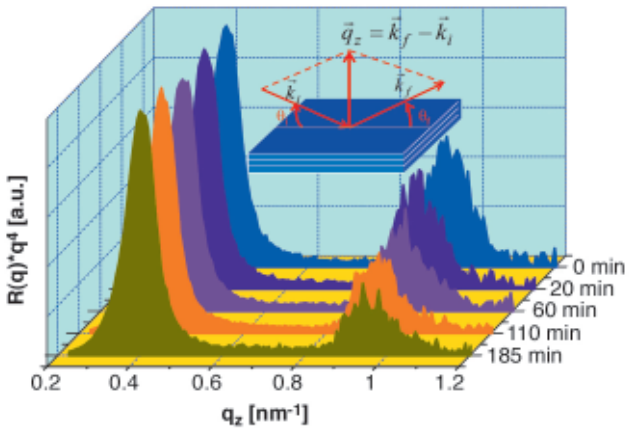

Fig. 6: Nuclear resonance reflectivity of the [^{57}FeNZr (4nm)/FeNZr (3nm)]$_{20}$ multilayer taken at the Mössbauer resonance energy of ^{57}Fe (14.413 keV), as a function of annealing time at 393 K.

Figure 6 shows nuclear resonance reflectivity of isotopic multilayer of nanocrystalline FeNZr having structure [^{57}FeNZr (4nm)/FeNZr (3nm)]$_{20}$. The film is chemically homogeneous, however, scattering contrast between adjacent layers emanates due to the nuclear resonance scattering of 14.413 keV X-rays from ^{57}Fe isotope. Measurements were done at beamline ID22N.

A Bragg peak around q_z = 0.9 nm^{-1} is observed due to isotopic periodicity. As the multilayer is annealed, iron atoms diffuse across the isotopic interfaces, and the intensity of the Bragg peak decays with annealing time, yielding the diffusion length through the relation, $ln[I(t)/I(0)] = -4\pi^2n^2L_d^2/d^2$, where $I(t)$ is the intensity of the Bragg peak after annealing time t, n is the order of Bragg reflection, L_d is the diffusion length and d is the bilayer periodicity. **Figure 7** gives L_d as a function of annealing time at three different temperatures. It increases initially at a faster rate and after a certain annealing time the rate becomes constant. The initial faster increase in the diffusion length is associated with the structural relaxation in the system, similar to amorphous alloys. This relaxation is associated with the relaxation of the highly disordered grain boundary region, stress relaxation in the film and annealing out of the defects inside the nanocrystals. After sufficiently long annealing time, the diffusion length increases linearly with annealing time and the diffusivity was obtained by a linear fit using the relation: $L_d^2 = 2D(T)t$.

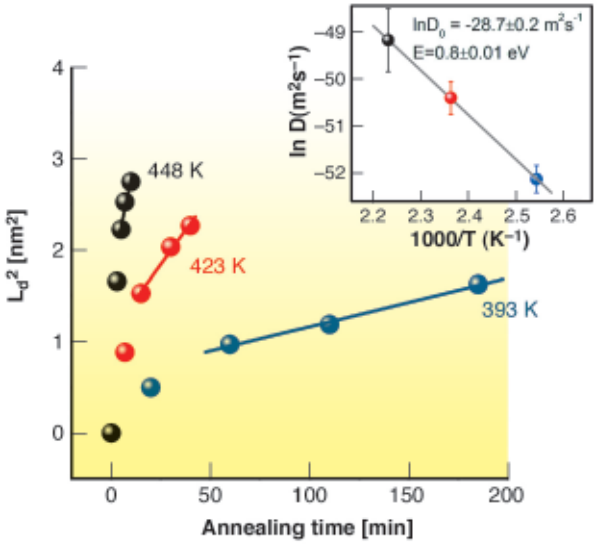

Fig. 7: Evolution of interdiffusion length L_d as a function of annealing time at different temperatures. The inset shows the Arrhenius behaviour of diffusion coefficient with isothermal annealing temperature, yielding the activation energy and pre-exponent factor for self-diffusion of Fe.

The diffusivity follows Arrhenius type behaviour with temperature, as shown in the inset of **Figure 7**. The solid line in the figure is a fit to the experimental data obtained using the relation $D = D_0exp(-E/k_BT)$, where E is the activation energy *and* D_0 is the pre-exponential factor which contains the details of the diffusion mechanism. The obtained values of activation energy and pre-

exponential factor are E = 0.8 ± 0.01 eV and D_0 = exp (–28.67 ± 0.23). The activation energy for self-diffusion of Fe in the present system is significantly lower than that in the amorphous FeN of similar composition [1]. This result is in general agreement with the earlier studies where the low activation energy for diffusion in nanocrystalline alloys has been attributed to a higher density of grain boundaries. Further, the observed values of D_0 and E suggest that the mechanism of diffusion in this system is similar to that in amorphous alloys [2].

It may be noted that the high sensitivity of the present technique enables one to clearly see the initial variation in the diffusivity because of the structural relaxation in the system even at temperatures as low as 393 K, although the typical diffusion lengths involved are of the order of 0.1 nm.

References

[1] M. Gupta, A. Gupta, S. Rajagopalan, and A. K. Tyagi, *Phys. Rev. B* **65**, 214204 (2002).

[2] F. Faupel, W. Frank, M.P. Macht, H. Mehrer, K. Rätzke, H.R. Schober, S.K. Sharma, H. Teichler, *Rev. Mod. Phys.* **75**, 237 (2003).

Principal Publication and Authors

A. Gupta (a), M. Gupta (a,b), S. Chakravarty (a), R. Rüffer (c), H-C Wille (c), O. Leupold (c), Phys. Rev. B **72**, 014207 (2005).

(a) UGC-DAE Consortium for Scientific Research, Indore (India)

(b) Laboratory for Neutron Scattering, ETH Zürich & PSI, Villigen (Switzerland)

(c) ESRF

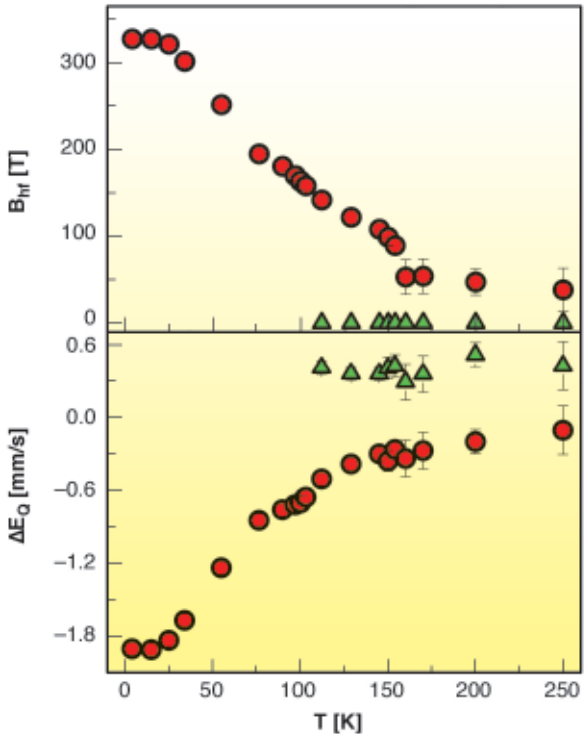

Fig. 8: Temperature dependence of the magnetic hyperfine field B_{hf} and of the electric quadrupole interaction ΔE_Q of $SmMn_2Ge_2$. The full circles refer to the magnetic component while the full triangles refer to the nonmagnetic one, which is present only for $T > 100$ K.

Magnetism

The Unusual Magnetic Properties of Samarium and its Compounds

Interest in the study of the lanthanides has recently been enhanced by the observation in some of their compounds of unconventional superconductivity appearing in the vicinity of a quantum critical point, where the magnetic order is destroyed. The originality of samarium, within the lanthanides, lies in two facts: *i)* the competition between its two stable valence states, nonmagnetic Sm^{2+} and magnetic Sm^{3+}, can lead to the formation of intermediate valence compounds, showing peculiar electronic properties [1], and *ii)* the presence of low-energy excited multiplets for Sm^{3+} can lead to a ground state which is not an eigenstate of the total angular momentum J (J = 5/2 for the ground multiplet). Moreover, the charge state can be tuned towards trivalency by the application of pressure, with the expected onset of long-range magnetic order owing to the fact that Sm^{3+} has an odd number of 4*f* electrons (*e.g.*, it is a Kramers ion). We have investigated these aspects by ^{149}Sm Nuclear Forward Scattering (NFS) of synchrotron radiation on beamlines **ID18** and **ID22N**.

An intriguing intermetallic compound of samarium is $SmMn_2Ge_2$, which has two magnetic sublattices (Mn and Sm) and shows multiple magnetic phase transitions with temperature (ferromagnetic for $T < 100$ K and $150 < T < 350$ K, antiferromagnetic for $100\text{K} < T < 150$ K and $350\text{ K} < T < 385$ K, and paramagnetic for $T > 385$ K) [2]. The role of samarium in these transitions is not clear, because of difficulties in separating its small magnetic moment from that of Mn by neutron diffraction. Our ^{149}Sm NFS investigations were performed on beamline **ID18**. **Figure 8** shows the temperature dependence of the hyperfine magnetic field and of the electric quadrupole interaction at the ^{149}Sm nuclei. These results show that Sm is in a trivalent state with fairly pure J = 5/2 character (magnetic moment ~ 0.65 μ_B), contrary to most other Sm compounds. They give the first direct evidence that samarium has an ordered magnetic moment at all temperatures between 4 and 250 K, spanning the three main magnetic phases, and rule out the possibility that the antiferromagnetic → ferromagnetic phase transition at 100 K could be due to the ordering of the samarium sublattice. However, above

100K, only about 50% of the samarium ions keep the ordered moment, the rest becoming paramagnetic. This suggests that the ordering of the 4*f* moments in this temperature range is favoured by the non-vanishing molecular field created by the Mn moments at about half of the lattice sites occupied by Sm.

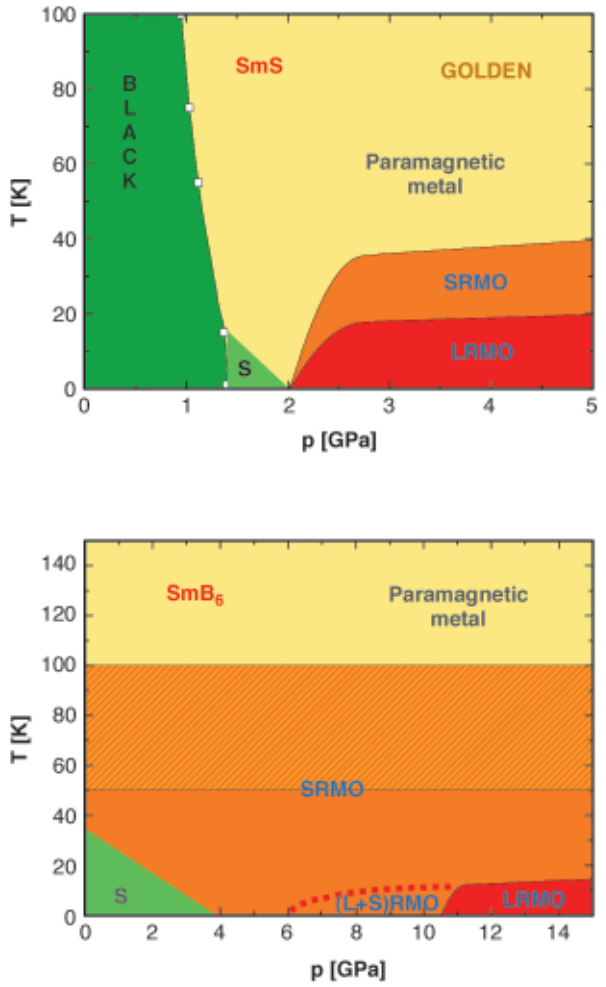

Fig. 9: The phase diagrams of SmS and SmB_6 as a function of temperature and pressure, with the magnetically-ordered phases as discovered by Nuclear Forward Scattering. Legend: SRMO = short-range magnetic order, LRMO = long-range magnetic order, S = semiconductor. The shaded region between 50 and 100 K in the phase diagram of SmB_6 indicates the smooth transition between the SRMO and the paramagnetic phases.

Examples of intermediate valence Sm compounds are the high pressure 'golden' phases of the Sm monochalcogenides (SmS, SmSe and SmTe) and SmB_6. They belong to the class of Kondo insulators or narrow-gap semiconductors, which behave at high temperature like an array of independent localised moments interacting with itinerant conduction electrons, whereas at low temperature they develop clear narrow-gap properties. Pressure was shown to increase the Sm valency in all of these compounds, so it was guessed that a trivalent state could be reached, where magnetic order would appear at low temperatures. However this order could never be observed. We have started a systematic investigation of the correlations between magnetism, electrical transport and valence in these compounds. The NFS measurements as a function of temperature and pressure on SmS and SmB_6 powders were performed on beamline **ID22N**. Our results are the first direct proof that pressure induces a magnetically ordered state for both compounds. This order likely appears when the semiconducting gap closes, for pressures which are unexpectedly much lower than those required to reach the fully trivalent state. The importance of short range magnetic correlations in the semiconducting phases could also be evidenced thanks to the use of a local probe like NFS. The phase diagrams which could be established for the two compounds by our and previous measurements are shown in **Figure 9**.

Our investigations show that NFS can be an invaluable tool for the study of magnetism of strongly correlated electron systems, thanks to its high sensitivity and its compatibility with the diamond anvil cell high pressure technique.

References

[1] P. Wachter, Handbook on the Physics and Chemistry of Rare Earths, vol. 19, ed. K. A. Gschneidner *et al.* (Amsterdam: North-Holland), p. 383 (1994).

[2] S. Chaudhary, M.K. Chattopadhyay, K.J. Singh, S.B. Roy, P. Chaddah, and E.V. Sampathkumaran, *Phys. Rev. B* **66**, 014424 (2002)

Principal Publication and Authors

A. Barla (a,b), J. Derr (a), J.P. Sanchez (a), B. Salce (a), G. Lapertot (a), B.P. Doyle (d), R. Rüffer (b), R. Lengsdorf (c), M.M. Abd-Elmeguid (c) and J. Flouquet (a), *Phys. Rev. Lett.* **94**, 166401 (2005).

(a) Département de Recherche Fondamentale sur la Matière Condensée, CEA, Grenoble (France)

(b) ESRF

(c) II. Physikalisches Institut, Universität zu Köln, Cologne (Germany)

(d) Laboratorio TASC-INFM, Trieste (Italy)

Magnetic Properties of EuS and EuSe at Extreme Pressures

The divalent Eu-chalcogenides EuX (X = O, S, Se, Te) are well-known model substances for Heisenberg magnetism because of the spin-only J = S = 7/2 4f-moment of the Eu^{2+}-ions and their simple NaCl structure. The variation of the magnetic ordering temperatures within the chemical series is described by the ferromagnetic J_1 exchange between neighbouring Eu-ions and the mostly antiferromagnetic J_2 exchange via the chalcogen ligands. High pressure studies of the EuX series with ^{151}Eu-Mössbauer spectroscopy and other

methods [1,2] have contributed important information on the magnetic interactions of EuX in their NaCl phases. Here we report on the first study of the magnetic properties of EuS and EuSe in the CsCl-type high-pressure phase at pressures up to 120 GPa using the ^{151}Eu nuclear forward scattering (NFS) technique developed at the ESRF [3].

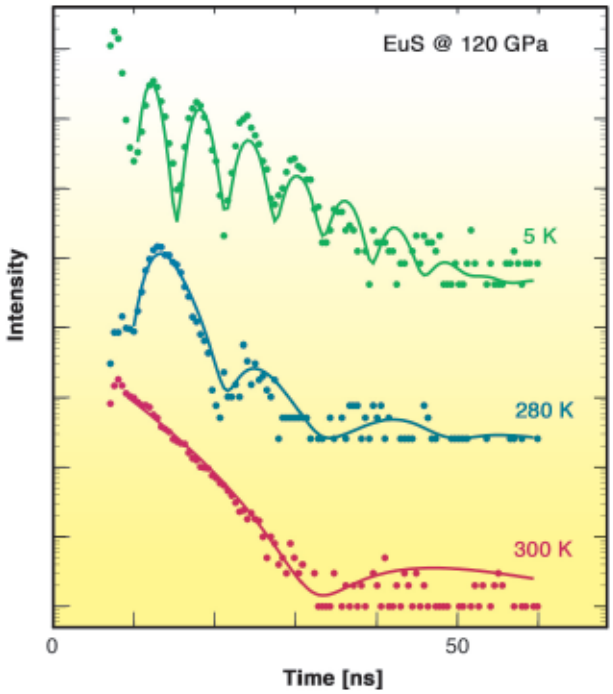

Fig. 10: ^{151}Eu-NFS spectra of EuS at 120 GPa below and above T_M = 295 K (note intensity in log scale).

Microgram samples of EuS and EuSe were pressurised in a special diamond anvil cell designed to fit into the cryomagnet at ID22N [3]; the NaCl to CsCl phase transitions occur around 20 and 15 GPa, respectively. For both samples we measured at each pressure a variety of NFS spectra at various temperatures (see **Figure 10**), from which we determined the magnetic ordering temperature T_M and the saturation magnetic hyperfine field B_{hf} ($T \rightarrow 0$ K). Above T_M we measured the isomer shift S_{IS} using an additional reference absorber [3]. Additional NFS-studies in external magnetic fields revealed the ferromagnetic nature of T_M as well as the sign of B_{hf}, similar to a previous study of EuTe at pressures up to 22 GPa [3]. The p-V relationship for EuS and EuSe was measured with energy-dispersive X-ray diffraction [4] to derive the interatomic distances used in **Figure 11**.

The present data on T_M, B_{hf} and S_{IS} for EuS and EuSe in the CsCl-phase are compiled in **Figure 11** together with the corresponding data in the NaCl phase. Within the NaCl structure a strong increase of the magnetic interactions is observed with decreasing Eu-Eu distance, reflected by the strong increase of T_M and B_{hf}. In the CsCl structure, we observe a further dramatic increase of T_M up to 295 K for EuS at 120 GPa and up to 300 K

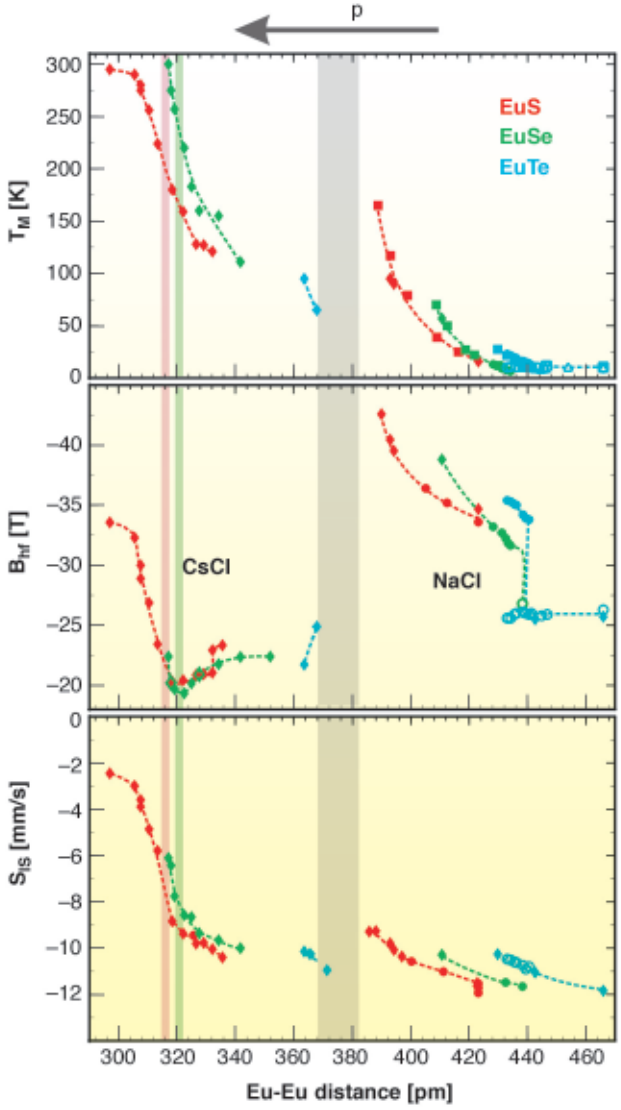

Fig. 11: Magnetic ordering temperature T_M, magnetic hyperfine field B_{hf} and isomer shift S_{IS} of EuS and EuSe (this study) together with EuTe [3] as a function of the Eu-Eu distance in the CsCl- and NaCl-structure.

for EuSe at 77 GPa. The corresponding hyperfine fields B_{hf} exhibit a markedly different behaviour in the CsCl phase. One observes first much smaller and initially decreasing values of B_{hf}. We attribute this to an alteration of the J_2 exchange, which contributes now, due to the different coordination and exchange paths, ferromagnetically (and therefore positively) to the negative values of B_{hf} [4].

Above 50 GPa for EuS and 60 GPa for EuSe, marked by vertical lines in **Figure 11**, a drastic change in the pressure dependent slope of S_{IS} and B_{hf} was observed. The strong increase of S_{IS} towards trivalent Eu indicate the onset of a mixed valence, more pronounced for EuS than for EuSe. The concomitantly observed increase of B_{hf} is attributed to admixtures of higher magnetic states with J = 1, 2 of the Eu^{3+} $4f^6$ ($^7F_{J=0,1,2}$) multiplet to the wavefunction of the mixed-valent Eu-ions. Details of this mechanism are described in [4]. From the additional strong increase of the isomer shift we estimate the valence v' of the Eu-ions in EuS at 120 GPa as v' = 2.5(1)

and in EuSe at 77 GPa as v' = 2.2(1) [4]. Most interestingly, the variation of T_M, B_{hf} and S_{IS} seems to saturate for EuS at that high pressures, while for EuSe a further strong increase of T_M well above 300 K is expected from the slopes of T_M, B_{hf} and S_{IS}.

This first study of CsCl-type EuS and EuSe yielded a wealth of information about the magnetic and electronic properties at these ultrahigh pressures. To the best of our knowledge there are no comparable studies of rare-earth systems in the 100 GPa range. The observation of the coexistence of strong ferromagnetic order and mixed valence in EuS in the CsCl-phase is completely different to the behaviour of EuO in the NaCl-phase [1], where a strong decrease of T_M in conjunction with the onset of a mixed valence was observed. Therefore similar high-pressure ^{151}Eu-NFS studies of EuO in the CsCl-phase are asked for.

References

[1] M.M. Abd-Elmeguid, R.D. Taylor, *Phys. Rev. B* **42**, 1048 (1990).
[2] R. Lübbers, K. Rupprecht, G. Wortmann, *Hyperfine Interactions* **128**, 115 (2000) and references therein.
[3] O. Leupold *et al.*, *Europhys. Lett.* 35, 671 (1996); O. Leupold, K. Rupprecht, G. Wortmann, *Structural Chemistry* 14, 97 (2003).
[4] K. Rupprecht, PhD thesis, Paderborn (2004); K. Rupprecht *et al.*, submitted.

Authors

K. Rupprecht (a), U. Ponkratz (a,b), O. Leupold (c), G. Wortmann (a)
(a) Department Physik, Universität of Paderborn (Germany)
(b) ESRF
(c) ESRF, now at HASYLAB, DESY, Hamburg (Germany)

New Applications

Hard X-ray Photoemission Spectroscopy from Solids with High Energy Resolution and Bulk Sensitivity

Photoemission spectroscopy (PES) is a powerful tool to investigate the electronic properties of materials, with impressive technical achievements in terms of energy, momentum, and angular resolution. Over the last two decades, PES experiments with synchrotron radiation exploited one of the key features of this technique, *i.e.* its surface sensitivity. By tuning the kinetic energy E_k of photoelectrons to the minimum of their mean free path λ in the solid, the measurement is sensitive to the topmost atomic layers only. However, this poses severe limitations to the investigation of bulk electronic properties. The use of hard X-rays (5-10 keV) is a possible route to perform volume sensitive PES. After the pioneering experiment by Lindau *et al.* [1], the development of Hard X-ray PES (HAXPES) has been restrained mainly by the poor resolving power of both photon source and electron analyser. Technical conditions have since improved considerably on modern high-resolution/high-flux beamlines, giving new impetus to the measurement of bulk sensitive PES spectra [2].

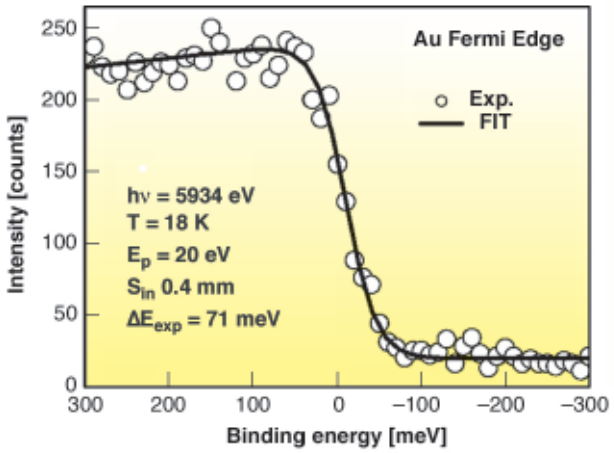

Fig. 12: Au Fermi level (circles) measured at hν = 5934 eV with pass energy E_p = 20 eV and analyser slits s_{in} = 0.4 mm. The acquisition time was 150 minutes and the counts correspond to an integration over 8 mm of detector active area. The overall energy resolution, as obtained from the fit of the Fermi edge (solid line), is about 71 meV FWHM (50 meV photons + 50 meV analyser).

We have developed a new electron spectrometer (VOLPE: VOLume PhotoEmission from solids) dedicated to HAXPES experiments and now fully operational at beamline ID16. During the commissioning phase, we tested the performance of our spectrometer in terms of energy resolution and probing depth, using polycrystalline noble metals and wedge-shaped thin layers grown on Silicon substrates, respectively. **Figure 12** shows the Fermi level of polycrystalline Au measured at T = 18 K and hν = 5934 eV. The total width of the Fermi edge is given by the temperature broadened Fermi distribution, convoluted with a Gaussian whose FWHM equals the overall experimental resolution (electron analyser + photons). The best fit (solid line in **Figure 12**) was obtained using a FWHM of 71 ± 7 meV, corresponding to a resolving power of $8x10^4$. The photon energy resolution was measured independently to be 50 meV, giving, for the analyser alone, an energy resolution of 51±8 meV (resolving power of 1.2×10^5).

We have also determined λ over the 4-6 keV range of electron kinetic energy E_k, using the so-called overlayer method (see **Figure 13a**), *i.e.*, measuring the intensity of

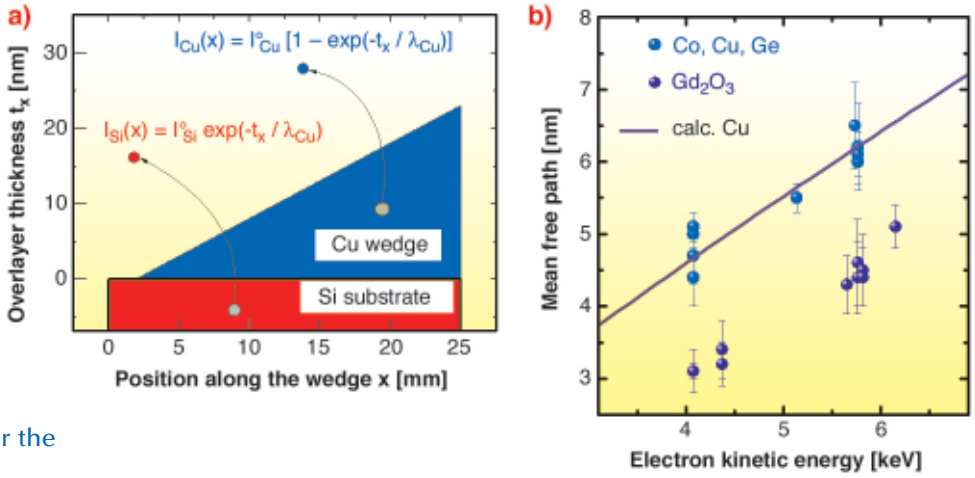

Fig. 13: Experimental determination of the mean free path λ. a) schematics of the overlayer experiment. The intensity of core level photoemission peaks from both the substrate (I_{Si}) and the overlayer materials (*e.g.*, I_{Cu}) is recorded as a function of the thickness t and related to the value of λ in the overlayer material. b) experimental values of λ in Co, Cu, Ge and Gd_2O_3 over the 4-6 keV range of kinetic energies.

substrate and overlayer core level peaks *vs*. the overlayer thickness [3]. Experimental values of λ for Co, Cu, Ge and Gd_2O_3 are shown in **Figure 13b**. In the case of Cu, for instance, we find λ = 62 Å at E_k = 6 keV, to be compared with λ = 8 Å at 600 eV. These values lead to some important remarks:

a) the information depth (defined as the thickness producing 95% of the total signal) is ~ 200 Å at 6 keV, against ~ 24 Å at 600 eV;

b) the contribution to the total intensity coming from the first atomic layer (≡ 2 Å) is 3% at 6 keV and 25% at 600 eV;

c) photoemission from a 10 Å thick layer buried under 100 Å of Cu will still be measurable at 6 keV (~3 x 10^{-2} reduction), but not at 600 eV (~3 x 10^{-6} reduction).

To conclude, our HAXPES measurements on ID16 set realistic conditions for photoemission in terms of both energy resolution and bulk sensitivity. The large probing depth achieved will have an immediate bearing on the measure of electronic properties in strongly correlated systems.

References

[1] I. Lindau, P. Pianetta, S. Doniach and F. Spicer, *Nature* **250**, 214 (1974).

[2] K. Kobayashi *et al. Appl. Phys. Lett.* **83**, 1005 (2003); M. Taguchi *et al. Phys. Rev. Lett.* **95**, 177002 (2005) and refs therein.

[3] M. Sacchi *et al.*, *Phys. Rev.* ***B*** **71,** 155117 (2005).

Principal Publication and Authors

P. Torelli (a), M. Sacchi (a), G. Cautero (b), M. Cautero (b), B. Krastanov (b) P. Lacovig (b), P.Pittana (b), R. Sergo (b), R. Tommasini (b), A. Fondacaro (c), F. Offi (c), G. Paolicelli (c), G. Stefani (c), M. Grioni (d), R. Verbeni (e), G. Monaco (e) and G. Panaccione (f), *Rev. Sci. Instr.***76**, 023909 (2005).

(a) Lab.LURE, Centre Univ. Paris Sud, Orsay (France)

(b) Sincrotrone Trieste S.C.p.A. (Italy)

(c) Dip. di Fisica Univ. Roma III (Italy)

(d) EPFL, Lausanne (Switzerland)

(e) ESRF

(f) TASC Laboratory, INFM – CNR, Trieste (Italy)

Improving X-ray Crystal Spectrometers with Position-sensitive Detectors

Inelastic X-ray scattering (IXS) spectrometers are often based on analyser crystals operating in the Rowland circle geometry. The crystal is used to select a desired bandwidth of radiation scattered by the sample and simultaneously to focus the gathered radiation onto an X-ray detector. To achieve the focusing properties, the crystal wafers are typically bent to have a spherical or cylindrical shape. Bending, however, increases the bandpass of the crystal due to elastic deformations. This is desirable in many applications where high flux is preferred over a high energy-resolving power. In cases where the resolving power is needed to exceed 10^5, these elastic deformations may become too large and other solutions need to be sought. For instance, in many very high energy resolution applications so-called diced analyser crystals are utilised. In this scheme, thousands of small flat crystals (dices or cubes) are arranged to mimic the shape of the spherical surface. Since each crystalline is flat, it behaves as a perfect single crystal with a very narrow reflection width. However, the price to pay is that the finite size of the cubes causes a geometrical contribution to the resolution function, of the form $\Delta E/E = c/R \cot\theta$, where c is the dice size (typically c = 0.7 mm), R the crystal curvature radius, and θ the Bragg angle.

So far, this cube-size contribution was considered inevitable. The only ways to minimise this effect have been reducing the cube size c, increasing the bending radius R, and selecting a photon energy and the reflection as close to backscattering as possible. These constraints have for instance forced the construction of very large experimental stations (*e.g.* at ESRF ID16 R = 6.5 m and θ = 89.98°). In a recent study at ID16 it was found that the cube-size contribution can be eliminated by noting that it corresponds to a dispersion of photon energies within the spatial focus. The focus of the analyser was found to be a square with dimensions 2c x 2c, with a position-energy

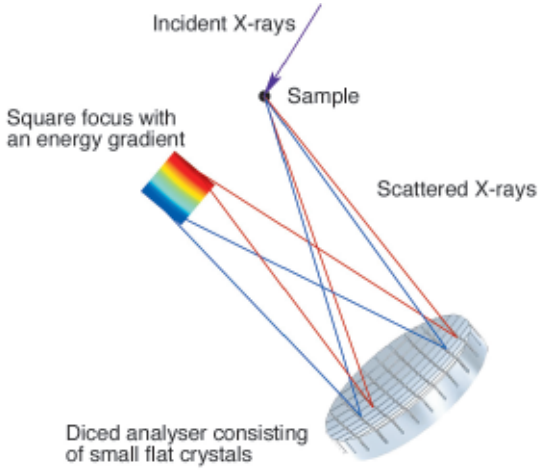

Fig. 14: A diced analyser crystal acts like a prism, *i.e.* it sorts out the spectrum of scattered radiation in space. This enables an analysis of the photon energy by observing its position in the focus.

relationship such that constant-Bragg-angle contours were observed. When c/R << sin(2θ), only a small part of the ring-like contour is observed and the position-energy dependence is close to linear (see **Figure 14**). The detector used in this experiment was a CMOS-based Medipix2 photon-counting pixel detector with a pixel size of 55 µm and sensitive area of 14 x 14 mm^2 [1]. Using this setup with R = 1 m, an unprecedented spectrometer resolution of 23 meV was achieved at 9.9 keV, and 10 meV at 13.8 keV, utilising the Si(555) and Si(777) reflections, respectively (see an example of a phonon spectrum in **Figure 15**). Without this method the resolution would have been 190 meV and 250 meV, respectively. This can be compared to the resolution at 7 meV achieved typically with a 6.5-m Rowland circle spectrometer at a photon energy of 13.8 keV.

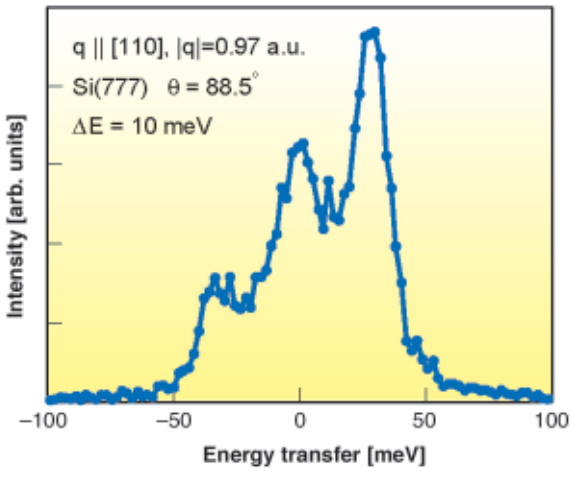

Fig. 15: Phonons in aluminium measured with 10 meV resolution with a IXS spectrometer based on 1-m Rowland circle and a position sensitive detector.

It was thus demonstrated that new photon-counting position-sensitive detectors can be used to enhance the resolution of IXS spectrometers considerably. The presented method allows for a marked increase in resolving power, while preserving all counted photons so that the improvement in resolution is not accompanied by any loss of signal intensity. This gives new possibilities for the construction of a much more powerful and compact high-resolution IXS instruments than has been possible this far, which may affect the design of future non-resonant and resonant IXS spectrometers.

References

[1] X. Llopart, M. Campbell, R. Dinapoli, D. San Segundo, E. Pernigotti, *IEEE Trans. Nucl. Sci*. **49**, 2279-2283 (2002).

Principal Publication and Authors

S. Huotari, Gy. Vankó, F. Albergamo, C. Ponchut, H. Graafsma, C. Henriquet, R. Verbeni and G. Monaco, *J. Synchrotron Rad.* **12**, 467-472 (2005).
ESRF

Phonon Density of States Probed by Inelastic X-ray Scattering

The shape of the frequency distribution function g(ω) of the normal modes of vibration of a crystal determines an important part of its properties, since it contains many relevant elastic and thermodynamic information. From the overall spectrum, temperature dependencies of the lattice contribution to the specific heat and the internal energy, the vibrational entropy, the mean force constant and the Debye temperature are obtained, whereas from the low frequency part the Debye velocity can be derived, giving access to aggregate elastic properties. Experimentally, g(ω), or the vibrational density of states (VDOS), is commonly determined by inelastic neutron scattering (INS) or by nuclear inelastic scattering. Here, we show that inelastic X-ray scattering (IXS) offers an alternative experimental method.

In analogy to coherent INS, inelastic scattering spectra of polycrystalline samples have to be recorded over a large range of momentum transfers (Q), but due to the Q-dependence of the atomic form factor, this sampling range needs to be optimised. We have developed semi-quantitative criteria, which are independent of any specific lattice dynamics model, and result only from simple symmetry considerations. The advantage of their use is that no *a priori* knowledge of the lattice properties is needed. The validity of our approach was checked by comparison of results for diamond with *ab initio* lattice dynamics calculations [1] and thermodynamic measurements.

The experiment was performed on **ID28**, utilising the silicon (9 9 9) setup, providing a total energy resolution of 3.0 meV. The momentum resolution was set to 0.7 nm^{-1} both in horizontal and vertical directions. As the spectrometer arm is equipped with five analysers, the spectra were recorded for two angular settings of the

Parameter	Calculated from VDOS	Other experimental data [3,4]
θ_D – high temperature	1930 K	1860 K
θ_D – low-temperature limit	2250 K	2240 K
Debye velocity	13550 m/s	13455 m/s

Table 1: Selected macroscopic parameters for diamond.

spectrometer arm, thus covering a *Q*-range from 60 to 75 nm^{-1} (approximately) and yielding ten IXS spectra. The total acquisition time per point was ~ 235 s with a maximum inelastic count rate of ~ 2.5 s^{-1}. The sample was polycrystalline diamond with an average grain size of 3-5 μm, and the resulting effective scattering volume amounted to 0.08 mm^3. For the data treatment we followed the same approach as for nuclear inelastic scattering, where the multiphonon term is eliminated simultaneously with the deconvolution of the data with the instrumental function [2].

Figure 16 shows the VDOS obtained, together with the result of an *ab initio* calculation [1]. The agreement is quite remarkable: the position of special points is nearly identical, and the high-energy peak, due to the overbending of the optical phonon branch, is clearly visible.

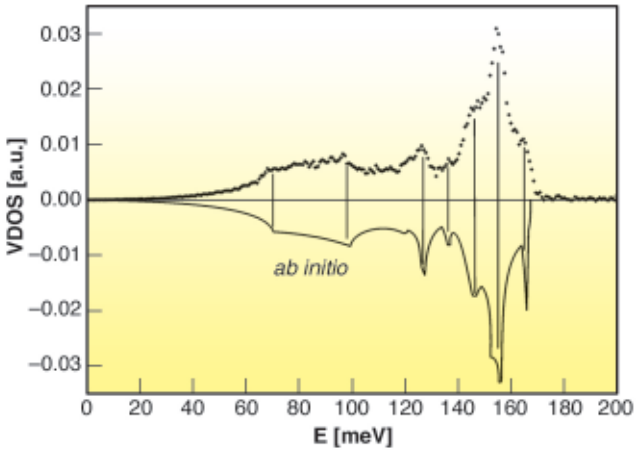

Fig. 16: Reconstructed vibrational density of states of diamond vs. calculated *ab initio* results [1].

The excellent quality of our experimental VDOS allowed the determination of several macroscopic parameters such as the specific heat at constant volume, the low- and high-temperature limit of the Debye temperature θ_D, and the Debye velocity V_D. **Table 1** shows a selection of our derived macroscopic parameters, compared to other experimental results.

The VDOS data were complemented by IXS measurements in the low-*Q* region which provide the orientationally averaged longitudinal acoustic dispersion. The resulting sound velocity V_L = 18.24 km/s, combined with the Debye velocity V_D, allows the extraction of the effective shear velocity V_S = 12.43 km/s. These values give an appropriate description of the macroscopic aggregate elasticity of diamond.

Further experiments were performed on MgO, BN (zincblende and wurtzite polymorphs) and various ice polymorphs. The general applicability of the method for the study of elementary solids is easily estimated, showing that the VDOS can be determined with an appropriate accuracy for essentially all elemental solids. One of the potential applications of this novel technique is the VDOS determination of samples submitted to very high pressures. In this case the signal level for elements heavier than, say, scandium should be sufficiently high to allow measurements on tiny amounts of samples as in a diamond anvil cell.

It is worth noting that with respect to INS, the amount of material needed is 3-5 orders less, and anomalous absorption (like for B, Cd, Gd…) or anomalously high cross-sections (H) are not present. Since the scattering strengths for neutrons and X-rays are essentially different, it opens the possibility to extract directly the partial densities of states in at least binary systems from combined measurements.

References

[1] P. Pavone *et al.*, *Phys. Rev. B,* **48**, 3156-3163 (1993).
[2] V.G. Kohn and A.I. Chumakov, *Hyperfine Interactions* **125**, 205-221 (2000).
[3] E.S. Zouboulis, M. Grimsditch, A.K. Ramdas, S. Rodriguez, *Phys.Rev. B*, **57**, 2889-2896 (1988).
[4] Specific heat: non-metallic solids. Eds. Y.S. Touloukian, E.H. Buyco, IFI/Plenum New York – Washington 1970.

Principal Publications and Authors

A. Bosak, M. Krisch, *in press, Phys. Rev. B; in press, Radiation Physics and Chemistry.*
ESRF

Further Experiments

Lattice Dynamics of MgO at High Pressure: Theory and Experiment

The experimental determination of the phonon dispersion at high pressure constitutes an important ingredient for the characterisation of the physical properties of materials at extreme conditions. It gives access to valuable quantitative information concerning

elasticity, thermodynamic properties, and the dynamics of phase instabilities. Furthermore, the experimental data provide important tests for the accuracy of theoretical lattice dynamical models. Among these the most advanced ones are *ab initio* quantum mechanical calculations, using density functional perturbation theory. Critical inputs are the appropriate choice of the potential (all-electron or pseudopotential approaches) and the correct description of the exchange-correlation term. If a good agreement with the experimental phonon dispersion is observed, these calculations can then be used with increased confidence to describe the physical properties at very high pressures beyond the reach of current experimental methods.

Here we present experimental and theoretical results on MgO, a prototype oxide due to its simple structure and the large stability field (in pressure and temperature) of the NaCl structure. MgO is furthermore an important ceramic for industrial applications, and of great interest for Earth sciences, since it is a major mineral phase of the Earth's lower mantle. A doubly polished single crystal of MgO of (100) orientation, 30 x 50 µm size and a thickness of 20 µm was loaded in a diamond-anvil cell with He as pressure transmitting medium. The IXS experiment was performed on beamline **ID28** with an overall energy resolution of 3 meV. Theoretical phonon dispersion curves were calculated using density-functional perturbation theory using the pseudopotential plane wave code ABINIT [1]. Details on the calculations can be found elsewhere [2].

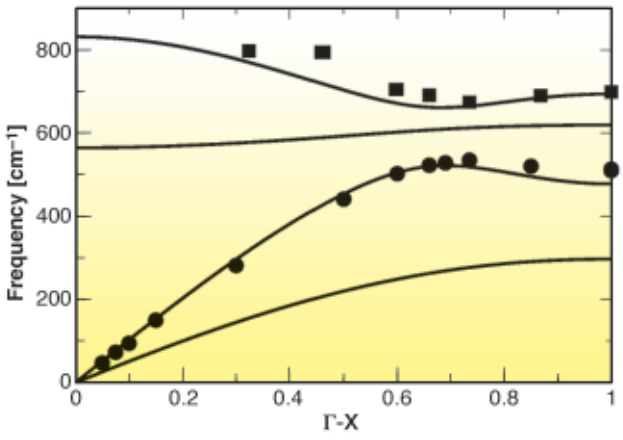

Fig. 17: Phonon dispersion of MgO along the Γ-X direction at 35 GPa. Experimental data are shown by symbols (full circles: LA branch; full squares: LO branch). Results of the *ab initio* calculations, which include the transverse acoustic and optic branch, are shown as solid lines.

Figure 17 shows the accordance between the two longitudinal phonon branches, acoustic and optic, measured along the Γ– X direction at 35 GPa with those calculated by *ab initio* methods. The fact that characteristic features in the phonon dispersion are well reproduced by calculations gives confidence that *ab initio* predictions of thermodynamic properties of MgO at high pressure will be accurate. The determination of a thermodynamic property at high pressure requires experimental determination of the thermal expansion and bulk modulus, which are recast into an equation of state (EOS). Such EOS data are very few and when available, the data usually requires large extrapolation. Thermodynamic properties at high pressure may be calculated from a combination of calorimetric data at 1 bar and the volume integral with changing pressure and temperature [3]. Using the available thermodynamic data we obtain C_V = 30 (+/-5) and ΔS = 20.68 (+/-1) Jmol^{-1}K^{-1}. From the calculated phonon density-of-states at 35 GPa we determine C_V = 31.71 and S = 20.04 Jmol^{-1}K^{-1}. The two data sets match within the errors of experimental data.

In summary, we demonstrate the ability of modern theory to reproduce experimental data on lattice dynamics of an inorganic compound at very high pressure. Expanding such tests to other, more complex systems could be beneficial for the development of both theory and experiment. These tests, validating the approximations done in the calculations, will allow the reliable determination of the thermodynamic properties of materials at high pressure, which are otherwise extremely difficult to assess by experimental methods.

References

[1] X. Gonze *et al.*; *Comp. Mater. Sci.* **25**, 478 (2002).
[2] A.R. Oganov, M.J. Gillan, and G.D. Price; *J. Chem. Phys.* **118**, 10174 (2003).
[3] S.K. Saxena, N. Chatterjee, Y. Fei and G. Shen in *Thermodynamic data on oxides and silicates;* Springer Verlag, Berlin, 428 p (1993).

Principal Publication and Authors

S. Ghose (a), M. Krisch (b), A.R. Oganov (c), A. Beraud (b), A. Bossak (b), R. Gulve (d), R. Seelaboyina (d), H. Yang (d) and S.K. Saxena (d), *accepted in Phys. Rev. Lett.*
(a) Mineral Physics Group, University of Washington, Seattle (USA)
(b) ESRF
(c) Laboratory of Crystallography, Department of Materials, E.T.H., Zurich (Switzerland)
(d) Center for Study of Matter at Extreme Conditions, Florida International University Park, Miami (USA)

Non-ergodicity in Locally-ordered Systems in the Proximity of the Glass Transition

When a simple liquid is cooled below its melting temperature, each particle becomes trapped progressively in the transient cage formed by its nearest neighbours, and partakes in correlated collisions

inducing a strong damping of the motion. Successive diffusion out of the cage needs a cooperative rearrangement of many particles and provides long-range transport motion, which lessens drastically as the temperature is lowered. This cage effect mechanism can be regarded as the microscopic origin of the eventual structural arrest of the liquid occurring at the glass-transition. In more complex systems like associated and covalent liquids, the ubiquitous class of liquids including water and silica, the cage effect manifests a different nature since molecules are trapped in energetic cages of hydrogen or covalent bonds, and bond breaking and formation is needed for diffusion to occur. Finding a common paradigm to explain the structural arrest in the different classes of liquids represents an important challenge for condensed matter physics.

The mode coupling theory (MCT) was introduced to give a self-consistent description of the density-fluctuation dynamics and of the particle caging in liquids [1]. The derived equations of motion for the density-fluctuations lead to a bifurcation of the long-time limit of the density correlators, the so-called non ergodicity factor f_Q, if a control parameter like temperature crosses a critical value, T_c. Within MCT, specific predictions are advanced for the temperature and wave vector dependence of f(Q,T): i) A square-root temperature behaviour below T_c, *i.e.*, $f_Q(T) = f_Q^c + h_Q \sqrt{T_c - T/T_c}$, where f_Q^c is the critical non-ergodicity parameter and h_Q the critical amplitude at a fixed wavevector Q; ii) A Q-dependence of f_Q^c and of h_Q that follows the oscillations of the static structure factor S(Q).

While a large number of experimental and theoretical studies have been devoted to the verification of the MCT predictions in Van-der-Waals molecular liquids, not as much attention has been devoted to associated and covalent liquids, and the results are often mutually conflicting. In these liquids, the local order extends over several neighbouring molecules reflecting a non-trivial Q behaviour in the low-Q region of the static structure factor, S(Q). This Q regime has only recently been made accessible to experimental investigations thanks to development of the high-resolution inelastic X-ray scattering (IXS) technique.

The molecular system of interest here, m-toluidine, is characterised by a spatial organisation of the molecules induced by hydrogen bonds extending over several molecular diameters and giving rise to nanometre-size clusters [2]. The non-ergodicity factor of supercooled and glassy m-toluidine has been measured, through IXS experiments performed at beamline **ID16**, in the mesoscopic Q range between 1 and 10 nm^{-1}, around the prepeak in the static structure factor related to the local order (Q_{pp} = 5 nm^{-1}).

We show that the basic general predictions of MCT about the non-ergodicity factor are verified in m-toluidine

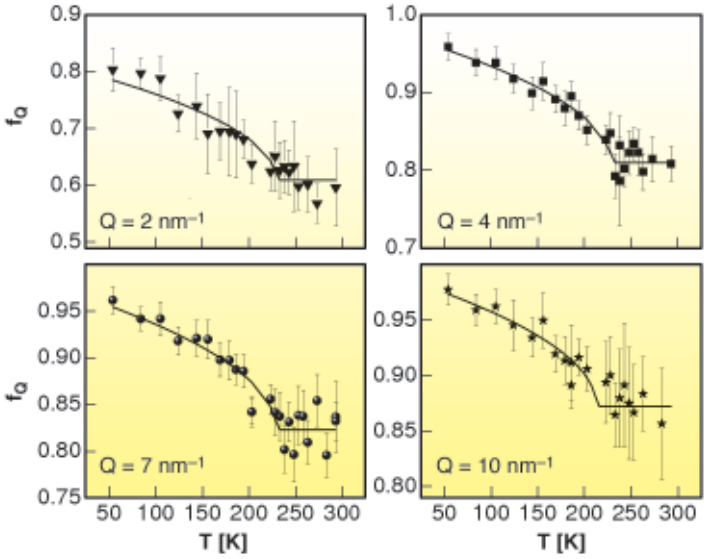

Fig. 18: Temperature dependence of the non-ergodicity factor f_Q of m-toluidine for different values of the exchanged wavevector Q. The solid lines are the best fits obtained using the square-root function predicted by the MCT.

(see **Figure 18** and **Figure 19**), providing experimental evidence that the signature of the ergodic to non-ergodic transition, valid for simple liquids, lives on in clustering systems. The present findings indicate that the early stage of the cooperative rearrangements, where the cage effect dominates the molecular dynamics, exhibits a universal character, common to simple liquids and liquids with a local order. This generality is not so obvious, because it puts on the same level the structural arrest in simple and in locally ordered liquids, notwithstanding that cage formation is controlled by different mechanisms. This picture opens the way to the investigation of the fast dynamics of a wider class of clustering systems, including network forming polymers,

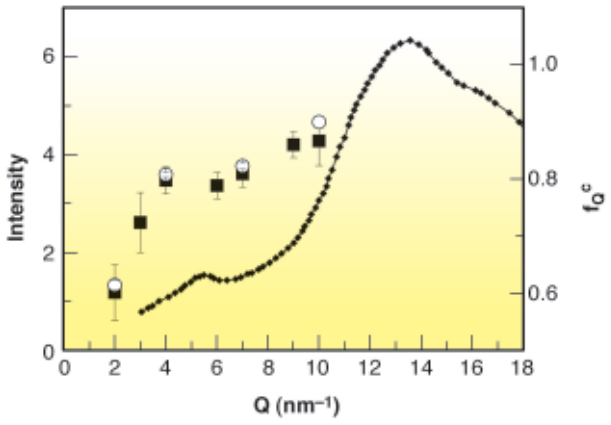

Fig. 19: X-ray diffraction pattern (left axis) of liquid m-toluidine at ambient temperature taken from Ref. [2], compared with the parameter f_Q^c (right axis) obtained from the fit of the experimental $f_Q(T)$ data (open circles); full squares indicate the values of f_Q at T = 263 K — a temperature in the plateau region of $f_Q(T)$ — for all the available Q.

where the structural arrest is controlled by irreversible bond formation.

References

[1] W. Götze, and L. Sjögren, *Rep. Prog. Phys.*, **55**, 241 (1992).
[2] D. Morineau *et al.*, *Europhys. Lett.*, **43**, 195 (1998); M. Descamps *et al.*, *Prog. Theor. Phys. Suppl.* 126, 207 (1997).

Principal Publication and Authors

L. Comez (a,b,c), S. Corezzi (a,b,d), G. Monaco (e), R. Verbeni (e), and D. Fioretto (a,b,c), *Phys. Rev. Lett.*, **94**, 155702 (2005).
(a) INFM CRS-SOFT, c/o Universita´ di Roma "La Sapienza", (Italy)
(b) INFM UdR-PG, c/o Dipartimento di Fisica, Universita´ di Perugia (Italy)
(c) Dipartimento di Fisica, Universita´ di Perugia, (Italy)
(d) Dipartimento di Fisica, Universita´ di Roma "La Sapienza" (Italy)
(e) ESRF

Intrinsic Double-plasmon Excitations in Simple Metals

The plasmon is a unique and well understood collective excitation in the interacting electron gas. More than three decades ago the simultaneous excitation of two plasmons was predicted as a special correlation effect [1]. The quantitative theoretical treatment of this intrinsic plasmon-plasmon (pl-pl) excitation has to consider effects beyond the so-called random-phase approximation, which has explained the single-plasmon excitation reasonably well. Thus, a calculation of the intrinsic pl-pl excitation for arbitrary momentum transfer **q** and energy transfer ω was accomplished only recently [2]. These calculations predict that this manifestation of a pure correlation effect becomes experimentally observable in the high energy-loss tail of the dynamic structure factor S(**q**,ω) of simple metals.

Inelastic X-ray scattering (IXS) is the favourable technique to study the high energy tail of the dynamic structure factor for large momentum transfers because multiple scattering does not affect the experimental spectra in contrast to electron energy loss spectroscopy, where extrinsic plasmon losses can obscure the information on electron correlations. IXS measurements of the dynamic structure factor were performed for aluminium single crystals and polycrystalline sodium at different momentum transfer around the plasmon cut-off vector q_C at beamline ID16 utilising the Rowland-type spectrometer. The experimental results of aluminium for **q** ∥ [100] are presented in **Figure 20**. The dominating feature in the spectra is the single-plasmon excitation

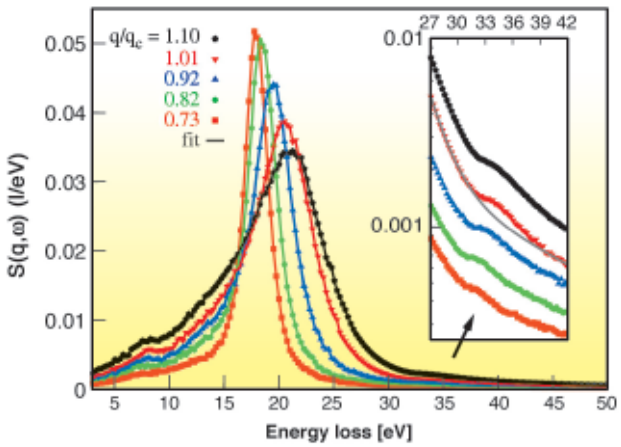

Fig. 20: Measurements of the dynamic structure factor of aluminium for different momentum transfer. The inset highlights the intrinsic double-plasmon feature in the tail of the plasmon excitation.

around an energy loss of 20 eV. Nevertheless, in the high energy-loss tail a structure around 35 eV is visible which is highlighted in the inset of this figure. This structure is extracted from the slowly decreasing tail of the plasmon excitation and is presented in **Figure 21**. The theoretical pl-pl excitation spectra calculated using many-body perturbation theory of the homogeneous-electron-gas model beyond the random-phase approximation [2] are shown in the inset of **Figure 21** for comparison. Based on the q-dependence of both the intensity and the peak position of this feature it could be unambiguously attributed to the predicted intrinsic pl-pl excitation when compared to theory. The experimental and computed pl-pl spectra exhibit also the same shape but the theory overestimates the energy-loss position of the pl-pl excitation by 2 eV which could be related to band structure and correlation effects beyond this theoretical approach. Moreover, the measurements for **q** ∥ [100] and **q** ∥ [110] on aluminium single crystals show no significant **q**-orientation dependence of the intrinsic double-plasmon feature even though the shape S(**q**,ω) is strongly **q**-orientation dependent. The pl-pl excitation

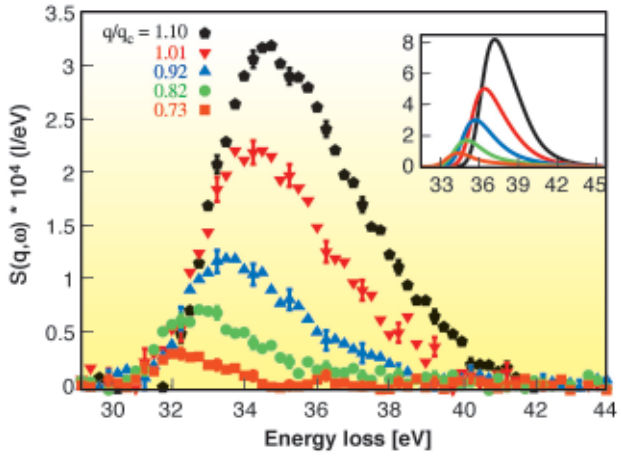

Fig. 21: Extracted double-plasmon excitation spectra compared to theoretical predictions (inset).

was also measured in the high energy-loss tail of the dynamic structure factor of polycrystalline sodium and was found to be in good agreement with theory.

In conclusion, new structures in the high energy-loss tail of the dynamic structure factor of simple metals, aluminium and sodium, have been found and could be clearly attributed to intrinsic pl-pl excitations. These structures are a unique manifestation of electron correlation and are hardly influenced by lattice effects. Therefore, intrinsic double-plasmon excitations offer a new testing ground for the theoretical description of correlation effects for systems which closely resemble the jellium model by means of a diagrammatic expansion of the polarisability.

References

[1] M. Hasegawa and M. Watabe, *J. Phys. Soc. Jpn.* **27**, 1393 (1969); D. F. DuBois and M. G. Kivelson, *Phys. Rev.* **186**, 409 (1969).
[2] K. Sturm and A. Gusarov, *Phys. Rev.* B **62**, 16474 (2000).

Principal Publication and Authors

C. Sternemann (a), S. Huotari (b), G. Vankó (b), M. Volmer (a), G. Monaco (b), A. Gusarov (c,d), H. Lustfeld (c), K. Sturm (c) and W. Schülke (a), *Phys. Rev. Lett.* **95**, 157401 (2005).
(a) Department of Physics, University of Dortmund (Germany)
(b) ESRF
(c) Forschungszentrum Jülich GmbH (Germany)
(d) SCK.CEN (Belgium)

Photosynthetic Dioxygen Formation Tracked by X-ray Experiments with Microsecond Resolution

In plants, algae and cyanobacteria, electrons and protons are extracted from water molecules in a light-driven process denoted as photosynthetic water oxidation. Thereby the atmospheric dioxygen (O_2) is formed. The reactions are catalysed by a tetra-manganese complex bound to the proteins of photosystem II (PSII). For more than 30 years, the paradigm for understanding O_2 evolution has been the S-state cycle model [1] of water oxidation involving transitions between five states (S_0, S_1,...S_4) of the Mn complex. Dioxygen is formed in the $S_3 \Rightarrow S_0$ transition. A crucial intermediate of this transition, the S_4-state, remained enigmatic.

One round of the S-cycle requires four light quanta. Here, these were provided by successive laser flashes that drive isolated PSII particles through the reaction cycle. Each light flash leads to the formation of an oxidised tyrosine residue ($Tyr_Z^{\bullet}$) which then extracts an electron from the Mn complex. We monitored the redox processes of the protein-bound Mn complex by fluorescence-detected X-ray absorption spectroscopy (XAS) at the Mn K-edge in real time [2]. Facilitated by the high flux and stability of the X-ray beam at beamline ID26, for the first time we could follow changes in the Mn X-ray fluorescence after laser-flash illumination of PSII samples with a time resolution of 10 µs thereby directly watching the S-transitions (**Figure 22a**). At an excitation energy of 6552 eV, for $S_1 \rightarrow S_2$ (first flash), $S_2 \rightarrow S_3$ (second flash), and $S_0 \rightarrow S_1$ (fourth flash), the exponential absorption decrease indicated oxidation of the Mn complex with the halftimes shown in **Figure 22**.

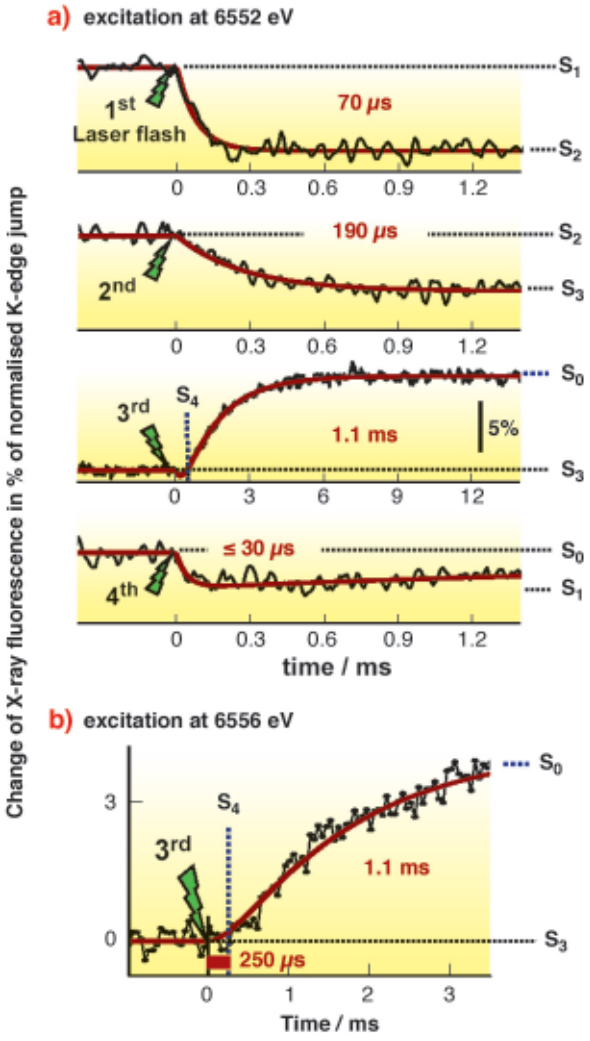

Fig. 22: (a) Oxidation and reduction of the Mn complex of PSII monitored by time-resolved X-ray measurements. Nanosecond flashes (20 ms duration) of green Laser light initiated the S-state transitions in PSII samples monitored by X-ray fluorescence (excitation energy of 6552 eV). The time course of the Mn K_α-fluorescence was recorded with a time resolution of 10 µs per data point. Solid lines represent simulations. (b) X-ray fluorescence change on the O_2-evolving transition induced by the third laser flash (X-ray excitation at 6556 eV). The lag phase of ~ 250 µs duration can be assigned unambiguously to intermediate formation. The simulation (line) involves two successive reaction steps.

The third Laser flash induced the S_3 to S_0 transition. An absorption increase due to Mn reduction by the substrate water upon O_2 formation was observed. The absorption increase was preceded by a lag phase of about 250 µs duration (**Figure 23**). This lag phase suggested a kinetically resolvable intermediate. However, a minor fraction of PSII that undergoes the $S_2 \rightarrow S_3$ transition on the third flash (due to PSII which did not turn over on the first laser-flash) might mimic a delay phase in the $S_3 \Rightarrow S_0$ transition. A time-resolved XAS experiment at 6556 eV clarified the situation since no change in the X-ray absorption is observed for $S_2 \rightarrow S_3$ at this energy. A sizable lag phase still was present (**Figure 22b**), proving the existence of a kinetically resolvable intermediate. The intermediate is formed prior to the Mn-reducing/O_2-forming step and thus represents the long-searched-for S_4-state.

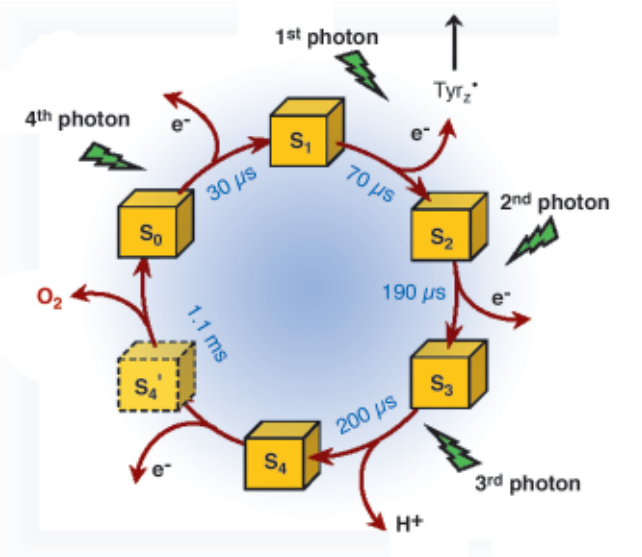

Fig. 23: Extension of the classical S-state cycle of photosynthetic oxygen evolution. The half-times of the S-transitions were determined by the X-ray experiment at the Mn K-edge. Existence and formation rate of the S_4 state have been uncovered in the present investigation. S_4 is not formed by electron transfer to Tyr_Z•, but by a deprotonation reaction and represents the starting point for O-O bond formation. S_4' denotes a hypothetical intermediate where four electrons have been extracted from the Mn complex, but O_2 has not been formed.

Further characterisation of the intermediate enabled us to identify the chemical nature of the S_4-state. We propose a 'proton-first' reaction sequence on the oxygen-evolving transition, where the Tyr_Z• radical induces, likely electrostatically, the deprotonation reaction which is a prerequisite to the subsequent electron transfer from the manganese/water complex to Tyr_Z•. Our identification of the S_4 state will spur further investigations on this key step in photosynthetic water oxidation. It leads to an extension of the classical S-state cycle because the deprotonation must be followed by electron transfer to Tyr_Z•, this implying an S_4'-state (**Figure 23**). The described progress was facilitated by a novel time-resolved X-ray experiment. This represents another step forward towards a structural biologist's dream: watching biological function in real time.

Acknowledgements

We thank Drs. T. Neisius, S. Eeckhout, and P. Glatzel (all ESRF) for excellent support and P. Loja (our group) for her important contributions to XAS data collection. Financial support by the Deutsche Forschungsgemeinschaft (SFB 498, projects C6 and C8) and the Bundesministerium für Bildung und Forschung (grant 05KS1KEA/6) is gratefully acknowledged.

References

[1] B. Kok, B. Forbush, M. McGloin, *Photochem. Photobiol*. **11**, 457-475 (1970).

[2] M. Haumann, C. Müller, P. Liebisch, L. Iuzzolino, J. Dittmer, M. Grabolle, T. Neisius, W. Meyer-Klaucke, H. Dau, *Biochemistry* **44**, 1894-1908 (2005).

Principle Publication and Authors

M. Haumann, P. Liebisch, C. Müller, M. Barra, M. Grabolle, H. Dau, *Science* **310**, 1019-1021 (2005).

Freie Universität Berlin, FB Physik (Germany)

Iron Oxidation State in Impact Glass by High-resolution XANES Spectroscopy: Implications on the Formation Conditions

An impact event marking the limit between the Cretaceous and Tertiary (K/T) ages resulted in the formation of a ~ 180 km wide impact crater and possibly triggered the K/T mass extinction event. The impact event distributed a huge mass of ejecta material worldwide, including impact glass spherules resulting from the quenching of molten target rock. While most of the glassy spherules worldwide are almost completely recrystallised, fresh unaltered impact glass can be recovered at few sites, *e.g.*, at Beloc, Haiti and Mimbral, Mexico. Three glass varieties have been found so far at Haiti: black, yellow, and HSiK impact glass. Black impact spherules consist of silicate glass of andesitic composition (63 wt% SiO_2, 7 wt% CaO), whereas the much rarer yellow variety consists of silicate glass (49 wt% SiO_2) with high Ca (about 25 wt% CaO) and S contents (0.5 to 2 wt% S). The HSiK glass is represented by a single sample with very high Si content (86 wt% SiO_2) and especially low Ca content (0.38 wt% CaO). Although several studies on the chemical and isotopic composition of these impact glasses exist, almost no studies on the Fe coordination number and oxidation state have been reported. Such studies are however of utmost importance to reconstruct the oxygen fugacity conditions prevailing during impact melt formation.

We examined the iron local environment in a suite of impact glasses (**Figure 24**) from the Cretaceous-Tertiary (K/T) boundary section at Beloc spanning the widest possible variety of glasses (9 black impact glasses, 5 yellow impact glasses, and the only HSiK impact glass available so far) by Fe K-edge high-resolution X-ray Absorption Near Edge Structure (XANES) spectroscopy at the ID26 beamline. The very high intensity and collimation of the X-ray beam allowed us to collect data on glass samples as small as 100 micrometres. The pre-edge peaks of our XANES spectra (**Figure 25**) display noticeable variations which are indicative of significant changes in the Fe oxidation state, spanning a wide range from about 20 to 100 mol% trivalent Fe. All data plot along a trend, falling between two mixing lines joining a point calculated as the mean of a group of tektites studied so far (consisting of 4- and 5- coordinated Fe^{2+}) to $^{[4]}Fe^{3+}$ and $^{[5]}Fe^{3+}$, respectively. Thus, the XANES spectra can be interpreted as a mixture of $^{[4]}Fe^{2+}$, $^{[5]}Fe^{2+}$, $^{[4]}Fe^{3+}$ and $^{[5]}Fe^{3+}$. There is no evidence for six-fold coordinated Fe; however, its presence in small amounts cannot be excluded from XANES data alone. Our observations are explained by a very large variety of oxygen fugacity conditions prevailing during melt formation. Furthermore, there is a clear positive relationship between the $Fe^{3+}/(Fe^{2+} + Fe^{3+})$ ratio and the Ca content of the studied glasses, suggesting that the Fe oxidation state was affected by the variable contribution of the Ca-sulphate bearing sedimentary rocks overlying the target rock at the impact site.

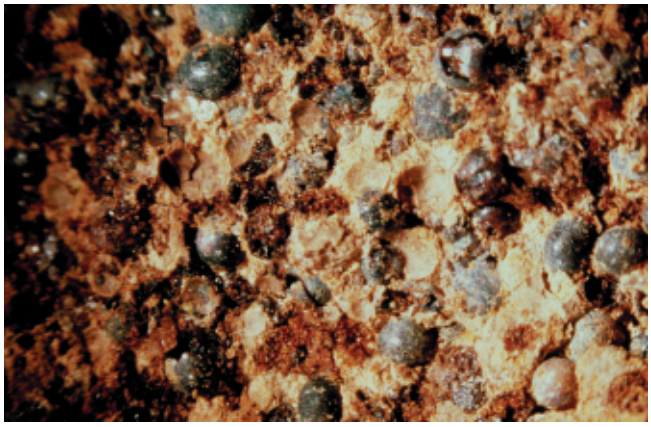

Fig. 24: Microphotograph of black impact glass spherules.

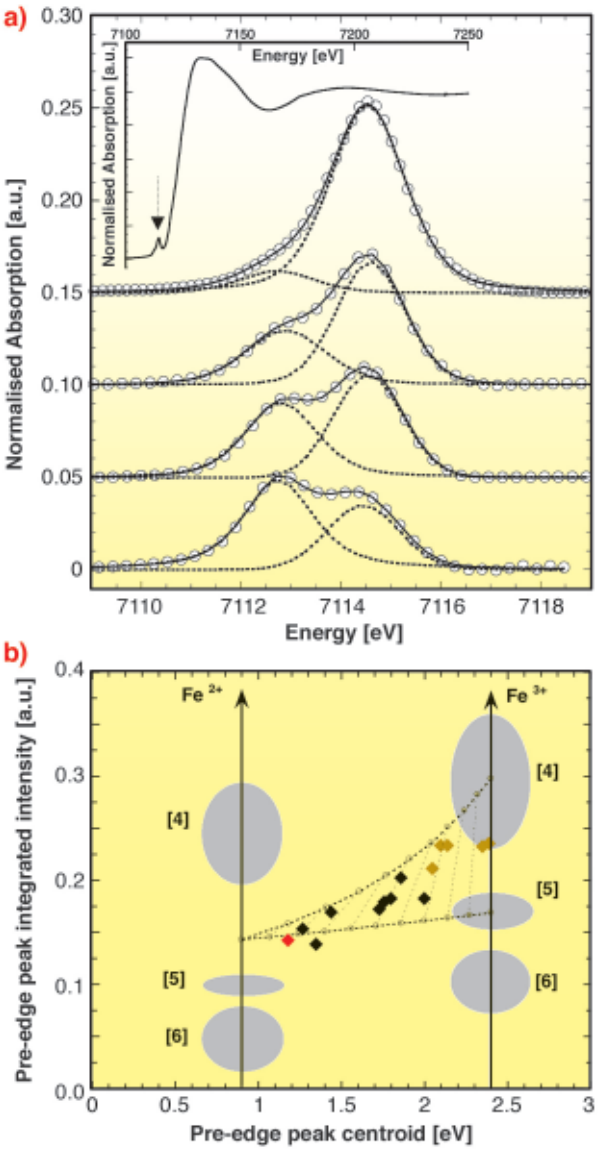

Fig. 25: a) Pre-edge peaks of Fe K-edge XANES spectra of impact glasses form the K/T boundary layer. The calcium concentration in the samples increases from bottom to top spectra. The experimental data (empty circles) are shown along with the fitted components (dashed line) and their sum (solid line). In the inset the XANES spectrum of a sample is shown. The arrow points to the pre-edge region. b) Plot of the pre-edge peak integrated intensity vs. centroid energy (zero refers to the edge energy of metallic iron). Diamond symbols refer to the samples studied here (black, yellow and red for black, yellow and HSiK spherules respectively). The shaded ellipses indicate the field of data occupied by Fe model compounds of known oxidation state and coordination number (Giuli *et al.*, 2005). Also shown are the mixing lines (dashed lines + circles) between $^{[4]}Fe^{3+}$ or $^{[5]}Fe^{3+}$ and Fe^{2+} in a mixture of 4- and 5-fold coordinated sites.

References

[1] G. Giuli, S.G. Eeckhout, E. Paris, C. Koeberl and G. Pratesi, *Meteoritics and Planetary Science*, **40**, 1575-1580 (2005).

Principal publication and authors

G. Giuli (a), S.G. Eeckhout (b), E. Paris (a), C. Koeberl (c), and G. Pratesi (d) (2006) (in preparation).
(a) Dipartimento di Scienze della Terra, Università di Camerino (Italy)
(b) ESRF
(c) Department of Geological Sciences, University of Vienna (Austria)
(d) Dipartimento di Scienze della Terra, Università di Firenze (Italy)

Element Specific Vibrational Dynamics in Filled Skutterudites

Thermoelectric devices convert thermal energy into electric energy and vice-versa through the Seebeck and Peltier effects, respectively. These devices are environmentally friendly and highly reliable. Because their efficiency is relatively poor when compared to conventional power plants or compressor-based refrigerators, present use is limited to critical applications, such as deep space probes and submarines. During operation, the thermoelectric material must sustain a temperature gradient and thus, its thermal conductivity must be low. In contrast, the thermoelectric material must exhibit a high electrical conductivity to minimise energy dissipation or maximise the current. Thus, a suitable thermoelectric material must behave [1] as a "phonon glass and an electron crystal". One way to achieve the reduction in thermal conductivity of a crystal, without significant reduction of the electrical conductivity, is to insert loosely bound atoms into voids or cages of a crystalline solid.

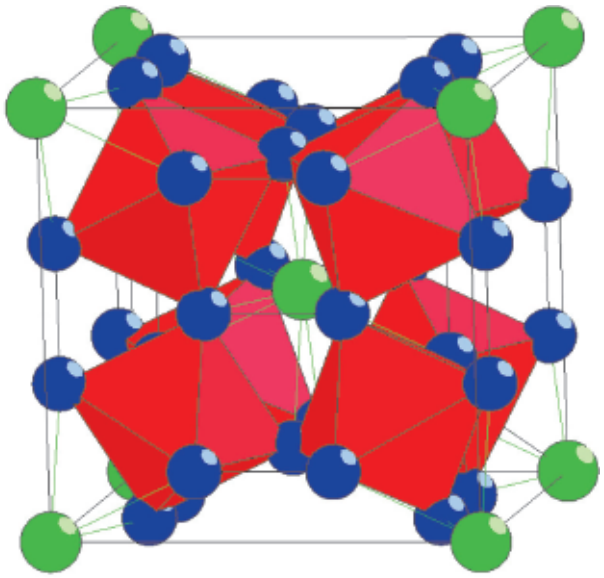

Fig. 26: The crystal structure of $EuFe_4Sb_{12}$. The green and blue spheres are europium and antimony, respectively. The iron atoms are at the centre of the red octahedra.

The lattice of the $CoSb_3$ skutterudite provides voids that can be filled with rare-earth elements, *R*, to form filled skutterudites, RM_4Sb_{12}, where *M* is Co or Fe. **Figure 26** shows the crystal structure of $EuFe_4Sb_{12}$, in which europium ions are loosely bound in their Fe-Sb cage and are believed to be responsible for the observed reduction in thermal conductivity. The experimental characterisation of the vibrational modes of the filling europium and of its cage is instrumental in understanding the role of the filling element in reducing the thermal conductivity. Among the available techniques, only nuclear inelastic scattering provides access to the *partial*, element specific, density of vibrational states of an atom that must have a Mössbauer active nuclide. Fortunately, all three elements in $EuFe_4Sb_{12}$ fulfil this condition.

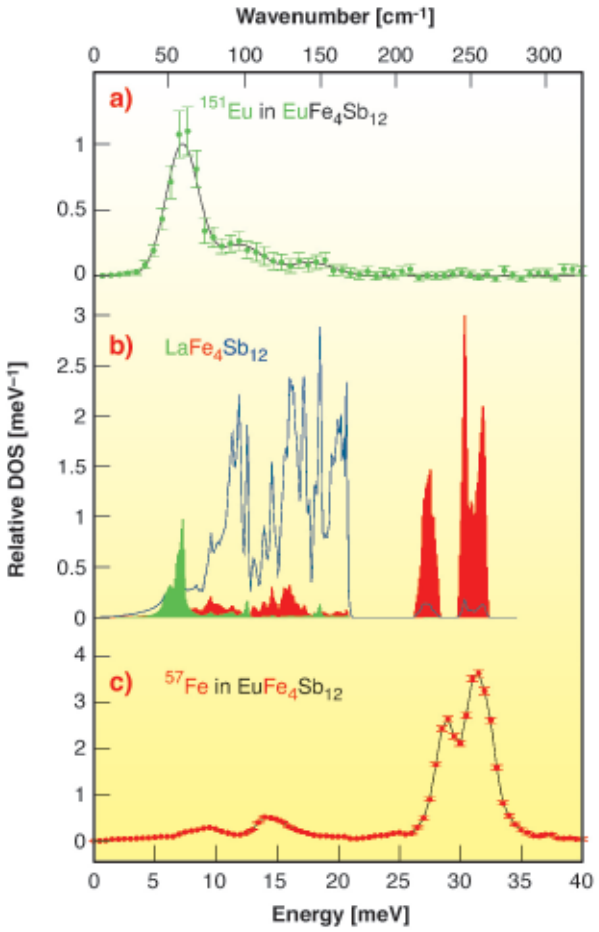

Fig. 27: (a) The europium partial DOS in $EuFe_4Sb_{12}$ obtained at 25 K by europium-151 nuclear inelastic scattering. (b) The calculated La, green, Fe, red, and Sb, blue, vibrational DOS in $LaFe_4Sb_{12}$. (c) The iron partial DOS in $EuFe_4Sb_{12}$ obtained at 295 K by iron-57 nuclear inelastic scattering.

The europium-151 and iron-57 partial vibrational density of states (DOS) obtained from nuclear inelastic scattering, measured at ID22N and ID18, are shown in **Figure 27**, together with the calculated La, Fe, and Sb vibrational DOS in $LaFe_4Sb_{12}$. The iron partial DOS consists of two main peaks at ca. 29 and 33 meV and smaller contributions at 9 and 15 meV, in excellent agreement with the calculations that predict two main peaks at ca. 27.5 and 31 meV in $LaFe_4Sb_{12}$. The europium partial DOS was fitted with three Gaussian peaks with energies of 7.3 ± 0.1, 12.0 ± 0.4, and 17.8 ± 0.5 meV, with relative areas of 3.4 ± 0.2, 1.1 ± 0.2, and 0.5 ± 0.1, and with linewidths of 3.2 ± 0.2, 4.4 ± 0.7, and 4.4 ± 0.7 meV. These energies are in excellent agreement with the calculated energies of 7.1, 12.4, and 18.5 meV in $LaFe_4Sb_{12}$. The peak at 7.3 meV is characteristic of the Einstein oscillator behaviour of the europium in $EuFe_4Sb_{12}$. Its experimental width of 3.2 meV corresponds to a natural width of 2.7 meV, when the experimental resolution of 1.6 meV is taken into account. This small width indicates that there is

at most a weak hybridisation between the europium vibrational mode at 7.3 meV and the iron vibrational mode at 9 meV. The peaks at 12.0 and 17.8 meV result from a small hybridisation of the europium vibrations with the antimony vibrations.

In conclusion, the europium-151 and iron-57 nuclear inelastic scattering experiments on $EuFe_4Sb_{12}$ reveal the localised nature of the europium vibrations at 7.3 meV, the strong decoupling of the iron and europium vibrations, and the weak coupling of the europium and antimony vibrational modes. Hence, nuclear inelastic scattering has proven to be a powerful technique for the investigation of the lattice dynamics of the filled skutterudites, compounds in which this lattice dynamics strongly influences their thermoelectric properties. Antimony-121 nuclear inelastic scattering experiments will soon be undertaken at ESRF and are expected to complete the picture of the lattice dynamics in $EuFe_4Sb_{12}$. To date, the filled skutterudites probably provide the best example of an Einstein oscillator [2]. However, the precise mechanism by which the addition of this filling atom, that essentially behaves as a harmonic oscillator, yields a significant reduction in the thermal conductivity of the filled skutterudites is still to be understood.

References

[1] G. A. Slack, "New materials and performance limits for thermoelectric cooling," *CRC Handbook of Thermoelectrics,* ed. D. M. Rowe (CRC Press, Boca Raton, FL, 1995), pp. 407.
[2] A. Einstein, *Ann. Phys.* **22**, 180 (1907).

Principal Publication and Authors

G.J. Long (a), R.P. Hermann (b), F. Grandjean (b), E.E. Alp (c), W. Sturhahn (c), C. E. Johnson (c), D.E. Brown, (c), O. Leupold (d), and R. Rüffer (d), *Phys. Rev. B* **71**, 140302 (2005).
(a) Department of Chemistry, University of Missouri-Rolla (USA)
(b) Department of Physics, University of Liège, Sart-Tilman (Belgium)
(c) Advanced Photon Source, Argonne National Laboratory, Illinois (USA)
(d) ESRF

Oxidation State of Vanadium in Natural V-bearing Titanomagnetite

Vanadium is a widely spread element in nature, which may occur in three different redox states, from trivalent to pentavalent, in terrestrial magmatic systems. Its abundance in rock forming minerals is a valuable geochemical indicator, holding information on the oxygen fugacity (*i.e.* oxidative) conditions prevailing

Fig. 28: High-temperature extraction of vanadium from vanadiferous titanomagnetite in South Africa. Insert: Structure of titanomagnetite. Ti occurs in the octahedral sites whereas Fe occupies both tetrahedral and octahedral sites of the spinel-type structure.

during the formation of igneous rocks. Vanadium is also an element of significant industrial importance, being a component of high-performance steels (**Figure 28**). However, ore minerals with vanadium as the primary metal rarely occur in nature. Rather, vanadium is extracted from V-rich titanomagnetite ($Fe_{3-x}Ti_xO_4$) cumulates in the upper part of layered basic intrusions. The largest vanadium ore deposits in the world are found in the Bushveld Complex (Republic of South Africa), which hosts more than one-third of the world's vanadium reserves. In this giant (450 x 370 x 7 km^3) layered intrusion, about 2 billion years old, the metal is encountered in 2 to 10 m thick layers of massive titanomagnetite. However, the chemical form of the vanadium (*i.e.* oxidation state) in these magnetites is largely unconstrained. Its accumulation in only a few magnetite layers, among 25 identified in the upper part (2 km thick) of the complex, together with the mechanisms leading to the formation of metre-thick monomineralic magnetite layers, are still poorly understood. Experimental vanadium partitioning data between magnetite and iron-bearing silicate liquids suggest that V-rich magnetites may result from the partial crystallisation of a basaltic melt in a narrow range of oxygen fugacity [1].

To understand the factors controlling the incorporation of vanadium in magnetite, we have investigated the crystal-chemistry of vanadium in natural titanomagnetite samples from two magnetite seams of the Bushveld complex using X-ray absorption near-edge structures (XANES) (**Figure 29**). We focused on the pre-edge features observed in the X-ray absorption spectra at the V K-edge, which depend on the valence state and coordination number of transition elements. However, Ti K-fluorescence makes it difficult to obtain high quality

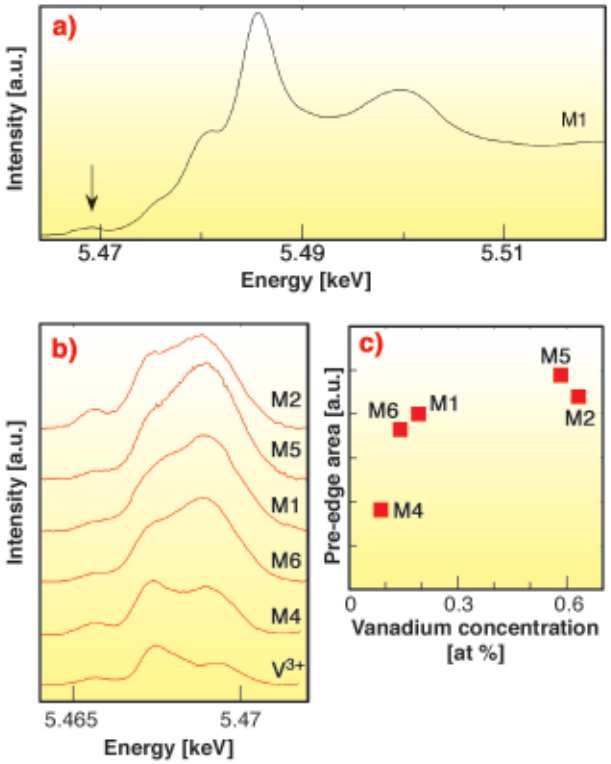

Fig. 29: (a) V K-edge XANES spectra of a titanomagnetite sample (Bierkraal borehole). Arrow: position of pre-edge features. (b) Pre-edge peaks of titanomagnetite samples after baseline subtraction. For comparison, the pre-edge of a tsavorite crystal, a reference V^{3+}-bearing garnet, is reported at the bottom. The V concentration of titanomagnetite increases from bottom to top. (c) Pre-edge area as a function of vanadium concentration in the Bushveld samples.

XANES spectra in titanomagnetite with a conventional fluorescence setup. The use of the high energy-resolution emission spectrometer installed on the ID26 beamline, based on a spherically bent Ge (331) crystal analyser, made it possible to resolve this difficulty by selecting the V $K\alpha_1$ fluorescence line, hence obtaining the first high energy-resolution XANES spectra of V-bearing titanomagnetite samples at the V K-edge. The resulting sharper pre-edge features [2] show that vanadium is mostly in the trivalent state, by comparison with crystalline references. However, the modification of the pre-edge shape and intensity in the more concentrated samples suggests that they contain a small but significant (~ 10 %) fraction of V^{4+} (**Figure 29**). Low magnetite/melt partition coefficients show a preferential trapping of V^{4+} in the structure of the magmatic liquid. The measured fraction of V^{4+} thus indicates relatively oxidising conditions during the crystallisation of V-rich titanomagnetite. The occurrence of small quantities of V^{4+} in the vanadium-rich titanomagnetites of the Bushveld Complex is consistent with previous petrological modelling [1], which shows that extreme enrichments of vanadium in magnetite will only occur for a relatively small range of oxygen fugacity conditions, close to the Ni-NiO buffer. Valence-selective XANES spectroscopy of vanadium in magnetite may thus provide unique information on the redox conditions prevailing during the formation of large-scale magmatic vanadium ore deposits.

References

[1] M. Toplis, A. Corgne, *Contrib. Mineral. Petrol.*, **144**, 22-37 (2002).
[2] P. Glatzel, U. Bergmann, *Coord. Chem. Rev.*, **249**, 65-95 (2005).

Principal Publication and Authors

E. Balan (a,b), J.P.R. De Villiers (c), S.-G. Eeckhout (d), P. Glatzel (d), M. Toplis (e), E. Fritsch (a,b), T. Allard (b), L. Galoisy (b), and G. Calas (b), *Amer. Mineral.*, submitted.
(a) UR T058, Institut de Recherche pour le Développement (IRD), Paris (France)
(b) Institut de Minéralogie et Physique des Milieux Condensés (IMPMC),UMR CNRS 7590, Universités Paris VI et VII, IPGP (France)
(c) Department of Materials Science and Metallurgical Engineering, University of Pretoria, (Republic of South Africa)
(d) ESRF
(e) Laboratoire Dynamique Terrestre et Planétaire, UMR CNRS 5562, Observatoire Midi-Pyrénées, Toulouse (France)

Characterisation of the Glass Transition in Vitreous Silica by Temperature-scanning SAXS

Vitreous silica is a key material for fiber optics communication, technology and science [1]. For pure SiO_2 only incomplete information is available for the transition from the supercooled liquid to the frozen glass state. The hysteresis that glasses typically exhibit as they are cooled and heated through the glass transition had never been observed for SiO_2, mainly due to the high temperatures involved.

Small angle X-ray scattering (SAXS) by liquids and glasses, extrapolated to the zero angle ($q = 0$), reveals static and dynamic density fluctuations. Density fluctuations in liquids depend only on temperature, whereas the glass state depends also on the history of the material. A high-temperature molybdenum furnace and a CCD camera were used in conjunction with the **D2AM** experimental setup to measure the SAXS as a function of temperature. The camera continuously recorded the X-rays scattered by 1.0 mm thick glass plates that were heated and cooled at fixed rates.

The scattered intensity, extrapolated to $q \rightarrow 0$ (the centre of the CCD image), is shown in **Figure 30a** for two

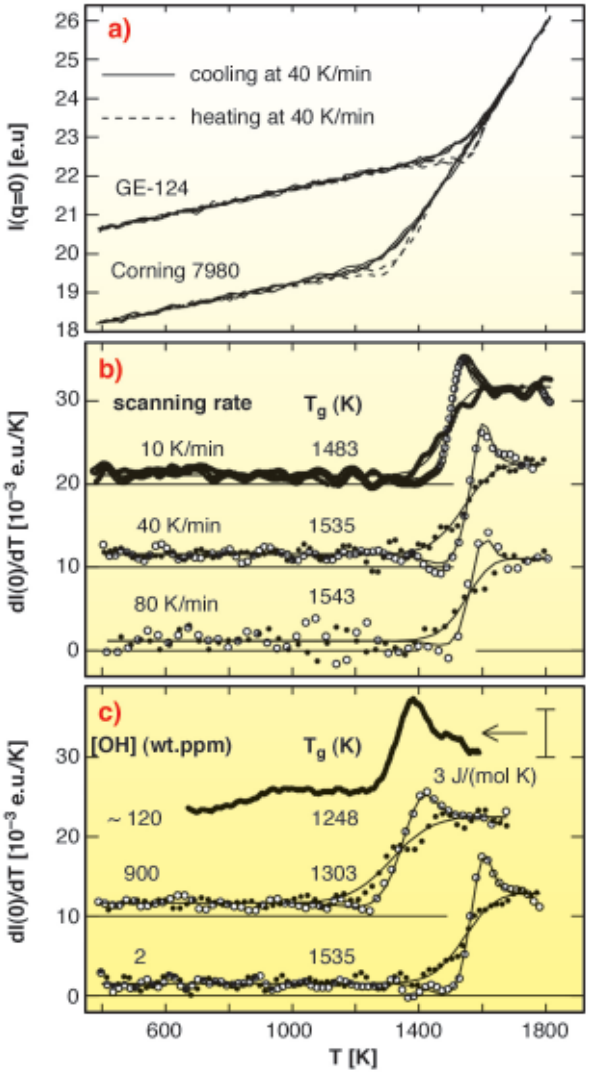

Fig. 30: (a) X-ray scattering intensity, extrapolated to $q = 0$, as a function of temperature. GE 124 contains 2 wt. ppm H_2O, and Corning 7980 contains 900 wt. ppm H_2O. (b) Temperature derivatives of I(0), obtained for GE-124 upon scanning the temperature at different rates. Full and open symbols show cooling and heating data, respectively. (c) Temperature derivatives of $I(0)$ data obtained at 40 K/min for GE-124 and Corning 7980, and heat flow upon heating a sample with 120 wt. ppm at 40 K/min.

commercial glasses. The curves show the strong influence of even small amounts of residual water on the glass transition temperature, T_g. The hysteresis of the density fluctuations can be seen clearly in the $I(q = 0)$ curves and in their derivatives (**Figures 30b** and **c**). These differentiated signals match to the signature of the glass transition seen by calorimetry (**Figure 30c**). The slopes of the $I(q = 0)$ curves above and below T_g agree with the slopes found by light scattering experiment to within 14% [2]. This is interesting as light probes the structure of the material at length scales that are larger by about a factor of 100. Standard kinetic parameters like the Kohlrausch stretching exponential have been obtained from the data by fitting. The fits are shown as solid lines in **Figures 30b-c**.

In conclusion, temperature-scanning SAXS resolved the glass transition in vitreous silica. A higher amount of residual water decreases T_g, and broadens the glass transition.

References

[1] M. Tomozawa, in *Silicon-Based Materials and Devices* H.S. Nalwa (Ed.), Academic Press, New York, **127** (2001).

[2] K. Saito, A.J. Ikushima, *Appl. Phys. Lett.*, **70**, 3504 (1997).

Principal Publication and Authors

R. Brüning (a), C. Levelut (b), A. Faivre (b), R. Le Parc (b), J.-P. Simon (c), F. Bley (c), J.-L. Hazemann (d), *Europhys. Lett.*, **70**, 211-217 (2005).

(a) Physics Dept., Mount Allison University (Canada)

(b) Laboratoire des Colloïdes, Verres et Nanomatériaux, Montpellier (France)

(c) LTPCM-CNRS-INPG-UJF, Grenoble (France)

(d) Laboratoire de Cristallographie, CNRS-Grenoble (France)

ESRF

Highlights 2005

Materials Science

Introduction

Materials science and materials engineering involves the investigation of structure property relationships and the use of these findings to produce materials with predetermined properties. Studies of this type play a major role at the ESRF and span a wide range of applications from chemical bonding, electronic applications, and novel synthesis to studies of grain growth, dynamic evolution of materials properties and design and understanding of catalytic processes. All aspects of materials science studies cannot be covered by this brief showcase. The trend in materials science research at the ESRF is that microfocussing; time-resolved studies *in situ* and the application of combinations of techniques are on the rise. In order to illustrate these trends we have chosen a few examples in the categories: extreme conditions, stress and strain studies and some general applications of X-ray diffraction to problems in materials science.

Enormous advantages in examining materials under non-ambient conditions such as high pressure or high temperature have been made due to developments in diamond-anvil cells, large-volume presses and laser heating in combination with the third-generation X-ray source at the ESRF.

The physical properties of materials can be dramatically changed under non-ambient conditions. In two studies of sulfur it is shown that non-incommensurate structures can exist at high pressures and that sulfur behaves like its group VI neighbours. It is also shown that molecular S_6 is only formed under high pressure at high temperatures. These findings can explain the change in properties such as resistivity. In a study of neodymium/calcium manganites it was found that shear strain is of importance for the structure/property relationship in colossal magneto resistance. In a series of studies of actinides under high pressure it was found that a new structure of curium (Cm-III) is stabilised by magnetic interactions. An experimentally challenging study of hydrogen at high pressures reveals the structure of the high pressure phase II of D_2 showing that a combination of neutron and X-ray diffraction can now determine complicated structures even at high pressures in diamond anvil cells.

X-ray diffraction and tomography are non-destructive methods providing data on bulk materials. A combination of these methods has revealed that void growth kinetics in bulk samples of $CuZn_{40}Pb_2$ brass can be studied and that void size and shape evolution can be followed during creep.

Control of relaxation processes and nucleation are important for the tailoring of materials to the desired properties. X-ray diffraction *in situ* is rapidly developing into an essential tool in this process. Bulk metallic glass, for instance, is an interesting new class of construction material and the control of the ductility in the nanocomposites are essential for the usefulness of these materials. In a temperature dependent diffraction study of Pd based metallic glasses the important relaxation processes of the excess free volume have been studied.

The crystallisation processes during solidification has been studied in a time-resolved diffraction of Al with solute Ti and TiB_2 particles and the first *in situ* information on growth kinetics and nucleation of individual grains during solidification has been obtained. These processes govern the basic properties such as ductility and hardness. During deformation of metals and alloys dislocations are introduced and during

subsequent annealing the stored energy is released. The 3D X-ray microscopy technique at ID11 was used to study the *in situ* recovery of cold rolled Al during annealing on a sub grain level.

High-resolution powder diffraction has proven to be a very useful tool in many materials science applications. A study of a C_{60} based polymer (Li_4C_{60}) revealed a new mixed bonding scheme for fullerides showing both [2+2] cycloadditions and single C-C bridging motifs indicating routes to the synthesis of new polymers with interesting properties. A combined X-ray diffraction/mass spectrometry study of anaerobic methane CH_4 combustion explains the catalytic steps when CH_4 under high temperature, using CeO_2/Fe_2O_3 solid catalysts, is transformed to H_2. Information of this type is of importance for the development of new, clean routes to the use of hydrogen as fuel.

A high resolution study of ferromagnetic $La_{1-x}Ca_xMnO_3$ manganite has provided information on the poorly understood ferromagnetic insulating state suggesting that a specific orbital ordering takes place.

X-ray diffraction at synchrotron facilities gives the possibility of obtaining information on the site occupancy by chemically different cations in powder. Examples of the determination of the cation distribution in bicationic zeolites illustrates the power of the resonant contrast diffraction.

Å. Kvick

High Pressure

Incommensurate Metallic Sulfur above 100 GPa

The physical properties of a material at high pressure can be dramatically different to those observed at ambient conditions. For example, sulfur at ambient pressure is a yellow molecular insulating solid. Under compression, its resistivity decreases rapidly, until it becomes a metallic superconductor above 90 GPa. The superconducting temperature increases from T_c = 10 to 14 K over the pressure range 90–160 GPa [1], and at still higher pressures there is a further structural transition to another superconducting phase with a maximum T_c of 17.3(5) K at 200 GPa.

The crystal structure of the metallic phase of sulfur at 100 GPa has long been reported to be orthorhombic, and isostructural with the high-pressure phases of the other group VIa elements selenium (Se-IV) and tellurium (Te-III). However, using high-pressure diffraction techniques at both the ESRF and the SRS, we have recently shown that both Se-IV and Te-III are in fact monoclinic, with incommensurately modulated atomic coordinates [2]. Using X-ray powder diffraction techniques on beamline ID09, we have now investigated the structures and transitions in sulfur up to 101 GPa with the aim of determining whether the metallic phase is also incommensurately modulated. We used an X-ray wavelength of 0.418 Å focused down to a beamsize of 10 µm x 10 µm, and the 2-dimensional (2D) diffraction patterns were collected on a MAR345 image plate before being integrated azimuthally to give standard 1D diffraction profiles.

To obtain the highest quality diffraction data, we loaded powdered sulfur with helium as a pressure transmitting medium, which made it possible to determine the pressure of the illuminated part of the sample from the helium's diffraction pattern and known equation of state.

The structural phase transition to the metallic phase was observed to start at 75 GPa, somewhat lower than previous studies, and single-phase profiles were observed above 95 GPa. A micrograph of the sample at 101GPa, which had the approximate dimensions 30 µm x 30 µm x 5 µm at this pressure, is shown in **Figure 31**, and illustrates

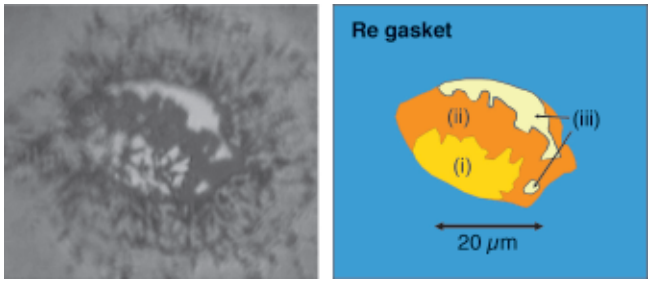

Fig. 31: Micrograph of the metallic sulfur sample at 101 GPa, as viewed through one of the diamond anvils of the pressure cell. The schematic diagram identifies (i) highly reflecting sulfur in contact with the diamond face, (ii) sulfur with helium between it and the diamond, and (iii) some of the transparent helium pressure medium illuminated from behind.

the highly reflecting nature of the metallic phase. A diffraction pattern from the sample at the same pressure is shown in **Figure 32**, and is very similar to that observed previously from incommensurate Se-IV and Te-III. A Rietveld refinement to the same incommensurate structure is shown in **Figure 32**, and gives an excellent fit. All the diffraction peaks can be accounted for by the 4D superspace group I'2/m(0*q*0)s0, with the incommensurate wavevector q = 0.281(1) at 101 GPa and a single atom located at (0,0,0).

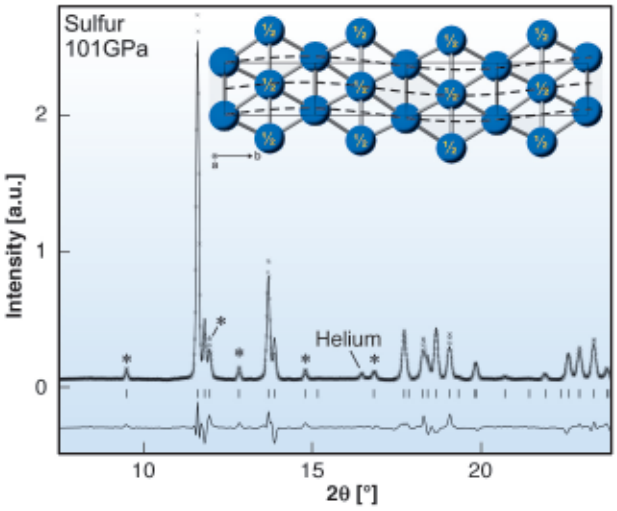

Fig. 32: Rietveld refinement of incommensurate sulfur at 101 GPa. Tick marks show calculated positions of main and modulation peaks: asterisks identify some modulation reflections. The difference between the observed and calculated profiles is shown below the tick marks. Inset: four unit cells of the modulated structure viewed down the a axis. The modulation wave is indicated with dashed lines.

Four unit cells of the structure of S-III at 101 GPa are shown as an inset to **Figure 32**. In the absence of the incommensurate modulation, all would be identical. However, the modulation, which has a wavelength of 1/q unit cells as shown with a dashed line in the inset to **Figure 32**, is incommensurate with the unit cell repeat, and thus the atomic coordinates in each unit cell are different.

On pressure decrease from the incommensurate phase, we found a previously unknown phase of sulfur below 90 GPa. The similarity of the diffraction patterns with those obtained previously from Se-III and Te-II shows that all three phases have the same triclinic structure [3].

In conclusion, we have shown that sulfur joins its group VIa neighbours selenium and tellurium in having a phase with an incommensurately modulated crystal structure at high pressure, and is the first element observed to have such a structure above 100 GPa. The results show that incommensurate structures are not limited to lower pressures, and suggest that further such structures will be found in other elemental systems at very high pressures.

References

[1] E. Gregoryanz, V.V. Struzhkin, R.J. Hemley, M.I. Eremets, H.K. Mao, and Y.A. Timofeev, *Phys. Rev. B* **65**, 064504 (2002).
[2] C. Hejny and M.I. McMahon, *Phys. Rev. Lett.* **91**, 215502 (2003).
[3] C. Hejny and M.I. McMahon, *Physical Review B* **70**, 184109 (2004).

Principal Publication and Authors

C. Hejny (a), L.F. Lundegaard (a), S. Falconi (a), M.I. McMahon (a) and M. Hanfland (b), *Physical Review B Rapid Communications* **71**, 020101(R) (2005).
(a) SUPA, School of Physics and Centre for Science at Extreme Conditions, The University of Edinburgh (UK)
(b) ESRF

Alternating Sequence of Ring and Chain Structures in sulfur at High Pressure and Temperature

The behaviour and structure of sulfur under high pressure and temperature conditions is currently the subject of a renewed research effort [1,2]. However, there still exist disparities between the data and interpretations of results coming from the use of different techniques. In view of this, we have reinvestigated the structures of sulfur formed though direct transformation at pressures between 6 – 11 GPa and from room temperature to 1000 K. Over this same pressure range, in experiments conducted at room temperature, there is spectroscopic evidence for the existence of both non-molecular helical sulfur and a molecular S_6 forms of sulfur, yet even the most recent diffraction experiments, also conducted at room temperature, show no evidence for any such structures in sulfur at pressures exceeding 25 GPa.

In conducting our experiments, we have encountered the non-molecular forms of sulfur previously observed as trigonal helical by Crichton *et al.* [1] and tetragonal helical by Fujitsa *et al.* [2]. In addition, we observe an intermediate structure, which does transform reversibly and is described as identical to the molecular S_6 form that can be prepared by chemical methods at ambient conditions. The positions of the transitions from trigonal-S_6 and S_6-tetragonal structures have been delineated. Rietveld refinement of data collected *in situ* at 7.2 GPa and 950 Kelvin (**Figure 33**), with the Paris-Edinburgh large volume press, resulted in an *R-3* symmetry, with 18 atoms per unit cell located at x = 0.17581(5), y = 0.19250(5) and z = 0.15027(5). This results in an S-S bond length of 2.1762(1) Å and torsion angle of 78.82°.

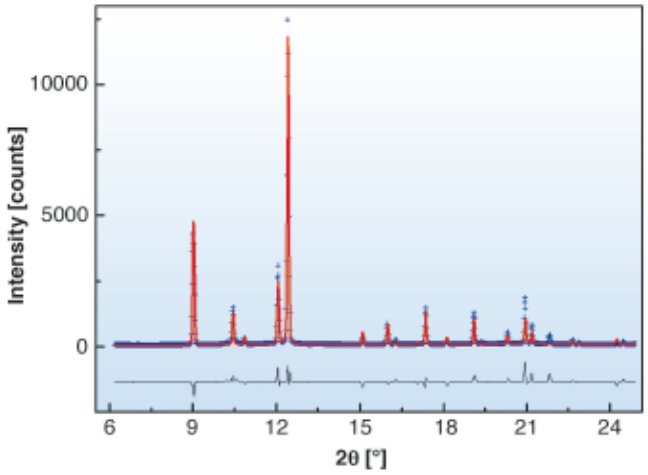

Fig. 33: Diffraction pattern of the S_6 rhombohedral phase. Refinement results on the diffraction pattern obtained from *in situ* measurements at 7.2 GPa and 950 K; the data are represented by blue crosses, the red line corresponds to the Rietveld refinement and the black line to the difference between the observed and calculated data.

The existence of this S_6 phase is important as it shows directly that the S_6 phase can only be observed, via direct transformation, at high temperature. Therefore, it explains why X-ray diffraction experiments conducted at room temperatures are unable to confirm the results of several independent Raman measurements.

Given that the temperatures that we have observed the transitions to trigonal, S_6 and tetragonal phases are too high for Raman lasers to induce, and that there is also evidence that if sulfur is illuminated with weak laser light no transition is observed up to at least 10 GPa, other mechanisms must be proposed for the Raman observations. Considering the pressure dependent red shift of the optical absorption edge of the S_8 molecule, Eckert and Steudel [3] explain the room temperature S_8 to trigonal phase transition, only observed in Raman studies, suggesting that the absorption of laser light can furnish the activation energy necessary to break the S_8 molecules promoting polymerisation to, for example, the trigonal helical phase. This mechanism is further complicated by the fact that the optical absorption can change with pressure and at each phase transition. Nonetheless, within this framework of laser-induced transition it is also noted that the sequence $S_8 \rightarrow$ polymeric $\rightarrow S_6$ observed by Raman spectroscopy at room temperature corresponds to the same sequence observed by X-ray diffraction at high temperature and in the same pressure range. This indicates that, the photo-induced phase transitions observed by Raman measurements correspond to existing structural transitions in the phase diagram. It is most likely that the effect of suitable laser illumination and temperature is to induce these transitions by overcoming the high kinetic barrier related to the breakdown of the S_8 molecule.

With regard to other members of the Group VI elements, it is now clear that the structure S_6 described here is similar to that of Se_6; a phase that metalises at high pressure. In sulfur, Brazhkin *et al.* [4] describe metalisation of liquid sulfur at a pressure of 8 GPa, around a maximum in the melting curve, indeed in the region where we observe the solid S_6 phase. Considering this, it would be interesting to look at the structure of the liquid in this region, to identify whether the liquid has a molecular nature like the solid phase below the melting curve.

References

[1] W.A. Crichton, G.B.M. Vaughan and M. Mezouar, *Z. Kristallogr*. **216**, 417-419 (2001).
[2] H. Fujihisa, Y. Akahama, H. Kawamura, H. Yamawaki, M. Sakashita, T. Yamada, K. Honda and T. Le Bihan, *Phys. Rev. B* **70**, 134106 (2004).
[3] B. Eckert and R. Steudel, *Topics in Current Chemistry* **231**, 31-98 (2003).
[4] V.V. Brazhkin, S.V. Popova and R.N. Voloshin, *Physica B* **265**, 64-71 (1999).

Principal publication and authors

L. Crapanzano, W.A. Crichton, G. Monaco, R. Bellissent and M. Mezouar, *Nature Materials* **4** 550-552 (2005).
ESRF

Shear Strain in $Nd_{0.5}Ca_{0.5}MnO_3$ at High Pressures

Colossal magnetoresistance (CMR) indicates that the electrical resistance of a material changes dramatically on application of a magnetic field. This property is related to a phase transition involving both magnetic and lattice degrees of freedom that may be triggered by changing either temperature or magnetic field. An important class of CMR materials is formed by the manganites $L_{1-x}A_xMnO_3$ (L = trivalent rare earth; A = divalent alkaline earth; $0 < x < 1$) with a distorted perovskite-type structure [1]. Depending on composition and temperature, rich phase diagrams have been discovered, involving phases with differently distorted crystal structures interacting with various states of magnetic order and charge order. The intricate relationship between spin, charge, orbital and lattice degrees of freedom is generally recognised as the origin of this wide variety of properties within this class of simple compounds [2]. However a quantitative understanding has not yet been achieved between physical properties of CMR manganites and their chemical compositions and crystal structures.

In order to uncover the delicate variations of atomic arrangements, we have studied the pressure dependence of the crystal structure of the half-doped

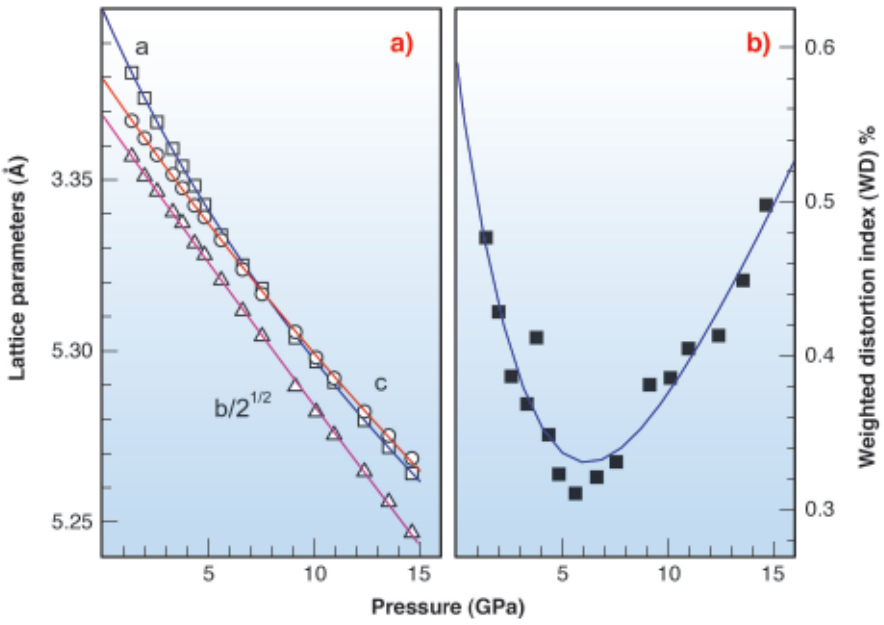

Fig. 34: Pressure dependence of (a) lattice parameters, and (b) lattice strain (WD).

manganite $Nd_{0.5}Ca_{0.5}MnO_3$. A polycrystalline sample was loaded into a diamond anvil cell (DAC). X-ray powder diffraction was measured at beamline ID9a, employing a MAR image plate detector. Diffraction has been collected at selected pressures up to p = 15 GPa. Both the lattice parameters and the atomic coordinates were determined at each pressure by Rietveld refinements against the diffraction data. The lattice strain of the orthorhombic structure can be characterised by a distortion index *WD*, that is defined as $WD = 1/3\ \sum|a_i-a_0|/a_i$ with $a_0 = (a_1a_2a_3)^{1/3}$ and a_i (i = 1,2,3) being the appropriately scaled lattice parameters. The pressure dependence of *WD* has a minimum at $p^* \approx 7$ GPa, that is the same pressure at which a crossover occurs from $a > c$ for $p < p^*$ towards $a < c$ for $p > p^*$ (**Figure 34**). These results suggest two regimes. For $p < p^*$ increasing pressure reduces the distortion, while for $p > p^*$ increasing pressure enhances the distortion.

Distortions of crystal structures of CMR manganites are usually characterised by tilt rotations and Jahn-Teller (JT) distortions of the MnO_6 octahedral groups. Lattice strain is considered to be the result of combining both modes of distortion. **Figure 35a,b** shows that Mn-O bond lengths evolve towards each other up to $p = p^*$, indicating a decrease of the JT distortion on increasing pressure. For $p > p^*$ the JT distortion is small and independent from pressure. As the tilt does not depend on pressure, these results fail to explain the increase of *WD* for pressures beyond p^*. Instead, the off-diagonal components of the local strain tensor indicate that shear strain of the MnO_6 groups develops for $p > p^*$ (**Figure 35c,d**). Shear strain corresponds to bond angles O-Mn-O being different from 90 degrees (see the publication for details). It is thus found that a single state of lattice distortion (single value of *WD*) can be achieved alternatively by compressive strain (JT type distortion) of MnO_6 groups at low pressures or by shear strain at high pressures.

Fig. 35: Pressure dependence of (a) bond lengths of the two equatorial Mn-O bonds, (b) the apical Mn-O bond, (c) diagonal elements of the local strain tensor (e_{ii}), and (d) off-diagonal elements e_{ij}.

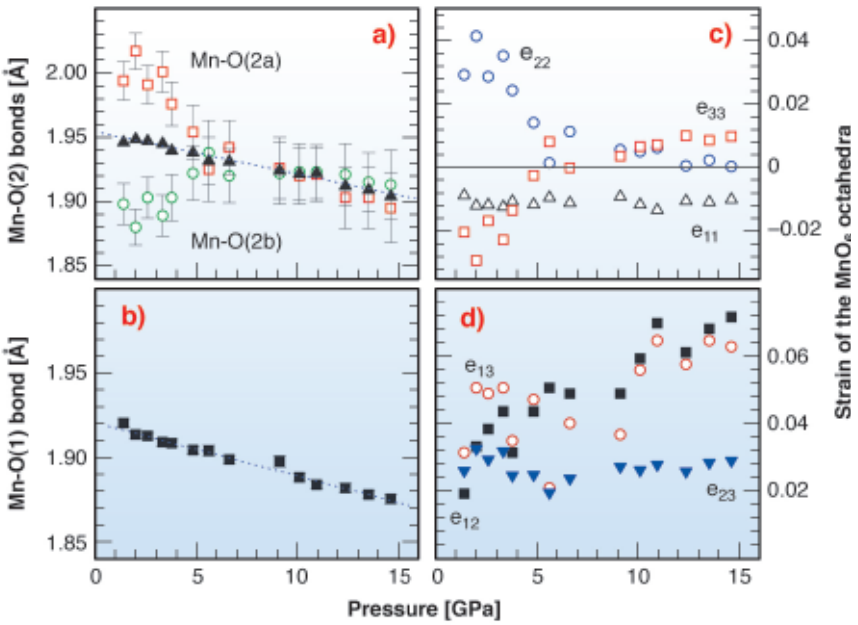

In conclusion, we have found that shear strain of MnO_6 octahedral groups develops at high pressures in $Nd_{0.5}Ca_{0.5}MnO_3$. Shear strain is important, because it necessarily leads to a decrease in the overlap between e_g orbitals of Mn and *p* orbitals of oxygen, and hence it provides a mechanism for the localization of the conduction electrons in CMR manganites. Therefore, shear-type distortions would always lead to more insulating behaviour, but they could also affect the magnetic interactions that involve e_g and t_{2g} orbitals on Mn, and *p* orbitals on O. Thus, any amount of shear strain will be important for the correct understanding of structure-properties relations in CMR manganites. The precise role of shear strain in other manganites is yet to be established.

References

[1] *Nanoscale Phase Separation and Colossal Magnetoresistance The Physics of Manganites and Related Compounds*. E. Dagotto (Ed.), Springer (2003).
[2] A.J. Millis, *Nature* **416**, 518 (2002).

Principal Publication and Authors

A. Arulraj (a), R.E. Dinnebier (b), S. Carlson (c), M. Hanfland (d) and S. van Smaalen (a), *Phys. Rev. Lett.* **94**, 165504 (2005).
(a) Laboratory of Crystallography, University of Bayreuth, Bayreuth (Germany)
(b) Max Planck Institute for Solid State Research, Stuttgart (Germany)
(c) MAX-lab, Lund University (Sweden)
(d) ESRF

A High-pressure Structure in Curium linked to Magnetism

The actinide series, elements after actinium and containing Th, U, Np, Pu, Am, Cm, etc., are a fascinating series that are characterised by the progressive filling of the 5*f* electron shell. Our understanding of these elements is greatly advanced by modern theory that can simulate the complex electron interactions in the solid. However, studies of these materials under extreme conditions, such as pressure, test such theories. As the materials are compressed and the atoms move closer together the interactions increase, resulting in dramatic changes in crystal structure and other properties. A challenge is to determine such structures and compare them with theoretical predictions.

Enormous advances in examining materials at high pressures have been possible because of the development of diamond-anvil technology and the third-generation synchrotron sources, such as the ESRF. However, the application of this technology to radioactive (and toxic) materials is far from straightforward. These experiments have been performed up to 100 GPa at the **ID30** beamline on protactinium (Pa), uranium (U), [1] americium (Am) [2] and latterly on curium (Cm).

Figure 36 shows that the compressibility (variation of V/V_0 with pressure) at low pressure of Am and Cm, on the one hand, and U and (Pa, not shown but similar to U) on the other hand, are quite different. This is because, for the early actinides Pa to Pu, the 5*f* states contribute to the "bonding" and they make the atomic volumes small, and the materials "hard". For the heavier actinides, Am and beyond, the 5*f* states are "localised" and these materials are subsequently "soft". However, at a certain pressure the 5*f* states actually change their character, and we see a "harder" material developing, as in the case of Am [2] at 18 GPa, and Cm above 36 GPa.

There is no reason that Am and Cm should be different (except that Cm should be slightly less compressible), but it can be seen that Cm has *five* phases up to 100 GPa,

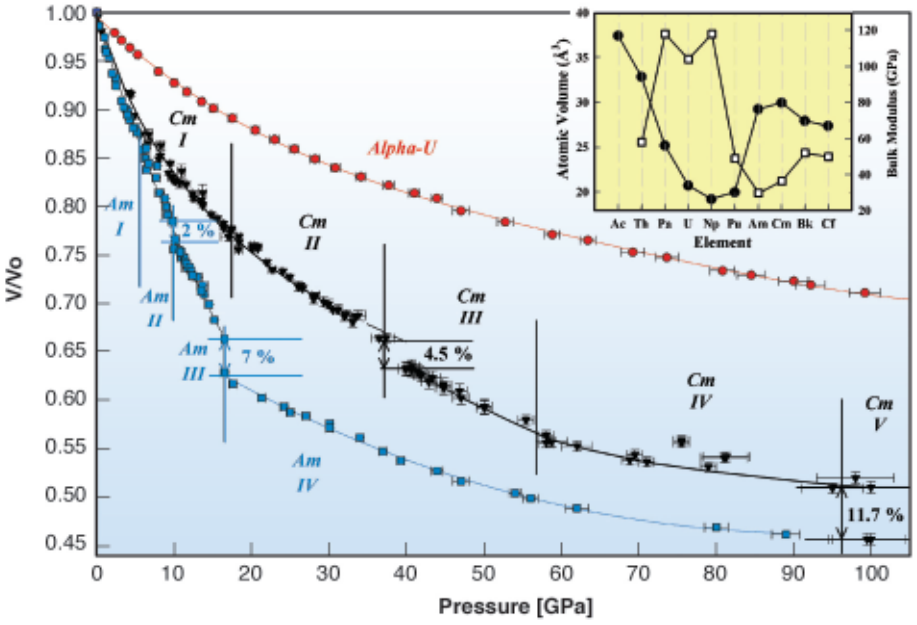

Fig. 36: Relative volume versus pressure for curves of α-U [1], Am [2] and Cm (this work). Inset shows ambient pressure atomic volumes (solid circles, left-hand side) and bulk moduli (open squares, right-hand side) across the actinide series.

whereas Am has only *four*. It was quickly established that the first two and last two phases of both elements are identical. The odd phase is Cm-III, which exists between 36 and 56 GPa. The diffraction pattern for this phase is complex; the structure has a low monoclinic symmetry with space group C2/c. This structure has never been found for any element with *f* electrons. The diffraction pattern, together with the Rietveld fit are shown in **Figure 37**, with the monoclinic structure of Cm III in the inset.

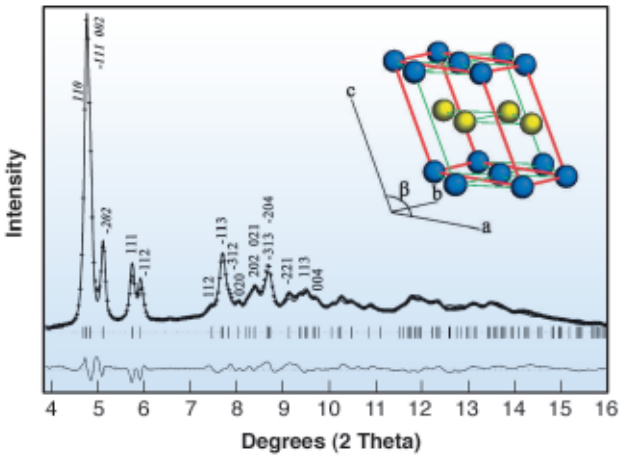

Fig. 37: Rietveld refinement of Curium III at 45 GPa showing calculated reflection tick marks, principal reflections and difference profile. The insert shows a model of this monoclinic (s.g. C2/c) structure.

With the structure identified, the question became why this phase should appear in Cm and not in Am? Modern calculations, while unable to predict structures from first principles for heavier elements, are able to compare the ground-state energies from different crystal structures. In these calculations for Cm, an unusual situation emerged. It appears that the Cm-III phase is stable because of the special half-filled nature of the 5*f* shell, and the associated magnetism present in Cm, and which is not present in Am or any of the preceding actinide elements. Am, for example, has 6 5*f* electrons that fill the j = 5/2 subshell and result in no ordered magnetism. Normally, magnetic interactions have small energies compared to structural terms, but this is a rare case in which the energy added by the magnetic interaction is sufficient to stabilise a completely new structure.

With the discovery of the Cm-III structure and the prediction that it is stabilised by magnetic interactions, a new perspective is opened on the heavier actinides and by inference (although certainly at even higher pressures) also on the heavy rare-earth metals.

References

[1] T. Le Bihan *et al,. Phys. Rev. B* **67,** 134102 (2003).
[2] S. Heathman *et al,. Phys. Rev. Lett,* **85,** 2961(2000).

Authors and Principal Publication

S. Heathman (a), R.G. Haire (b), T. Le Bihan (c), A. Lindbaum (d), M. Idiri (a), P. Normile (a), S. Li (e), R. Ahuja (e), B. Johansson (e), and G.H. Lander (a), *Science* **309** 110 (2005).
(a) European Commission, JRC, Institute for Transuranium Elements, Karlsruhe (Germany)
(b) Oak Ridge National Laboratory, Tennessee (USA)
(c) CEA-Valduc, DRMN/SEMP/LECP, Is-sur-Tille (France)
(d) Vienna University of Technology, Institute for Solid State Physics (Austria)
(e) Department of Physics, Uppsala University (Sweden)

The Broken Symmetry Phase of Solid Deuterium

The solid hydrogens (H_2, D_2, HD) are considered essential for the discovery of new quantum many-body effects of density. Numerous calculations of exciting properties of dense hydrogen have been made, such as the recently predicted 'metal superfluid' state [1]. However, experimental verification presents technical challenges and often the observed properties are more subtle than predicted. Determination of the structure of phase II of deuterium is a clear illustration of the special status of the solid hydrogens.

From spectroscopic studies, three phases of solid hydrogens have been discovered up to the maximum pressure achieved, 320 GPa. The solid hydrogen compounds D_2, HD and H_2 remain quantum molecular solids up to the 100 GPa range. A remarkable macroscopic consequence is the existence of a pressure-induced broken symmetry phase (BSP) transition from phase I to phase II, in which the molecules go from a spherical rotational state to an anisotropic rotational state. The high temperature phase I consists of a closed packed hexagonal lattice of freely rotating molecules. Despite many theoretical studies, the nature of phase II remained unknown.

Solid D_2 is the isotope for which the BSP transition occurs at the lowest pressure (at T = 4K, 28 GPa for D_2, 69 GPa for HD and 110 GPa for H_2). However, X-rays are almost insensitive to the individual positions of D atoms in the molecules and to orientational ordering because D_2 has no inner electronic shells, and X-rays are scattered by electrons in molecular orbitals. Also, because of the very small scattering power of a hydrogen crystal in a diamond-anvil cell, the use of a third-generation synchrotron source and the growth of a single crystal in helium were previously needed to measure the EOS of D_2 to 120 GPa in phase I [2]. This X-ray approach has been extended here to low temperature. Contrarily, neutrons are scattered by individual nuclei, and therefore can be used to determine the individual positions of D in the structure, as well as the orientations of the molecules. Owing to the low

intensity of neutron sources, the high pressure neutron study of solid D_2 is even more challenging. Consequently, a combination of X-ray and neutron measurements were needed to solve the structure. The X-ray work at beamlines ID9 and ID27 was useful to study the change of the unit cell at the BSP transition, to explore a large domain of P-T and to detect the appearance of a superstructure, to test the reproducibility of the observation on various samples, the effect of strain and to orient the single crystal for the neutron experiment. Four different D_2 crystals were studied by X-ray diffraction: two of them embedded in helium pressure transmitting medium. The neutron study was performed on one D_2 single crystal in helium at a constant pressure of 38 GPa to measure the change of intensity of the various peaks at the BSP transition.

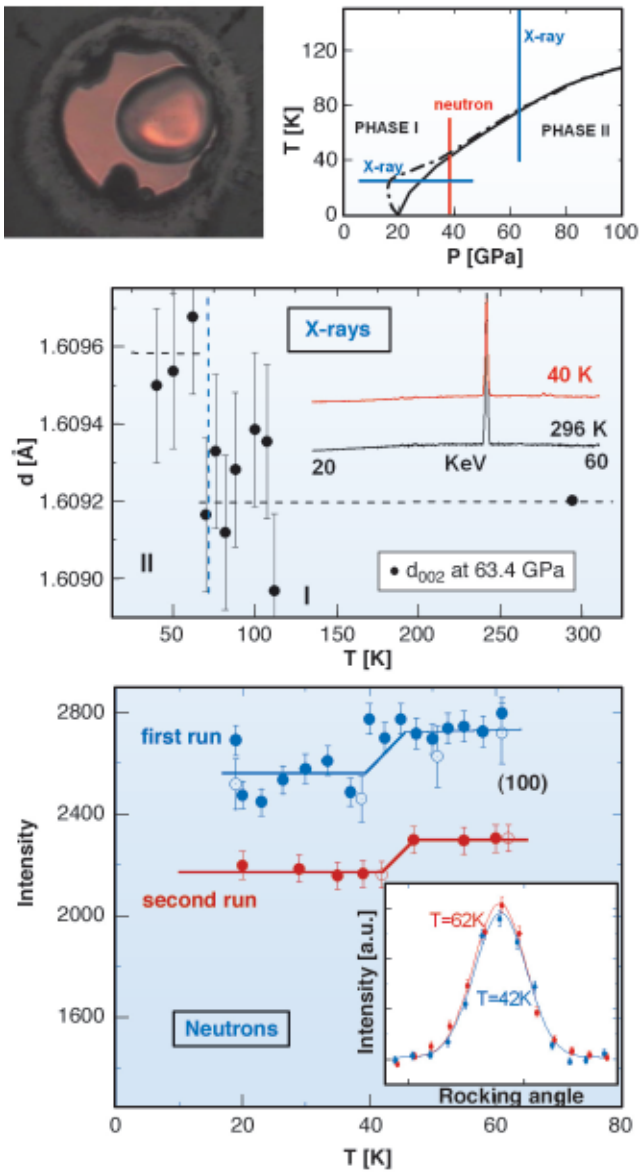

Fig. 38: (a) Single-crystal of D_2 in helium; Phase diagram (b) and the P-T paths of the X-ray (c) and neutron measurements (d). The evolution of the 002 d-spacing (X-rays) and the intensity of the 010 reflection (neutrons) show the changes at the I-II phase transition upon cooling.

The (100), (010), (1-10) (101), 110), (1-10) and (002) reflections were collected in the X-ray and neutron experiments. The **Figure 38** presents the precision of both X-ray and neutron data that were achieved. From X-ray measurements, we find that the I-II transition does not affect the diffraction peak of the hcp lattice, except for a very small volume discontinuity (a $\Delta V/V = -10^{-3}$ is measured). The quality of the crystal at 38 GPa (rocking curve of 1°) allowed an accurate determination of the intensity of the various peaks. The integrated intensity of the various reflections changes very weakly at the transition, in contrast to the more than 20% intensity change for the strongest candidates of the structure of phase II (orthorhombic modifications of the hexagonal phase I). To explain the data, we followed a theoretical prediction that the BSP transition could be purely rotational forming four sublattices with molecular axes directed perpendicular to the four different faces of a tetrahedron. This structure is shown in **Figure 39** and it explains most of the intensity changes measured. But this type of local order has a topological frustration when built in a hexagonal lattice. That is resolved in developing an incommensurate long-range order. Indeed, incommensurate reflections are observed in phase II both with X-rays and with neutrons.

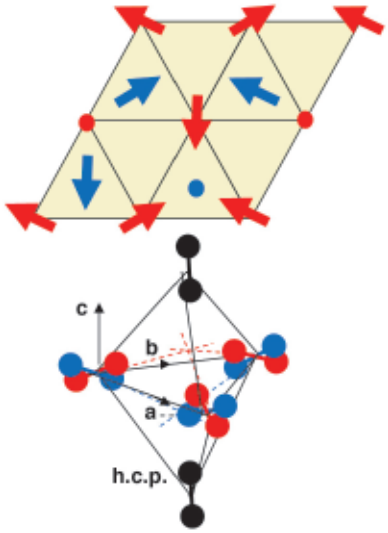

Fig. 39: Proposed structure for phase II of solid D_2. The unit cell is P-3 symmetry, with eight molecules. Arrows point to the positive z-hemisphere, circles depict molecules lying along the c-axis. The molecular axes of the molecules are locally directed towards the centre of a tetrahedron.

In addition to the resolution of the structure of phase II of solid D2, this work opens new possibilities for high pressure crystallography. Combining the X-ray and neutron structural studies has certainly been used previously to resolve complex structures near ambient pressure. The present work demonstrates that this is now feasible at very high pressure in a diamond anvil cell.

References

[1] E. Babaev, A. Sudbo and N. Ashcroft, *Phys. Rev. Lett.* **95**, 105301 (2005).

[2] P. Loubeyre, R. LeToullec, D. Hausermann, M. Hanfland, R.J. Hemley, H.K. Mao and L.W. Finger, *Nature* **383**, 702 (1996).

Principal publication and authors

I. Goncharenko (a), P. Loubeyre (b), *Nature* **435**, 1206 (2005).
(a) Laboratoire Léon Brillouin (France)
(b) Commissariat à l'Energie Atomique (France)

Stress and strain

Combined Diffraction and Tomography Reveal Creep Damage

In electricity–generating plants, steam and gas turbines and other machinery components are subjected to mechanical loading at elevated temperatures. Under constant mechanical stress these components will show a progressive elongation, referred to as creep deformation. Depending on the magnitude of both the mechanical loading and the temperatures components encounter, they can fracture after creep times between minutes and several hundreds of thousands of hours.

On the level of the material microstructure creep processes are characterised by diffusion, dislocation movement, grain boundary sliding and creep-induced cavity growth, which controls the service lifetime of the component. In order to quantify the remnant lifetime of creep-loaded components, many different models have been proposed, which are based on assessing damage by cavity and crack growth. Creep damage, however, could only be determined from two-dimensional images obtained *e.g.* using optical and scanning electron microscopy. Since microscopical methods also necessitate cutting the sample, only a snapshot of the damage evolution was available.

In contrast, synchrotron X-ray tomography is non-destructive and it provides data of damage in the bulk, which often significantly differs from damage at the surface [1]. It also reveals the chronology of damage events and it shows damage location in a defined volume. Diffraction using high-energy synchrotron radiation is also non-destructive and it provides complementary information to tomography, *e.g.* about texture (orientation distribution of the crystallites), changes in domain size, dislocation density and internal strains/stresses. Using both white high-energy synchrotron radiation and monochromatic high-energy synchrotron radiation the advantages of allowing a fast simultaneous recording of several reflections respectively and providing reflection profiles with high angular resolution could be combined.

Combining for the first time tomography and diffraction within the same experiment, the creep void evolution in CuZn40Pb2 brass (an α/β-brass) and its correlation to texture and microstructure development was studied. Sample and experimental conditions were selected in such a way that the timescale of the creep process is much longer than the time required for collecting the microtomography data and the diffraction data. A novel miniature creep device was developed where the path of the incoming and the emerging X-rays over a complete 180° turn of the sample is identical. The experimental setup at beamline ID15A consisted of three detection systems, which allowed us to sequentially perform white beam tomography [2], energy-dispersive diffraction and angle-dispersive diffraction without further alignment or calibration procedures during the experiment (**Figure 40**).

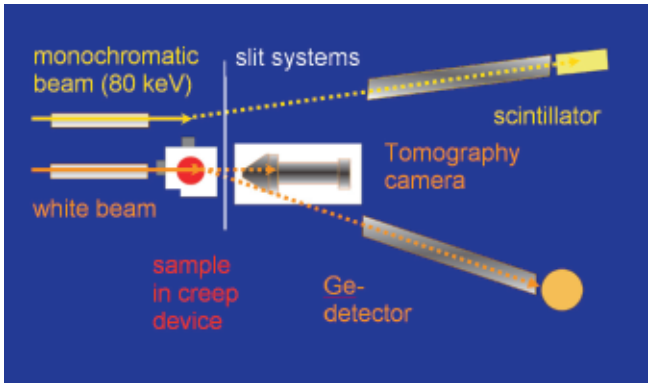

Fig. 40: The experimental setup at beamline ID15A.

The results of the tomography showed that the sample (initially pre-deformed 4.47% at room temperature) contained some small voids oriented in the longitudinal direction of the sample. With increasing creep time, further voids nucleated and the number and size of the voids increased (**Figure 41**). In longitudinal slices void chains are visible that form void networks preferentially oriented app. 90° to the sample longitudinal axis, presumably along grain boundaries and along phase boundaries between α and β-brass. Voids coagulated and subsequently micro cracks became visible. Detailed investigations revealed that the void volume versus creep time obeyed an exponential growth law.

Analyses of the integrated intensity of the α and β-brass reflections revealed the formation of a fibre texture during the creep process, which became strong once the pore volume increases substantially. The diffractograms obtained with white high energy synchrotron radiation revealed that the full width at half maximum (FWHM) of all reflections decreased in the early stage of the creep processes due to an annihilation of the dislocations produced by the pre-deformation of the sample. Later, the FWHM remained constant revealing an equilibrium

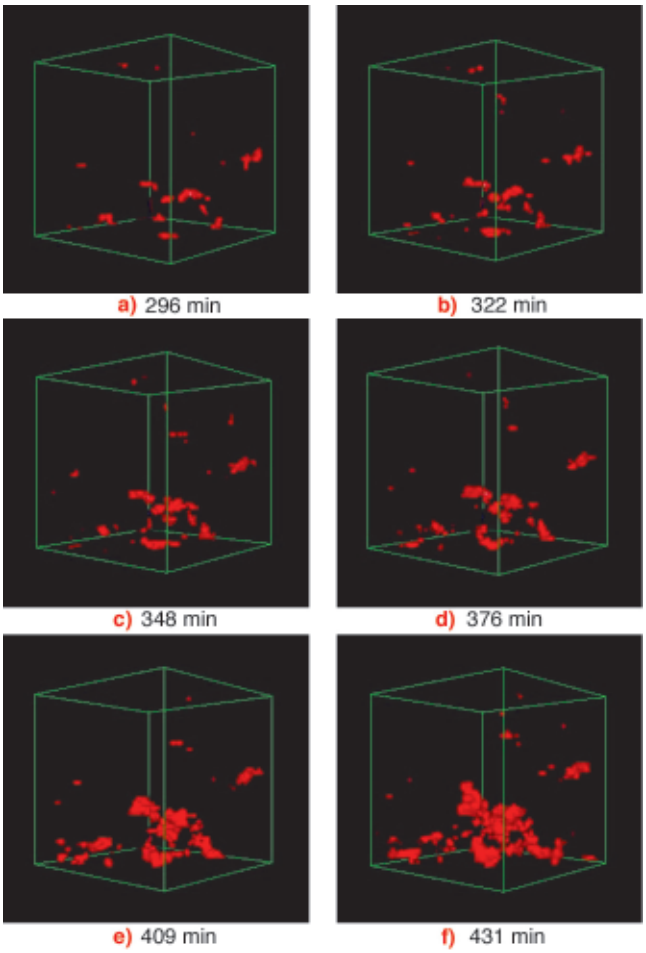

Fig. 41: Progression of the voids (red) with increasing creep time within a sample of CuZn40Pb2 brass.

state of dislocation generation and annihilation. The reflection profiles obtained using monochromatic high-energy synchrotron radiation additionally showed grain growth with increasing creep time.

In conclusion the experiment revealed that using synchrotron radiation tomography, void growth kinetics during creep could be studied in the bulk material *in situ* for the first time. The access to three-dimensional bulk information allowed a quantitative determination of void size and void shape evolution during creep. Combined diffraction and tomography experiments in future will also allow observations of other damage processes such as changes in the stress field and plastic zone around growing cracks or load partitioning, deformation and fracture in multiphase materials.

References

[1] J.-Y. Buffière, E. Maire, P. Cloetens, G. Lormand, R. Fougères, *Acta Mat.* **47**, 1613-1625 (1999).
[2] M. Di Michiel, J.M. Merino, D. Fernandez-Carreiras, T. Buslaps, V. Honkimäki, P. Falus, T. Martins, O. Svensson, *Rev. Sci. Inst.*, **76,** 1-7 (2005).

Principal Publication and Authors

A. Pyzalla (a,b), B. Camin (c), T. Buslaps (d), M. Di Michiel (d), H. Kaminski (a), A. Kottar (a), A. Pernack (c), W. Reimers (c), *Science*, **308,** 92-95 (2005)
(a) Institute of Material Science and Technology, TU Wien (Austria)
(b) MPI for Iron Research, Düsseldorf (Germany)
(c) Institut of Material Science and Technology, TU Berlin (Germany)
(d) ESRF

X-ray Diffraction in Materials Science

Excess Free Volume ΔV_f in Metallic Glasses Measured by X-ray Diffraction

In 1960, Simmons and Balluffi [1] measured the concentration of lattice vacancies $C_v(T)$ in crystals. They used the lattice parameter change $\Delta a\,(T)/a_o$ measured by X-ray diffraction to remove the part of the length-change due to the thermal expansion of the lattice measured by dilatometry $\Delta L\,(T)/L_o$. What remains of $\Delta L\,(T)/L_o$ then yields the increase in vacant lattice sites.

Their experiments which contributed to the quantitative understanding of point defects in solid-state physics were based on:

$$C_v(T) = 3\left\{\frac{(\Delta L(T)}{L_0} - \frac{\Delta a(T)}{a_0}\right\} \quad \textbf{(1)}$$

where $\Delta a\,(T)\,/a_o = \alpha_{th}\,(T) * (T\text{-}T_o) / a_o$, L_o and a_o are the crystal length and lattice parameter at a reference temperature T_o, and $\alpha_{th}\,(T)$ the linear coefficient of thermal expansion.

The quenched-in free-volume, ΔV_f, controls atomic mobility in metallic glasses like vacancies do in crystals. Hence, for the present experiment, our aim was to discover whether quenched-in free-volume takes the form of atomic-sized holes in the glassy state as in crystals. To discover this, a combination of dilatation and X-ray diffraction measurements would be needed to determine ΔV_f in the same way as for vacancies $C_v(T)$ in crystals. On the other hand, computer simulation predicts [2] atomic size holes or vacancies in the glass are unstable and the quenched-in free volume in liquids and glasses is randomly distributed. If this were the case, then **eq.(1)** of Simmoms and Balluffi would not apply, $\Delta V\,(T)\,/V_o$ would be equal to $3\Delta L(T)/L_o$ and the mean atomic volume and the sample dimensions would evolve together with temperature.

Using diffraction in transmission, we determined the evolution of the "average" interatomic distance and the excess free volume ΔV_f from the difference between the

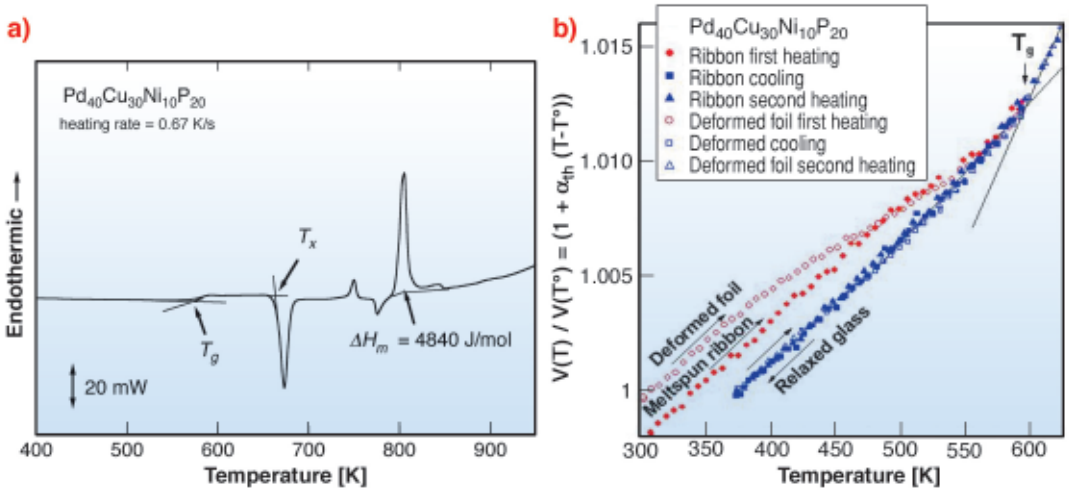

Fig. 42: (a) Calorimetric data of a Pd-based glass [3]; (b) Reduced volume per atom measured by XRD showing relaxation in the as-quenched state and after heavy deformation of the glass towards the same relaxed glassy state at T_g.

interatomic distance versus temperature curves (dilatation) during initial heating to the supercooled liquid state above the glass transition T_g (see **Figure 42a**) of the quenched glass (containing ΔV_f) versus the second heating of the then relaxed glass having already been heated to T_g (with ΔV_f annealed out). ΔV_f were found to be about 2000 ppm in quenched metallic glasses. Deformation-induced ΔV_f was also measured (about 5000 ppm). Dilatation curves (see **Figure 42b**) were found to be identical to those obtained by dialatometry to within experimental error (see ref. [3]). This indicates that, contrary to the Simmons and Balluffi formulation eq.(1) for crystals, the situation is different for metallic glasses, $\Delta L(T) / L_o = \Delta a(T) / a_o$, and atomic-size holes are unstable with ΔV_f distributed randomly, as predicted by simulation [2]. The measured thermal expansion coefficients α_{th} were the same as for dilatometry. The glass transition T_g appeared as a break in the value of σ_{th} at T_g.

Metallic glasses are of the "fragile" type corresponding to an activation energy E for relaxation that increases with T (a non-Arrhenius behaviour) as expected, for example, for a Vogel–Fultcher–Tamman viscosity relation. If during isothermal relaxation, the temperature is abruptly changed at time t* from T_1 to T_2, the activation energy E can be obtained from the slope change according to [4]:

$$\ln \frac{dV_f(T_1,t^*) / dt}{dV_f(T_2, t^*) / dt} = \frac{E}{R} \{ \frac{1}{T_1} - \frac{1}{T_2} \} \quad \textbf{(2)}$$

Figure 43 shows the result of such experiments. E increases from 92 kJ/g.at near 400 K to 114 kJ/g at near 500 K. Our new understanding of relaxation kinetics has allowed us to perform *in situ* fabrication of bulk metallic glasses (BMG-based) nanocomposites with enhanced ductility for structural applications.

Acknowledgements

This work was performed in the framework of the EU Network contract (MRTN-CT-2003-504692 <Ductile BMG Composites>).

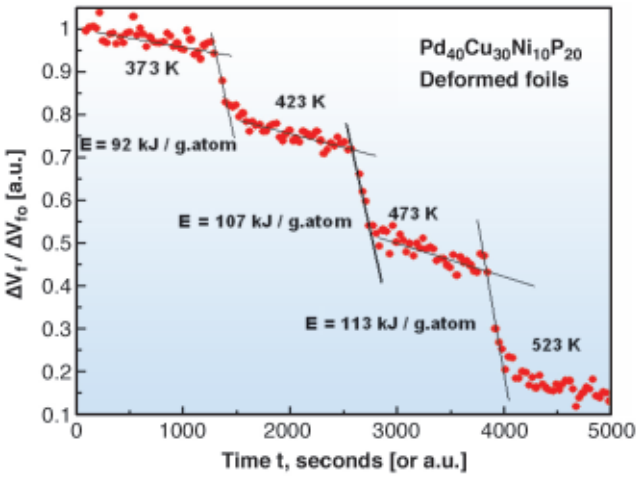

Fig. 43: Isothermal relaxation kinetics of excess free volume ΔV_f in heavily deformed glassy foil when the temperature is abruptly changed at time t* from T_i to T_{i+1}. Activation energy E can be obtained from the slope change $dV_f(T_1, t^*)/dt$ to $dV_f(T_2, t^*)/dt$ according to **eq.(2)**.

References

[1] R. Simmons and R. Balluffi R. *Phys. Rev*. 117-121 (1960).

[2] C.H. Bennett, P. Chaudhari, V. Moruzzi and P. Steinhardt *Philo. Mag. A*. **40**, 485-489 (1979) .

[3] H.S. Chen, *J. Appl. Phys*. **49**, 3289-3291 (1978).

[4] A.C. Damask and G.J. Dienes *"Point Defects in Metals"* Gordon and Breach, pp. 146-149 (1963).

Principal Publication and Authors

A.R. Yavari (a), A. Le Moulec (a) , A. Inoue (b), N. Nishiyama (b), N. Lupu (a,b,c), E. Matsubara (b), W.J. Botta (a), G. Vaughan (c), M. di Michiel (c) , Å. Kvick (c), *Acta Materialia*, **53**, 1611-1619 (2005).

(a) Euronano, LTPCM-CNRS, Institut National Polytechnique de Grenoble (France)

(b) Institute for Materials Research, Tohoku University, Sendai (Japan)

(c) ESRF

View on Grain Nucleation and Growth Kinetics during Solidification

Understanding the crystallisation process during solidification is an essential step in order to tailor the mechanical properties of solidified materials. The physical processes that govern crystallisation are grain nucleation and the subsequent grain growth [1]. In the industrial production process of aluminium alloys the addition of TiB_2 particles along with solute titanium is widely used to enhance the nucleation rate and control the grain growth during solidification [2]. This procedure is generally referred to as grain refinement. Although the mechanisms responsible for grain refinement were studied extensively during the last few decades, a comprehensive understanding is still lacking due to experimental difficulties in monitoring the grain nucleation and growth *in situ*. A question of particular interest is how added TiB_2 particles along with solute titanium results in grain refinement, while no grain refinement is observed if one of the two is missing.

Our present study investigates the nucleation and the growth of individual aluminium grains during solidification. An aluminium alloy with solute titanium (0.1 wt.%) and added TiB_2 particles (0.1 wt.%) was chosen as a model system. Time-resolved X-ray diffraction measurements during solidification of this alloy were performed at **ID11**. The evolution of 2D diffraction images during solidification is shown in **Figure 44**. Before solidification, the short-range order in the liquid gives rise to diffuse scattering, indicated by two broad rings L_1 and L_2 on the 2D image. During solidification, we observe the appearance of bright spots, which correspond to Bragg peaks from individual grains of the solid phase that grow within the liquid phase.

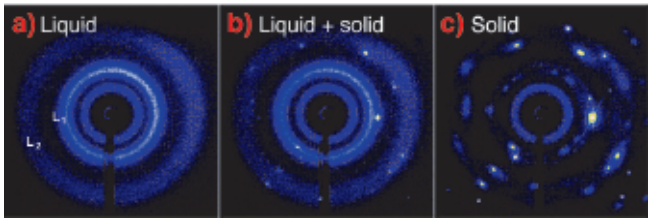

Fig. 44: X-ray diffraction patterns of the aluminium alloy with solute titanium and added TiB_2 particles at different stages of the solidification process during continuous cooling: (a) the liquid phase, (b) the mixed liquid-solid phase, and (c) the solid phase.

Extraction of quantitative information was performed by monitoring the number and intensity of individual diffraction spots during solidification. By counting the number of spots as a function of time, the evolution of the nucleation rate of the solid aluminium grains was obtained. The scaled intensity variation in the first liquid peak (L_1) provides information about the evolution of solid phase fraction. The growth behaviour of individual aluminium grains is determined by continuously monitoring the intensity of the each diffraction spot during solidification.

In **Figure 45a** the time evolution of nucleation process and the solid phase fraction is shown for solidification during continuous cooling at rate of 1 K/min. The results demonstrate that the nucleation process is limited to the initial stage of the solidification and is complete at a solid phase fraction of about 20%. In fact the growth of nucleated grains leads to a significant release of latent heat that limits the undercooling available to activate later nucleation events as the transformation proceeds. **Figure 45b** shows the evolution of the grain radius of an individual aluminium grain as a function of temperature during solidification. The observed growth behaviour of the aluminium grains is controlled by the diffusion of solute titanium and the release of latent heat. As titanium has a strong affinity for the solid phase, its concentration in the melt decreases as the solidification proceeds. A careful analysis of the measured diffraction patterns

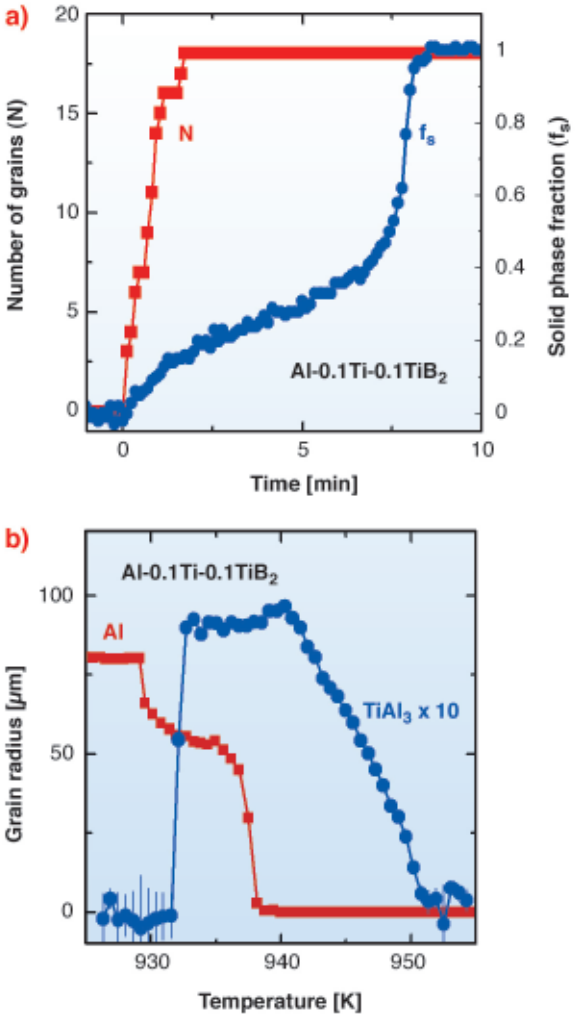

Fig. 45: Grain nucleation and growth in the aluminium alloy during solidification. (a) Total number of nucleated grains in reflection and the corresponding solid phase fraction as a function of time. (b) Grain radius of an individual aluminium grain and an individual $TiAl_3$ grain as a function of temperature during the same solidification experiment.

shows a limited number of weak diffraction spots, originating from a $TiAl_3$ that appears before the start of the solidification process. In **Figure 45b** the evolution of an individual $TiAl_3$ grain is shown. The $TiAl_3$ phase is found to form about 10 K above the experimental solidification temperature of aluminium. At the nucleation temperature of the aluminium, the intensity of the $TiAl_3$ grain starts to decrease, and finally vanishes near the end of the transformation. Due to its better nucleation efficiency, the formation of the $TiAl_3$ phase in the presence of both solute titanium and TiB_2 particles was long proposed, but due to the meta-stable nature of the $TiAl_3$ phase there was no experimental evidence available [2].

These experiments provide the first *in situ* information about the nucleation and growth kinetics of individual grains within the melt during solidification and confirm the mechanism responsible for grain refinement during solidification for the investigated aluminium alloys.

References

[1] J.W. Christian, *The theory of transformations in metals and alloys*, Pergamon, Oxford (2002).

[2] M. Easton. and D. StJohn, *Metall. Mat. Trans. A* **30**, 1613-1623 (1999).

Principal Publication and Authors

N. Iqbal (a), N.H. van Dijk (a), S.E. Offerman (b), M.P. Moret (c), L. Katgerman (b), G.J. Kearley (a), *Acta Mater.* **53**, 2875-2880 (2005).

(a) FAME, Faculty of Applied Sciences, Delft University of Technology (Netherlands)

(b) Department of Materials Science and Engineering, Delft University of Technology (Netherlands)

(c) ESRF

Observing Dislocation Structures Evolve During Annealing of Deformed Metals

When metals or alloys are deformed plastically, line defects – dislocations – are introduced. The dislocations typically self-assemble into structures, where dislocation walls separate small dislocation-free crystals - the sub-grains (see inset in **Figure 46**). During subsequent annealing the stored energy in the structure is released by two processes: recovery (coarsening of the sub-grains) and recrystallisation (nucleation and growth of new grains) [1]. These processes govern basic properties such as hardness and ductility.

The 3DXRD microscope situated at beamline **ID11** enables comprehensive 3D characterisation of the dynamics of grains within millimetre-thick polycrystalline specimens [2]. In this work the methodology is extended to the sub-micrometre scale for studies of sub-grains

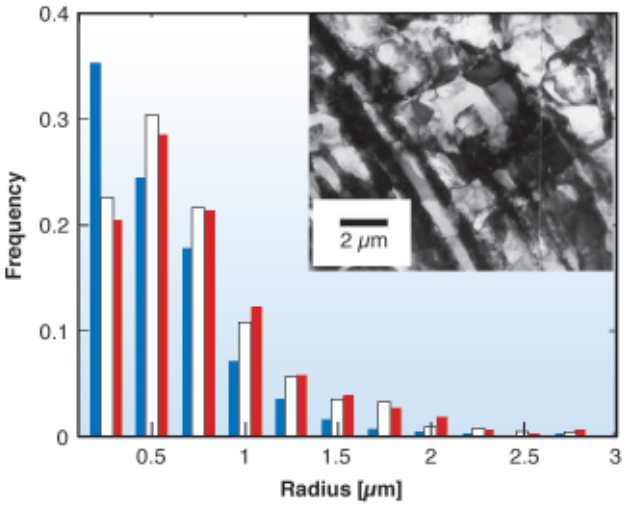

Fig. 46: Recovery of 38% cold-rolled Aluminium. Histograms of subgrain size (equivalent spherical radii) obtained from 500 diffraction spots in the as-deformed state (blue) and after 3 min (white) and 181 min (red) of *in situ* annealing at 300°C. Inset: Transmission Electron Micrograph of the as-deformed material.

during recovery. The number of simultaneously illuminated sub-grains is reduced by focusing the beam to 7 x 7 μm^2 and by studying a foil. (When the foil thickness is at least 10 times the sub-grain size, the sub-grains at the centre of the foil can be considered as representative of bulk.) In this way, distinct and non-overlapping diffraction spots from sub-grains as small as 70 nm can be observed. By monitoring the variation in position and intensity of any such spot, the evolution in orientation, strain, and volume of the sub-grain of origin can be inferred. Some results are shown in **Figures 46** and **47.**

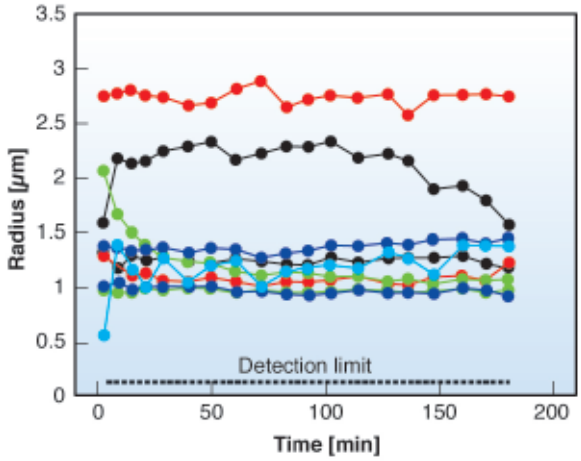

Fig. 47: Recovery of 38% cold-rolled Aluminium at 300 °C. Growth curves for 9 selected sub-grains as function of annealing time.

References

[1] *E.g.* F.J. Humphreys, M. Hatherley: *Recrystallization and Related Annealing Phenomena,* Pergamon Press, New York (1995).

[2] H.F. Poulsen: *Three-dimensional X-ray Diffraction Microscopy,* Springer, Berlin (2004).

Principal Publication and Authors

C. Gundlach (a), W. Pantleon (a), E.M. Lauridsen (a), L. Margulies (a,b), R.D. Doherty (c) and H.F. Poulsen (a), *Scripta Mater.*, **50**, 477-481 (2004).

(a) Centre for Fundamental Research: Metal Structures in Four Dimensions, Risø National Laboratory (Denmark)

(b) ESRF

(c) Drexel University, Department of Materials Science and Engineering (US)

Crystal Structure of Ferromagnetic Insulated $La_{1-x}Ca_xMnO_3$

The manganese perovskites ($L_{1-x}A_xMnO_3$, where L is rare earth and A is alkaline earth) provide an ideal physical system for the elucidation of a variety of fundamental physical questions related with the magnetic, electronic and structural properties of condensed matter in a strongly-correlated electronic system [1]. The most important topic to emerge from studies of manganites' physics is the competition between localising and delocalising effects in close connection with lattice, spin and charge degrees of freedom. The ferromagnetic metallic ground state has been partially explained, with consideration of a double exchange mechanism. However, the nature of the ferromagnetic insulating state (FMI) in lightly doped $La_{1-x}A_xMnO_3$ (A = Sr, Ca, x = 0.1-0.2) manganese perovskites continues to offer significant challenges for the understanding of the physical properties of these materials. Typically, insulating compounds of this category are antiferromagnetic, and ferromagnetism is associated with a metallic behaviour that arises from doping and double exchange. The FMI state can be achieved with a certain orbital ordering, favourable for ferromagnetism [2].

The interplay of orbital, charge, spin and lattice degrees of freedom in these materials produces small structural changes, in comparison to the high temperature structure. Consequently, high-resolution X-ray diffraction data, in stoichiometric samples are necessary. The required resolution is offered by the high-resolution powder diffractometer of beamline ID31.

We have studied the crystal and magnetic structures of the $La_{1-x}Ca_xMnO_3$ compound for ($0.11 \leq x \leq 0.175$) using stoichiometric samples. $La_{1-x}Ca_xMnO_3$ samples were prepared by thoroughly mixing high-purity stoichiometric amounts of $CaCO_3$, La_2O_3, and MnO_2. The mixed powders reacted in air at temperatures up to 1400°C, for several days, with intermediate grinding. Finally, the samples were slowly cooled to 25°C. These samples are cation deficient [3]. In order to produce stoichiometric samples, additional annealing in a He atmosphere was used.

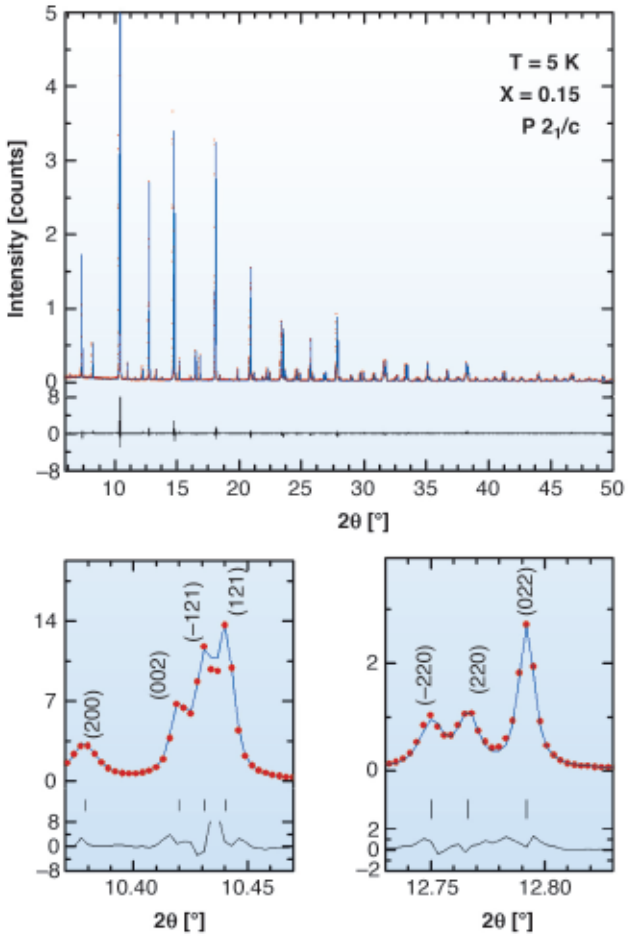

Fig. 48: Rietveld plot of $La_{0.85}Ca_{0.15}MnO_3$ compound at T = 5K. The experimental pattern was measured with the high-resolution diffractometer (wavelength 0.05 nm) on ID31. Shown are details of the diffraction peaks where the characteristic peak splitting compatible with $P2_1/c$ space group is expected.

For x < 0.13 the ground state is insulating canted antiferromagnetic. Thanks to the excellent resolution of ID31, we discovered that the high temperature (Pnma) crystal structure undergoes a monoclinic distortion for $0.13 \leq x \leq 0.175$, below the Jahn-Teller transition temperature (T_{JT}). **Figure 48** shows a representative Rietveld plot for $La_{0.85}Ca_{0.15}MnO_3$ sample at T = 5 K. The crystal structure can be described with the $P2_1/c$ space group, which contains two Mn sites. The unit cell strain parameter s = 2(a-c)/(a+c) increases for $T < T_{JT}$, taking the maximum value at the Curie point, and then decreases. Below $T_{M/M//} \approx 60$ K, s abruptly changes slope and finally approaches T = 0 K with nearly zero slope (**Figure 49a**). The change of s at $T_{M/M//}$ is connected to a characteristic feature in the magnetic measurements. As x increases towards the ferromagnetic metallic boundary, the monoclinic structure is preserved although s is reduced appreciably. The low temperature monoclinic structure contains two distinct Mn sites (**Figure 49b**) and in relation with the Mn-O bond lengths one could consider that a specific orbital ordering takes place in the ferromagnetic insulating regime. Using the Kanamori- Goodenough-

Anderson rules, a reasonable interpretation of the ferromagnetic insulating ground state can be given.

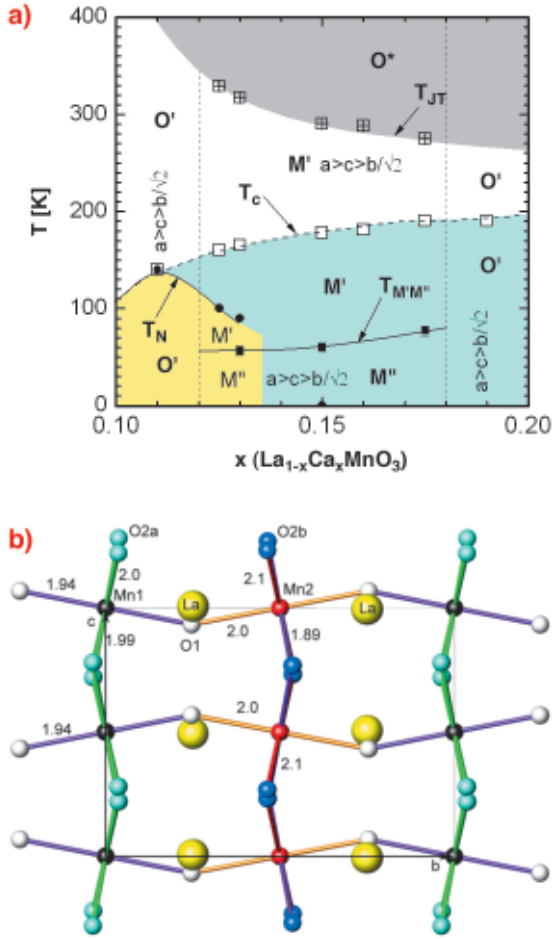

Fig. 49: (a) Ferromagnetic insulating part of the phase diagram of $La_{1-x}Ca_xMnO_3$ compound. The light yellow region corresponds to the canted-antiferromagnetic regime, and the light blue to the ferromagnetic-insulating regime. The symbols O*, O/, O//, M/ and M// have the following meaning: O* orthorhombic Pnma symmetry with c > a > b / √2; O/, (O//) orthorhombic Pnma symmetry with a > c > b /√2 and strong (intermediate) anisotropic bond lengths and [M/, (M//) monoclinic P 2_1/c symmetry with a > c > b / √2 and strong (intermediate) anisotropic bond lengths]. $T_{M/M//}$ is defined at the temperature where the slope of the a(T) and b(T) curves change slope abruptly upon heating from T = 0. The T_{JT} curve is defined at the temperature where the m(T) curves display a jump-like or slope-change behaviour. The T_C and T_N are both estimated from neutron and magnetisation data. (b) Projection of the unit cell of the monoclinic structure of $La_{0.85}Ca_{0.15}MnO_3$ compound, along the b-axis.

References

[1] Colossal Magnetoresistive Oxides, edited by Y. Tokura, Gordon and Breach, New York, 200; Colossal Magnetoresistance; Charge Ordering and Related Properties of Manganese Oxides, edited by C. N. R. Rao and B. Raveau World Scientific, Singapore, (1998).

[2] D. Khomskii and G. Sawatzky, *Solid State Comm.* **102**, 87 (1997).

[3] M. Pissas and G. Papavassiliou *J. Phys.: Condens. Matter* **16** 6527 (2004).

Principal Publication and Authors

M. Pissas (a), I. Margiolaki (b), G. Papavassiliou (a), D. Stamopoulos (a), D. Argyriou (c), Phys. Rev B **72**, 064425 (2005).

(a) Institute of Materials Science, National Center for Scientific Research, Athens (Greece)

(b) ESRF

(c) Berlin Neutron Scattering Center, Hahn-Meitner-Institut (Germany)

Mixed Interfullerene Bonding Motifs in C_{60}-based Polymers

An unexpected discovery in fullerene chemistry has been the ease with which C_{60} units can covalently bond together to give rise to polymerised fullerene networks with a variety of structural architectures. Such fullerene-bridged arrays display varying dimensionality and intriguing electronic (metallic behaviour) and magnetic (ferromagnetism above room temperature) properties. The predominant interfullerene bonding structural motifs are either 4-membered carbon rings arising from [2+2] cycloaddition reactions (**Figure 50a**) or single C-C covalent bonds (**Figure 50b**) bridging together adjacent molecules and propagating in one (1D chains) or two (2D layers) dimensions [1].

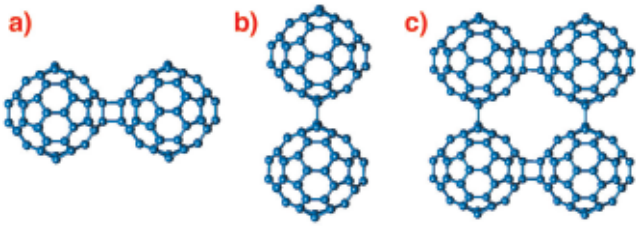

Fig. 50: Schematic drawing of the interfullerene C-C bridging structural motifs in polymeric fullerides. (a) [2+2] cycloaddition in AC_{60}, (b) single C-C covalent bonds in Na_2RbC_{60}, and (c) mixed bonding in Li_4C_{60}.

A prominent example of a fulleride polymer network is Li_4C_{60} whose structure has remained a subject of debate. When we probed its structural properties by high-resolution X-ray powder diffraction on beamline **ID31**, we found that Li_4C_{60} adopts a layered polymeric structure. However, unexpectedly, and in contrast to all other known fullerene polymers, each C_{60} unit in Li_4C_{60} bonds to its four nearest neighbours in the layers using both the [2+2] cycloaddition and the single C-C bridging motifs (**Figure 50c**), thereby giving rise to two types of differently-bonded chains running perpendicular to each

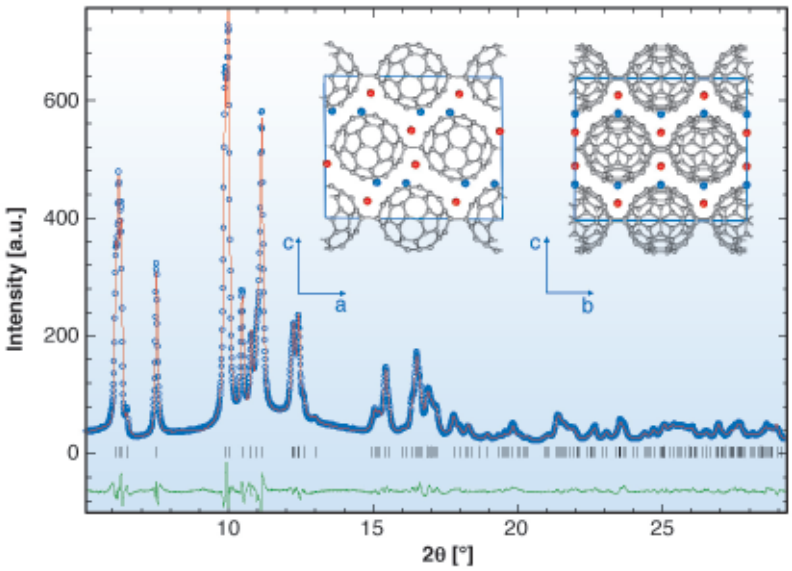

Fig. 51: Final observed (O) and calculated (–) synchrotron X-ray diffraction profile for Li_4C_{60} at 295K (λ = 0.85066 Å, agreement factors of the Rietveld refinement: R_{wp} = 5.12%, R_{exp} = 1.53%, R_{F2} = 3.46%). The lower solid line shows the difference profile and the tick marks show the reflection positions. *Inset.* The crystal structure of polymerised Li_4C_{60}: projections on the ac (left) and bc (right) basal planes. Li^+ ions residing in pseudo-tetrahedral and -octahedral holes are depicted as blue and red spheres, respectively.

other. The resulting unprecedented 2D fulleride network has neither been observed before experimentally nor been anticipated theoretically.

The X-ray powder diffraction profile of Li_4C_{60} obtained at ambient temperature (**Figure 51**) revealed that its structure was body-centred monoclinic with lattice parameters, *a* = 9.3267(3) Å, *b* = 9.0499(3) Å, *c* = 15.03289(1) Å, and β = 90.949(3)° (space group *I*2/*m*). A notable feature of this result is that Li_4C_{60} is strongly anisotropic with the closest centre-to-centre contacts between the C_{60} units of ~ 9.33 Å, ~ 9.05 Å, and ~ 9.95 Å along the *a* and *b* axis and the body diagonal, respectively. While the latter contact is comparable to those encountered in monomeric fullerenes and fullerides (~ 10.0 Å), the one along *b* is reminiscent of that in monoclinic polymerised AC_{60} (~ 9.11 Å) in which there are two bridging C-C bonds between C_{60}^- ions (**Figure 50a**). In addition, we note that short C-C contacts are also implied along the *a* axis, with the interfullerene distances comparing with those in fullerides with single C-C interfullerene connections (**Figure 50b**). The high-resolution synchrotron X-ray diffraction data allowed a detailed structural characterisation. Through a series of Rietveld refinements combined with Fourier analysis we were able to determine both the molecular bonding geometry and the precise location of the intercalated Li^+ ions. Perspective views of the refined structure of Li_4C_{60} highlighting the different bonding motifs on the *ac* and *bc* basal planes are shown in **Figure 51** (inset).

The origin of the different structures adopted by Li_4C_{60} and the related polymeric fullerides, Na_2RbC_{60} (chains bridged by one C–C bond) and Na_4C_{60} (layers bridged by four C–C bonds) is of considerable interest. The stability of polymeric fulleride structures is strongly associated with the charged state of the fulleride ions and the steric influence of the alkali ions. The small size of Li^+ (0.60 Å) is of paramount importance in minimising steric crowding and allowing the incorporation of two Li^+ in the space surrounding the pseudo-octahedral site. If Na_2RbC_{60} or Na_4C_{60} were to adopt structures similar to that of the Li_4C_{60} polymer, severe steric hindrance would be encountered. The Rietveld refinements indicate a Li doping level of *x* = 3.49(7). Considering the usual behaviour of Li for partial electron donation to the fullerene units, a formal charge smaller than –4 is expected for the C_{60}^{n-} anions. This is again inconsistent with the adoption of the 2D Na_4C_{60} structure, favoured for $n \approx -4$.

In this work, we have shown that the ground state of Li_4C_{60} is a two-dimensional polymer with monoclinic crystal symmetry and an unprecedented architecture, combining both the [2+2] cycloaddition and the single C-C bridging motifs. This tightly-packed structure, whose salient features we have now confirmed by NMR and Raman spectroscopy [2], is the first example of a fullerene polymer with a mixed mode of interfullerene bridging and opens the way for the synthesis and study of new C_{60}–based polymers where different types of bonding geometries can coexist and interconvert by the application of external stimuli such as light irradiation or high pressure.

References

[1] S. Margadonna and K. Prassides, *J. Solid State Chem.* **168**, 639 (2002).

[2] M. Riccò, T. Shiroka, M. Belli, D. Pontiroli, M. Pagliari, G.Ruani, D. Palles, S. Margadonna, M. Tomaselli, *Phys. Rev. B* **72**, 155437 (2005).

Principal Publication and Authors

S. Margadonna (a), D. Pontiroli (b), M. Belli (b), T. Shiroka (b), M. Riccò (b), M. Brunelli (c), *J. Am. Chem. Soc.* **126**, 15032-15033 (2004).

(a) School of Chemistry, University of Edinburgh (UK)

(b) Dipartimento di Fisica and CNISM, Università di Parma (Italy)

(c) ESRF

In situ Study of Methane Anaerobic Combustion on Iron Oxides: Towards a Clean Hydrogen Production Process

Hydrogen will be one of the most important fuels in a future sustainable economy. In the medium term, hydrogen production will still rely on fossil fuels, whose environmental impact has to be lowered both by modifying actual technologies and/or developing new ones capable of mitigating CO_2 emissions. ENI is developing a clean process for H_2 production from fossil fuels based on the properties of selected oxides that, once reduced with hydrocarbons, are capable of being re-oxidised by splitting H_2O into H_2 and [O], which in turn re-oxidises the solid closing the loop [1].

$$4Me_xO_y + CH_4 \rightarrow 4Me_xO_{(y-1)} + 2H_2O + CO_2$$
$$4MexO_{(y-1)} + 4\ H_2O \rightarrow 4Me_xO_y + 4H_2$$

$$CH_4 + 2\ H_2O \rightarrow 4H_2 + CO_2 \qquad \Delta H = 39.5\ Kcal$$

A redox solid circulating among three fluidised bed reactors is the asset developed to exploit the reaction scheme (**Figure 52**).

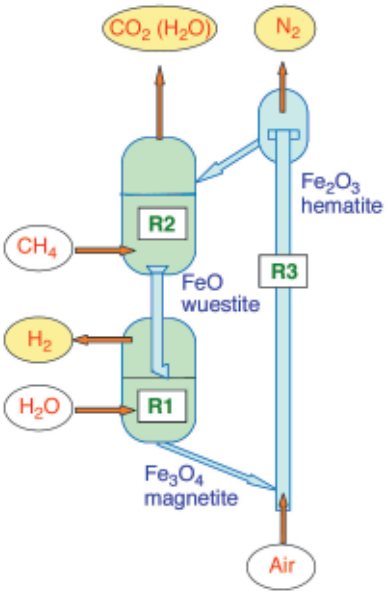

Fig. 52: Conceptual reactors design to exploit the redox concept on iron oxide based circulating solid. A concentrated stream of CO_2/H_2O (ready to be buried) is produced in reactor 2, when the solid is reduced by methane (Fe_2O_3/FeO). A stream of H_2 (virtually carbon free) is produced in reactor 1, when the solid is partly oxidised with water (FeO/Fe_3O_4). Thermal balance is achieved in reactor 3, where the solid is fully reoxidised (Fe_3O_4/Fe_2O_3).

We carried out a combined X-ray diffraction (XRD) / mass spectrometry (MS) experiment at the Italian CRG BM08 "GILDA" beamline, to study the structural evolution of an iron based solid exposed to methane under anaerobic combustion conditions as a first step of such a redox cycle.

The CeO_2/Fe_2O_3 solid investigated was exposed to a high temperature (~ 1000 K) CH_4 reducing flux followed by a re-oxidation in air. The sample was contained in an open quartz capillary. One side was connected to a gas injecting system (CH_4/Ar mixture, air and Ar for purging cycles), the other to a mass spectrometer (MS). X-ray powder diffraction was collected by a translating image plate system with a time resolution of one minute.

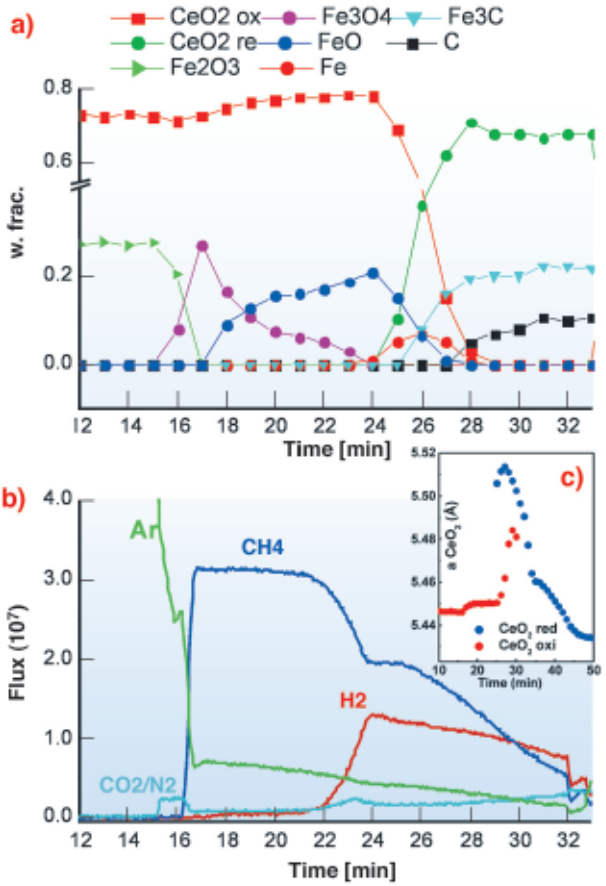

Fig 53: Evolution during the reduction cycle: a) Quantitative phase analysis; b) Evolved gases; c) Plot of the CeO_2 cell parameter.

All the collected powder patterns were analysed by the Rietveld method, obtaining a complete structure characterisation of the process in terms of quantitative analysis of the crystal phases involved (see **Figure 53a**). As soon as the CH_4 enters the capillary, a series of redox reactions take place. Iron present as Fe^{3+} in Fe_2O_3 is progressively reduced to $Fe^{+2}Fe^{+3}{}_2O_4$ (magnetite), $Fe^{+2}O$ (wuestite) and finally to Fe. The appearance of metallic iron in the XRD signal coincides with the H_2 emission and the decrease of the flow of outgoing CH_4 (**Figure 53b**) detected by MS. This is direct evidence of methane cracking ($CH_4 \rightarrow C + 2H_2$) catalysed by iron. The carbon produced by this reaction appears two minutes later as Fe_3C, which replaces iron in catalysing the cracking, and as a polymorph of graphite. We have clear evidence that CeO_2 participate to the reduction process. It is known that in a reducing environment ceria may convert into a non-stoichiometric reduced form (CeO_{2-x}), whose crystal structure has the same symmetry but a larger unit cell.

By mapping the variation of CeO_2 unit cell parameter, a small jump corresponding to CH_4 injection and a large jump corresponding to H_2 emission can be detected. The latter change is simultaneous with a splitting of the ceria diffraction peaks that can be interpreted as a mixture of two reduced ceria phases with different defectivity (**Figure 53c**). The stoichiometry of the reduced ceria is proportional to the unit cell variation and seems to be temperature independent [2]. The estimated compositions are $CeO_{1.99}$ after the CH_4 injection and $CeO_{1.88}$ for the most reduced form appearing after H_2 emission. Peak shape analysis demonstrates that during CH_4 combustion CeO_2 undergoes re-crystallisation since the full width half maxima of CeO_2 peaks constantly decrease. The oxidation follows the reverse path of the reduction except for the direct oxidation of Fe_3C to FeO without the intermediate formation of iron. The final solid has the same composition as the starting mixture demonstrating that the cycle is totally reversible.

References

[1] U. Cornaro, D. Sanfilippo US2004152790-A1.

[2] H. Chiang, R.N. Blumenthal, R.A. Fournelle, *Solid State Ionics* **66**, 85-95 (1993).

Principal Publication and Authors

M. Gemmi (a), M. Merlini (a), U. Cornaro (b), D. Ghisletti (b), G. Artioli (a) *J. Appl. Cryst* (2005) **38**, 353-360.

(a) Dipartimento di Scienze della Terra "A. Desio", Università degli Studi di Milano (Italy)

(b) Eni Tecnologie Spa, San Donato Milanese (Italy)

Resonant Contrast Diffraction for Direct Localisation of Atoms in Mixed Occupancy Powders

Describing detailed atomic order in complex powders such as natural samples or industrial materials (minerals, cement, catalysts) remains a challenge because X-ray powder diffraction discriminates poorly between elements with close atomic numbers occupying neighbouring sites. Here, we apply resonant contrast diffraction to complex powders via new methodologies of anomalous difference patterns for multi-wavelength refinement to accurately localise atoms, and produce dispersive difference maps to directly visualise them.

Resonant scattering variations near an absorption edge are used in Diffraction Anomalous Fine Structure (DAFS) [1], and to solve the structure factor phase problem in biocrystallography. The present contribution focuses on a third application, Resonant Contrast Diffraction (RCD), using the chemical sensitivity of resonant diffraction to extract the contribution of a single element to each crystallographic site.

The specificities of RCD were demonstrated on powders in the nineties [2], but *ab initio* structure determination using partial Patterson density maps and "maximum entropy methods" becomes inefficient for complex powders due to reflection overlap [3]. Partial structure factor analysis on the other hand, is efficient in studying poorly crystallised or amorphous samples [4]. Here, we develop resonant scattering for highly-crystallised solids of industrial interest: bicationic X zeolites.

Our methodology, using two methodological advances and simultaneous refinement of several diffraction patterns, was validated by the determination Sr^{2+} and Rb^{+} cation distributions in SrRbX. Since Sr^{2+} and Rb^{+} have the same number of electrons (Z = 35 e.u.) and similar neutron scattering lengths (b(Sr) = 0.702 x 10^{-12} cm; b(Rb) = 0.709 x 10^{-12} cm) this is a particularly difficult case for conventional X-ray or neutron diffraction.

Diffraction experiments (on **BM2** using Debye-Scherrer geometry) were performed 10 eV below the Rb and the Sr K edges and at 14.8 keV, far below both edges. An initial Fourier map calculated using the known zeolite structure (**Figure 54a**), gave rough and non element selective localisation of extra-framework atoms (cations, water molecules, etc). These are introduced as electron densities, with no assumption of the atom type, on sites I, I', II, II' and III (**Figure 54b**).

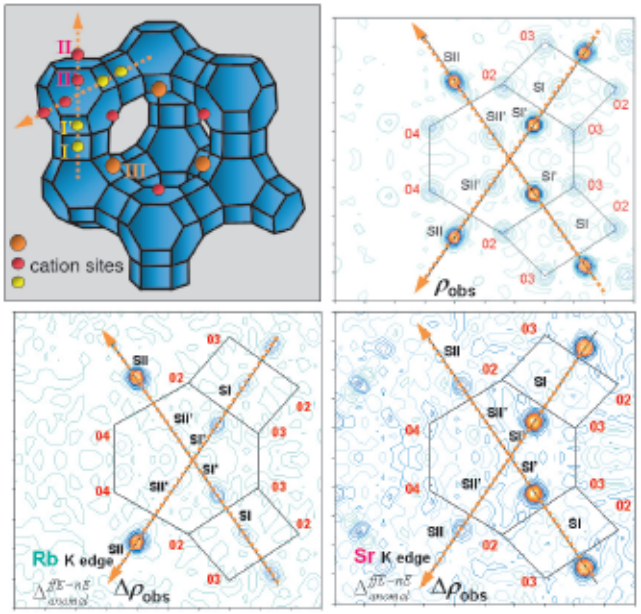

Fig. 54: The X zeolite structure: (a) the main cationic sites in the unit cell, (b) Intersection of two <111> axes defines the Fourier map section, (c) Dispersive difference map of Rb, (d) Dispersive difference map of Sr.

Resonant diffraction gives dispersive difference map between electron densities determined at Rb and Sr edges, with amplitudes proportional to the variation of the real resonant contribution ($\Delta f'$), allowing resonant cation localisation (**Figures 54c** and **54d**).

This selectivity can be seen directly in anomalous difference patterns calculated from data at $E_{K\text{-}Sr}$ – 10 eV and $E_{K\text{-}Sr}$ – 1300 eV (and at $E_{K\text{-}Rb}$ – 10 eV and $E_{K\text{-}Rb}$ – 400 eV), used in the refinement. Calculated and measured patterns, highly-sensitive to resonant atom location and occupancy, present close agreement after adjusting resonant atom occupancies (**Figure 55**).

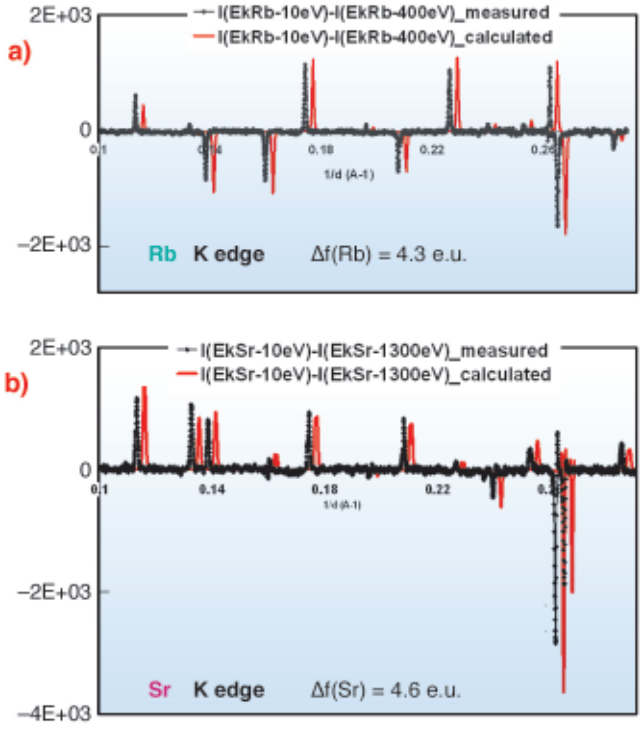

Fig. 55: Measured and calculated anomalous differential patterns (difference between diagrams obtained at different energies) at Rb- (a) and Sr- (b) K absorption edges, using the same intensity normalisation.

Using Resonant Contrast Diffraction, cation distribution was determined in several bicationic zeolites (SrRbX, SrCaX and CaRbX). Sr^{2+} occupies preferentially sites I', II and III whereas Rb^{+} occupies mainly site II and (if enough Rb^{+} is present) supercage site III. Ca^{2+} shows strong preference for sites I' and III. In all solids, site II' is mainly populated by water molecules.

In conclusion, resonant scattering enables accurate localisation of atoms in powders via dispersive difference maps in real space to locate resonant cations, and anomalous differential diffraction patterns in reciprocal space to quantify the structural model. Using this new methodology, Resonant Contrast Diffraction becomes an easily applicable key method to analyse site occupancies by chemically different cations.

References

[1] J.L. Hodeau, V. Favre-Nicolin, S. Bos, H. Renevier, E. Lorenzo, J.F. Berar, *Chem. Rev.* **101**, 1843 (2001).
[2] D.E. Cox, A.P. Wilkinson, In: Resonant anomalous diffraction X-ray scattering. Theory and applications. G. Materlik, C.J. Sparks and K. Fischer (Eds.), 195 (1994).
[3] K. Burger, D. Cox, R. Papoular, W. Prandl, *J. Appl. Crystallogr*. **31**, 789 (1998).
[4] E. Matsubara, Y. Waseda, In: Resonant anomalous diffraction X-ray scattering. Theory and applications. G. Materlik, C.J. Sparks and K. Fischer (Eds.), 345 (1994).

Principal publication and authors

H. Palancher (a,b), J.L. Hodeau (b), C. Pichon (a), J.F. Bérar (b,c), J. Lynch (a), B. Rebours (a) and J. Rodriguez-Carvajal (d), *Angew. Chem. Int. Ed.*, **44**, 1725-1729 (2005).
(a) Institut Français du Pétrole, Vernaison (France)
(b) Lab. de cristallographie, CNRS, Grenoble (France)
(c) French CRG D2AM, ESRF
(d) Lab. Léon Brillouin, CEA/Saclay, Gif sur Yvette (France)

Introduction

Highlights from the Soft Condensed Matter (SCM) Group and CRG beamlines show the large spectrum of scientific topics, which reaches into neighbouring disciplines such as materials science and in particular biological science. These results rely on a constant upgrade and refurbishment program of beamlines and annex facilities. Thus refractive lens optics are becoming an ubiquitous focusing tool at all SCM beamlines. The contribution by Schroer *et al.*, shows that 50 nm focal spots by refractive optics has become a reality and a further reduction is technically possible. Such optics will initially find use at the ID13 beamline's nanofocus extension hutch, which will be commissioned starting at the end of 2006. Promising results have also been obtained with the MEDIPIX 2 pixel detector chip on ID02/ID10A. Thanks to this, the dream of a large area detector with small pixel size, single photon counting capability, high dynamic range and submillisecond readout time is getting closer. The upgrade of SCM-laboratories with large-scale equipment, such as a Brewster angle microscope (ID10B), an optical microscope for micromanipulation (ID13) and a light-scattering setup (ID02/ID10) has continued during 2005 although space is increasingly becoming a problem. A future option for joining forces with external groups in a partnership model could provide the space and freedom for a new level of supporting laboratories. A workshop organised by the SCM group at the end of 2004 in collaboration with the ILL provided the occasion for discussing possible partnership models with a number of external groups.

C. Riekel

Dramatic Reduction of Surface Tension of Water

Controlling the surface tension of water has been a historical pursuit. Existing surfactants can lower it either as a monomolecular layer on water surface (Langmuir monolayers) or by forming microemulsions. In the former, the bulk water composition is unchanged but the surface tension can be reduced from 72 mN/m to only about 20 mN/m. The microemulsion can make the interfacial tension go to 1 μN/m but changes the water composition. We have shown, through measurement of capillary wave amplitudes using diffuse scattering of X-rays, that a bi-molecular layer of a three-tailed amphiphile, preformed ferric stearate (FeSt), on water surface [1], lowers the surface tension to about 1 mN/m.

Diffuse X-ray scattering experiments, using an 8.04 keV X-ray beam at grazing incidence, *i.e.* below the critical angle for total external reflection from water, were carried out at beamline **ID10B**. Preformed FeSt in chloroform solution was spread on water in a Langmuir trough, under He atmosphere, with the diffractometer centre lying on the water surface in the trough. Two different scattering geometries were used, one employing a 'point' NaI detector collected the scattered intensity in a vertical plane while the other, using a vertically mounted position-sensitive detector (PSD), collected the vertical scattered intensity profile at different positions on the horizontal plane. Intensity profile along the PSD as well as that collected by the 'point' detector is proportional to the out-of-plane structure factor of the film and intensity integrated over the PSD profile is proportional to the surface fluctuation spectrum integrated along propagation direction.

Figure 56 shows the vertically-scattered intensity profiles from water, stearic acid monolayer on ferric chloride solution and film of preformed ferric stearate on water.

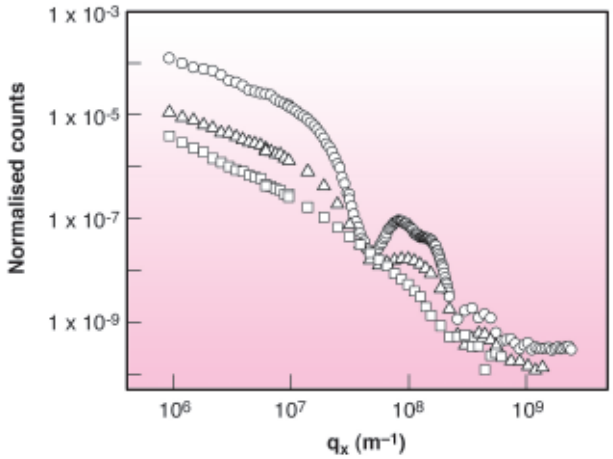

Fig. 56: X-ray scattering in the vertical plane from water (open squares), stearic acid film at π = 20 mN/m over aqueous solution of ferric chloride (open triangles) and preformed ferric stearate film at same surface pressure over water (open circles).

Whereas the acid monolayer behaves exactly as other Langmuir monolayers [2], the preformed fatty-acid salt film shows a split peak. The average structure factor of FeSt film in the total scattering function yields electron density profile along film depth (**Figure 57**). It corresponds to the bi-molecular layer shown in schematic, composed of molecules in symmetric configuration, on top of molecules in asymmetric configuration with ferric ions in contact with water. The most interesting feature, shown in **Figure 56**, as well as in the integrated in-plane scattered profile, is the enhancement by about two orders of magnitude, of the diffuse scattered intensity of the FeSt film at high surface pressure, i.e. high coverage. We ascribe this difference to enhanced conformal capillary wave height fluctuations at air-film and film-water interfaces. The only other possible source of large off-specular scattering is scattering from bimolecular domains, which was estimated from AFM measurements on FeSt films transferred onto Si substrates at low film coverage and was found to be much lower than the observed scattering. We fitted our data using the correlation function for a liquid surface, which gave excellent results over almost four orders of magnitude with surface tension = 1.3 mN/m.

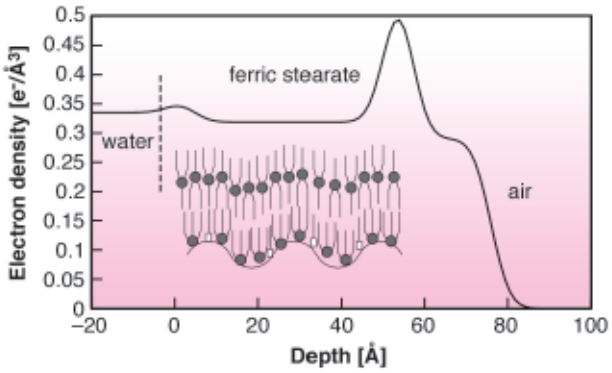

Fig. 57: Electron density of compressed ferric stearate film on water, extracted from the X-ray scattering profile shown in **Figure 56**. Inset: schematics of bi-molecular film with $(COO)_3Fe$ (circle) and COOH (square) groups.

In conclusion, we have demonstrated that a bi-molecular layer of a three-tailed amphiphile drastically enhances capillary wave fluctuations on water surface due to a reduction in surface tension to 1 mN/m. Unlike the usual Langmuir monolayers, this bi-molecular layer does not rupture under compression, but becomes thicker. This behaviour mimics folding of a membrane on a liquid surface and is closely related to the cohesive interaction brought by ferric ions.

This work was carried out under Project 2504-2 of the Indo-French Centre for Promotion of Advanced Research (IFCPAR). We would like to thank IFCPAR for financial assistance.

References

[1] A. Datta, M. K. Sanyal, A. Dhanabalan, and S. S. Major, *J. Phys. Chem. B* **101**, 9780 (1997).

[2] C. Fradin, J. Daillant, A. Braslau, D. Luzet, M. Alba, and M. Goldmann, *Eur. Phys. J. B* **1**, 57 (1998).

Principal Publication and Authors

A. Datta (a), S. Kundu (a), M. K. Sanyal (a), J. Daillant (b), D. Luzet (b), C. Blot (b) and B. Struth (c), *Phys. Rev. E*, **71**, 041604-1 – 041604-7 (2005).
(a) Saha Institute of Nuclear Physics, Kolkata (India)
(b) LIONS, CEA, Saclay (France)
(c) ESRF, Grenoble (France)

Microrheology of Polymeric Solutions using X-ray Photon Correlation Spectroscopy

Polymeric solutions exhibit a wide range of viscoelastic properties which are crucially important for their biological behaviour and a number of industrial applications *e.g.* muscular contractions, blood clotting and colloidal stabilisation. Microrheology is a field which considers the measurement of the viscoelasticity of materials as a function of length scale. Recently, a number of new microrheological techniques have been developed with numerous advantages over conventional rheological measurements; they are sensitive to a wider range of frequencies (~ 10^{-4} -10^{6} Hz), they only require minute quantities of polymer (10 µL) and they apply extremely small forces (pN), which enables the examination of delicate biological molecules [1].

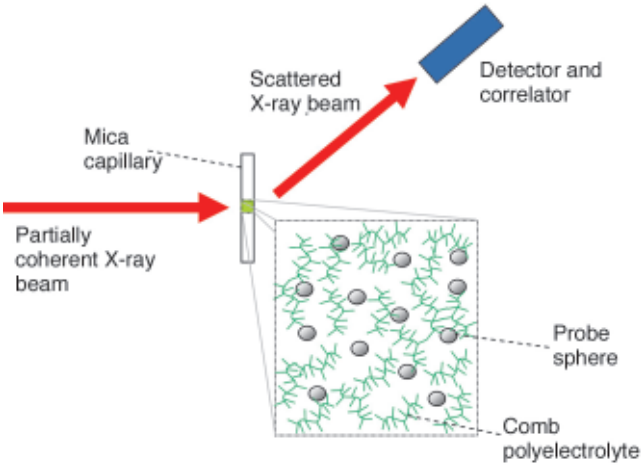

Fig. 58: X-ray photon correlation spectroscopy microrheology examines the viscoelasticity of polymeric solutions using the motion of embedded probe spheres. The polymer solutions were contained in capillaries (~ 10 µL) and mixed with 0.5 µm silicon probe spheres. The incident X-ray beam is partially coherent and the scattering volume must be restricted to the size of the coherence volume for the technique to work. An auto-correlator device is used to calculate $g^{(2)}(t)$, the temporal auto-correlation function of the scattered intensity, at various momentum transfers.

Based on X-ray Photon Correlation Spectroscopy (XPCS), we have developed a new microrheology technique to probe the dynamics of opaque materials in solution. XPCS exploits a partially coherent X-ray beam to quantify the motion of materials by monitoring fluctuations of the scattered intensity (**Figure 58**). In XPCS microrheology, probe spheres are embedded in the material of interest and the mean square displacement of the spheres is measured as a function of time and momentum transfer. The motion of the probes is sensitive to the viscoelasticity of the surrounding medium and can be quantitatively analysed to provide the shear moduli as a function of frequency (**Figure 59**).

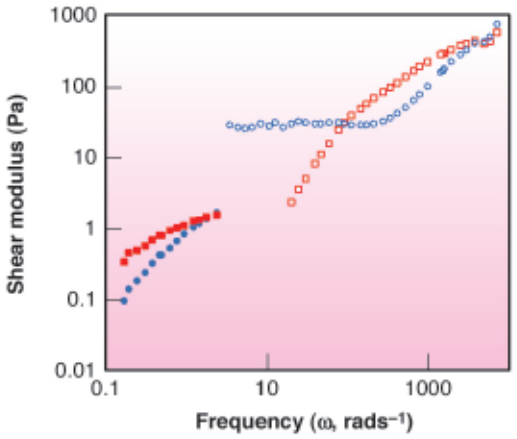

Fig. 59: The viscoelastic shear moduli for opaque comb polyelectrolyte (filled symbols) and gellan (open symbols) solutions calculated from XPCS microrheology experiments. The circles show the elastic shear moduli (G′) and squares the dissipative shear moduli (G″).

XPCS microrheology was performed at the TROIKA beamline ID10A to probe the viscoelasticity of biomimetic comb polyelectrolytes [2] and gellan (a bacterial polysaccharide). The X-rays are mainly scattered by the probe particles, *e.g.* colloidal silica, embedded in the samples. A wide range of materials can be examined by XPCS microrheology, since colloidal probes form stables phases in many polymeric and biological solutions. The XPCS measurements of the viscoelasticity of polystyrene sulphonate comb polyelectrolytes at low concentrations (**Figure 59**) were in good agreement with video particle tracking microrheology results on similar samples. The side-chains of the combs cause a dramatic effect on the viscoelasticity of the polyelectrolytes, inducing entangled dynamics immediately above the semi-dilute overlap concentration, and the viscosity is a strong function of the polymer concentration ($\eta \sim c^{1.5}$) [2]. Such comb materials are interesting because of possible applications in tissue engineering as a treatment for osteoarthritis. With gellan the elasticity of the network of double helical junctions is observed in the dominant contribution of the elastic shear modulus (G' > G") at lower frequencies (**Figure 59**). Gellan is used as a thickener in food materials such as yoghurts, drinks and sauces.

In conclusion, XPCS microrheology offers a new scattering technique to probe the dynamic properties of biological and soft-condensed matter materials. It has a large dynamic range, modest requirements on sample volume and does not suffer from constraints on sample opacity, which restrict analogous optical techniques (*e.g.* optical tweezers).

References

[1] T.A. Waigh, 'Microrheology of complex fluids', *Rep. Prog. Phys.* **68**, 685-742 (2005).
[2] A. Papagiannopoulos, C.M. Fernyhough, T.A. Waigh, Accepted for publication in *J. Chem. Phys.*.

Principal Publication and Authors

A. Papagiannopoulos (a), T.A. Waigh (a), A. Fluerasu (b), C.M. Fernyhough (c) and A. Madsen (b), *J. Phys.: Condens. Matter*, **17**, L279-285 (2005).
(a) Department of Physics and Astronomy, University of Leeds (U.K.)
(b) ESRF
(c) Department of Chemistry, University of Sheffield (U.K.)

X-ray Intensity Fluctuation Spectroscopy (XIFS) Studies of Ordering Kinetics in a Cu-Pd Alloy

A number of studies have used XIFS (also known as X-ray Photon Correlation Spectroscopy, XPCS) to examine fluctuation dynamics particularly in soft condensed matter, but few have attempted to use it to probe the kinetics of phase transitions. Here we report a XIFS study of the ordering kinetics in the classic long-period superlattice (LPS) alloy Cu-Pd using the **ID10A** "Troïka" beamline. In such LPS alloys there can be an equilibrium periodic modulation of the atomic order in one or two dimensions, giving a complex alloy structure. In order to better understand the complicated ordering process, this study examines the two-time pair-correlation function $C(q,t_1,t_2)$ during the ordering process on length scales of 10^1-10^3 nm and time scales of 10^2-10^4 sec. This corresponds to the regime of late-stage domain coarsening in the alloy. This two-time correlation function contains information beyond that available from the structure factor $S(q,t)$ obtained from traditional time-resolved X-ray scattering experiments. In contrast to the situation for equilibrium speckle measurements, the two-time correlation function is necessary due to temporal evolution of the nonequilibrium system.

To investigate the behaviour of $C(q,t_1,t_2)$, the evolution of both superlattice and satellite peaks, which are sensitive

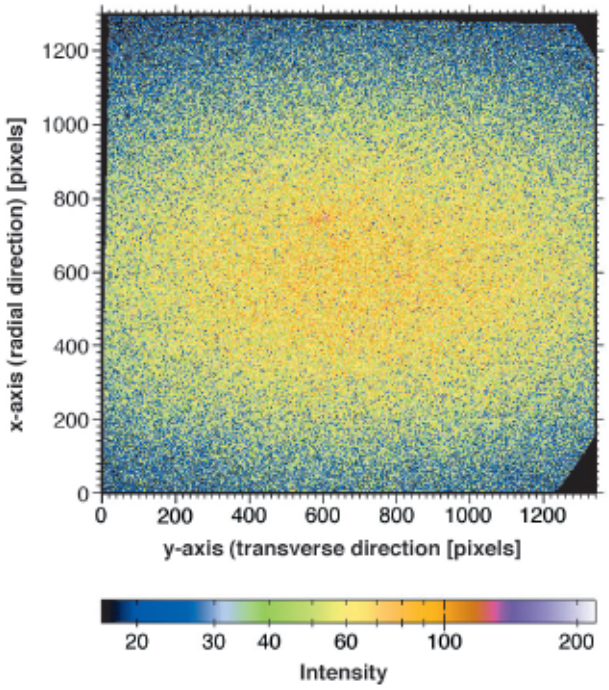

Fig. 60: Speckles in the superlattice peak after 35991 s of ordering. Dark regions around the image edge are due to masking of the scattered X-rays.

to local order and modulated order respectively, were examined. **Figure 60** shows a typical speckle pattern obtained from the (100) superlattice peak during the ordering process. Theory and simulations [1] suggest that, with increasing time, the speckles themselves become longer lived. Indeed comparison of the different experimental speckle patterns taken as the domain coarsening progressed shows that individual speckles develop with lifetimes comparable to the duration of the experiment. Interestingly, the peak centres move a small amount during the coarsening process, but examination of the speckle patterns shows that the speckles themselves do not follow this motion. This unexpected

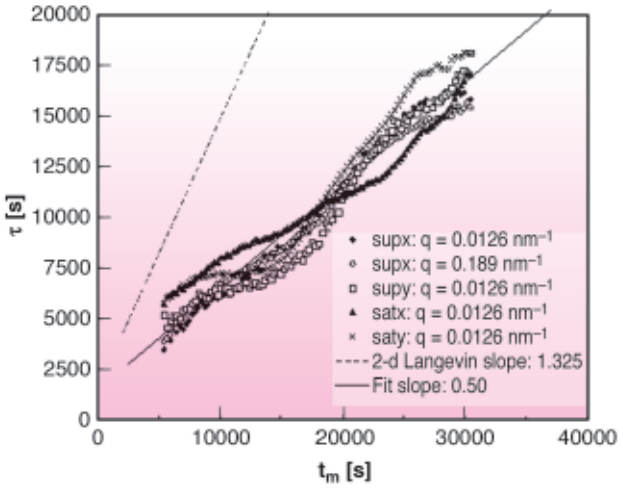

Fig. 61: Half-width decay time τ of the normalised two-time correlation functions $C_{norm}(q,t_m,\Delta t)$ for the superlattice and satellite peaks in x- and y- directions as a function of the mean transformation time t_m. Also shown are lines with the 2-d Langevin slope and data fit slope.

phenomenon may be due to the elimination of lattice distortions distributed inhomogeneously in the sample at domain boundaries[2] during the ordering process.

In the coarsening regime, the two-time pair-correlation function, $C(q,\Delta t,t_m)$ with $\Delta t = |t_2-t_1|$ and $t_m = (t_1+t_2) / 2$, should obey scaling laws [1]. In particular, they predict that close to the central part of the peak the characteristic decay time of the two-time correlation function is proportional to the mean coarsening time t_m. **Figure 61** shows the experimental results. As predicted by theory, the experimentally determined correlation decay time increases linearly with t_m.

One notable difference between predictions of theory/simulation and these experimental results, however, is the significantly slower rate of growth of the correlation decay time τ observed here. The τ/t_m slope is a dimensionless quantity. Langevin calculations and simulations give a τ/t_m slope of 1.325 in two dimensions. In three dimensions, the Langevin model would give a slightly higher ratio. In contrast, the observed slopes in both the superlattice and the satellite peaks are approximately 0.50. In the coarsening regime, the elapsed time is proportional to the square of average domain size and the correlation time measures the rate of structural rearrangements in the crystal. This slope therefore might be viewed as measuring how efficiently structural rearrangements lead to average domain growth with increasing coarsening. The low measured slope suggests that the growing average domain size leads to more structural rearrangement than is the case in the Langevin model. However, it is difficult to understand why this would be the case, and this remains an issue for future exploration.

References

[1] G. Brown, P.A. Rikvold, M. Sutton and M. Grant, *Phys. Rev. E* **56**, 6601 (1997).
[2] A. Fluerasu, M. Sutton and E.M. Dufresne, *Phys. Rev. Lett.* **94**, 055501 (2005).

Principal Publications and Authors

K. Ludwig (a,b), F. Livet (a), F. Bley (a), J.-P. Simon (a), R. Caudron (c,d), D. Le Bolloc'h (e), A. Moussaid (f), *Phys. Rev. B* **72**, 144201 (2005).
(a) LTPCM-ENSEEG-INPG, Saint Martin d'Hères (France)
(b) Permanent address: Boston University (USA)
(c) ONERA-LEM, Chatillon (France).
(d) Laboratoire Léon Brillouin, Saclay, Gif-sur-Yvette (France)
(e) Laboratoire de Physique des Solides, Orsay (France)
(f) ESRF

Structural Basis of the Regulation of Cell Adhesion in Brain Development and Disease

The neural cell adhesion molecule (NCAM) is one of the most abundant adhesion proteins in the central nervous system. It is critical in brain development, directing cell growth and forming adhesive contacts between neural cells. The polypeptide chain folds into seven linearly arranged 3.5-4 nm domains (**Figure 62a**). NCAM mediates intercellular adhesion by binding to identical proteins on adjacent cells (**Figure 62a**). One of the significant features of NCAM is that it occurs in both adhesive and anti-adhesive forms. The anti-adhesive form contains 1-2 linear polymers of sialic acid (PSA) attached to the fourth domain (**Figure 62b**). This modification dramatically affects both the architecture of neural tissues and biological function [1]. PSA-NCAM increases the spacing between cells in tissues, it increases neural plasticity, allowing cells to more easily break and form contacts, and the abnormal expression of PSA-NCAM in cancer increases tumour aggressiveness.

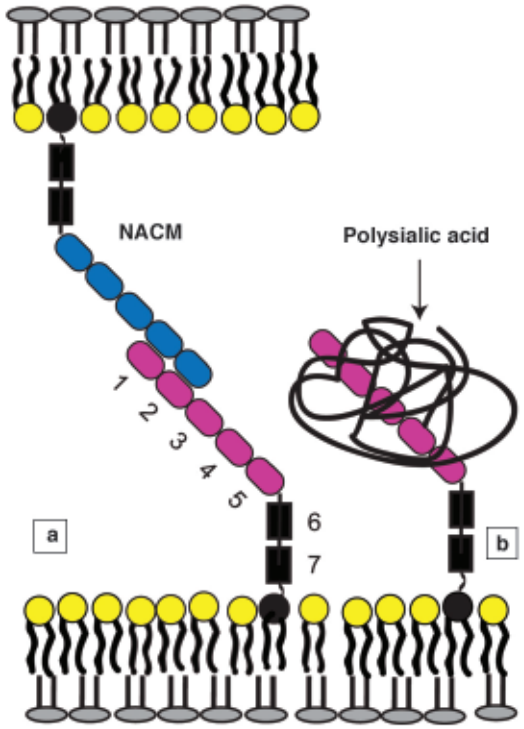

Fig. 62: (a) Overall structure of NCAM on the cell membrane. The seven-domain protein binds to an identical NCAM on the opposing membrane to form cell-cell junctions. (b) PSA-NCAM is modified with up to two linear polysialic acid chains, which are negatively charged.

One model for the molecular basis of PSA's biological activity postulates that PSA increases the steric repulsion between cells, and counteracts protein binders [1]. This requires that the excluded volume of PSA be

sufficient to prevent the approach of adhesion proteins on adjacent cells. X-ray reflectivity studies at the Troika beamline at ID10B quantified the effect of PSA on the hydrodynamic volume of NCAM, and tested the hypothesis that the excluded volume of the PSA acts as a steric modulator of NCAM's adhesive function.

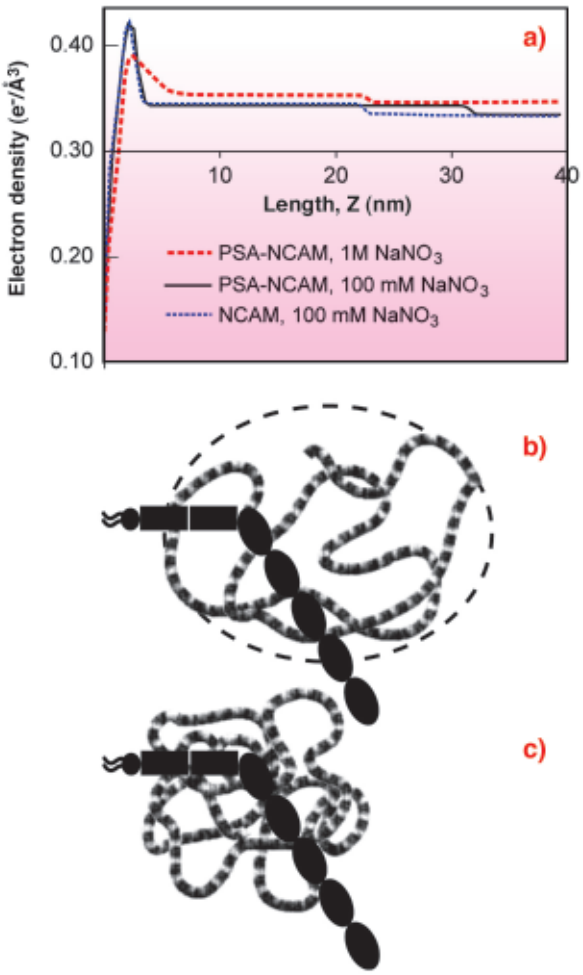

Fig. 63: (a) Electron density profiles of NCAM and PSA-NCAM monolayers bound to lipid monolayers. The peak at ~ 2.5 nm is due to the lipid monolayer. The NCAM box extends 20.6 ± 0.7 nm from the lipid monolayer (blue dash). The PSA-NCAM box extends 29.1±0.5 nm from the membrane in 100 mM $NaNO_3$ (black line), but the box thickness drops to 19.0 ± 0.7 nm in 1 M $NaNO_3$ (red dash). (b) Cartoon (model interpretation) of PSA-NCAM enveloped by swollen PSA in 100 mM salt. (c) Cartoon of PSA-NCAM with collapsed PSA at high salt.

The electron density profile of an oriented NCAM monolayer immobilised on a lipid monolayer at the liquid-vapour interface of a Langmuir trough (**Figure 63a**) revealed that the protein is bent or tilted at the membrane (**Figure 63b**). The end-to-end length of the NCAM extracellular region is 27 nm, but the protein box thickness was only 20.6 nm. Neutron reflectivity profiles of NCAM bound to a supported bilayer confirmed this.

The thickness of the PSA-NCAM monolayer was substantially greater at 29.1 nm (**Figure 63a**) [2]. The electron density extends beyond the protein core, and thus shows that the hydrodynamic volume of the polymer chain completely envelops the protein (**Figure 63b**). This accounts for the dramatic impact of the PSA attachment on both NCAM function and cell adhesion. The extension of the chains normal to the surface also suggests that PSA-NCAM could influence the function of other cell surface adhesion proteins. PSA is charged, so high ionic strength 1M NaCl screens the charges in the polymer backbone, causing the chains to collapse (**Figures 63a,c**) and the thickness of the protein box to decrease (**Figure 63a**). The latter finding reveals the structural basis for the salt-dependent increase in adhesion between cells that display PSA-NCAM on their surfaces. PSA collapse reduces the repulsion and the chain extension, enabling NCAM proteins to reform intercellular bonds.

In summary, these reflectivity studies provide unique insights into the structural basis for the modulation of NCAM adhesion by PSA, and the impact of PSA on cell adhesion and associated biological functions.

References

[1] L. Rutishauser, L. Landmesser, *Trends Neurosci.* **19**, 422, (1996).

Principal Publication and Authors

C.P. Johnson (a), G. Fragneto (b), O. Konovalov (c), V. Dubosclard (d), J.-F. Legrand (d) D. Leckband (a,e), *Biochemistry*, **44**, 546 (2005).
(a) Department of Chemistry, University of Illinois (USA)
(b) ILL
(c) ESRF
(d) CEA-CNRS-Universite J. Fourier, Grenoble (France)
(e) Department of Chemical and Biomolecular Engineering, University of Illinois (USA)

Nanocrystal-induced Organisation of a Langmuir Phospholipid Monolayer

A common attribute of quasi-two-dimensional systems like amphiphilic monolayers is liquid crystalline-like behaviour. At the air/water interface, in-plane ordering of such layers is generally limited to a subset of specifically designed molecules. For biomolecules such as phospholipids, the accessibility of an ordered phase depends on the shape and size of the hydrophilic headgroup and length of the hydrophobic alkane chains. Detailed here is the induction of molecular alignment in an inherently non-ordered phospholipid monolayer. This decrease of conformational entropy was achieved by the

adsorption of clay nanocrystals underneath the surfactant layer. The initiation of nucleation and growth in such a quasi-two-dimensional organic system leads our thoughts towards the influence of charged surfaces on elastic properties and phase behaviour of organisations such as cellular membranes. Recently molecular dynamics simulations have revealed that surface charge is an important determinant of the inflammatory potential of crystals causing rupture of cellular membranes [1]. As a model system, a combination of the Langmuir technique with X-ray surface diffraction was used to probe the interfacial issues of a lipid membrane in electrostatic interaction with negatively charged nanocrystals.

The phase behaviour of dimyristoylphosphatidylcholine (DMPC) monolayers was investigated using Langmuir pressure/area isotherms. On aqueous solutions of clay particles (hydrosols) an increase of the collapse pressure of the films was achieved. The slope of the isotherm and the area/molecule indicate a condensed state for surface pressures above 40 mN/m, which are not accessible in the absence of the nanocrystals. The general increase of molecular interactions can be attributed to a reduction of molecular motions within the film undoubtedly induced by the stiffening properties of the adsorbed nanocrystal layer. Grazing Incidence X-ray scattering Out of the Specular plane (GIXOS), a novel technique recently developed at **ID10B**, was used as a powerful method to investigate the organisation of thin films normal to the liquid surface on the molecular level. The information obtained is equivalent to electron density profiles determined via conventional reflectivity but the time needed for one spectrum is reduced from 1.5 hours to seconds or minutes. This opens up the possibility to investigate dynamic processes [2] or fragile systems, for which the new method was imperative due to the existence of a metastable hydrosol subphase. From the spectra (**Figure 64**), the tilt angles of the molecules with respect to the surface normal at 25 mN/m were found to be 50° and 42° in the absence and presence of the crystallites, respectively. For 50 mN/m on a sol the tilt angle was found to be reduced to 23°, another indication of an ordered condensed-like phase of the monolayer. No Bragg reflection from the membrane was observed from grazing-incidence diffraction (GID) experiments on a water subphase up to the collapse of the membrane at around 30 mN/m. Conversely, in the vicinity of the crystallites at 50 mN/m, a Bragg reflection was observed that appeared to be richly featured in the reciprocal space map (**Figure 65**). The contributions due to the alkane chain lattice of the phospholipid monolayer and due to the internal atomic structure of the nanocrystals were resolved by Bragg rod analysis. The Bragg reflections originating from the biomembrane reflect the induction of an ordered phase by electrostatic binding to the nanocrystals.

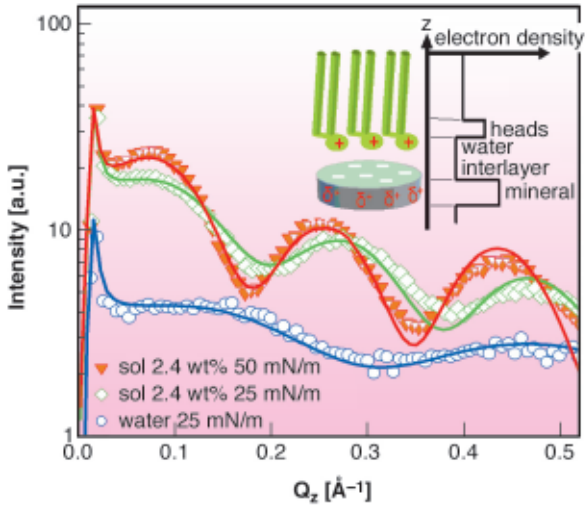

Fig. 64: GIXOS spectra of the membrane with and without minerals. Inset: sketch of the system and model for the electron density profile in the presence of mineral particles.

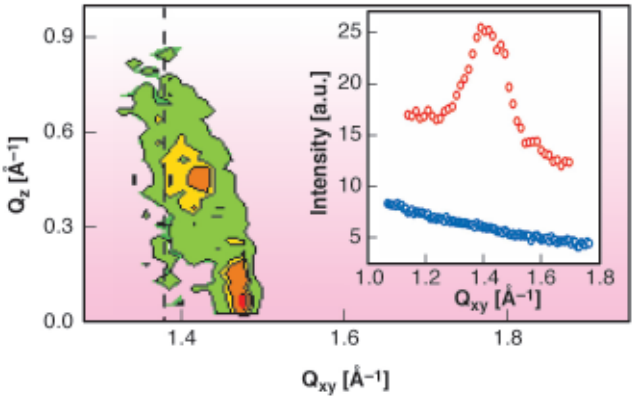

Fig. 65: Reciprocal space map of the Bragg reflection of the ordered membrane at 50 mN/m. The mineral distribution (along the dashed line) could be separated by Bragg rod analysis. Inset: in-plane Bragg peaks at a surface pressure of 50 mN/m in the vicinity of minerals (red symbols) and at 30 mN/m on pure water (blue symbols).

In conclusion we have overcome the issue of weak interaction between individual molecules of an inherently nonordered phospholipid monolayer and induced a phase shift towards an ordered phase. This effect is caused by the stiffening properties of the crystals and the anchoring of individual molecules to the charged surfaces of the nanocrystal templates.

References

[1] A. Wierzbicki, P. Dalal, J. D. Madura, H. S. Cheung, *J. Phys. Chem. B*, **107**, 12346-12351 (2003).

[2] L. Wiegart, S. M. O'Flaherty, P. Terech, B. Struth, *Soft Matter*, **2**, 54-56 (2006).

Principal Publication and Authors

L. Wiegart (a,b), S.M. O'Flaherty (a), B. Struth (a), Langmuir, 21, 1695-1698 (2005).

(a) ESRF

(b) CEA-CNRS-Université J. Fourier

X-ray Diffraction Reveals a New Mechanism of Muscle Contraction

Muscle force results from the interaction of the globular heads of myosin molecules with actin filaments. The structure-function relationship in the myosin motor was studied with low-angle time-resolved X-ray diffraction in contracting muscle fibres where force generation was triggered by temperature jump or length step. Both types of perturbations induce simultaneous changes in the muscle force and in the extent of labelling of the actin helix by stereo-specifically bound [1] myosin heads at a constant total number of attached heads [2]. The generally accepted hypothesis [3] assumes that muscle force is generated solely by tilting of the light chain domain of the myosin head about its catalytic domain, or by the lever arm mechanism. Data obtained suggest an additional force-generating step: the 'roll and lock' transition of catalytic domains of non-stereo-specifically attached heads to a stereo-specifically bound state. A suggested model quantitatively explains the data.

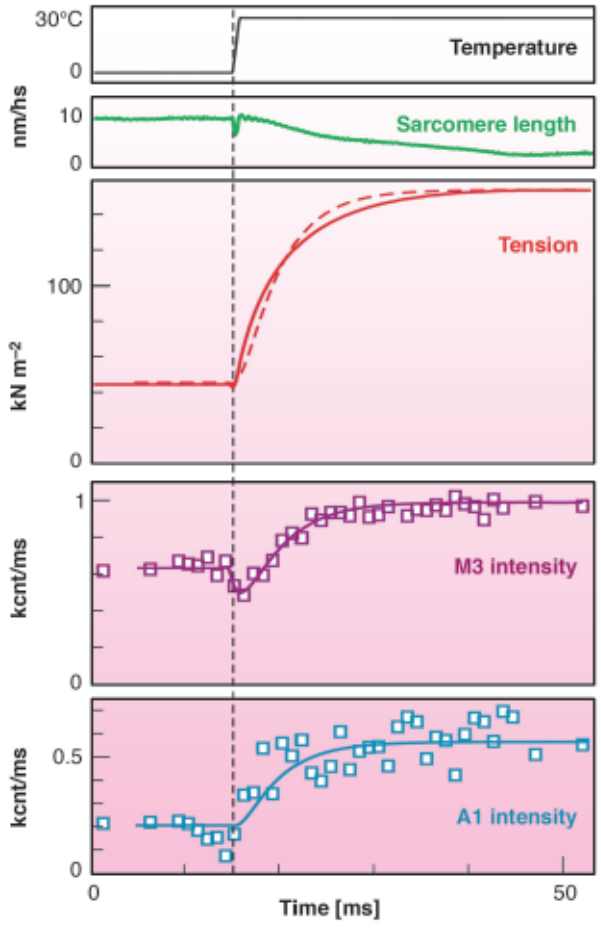

Fig. 66: Time course of mechanical and structural responses to the temperature jumps. Top to bottom: averaged temperature, sarcomere length, averaged tension, I_{M3}, and I_{A1}. The smooth lines on I_{M3} and I_{A1} data and the dashed line on the tension trace are the results of modelling. The vertical line marks the time when the 1ms–long T-jump was half-complete.

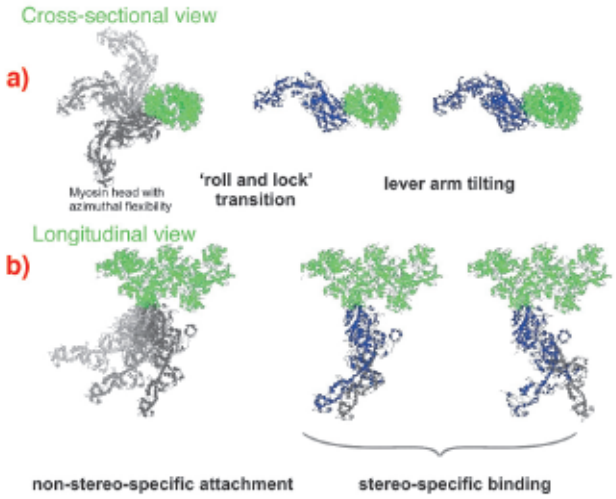

Fig. 67: Suggested scheme of the mechanism of force generation by myosin heads. Attached states of a myosin head (blue or grey) bound to actin (green) are shown in two projections with the actin axis: (a) azimuthal and (b) axial. Force or displacement is produced during both the 'roll-and-lock' transition and the lever-arm tilting.

The temperature jump from 5°C to 30°C in permeabilised fibres from rabbit muscle induced a three-fold increase in active tension. Time course of changes in tension and in the 2D X-ray diffraction pattern collected at ESRF ID02 with the RAPID detector (Daresbury Laboratory, UK) from muscle fibres with 1 ms time resolution is shown in **Figure 66**. It was found that the intensities of all recorded layer lines originating from the actin helix increase with temperature in parallel with tension. When myosin heads bind actin stereo-specifically they adopt the symmetry of the actin helix so that the axial spacing of the layer lines remains the same but the intensities are higher as they are determined by the number of heads incorporated in the actin helix.

The apparent rate constants of the rise in tension and in I_{A1} (intensity of the first actin layer line) were about 200 s^{-1}. The intensity of the third myosin reflection, IM3, dropped during the temperature jump and then increased with an apparent rate constant similar to that for tension. Temperature independence of fibre stiffness [2] indicates that the number of myosin heads attached to actin does not change with temperature and that the increase in tension with temperature is caused by an increase in force produced by each head. The significant increase in I_{A1} after the temperature jumps must be caused by a stereo-specific 'locking' of myosin heads on actin. The contribution of non-stereo-specifically bound heads to the layer line intensities is low because the distribution of their electron density in space does not follow helical symmetry.

A kinetic and structural model (**Figure 67**) was suggested. The structure-function relations obtained from time-

resolved mechanical and structural data as well as the known kinetic data were integrated to link together the lever arm mechanism [3] with the idea of a preceding stereo-specific 'locking' of the myosin molecule on the actin filament. The 'roll and lock' mechanism suggested here and the kinetic and structural model based on this mechanism quantitatively explain both the mechanical and the structural behaviour of myosin heads in temperature jump experiments and specifies structural and kinetic characteristics of the two-step force generation by muscle myosin. An increase in I_{A1} after muscle shortening predicted by the 'roll and lock' model was verified experimentally. The two-step force generation mechanism suggested here is consistent with the electron microscope tomography on insect flight muscles [4] where myosin heads in configurations similar to those assumed for attached states of our model were observed.

References

[1] S. Bershitsky, A. Tsaturyan, O. Bershitskaya, G. Mashanov, P. Brown, R. Burns and M. Ferenczi, *Nature* **388**, 186 (1997).
[2] S. Bershitsky and A. Tsaturyan, *J. Physiol.* **540**, 971 (2002).
[3] K. Holmes, *Curr. Biol.* **7**, R112 (1997).
[4] K. Taylor, H. Schmitz, M. Reedy, Y. Goldman, C. Franzini-Armstrong, H. Sasaki, R. Tregear, C. Lucaveche, R. Edwards, L. Chen, H. Winkler and M. Reedy, *Cell* **99**, 421 (1999).

Principal Publication and Authors

M. Ferenczi (a), S. Bershitsky (b), N. Koubassova (c), V. Siththanandan (a), W. Helsby (d), P. Panine (e), M. Roessle (e), T. Narayanan (e) and A. Tsaturyan (c), *Structure* **13**, 131 (2005).
(a) Imperial College London (UK)
(b) Institute of Immunology and Physiology, Yekaterinburg (Russia)
(c) Institute of Mechanics, Moscow University, Moscow (Russia)
(d) Daresbury Laboratory, Cheshire (UK)
(e) ESRF

Magnetic-Field-Induced Nematic to Columnar Phase Transition

Rod-like nanometric objects such as molecules, polymers, aggregates and particles, either in pure form or dispersed in a solvent, can form liquid-crystalline phases of various symmetries [1]. The transitions between these phases generally occur because of a change of temperature or concentration. Recently, at the ESRF, we discovered a case where the transition between two liquid-crystalline phases can actually be induced by applying a magnetic field. We were investigating the magnetic-field influence on suspensions of goethite (α-FeOOH) lath-shaped nanorods of average dimensions 150 x 25 x 10 nm^3. In zero-field, these aqueous colloidal suspensions display three different phases, depending on volume fraction. Dilute suspensions form the usual isotropic liquid phase; upon increasing concentration, a transition is reached, leading to a nematic phase that shows long-range orientational order but only short-range (liquid-like) positional order. A further concentration increase leads to a transition to a columnar liquid-crystalline phase that has 2-dimensional long-range positional order. All these phase transitions are first-order (*i.e.* with phase coexistence).

The small-angle X-ray scattering (SAXS) pattern of a single domain of the nematic phase displays two diffuse spots that arise from interferences between the nanorods in planes perpendicular to their common alignment direction, called the nematic director (**Figure 68a**). The position of these diffuse spots is related to the average distance (~ 50 nm) between particles in planes perpendicular to the director while the width of the spots (along a radius) is related to the distance over which the short-range positional order extends [2]. Interestingly, when the magnetic-field intensity was raised beyond about 1 Tesla, the SAXS pattern displayed sharp reflections that point to the onset of long-range

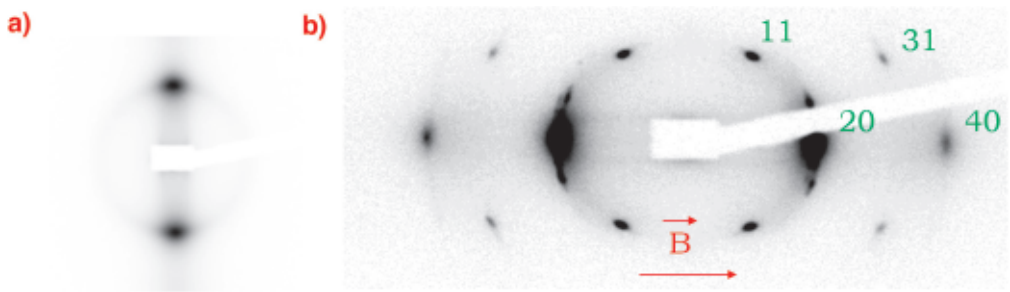

Fig. 68: a) Small-angle X-ray scattering pattern of a single domain of the nematic phase showing two diffuse spots. The goethite nanorods are aligned in the horizontal direction, perpendicular to the X-ray beam. b) Small-angle X-ray scattering pattern of the same sample submitted to a strong magnetic field (B = 1.5 T), in the columnar phase (The (20) reflections are overexposed). The nanorods are aligned parallel to the X-ray beam.

positional order (**Figure 68b**). Goethite nanorods then assemble on a 2-dimensional lattice perpendicular to the director, which is typical of the columnar phase. Moreover, instead of a "powder" (*i.e.* random) distribution of small crystallites, a large single domain grew and gave rise to the pattern in **Figure 68b**. This large domain has grown in the so-called homeotropic orientation, *i.e.* with the nanorods main axis parallel to the beam and perpendicular to the surfaces of the flat glass capillary that held the sample. The production of a single domain allowed us to determine the 2-dimensional space group (c2mm) of the columnar phase and to understand its organisation (**Figure 69**). Due to their magnetic anisotropy, the nanorods orient their main axis perpendicular to the magnetic field and their thickness parallel to it. This orientation was confirmed by optical measurements. The 2-dimensional unit-cell parameters naturally depend on volume fraction, with typical values of a ~ 100 nm and b ~ 70 nm. There are two nanoparticles per unit cell. Since the particles cross-section is not circular, the columnar phase has rectangular rather than hexagonal symmetry. As expected for a liquid-crystalline phase, no periodic order could be detected in the direction perpendicular to the 2-dimensional lattice. The phase transition is actually first-order since SAXS patterns showing both the nematic diffuse spots and the columnar sharp reflections could be observed.

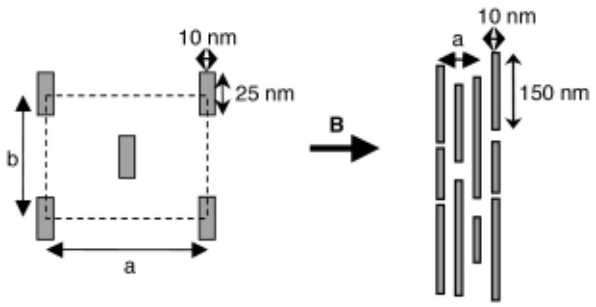

Fig. 69: Schematic representation of the organisation of the nanorods in the columnar phase, left: in the plane perpendicular to the rods main axis, right: in a plane parallel to the rods main axis.

This magnetic-field-induced phase transition is fully reversible (possibly with some field hysteresis) as the sharp reflections disappear and the diffuse spots reappear when the magnetic field is suppressed. Moreover, these experiments could be reproduced many times both with the same and with different goethite samples. The critical field required to achieve the nematic to columnar transition is a decreasing function of the volume fraction. In other words, in a volume fraction - field intensity phase diagram, the transition line is clearly tilted towards lower volume fractions, which is very unusual for liquid crystals. This result means that, quite unexpectedly, the magnetic field affects not only the orientational degrees of freedom but also the translational ones. To this date, we have no complete explanation for this unusual transition and understanding its mechanism in detail remains a tantalising but challenging theoretical question.

References

[1] P.G. De Gennes, "The Physics of Liquid Crystals", Clarendon press, Oxford (1979).
[2] B.J. Lemaire *et al.*, *Eur. Phys. J. E*, **13**, 309 (2004).

Principal Publication and Authors

B.J. Lemaire (a), P. Davidson (a), P. Panine (b), J.P. Jolivet (c), *Phys. Rev. Lett.*, **93**, 267801 (2004).
(a) UMR 8502 CNRS, Orsay (France)
(b) ESRF
(c) UMR 7574 CNRS, Paris (France)

Kinetics and Mechanisms of Electric Field Induced Alignment of Block Copolymer Solutions

The microphase separation of block copolymers has been studied extensively over the past two decades both experimentally and theoretically. In the ordered state, these materials exhibit highly regular mesoscopic microdomain structures with characteristic length scales of the order of several tens of nanometres. Similar to polycrystalline materials, typically small grains of microdomains are formed, the size of which may be of the order of micrometres. As a consequence, although a single grain may have a highly anisotropic structure (*e.g.* cylinders or lamellae), a bulk sample of a block copolymer typically exhibits isotropic materials properties. If macroscopic anisotropies are desirable, additional efforts have to be made to create macroscopic alignment of the microdomain structures. In the past, external mechanical fields have been successfully applied to orient block copolymer melts.

In addition to mechanical fields, the potential of electric fields for microdomain alignment has attracted increasing interest in the recent past as it may also be of considerable technical interest. It has been shown that - due to the differences in the dielectric constants ($\Delta\varepsilon$) of the blocks - both lamellar and cylindrical block copolymer microstructures orient parallel to the electric field vector when subjected to a DC electric field. Cylindrical microdomains can in principle be aligned along the field vector resulting in a single monodomain (*i.e.* a block copolymer "single crystal"). In a lamellar microdomain structure, on the other hand, all lamellar orientations containing the electric field vector within the lamellar planes are energetically equivalent.

Melt-based electric field procedures suffer from severe limitations due to the high melt viscosities typical for high molecular weight copolymers or copolymers of more complex architectures and the chemical instability at high temperatures. In order to overcome these limitations, we used concentrated block copolymer solutions, where a non-selective solvent is employed to induce sufficient mobility and investigated the kinetics and mechanisms of the microdomain orientation under a DC electric field by time-resolved synchrotron small-angle X-ray scattering (SAXS). As a model system, we use a lamellar polystyrene-*b*-polyisoprene block copolymer (PS-*b*-PI) dissolved in toluene [1,2].

In order to quantify the orientation kinetics, the orientational order parameter P_2 was calculated for each single scattering pattern acquired during the course of the experiment. The behaviour of P_2 as a function of time t could be fitted by a single exponential as described by:

$$P_2(t) = P_{2,\infty} + (P_{2,0} - P_{2,\infty})\, e^{-t/\tau} \qquad (1)$$

with $P_{2,0}$ and $P_{2,\infty}$ being the limiting values of the order parameter before application of the electric field and at late times, respectively, and τ being the time constant (**Figure 70**).

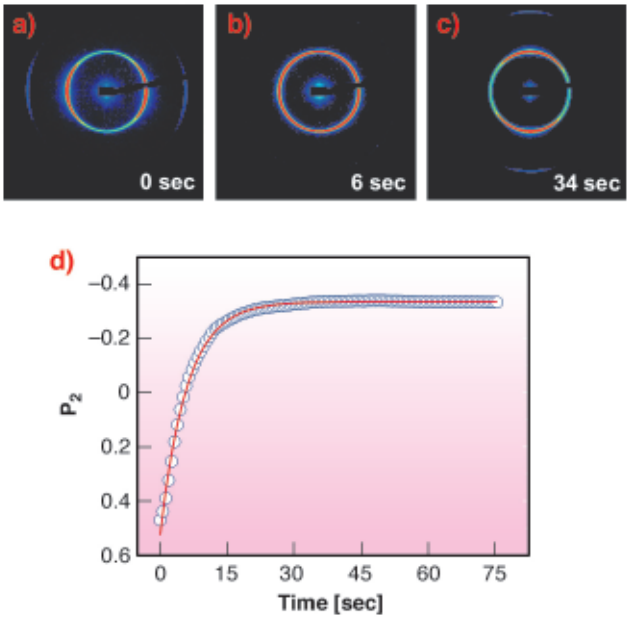

Fig. 70: (a-c) SAXS patterns of a 35 wt.-% solution of the lamellar PS-b-PI diblock copolymer in toluene taken at room temperature prior (a) and after (b, c) application of an electric field (E = 1 kV/mm). (d) Time dependence of the orientational order parameter P_2. The solid line is a least-squares fit to the data according to Equation 1 with $P_{2,0} = 0.52$, $P_{2,\infty} = -0.32$, and $\tau = 5$ sec.

In addition, from the azimuthal angular dependence of the scattering intensity, we could identify two different microscopic mechanisms:

Close to the order-disorder transition (weakly phase separated system), *i.e.* at low concentrations and high temperatures, microdomains aligned parallel to the electric field grow at the expense of those aligned parallel to the electrodes. Intermediate orientations, however, are not observed (**Figures 70a-c** and **Figure 71a**), but the the isotropoic background scattering increases.

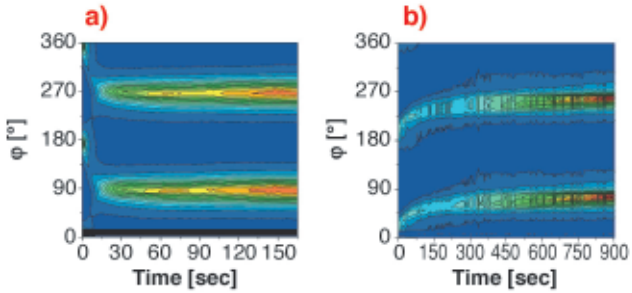

Fig. 71: Azimuthal angular dependence of the scattering intensity for different concentrations at 1 kV/mm. (a) 35 wt.-%, (b) 50 wt.-%.

Further away from the order-disorder transition (stronger phase separated system), *i.e.* for high concentrations and low temperatures, the scattering pattern seems to be preserved and merely shifts into the new orientation. This observation points to the rotation of entire grains as an alternative orientation process (**Figure 71b**). In contrast to the migration of grain boundaries, microdomain orientations intermediate between the original and the final orientations are observed. No increase in isotropic scattering is observed during the transition.

References

[1] A. Böker, A. Knoll, H. Elbs, V. Abetz, A.H.E. Müller, G. Krausch, *Macromolecules*, **35**, 1319-1325 (2002).

[2] A. Böker, H. Elbs, H. Hänsel, A. Knoll, S. Ludwigs, H. Zettl, A.V. Zvelindovsky, G.J.A. Sevink, V. Urban, V. Abetz, A.H.E. Müller, G. Krausch, *Macromolecules*, **36**, 8078-8087 (2003).

Principal Publication and Authors

A. Böker (a), K. Schmidt (a), G. Krausch (a), V. Urban (b), T.M. Weiss (b), *Phys. Rev. Lett.*, **89**, 135502 (2002).

(a) Physikalische Chemie II, Universität Bayreuth, Bayreuth (Germany)

(b) ESRF, ID02

Hard X-ray Nanoprobe Based on Refractive X-ray Lenses

Hard X-ray scanning microscopy allows one to perform X-ray analytical techniques, such as X-ray fluorescence analysis, absorption spectroscopy, or diffraction, with high spatial resolution. In this way, element distributions, the chemical state of an element, or the local (crystalline) structure of a heterogeneous specimen can be determined. In combination with tomographic techniques,

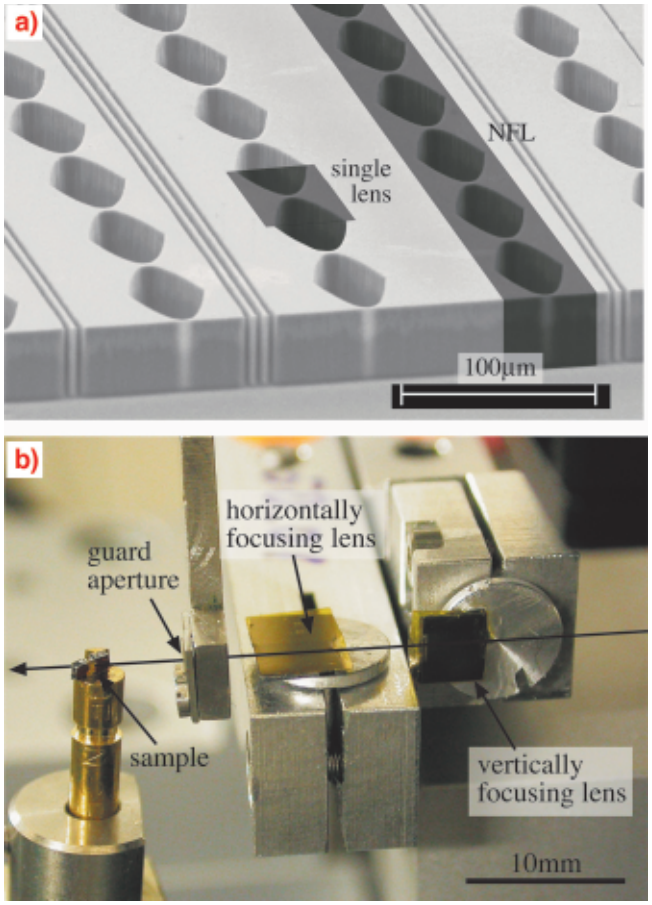

Fig. 72: (a) Scanning electron micrograph of nanofocusing lenses. A single lens and a nanofocusing lens are outlined by dark shaded areas. (b) Nanoprobe setup: the X-ray beam is focused onto the sample by two crossed nanofocusing lenses.

local information from the inside of a sample can be obtained without destructive sample preparation. This is beneficial to many fields of science, such as chemistry, materials, earth, environmental, and biomedical science. These hard X-ray scanning microscopy techniques greatly benefit from the recent advances in X-ray optics generating ever smaller and more intense nanobeams. Today, a variety of X-ray optics is capable of generating beams with a lateral beam size in the range of 100 nm and below. Among these are nanofocusing lenses (NFLs) [1,2], on the basis of which we are currently developing a hard X-ray nanoprobe station at beamline ID13. This hard X-ray scanning microscope can be operated in transmission, fluorescence, and diffraction mode. Tomographic scanning modes will allow one to obtain elemental and structural information from inside a specimen.

At the heart of the microscope are nanofocusing refractive X-ray lenses that image the synchrotron radiation source onto the sample position in a strongly reducing geometry. Their key strength is their short focal length that lies in the centimetre range. In this way, they can generate a sub-100 nm beam even at short source to experiment distances and do not require particularly long beamlines. In addition, the diffraction limit of these optics typically lies well below 50 nm. In their current design (cf. **Figure 72a**), these planar lenses generate a line focus. The latest generation of these optics is made of Si using lithographic processes optimised for 4''-wafers. In this way, the fabrication parameters are well controlled, reducing shape errors to a minimum. Several lenses are placed side by side on the same wafer. **Figure 72a** shows a scanning electron micrograph of part of such a set of lenses. Each of these lenses has a slightly different focal length for a given X-ray energy. In the microscope, the X-ray nanobeam is generated by two crossed nanofocusing lenses that are aligned along a common optical axis as shown in **Figure 72b**. The common aperture of the lens system is defined by a guard aperture.

During the first commissioning phase of the scanning microscope at beamline ID13 the nanobeam was characterised. It was set up at 47 m from the in-vacuum undulator source. Using a pair of nanofocusing lenses with a focal length of f_h = 10.7 mm and f_v = 19.4 mm for horizontal and vertical focusing, respectively, a hard X-ray beam (E = 21 keV) with a lateral extension of 47 x 55 nm^2 was generated (**Figure 73**). The flux in this beam is 1.7 x 10^8 ph/s at a ring current of 200 mA, resulting in a gain in flux density of more than 2 x 10^4. In the future, this beam will be used for fluorescence tomography and nanodiffraction.

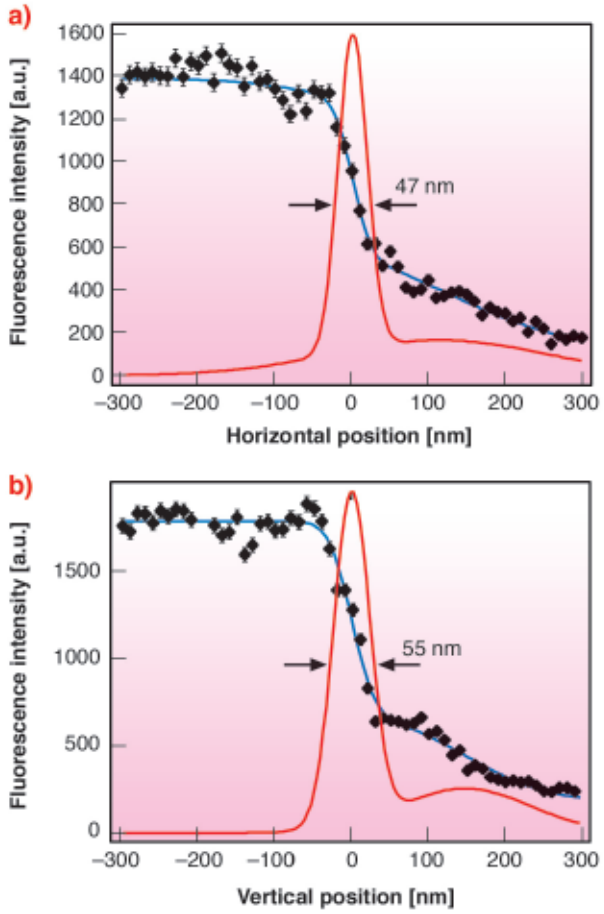

Fig. 73: (a) Horizontal and (b) vertical beam profile determined by fluorescence knife-edge scans. (Reprinted with permission from [1].)

The main advantage of this setup is that extremely small foci can be generated even at short beamlines. Using the available fabrication technology for a new lens scheme (adiabatically focusing lenses [3]), beams as small as 20 nm are conceivable in the current geometry. In addition, using other lens materials, such as boron or diamond, the flux and focus size can also be significantly improved. Besides scanning microscopy other techniques may profit from a small focus, such as diffraction with coherent X-rays and X-ray photon and fluorescence correlation spectroscopy.

References

[2] C.G. Schroer, M. Kuhlmann, U.T. Hunger, T.F. Günzler, O. Kurapova, S. Feste, F. Frehse, B. Lengeler, M. Drakopoulos, A. Somogyi, A.S. Simionovici, A. Snigirev, I. Snigireva, C. Schug, W.H. Schröder, *Appl. Phys. Lett.* **82**, 1485 (2003).
[3] C. G. Schroer and B. Lengeler, *Phys. Rev. Lett.* **94**, 054802 (2005).

Principal Publication and Authors

[1] C.G. Schroer (a), O. Kurapova (b), J. Patommel (b), P. Boye (b), J. Feldkamp (b), B. Lengeler (b), M. Burghammer (c), C. Riekel (c), L. Vincze (d), A. van der Hart (e), M. Küchler (f), *Appl. Phys. Lett.* **87**(12), 124103 (2005).
(a) HASYLAB at DESY, Hamburg (Germany)
(b) II. Physikalisches Institut, Aachen University (Germany)
(c) ESRF
(d) Department of Analytical Chemistry, Ghent University (Belgium)
(e) ISG, Forschungszentrum Jülich (Germany)
(f) Fraunhofer IZM, Dept. Microdevices and Equipment (Germany)

Microradian X-ray Diffraction in Colloidal Photonic Crystals and Liquid Crystals

Self-assembly of colloidal particles into various crystalline and liquid-crystalline structures have been widely studied as a model of crystallisation of atomic and molecular systems as well as a route to photonic materials. The application of X-ray diffraction (XRD) to colloidal crystals is challenging due to many orders of magnitude difference between the size of a colloid and an X-ray wavelength. Angular resolutions of the order of a microradian are required to measure the intrinsic width of the diffraction peaks. Recent experiments performed at beamlines **ID10A** TROÏKA and **BM26** DUBBLE met the challenge.

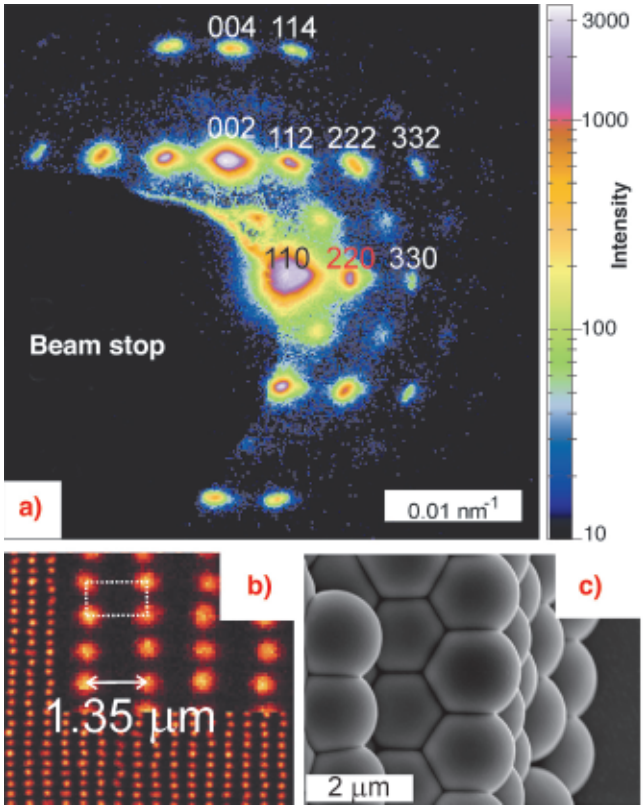

Fig. 74: (a) Diffraction pattern from a colloidal bct crystal, measured at the ID10A branch of the TROÏKA beamline. The angular resolution is 5 µrad. (b) Projection of four hexagonal crystal layers obtained with 3D confocal microscopy from the original colloidal bct crystal (allows for quantitative comparison with XRD). (c) SEM image of the same crystal after drying and silicon infiltration (3D microscopy is no longer possible).

In particular, it is demonstrated that an angular resolution better than 2 µrad can be achieved with compound refractive X-ray optics. For instance, microradian diffraction can now be used to study crystals with spacings *d* larger than a micrometre. Such crystals can be used as templates to fabricate photonic materials for near-infrared telecommunication applications, which can manipulate light in a way similar to semiconductors manipulating electrons [1]. **Figure 74** displays a diffraction pattern from a crystal of silica spheres (diameter 1.4 µm) with a body-centred tetragonal (bct) structure. The smallest diffraction angle of $2\theta_{110}$ = 69 µrad corresponds to d_{110} = 1.35 µm. Despite the tiny diffraction angles, the pattern is clearly resolved and the width of the diffraction peaks can now be determined. Another advantage of these large-spacing crystals is that they can be studied not only by XRD, but also – after index matching with a suitable liquid – with 3D confocal microscopy, which is complementary to XRD. In addition, XRD can be applied to crystals that are strongly scattering or absorbing in the visible. This makes microradian XRD a unique tool to quantify stacking disorder, density of scattering centres, and the spatial extent of the positional order at different steps of the fabrication process. These results can now be used to improve the quality of the resulting photonic materials.

Moreover, correct identification of thermodynamic phases in colloidal suspensions crucially depends on the resolution [2]. **Figure 75** presents results obtained in a concentrated suspension of colloidal gibbsite platelets (diameter 237 ± 49 nm, thickness 18 ± 3 nm), which form a columnar phase. The top part of the columnar phase consists of many small domains while a macroscopically large single-domain is observed in the bottom part, which looks well ordered at first sight. This is surprising since the particles have a very high diameter polydispersity. The nature of this surprising order is now seen clearly with the improved resolution. A radial peak broadening, which increases with the diffraction order, was detected. This indicates that the positional intercolumnar correlations are gradually lost. Such a fluid-like short-range positional order is typical for hexatic ordering [2], which is a compromise between the polydispersity-induced local frustrations and the long-range order. The significant difference in the spatial extent of the positional order, as well as a jump in the compressibility suggests that the single-domain is in fact a new liquid-crystalline phase: the hexatic columnar phase.

To summarise, small-angle X-ray diffraction from photonic colloidal crystals and liquid crystals has been performed with microradian angular resolution. This permits detailed characterisation of the structure and long-range order in strongly scattering photonic crystals with spacings larger than a micrometer [1]. We have also solved a long-standing problem of crystallisation in suspensions of highly polydisperse colloidal platelet-like particles [2].

References

[1] J.H.J. Thijssen, A.V. Petukhov, D.C. 't Hart, A. Imhof, C.H.M. van der Werf, R.E.I. Schropp, A. van Blaaderen, to be published.

[2] A.V. Petukhov, D. van der Beek, R.P.A. Dullens, I.P. Dolbnya, G.J. Vroege, H.N.W. Lekkerkerker, *Phys. Rev. Lett.*, **95**, 077801 (2005).

Principal Publications and Authors

A.V. Petukhov (a), J.H.J. Thijssen (b), D.C. 't Hart (b), A. Imhof (b), A. van Blaaderen (b), I.P. Dolbnya (c), A. Snigirev (d), A. Moussaïd (d), I. Snigireva (d), *J. Appl. Cryst.*, in press (2006).

(a) van 't Hoff laboratory, Utrecht University (The Netherlands)

(b) Soft Condensed Matter, Utrecht University (The Netherlands)

(c) BM-26 DUBBLE, ESRF; present address: Diamond Light Source (U.K.)

(d) ESRF

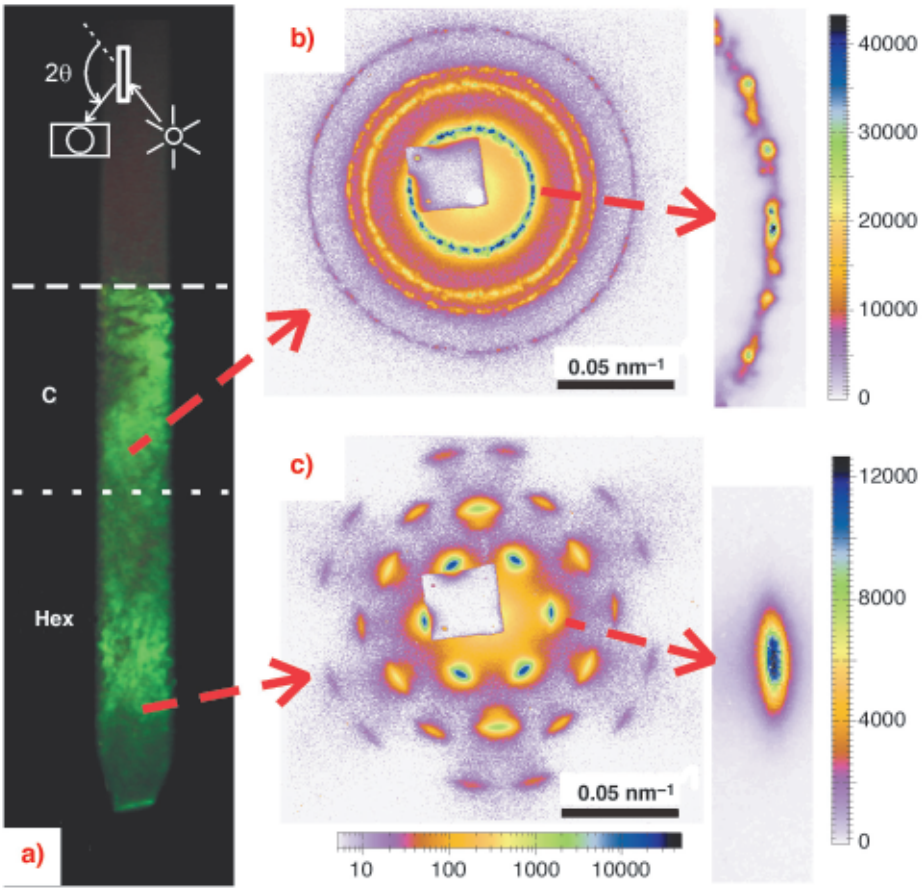

Fig. 75: (a) Photo of the sample in a Bragg-reflection geometry sketched in the inset. "C" and "Hex" denote hexagonal and hexatic columnar phases. Full XRD patterns and close ups of the (10) reflections in the multidomain hexagonal columnar (b) and the single domain hexatic columnar (c) regions, which are measured at BM26 DUBBLE. The angular resolution is 14 µrad.

ESRF

Highlights 2005

Structural Biology

Introduction

The year 2005 has been an extremely busy and productive year for the Macromolecular Crystallography (MX) Group. During the year we have seen the installation and commissioning of the ESRF-EMBL sample changers on all seven end-stations that fall within the remit of the group. The sample changers will fundamentally alter the way in which the beamlines are utilised, and will facilitate the investigation of increasingly complex systems via the screening of a large number of samples. The latest addition to the MX suite of beamlines became available for users during the autumn. This beamline (ID23-2) is a microfocus beamline 100% dedicated to MX. The beamline builds on in-house experience with Kirkpatrick-Baez focussing optics to provide a focal spot size of 9 µm (ultimately to be 5 µm), and is equipped with both a mini-diffractometer and a sample changer. A hectic year of beamline activity was completed by the installation of ADSC Q315r detectors on the beamlines ID23-1, ID29 and ID14-4. Together with the increasingly reliable and sophisticated automated beamline alignment tools, these beamline developments are outlined in more detail by X. Thibault on page 71. The very busy year on the beamlines was complemented, in October, by the completion of the MX Group's wet lab in the new PSB building. In January 2006 this building was inaugurated in honour of our late Director of Research Carl-Ivar Bränden, and the PSB building is now named in his honour.

The research programme in MX at the ESRF embraces that performed by the external MX community on both the public and CRG beamlines and that carried out by the ESRF in-house team. This latter includes structural biology and methods development as well as the technical developments already discussed.

As the highlights presented in this chapter demonstrate, the trend towards the study of complex systems shows no sign of abating. The mechanisms of DNA repair in bacterial systems is characterised by the action of the complex of proteins known as recBCD. The crystal structure analysis of recBCD in complex with DNA has allowed Singleton *et al.* (page 60) to propose a mechanism for the process of homologous recombination in bacteria. The outlier in terms of complexity among these articles is the work of Nelson *et al.* (page 61), where the ability to investigate microcrystals of the amyloid cross-β spine has allowed the investigators to propose a mechanism for the formation of amyloid fibrils associated with neurodegenerative diseases. The circadian rhythm is a fundamental biological mechanism that controls the functioning of our "body clock". The operation of this system is the subject of the work of Yidiz *et al.* (page 63), where they are able to propose the mechanism of interaction of two of the key components in the circadian cycle of the fruit fly *Drosophila*. Nature has evolved a number of molecular motors to accomplish motility. The myosin superfamily groups those motors that progress along an actin filament by conversion of chemical energy into movement. Within this family the action of myosin VI is anomalous due to the inversed directionality the system produces. Ménétry *et al.* (page 64) propose an explanation for this apparent anomaly thanks to the high-resolution crystal structure they have obtained using ESRF MX facilities.

The strength of the science carried out on the CRG beamlines is reflected in the contribution of two of the highlights presented in this chapter. Pizarro *et al.* (page 65) reveal the structure of Apical

Membrane Antigen 1 (AMA1), a candidate for a malaria vaccine that is currently undergoing clinical trials. In the second, an example of combined ESRF/CRG research, Dong *et al.* (page 68) report the native structure of a tryptophan 7-halogenase (PrnA) and the structures of PrnA in complex with substrate (tryptophan) and product (7-chloro-tryptophan). Together these structures allow the authors to propose a mechanism for the fantastic regioselectivity of these enzymes. Our examples of research from the public programme concludes with an example of the work that has for many years tested the limits of MX at synchrotron facilities: Wilson *et al.* (page 66) have determined the X-ray structure of the ribosome binding domain of RRF (RRF-DI) bound to the large ribosomal subunit of the eubacterium *Deinococcus radiodurans* and are able to propose a mechanism for ribosomal recycling.

In-house research continues to develop the understanding of the physical and chemical processes underlying the interaction of X-rays with matter and two highlights are presented here. In the first, Nanao *et al.* (page 70) turn the "problem" of radiation damage to macromolecular crystals into an opportunity for increased phasing power. It is expected that this method can be extended to become a routine tool for the enhancement of phasing information used in the *de novo* solution of crystal structures. Finally, Timmins *et al.* (page 68) present the crystal structure and mechanism of maltooligosyltrehalose trehalohydrolase (MTHase) from *Deinococcus radiodurans*. A presumed forerunner of the extreme radiation tolerance of this organism to ionising radiation is its tolerance to desiccation. Trehalose appears to be the most effective stabiliser of dried proteins and membranes with the available evidence suggesting that trehalose protects membranes and proteins by serving as a water substitute. In their report, the authors resolve key questions concerning how this enzyme produces the trehalose that is critical to the extremophile nature of *Deinococcus radiodurans*.

G. Leonard and S. McSweeney

RecBCD: A Molecular Machine for DNA Repair

The genetic integrity of all organisms is under constant threat from a variety of internal and external sources, such as radiation, chemical carcinogens and reactive cellular species. Often, these agents damage DNA directly. As a consequence, cells have evolved elaborate mechanisms to continuously scan for and repair such damage.

One of the major DNA repair pathways is that of homologous recombination (HR). In principle, this pathway allows an error-free restoration of the original genetic information. The repair process involves the copying of an undamaged strand of identical (homologous) DNA and splicing the resultant copy into the damaged strand. Taken as a whole, the process is quite complex, but a key step is the initial processing of the damaged DNA to generate free 3' single-stranded tails [1]. In the bacterium *E. coli*, the RecBCD multi-protein complex, mediated by an octameric DNA sequence known as Chi (χ), catalyses this process.

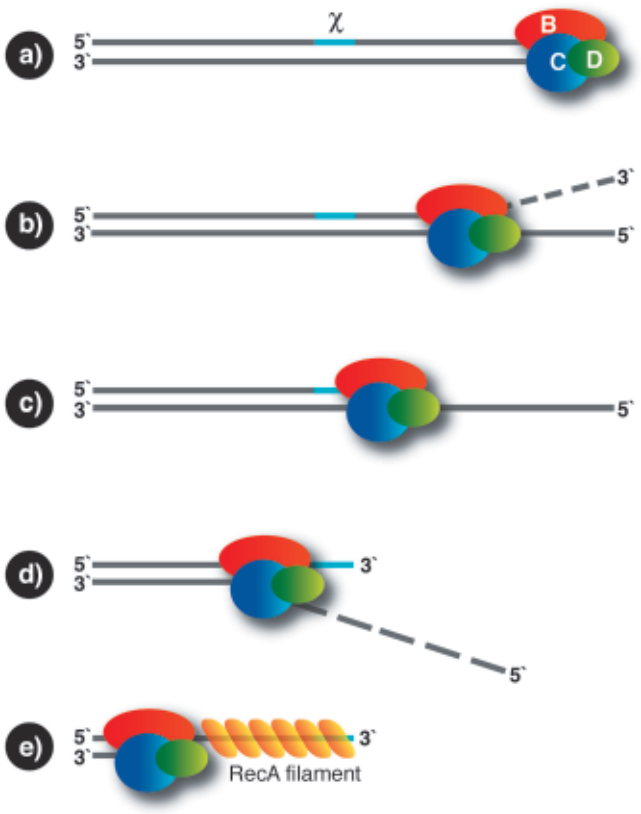

Fig. 76: Schematic diagram of the reaction catalysed by RecBCD. The enzyme binds to a free duplex end (a) and starts to unwind the DNA and digest the 3′ strand (b). Upon encountering the Chi site (c), the nuclease activity is switched and the enzyme continues; now digesting the 5′ strand (d). RecBCD is also capable of loading RecA onto the exposed 3′ strand to provide the substrate for the next step of homologous recombination (e).

The RecBCD enzyme binds at the broken DNA end and rapidly unwinds the duplex in an ATP-dependent manner. As unwinding proceeds, the 3' terminated strand is continuously degraded by an endonuclease activity. This unwinding and digestion continues until the Chi sequence is encountered, at which point the enzyme pauses, and the nuclease switches to the other DNA strand. The enzyme then continues unwinding the duplex, digesting the 5' terminated strand and loading the RecA strand-exchange protein onto the 3' strand, now capped by the Chi sequence (**Figure 76**) in preparation for the next stage of HR.

Considerable amounts of biochemical and genetic data have been obtained on the RecBCD system. Recent results have shown that the enzyme has a bipolar helicase activity, with one motor translocating along each strand, each running with opposite polarity [2]. It has been shown that the 3'-5' and 5'-3' helicase activities reside with the RecB and RecD subunits respectively, the nuclease is associated with the C-terminal domain of RecB and Chi recognition occurs in RecC.

We have recently determined the crystal structure of RecBCD bound to a blunt-ended DNA hairpin using data collected on ESRF beamlines **ID14-1** and **ID14-4**. The structure was solved in the absence of ATP and so represents an initiation complex prior to translocation (**Figure 77**). Despite this, the DNA substrate has been partially unwound, with four base-pairs of the duplex split.

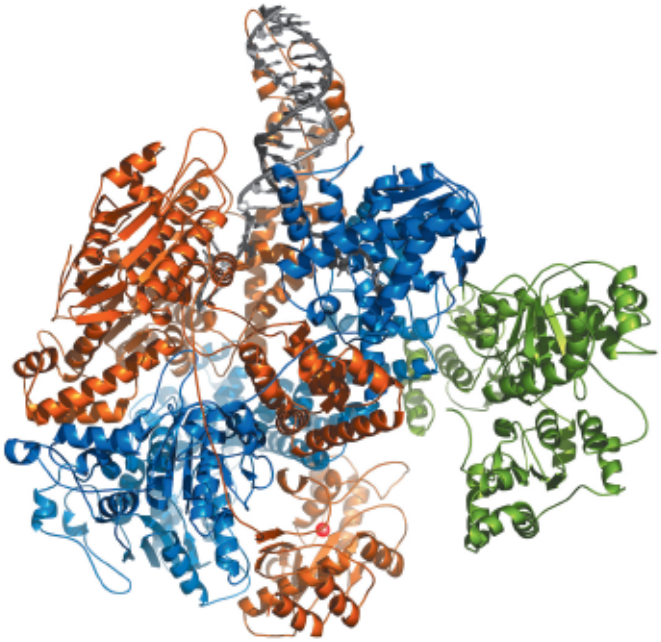

Fig. 77: Ribbon diagram of the RecBCD complex. RecB is shown in orange, RecC blue, and RecD green. The two strands of DNA (grey) are split at the top of the protein and enter tunnels directing the 3′ tail to the RecC Chi-recognition site and nuclease, and the 5′ tail to RecD. The active site of the nuclease is highlighted by a bound calcium ion, depicted as a red sphere.

As expected from sequence analyses, both RecB and RecD have folds characteristic of superfamily I DNA helicases, with the C-terminal nuclease domain of RecB attached by a long flexible linker. In the crystal structure a calcium ion replaces the native magnesium ion in the nuclease active site. The RecC protein forms a plate-like scaffold around which the RecB is tightly wrapped, while RecD maintains a looser association. RecC has three channels running through it; a large central cavity responsible for binding RecB, and two smaller channels for each of the DNA tails. These channels guide the 3' and 5' tails towards the nuclease and RecD respectively. Intriguingly, the 3' channel is partially formed from the N-terminal domain of RecC, which also has a characteristic helicase fold, a fact not apparent from the sequence. This observation suggests that RecC is in fact a defunct helicase, which has evolved the ability to recognise the Chi sequence. In the current crystal structure, the nuclease is ideally positioned to accept the 3' tail of the DNA following its passage through RecC. Presumably the Chi sequence induces some conformational switch, which alters the nuclease strand specificity as well as activating the RecA loading process.

These structural studies have shown how two helicases can combine to form a highly efficient molecular machine and provide a basis for an elaborate regulated nuclease system. Unravelling the details of this control mechanism should prove to be a rewarding exercise.

References

[1] S. C. Kowalczykowski, *Trends Biochem. Sci.*, **25**, 156-165 (2000).
[2] M.S. Dillingham, M. Spies, S.C. Kowalczykowski, *Nature* **423**, 893-897 (2003).

Principal Publication and Authors

M.R. Singleton (a), M.S. Dillingham (b), M. Gaudier (a), S. C. Kowalczykowski (c), D.B. Wigley (a), *Nature* **432**, 187-193 (2004).
(a) Cancer Research UK, London Research Institute (UK)
(b) University of Bristol, Department of Biochemistry (UK)
(c) University of California at Davis, Center for Genetics and Development (USA)

The Structure from Microcrystals of the Cross-β Spine of Amyloid Fibrils

Decades of research by medical and biological scientists have established that neurodegenerative amyloid diseases, such as Alzheimer's, are each associated with a particular protein that converts into fibrillar form. Although these various proteins differ in sequence and

three-dimensional structure, their fibrils share common properties: they are ~ 80-150 Å in diameter, highly elongated and unbranched; they bind flat dyes such as Congo Red and display a characteristic birefringence, showing that they harbour an apolar, periodically arrayed environment; they give a characteristic "cross-β" diffraction pattern, reflecting extended protein (beta) strands, perpendicular to the fibril axis, spaced about 4.8 Å apart. These similarities point to a common structure for the spine of all amyloid fibrils, including the "amyloid-like" fibrils formed from globular proteins by removing them from their native conditions. This common structure resisted detailed elucidation in the past because of the difficulty of extracting atomic-level detail from fibrillar samples, either by NMR or X-ray diffraction.

Our road to the atomic structure of the cross-β spine had to surmount two major barriers. The first was crystals. We selected the yeast protein Sup35 for X-ray crystallography because extensive studies in other laboratories have shown that its formation of amyloid-like fibrils is the basis of protein-based inheritance and prion-like infectivity. The fibril-forming tendency of Sup35 had been traced to the amino terminus of the protein and from this region we isolated a seven-residue, fibril-forming segment with sequence GNNQQNY [1].

This peptide dissolves in water, and at a concentration of approximately 400 μM, forms amyloid-like fibrils in a few hours. These fibrils display all of the common characteristics of amyloid fibrils. When dissolved at higher concentrations (about 10–100 mM), GNNQQNY forms elongated microcrystals, no larger than ~ 40 μm in length and ~ 1 μm in diameter. Although extremely small, these crystals were well ordered, and were the first truly crystalline form of amyloid-like substances ever discovered.

The second barrier to structure elucidation was how to collect single crystal X-ray diffraction data from such small crystals. Progress came when Dr. Carl-Ivar Branden, the former Scientific Director of ESRF put the UCLA amyloid group in touch with the ESRF team who had developed the microfocus beamline **ID13**. The diffraction data collected yielded structures for GNNQQNY and for its shorter version NNQQNY [2].

The atomic structure of GNNQQNY revealed some features that were expected, and also some surprises (**Figure 78**). As expected, each GNNQQNY molecule is an extended beta chain, and each is hydrogen bonded to identical molecules above and below it forming standard parallel β-sheets. Each sheet is related to a mating sheet by a two-fold axis, and a translation along the fibril axis by one half the inter-strand separation. Surprising to us is that the two sheets are unusually close, with their side-chains intermeshed, forming what we term a 'steric

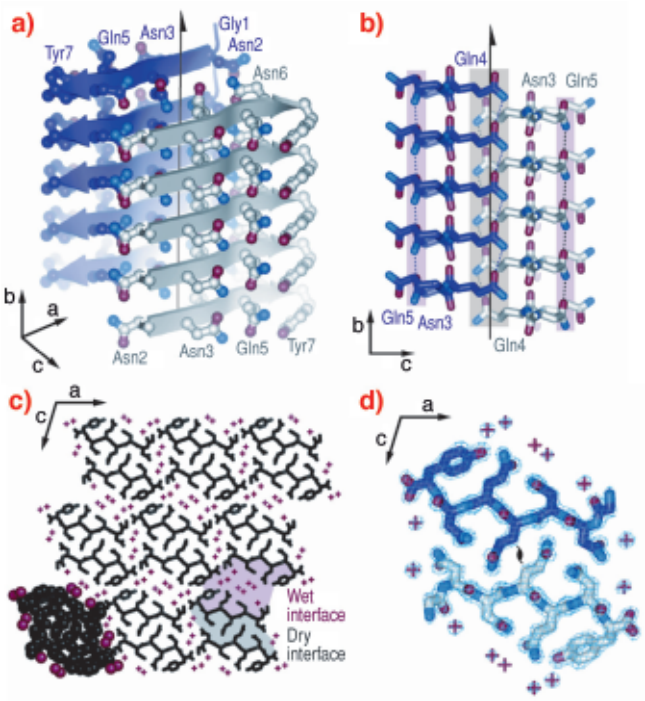

Fig. 78: Structure of GNNQQNY. Unless otherwise noted, carbon atoms are coloured in purple or grey/white, oxygen in red, and nitrogen in blue. (a) The pair-of-sheets structure showing the backbone of each β-strand as an arrow, with ball and stick sidechains protruding. (b) The steric zipper viewed down the **a** axis. The amide stacks of the dry interface are shaded in grey at the centre, and those of the wet interface are shaded in pale red on either side. (c) The GNNQQNY crystal viewed from the top of panel a, along the **b** axis. Nine pairs of β-sheets run horizontally. Peptide molecules are shown in black and water molecules are represented by red +. (d) The steric zipper: close-up view of a pair of GNNQQNY β-sheets from the same view as panel c, showing the remarkable shape complementarity of the Asn and Gln sidechains protruding into the dry interface. 2Fo-Fc electron density is shown, and the position of the central screw axis is indicated.

zipper'. This tight interface between the two sheets is utterly dry, with no water molecules and there are no hydrogen bonds from one sheet to its mate. It is this dry, closely-fitting steric zipper that holds the two sheets together. This same feature is found in microcrystals of other amyloid-forming peptides from proteins associated with human diseases that we have subsequently examined.

The biological implications of the structure of GNNQQNY are: (1) A short peptide of a few (4-7 residues), rather than an entire protein is sufficient to form amyloid-like fibrils. That is, the spine of amyloid fibril has a simpler structure than previously believed; (2) The amyloid state of protein is an unusually dry state; (3) The bond between the two sheets is extended, but formed by weak van der Waals forces. These suggest routes towards developing therapies for terrible diseases such as Alzheimer's and related amyloidoses.

References

[1] M. Balbirnie, R. Grothe, D. Eisenberg, *Proc. Nat. Acad. Sci. USA*, **95**, 22375-2380 (2001).

[2] R. Nelson, M.R. Sawaya, M. Balbirnie, A. Ø. Madsen, C. Riekel, D. Eisenberg, *Nature*, **435**, 77-778 (2005).

Authors

D. Eisenberg (a), C. Riekel (c), R. Nelson (a), M.R. Sawaya (a), M. Balbirnie (a), A.Ø. Madsen (b,c).

(a) Howard Hughes Medical Institute, UCLA-DOE Institute for Genomics and Proteomics, Los Angeles (USA)

(b) Centre for Crystallographic Studies, Department of Chemistry, University of Copenhagen (Denmark)

(c) ESRF

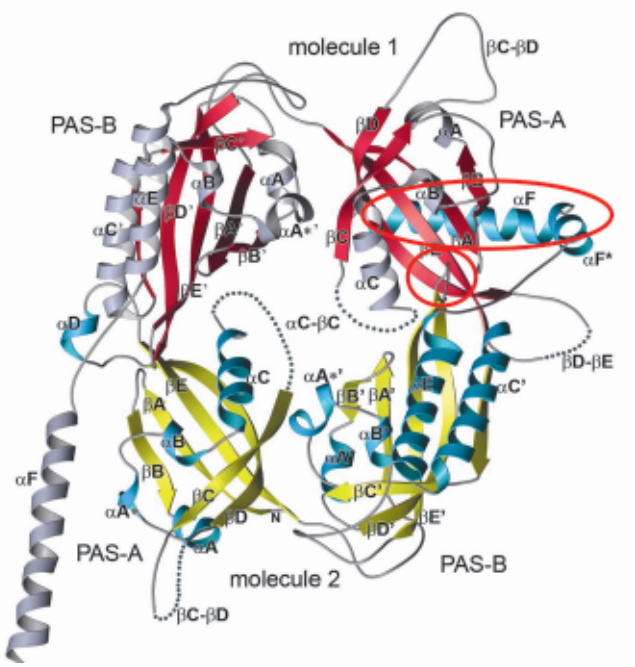

Fig. 79: Crystal structure of the *Drosophila* Period (dPER) dimer. Molecule1 is shown in red and grey, molecule2 in yellow and blue. PAS-A and PAS-B denote the two PAS domains in each monomer. The PAS-A dimer interfaces are highlighted by red circles.

Crystal Structure of Drosophila Period Protein: Insight into Circadian Clock Regulation

Most organisms exhibit 24-hour activity cycles called *circadian rhythms* (from the latin *circa diem* = about a day). Circadian rhythms are generated by circadian clocks, which are operated by interconnected transcriptional-translational feedback loops [1]. Period (PER) proteins are central components of the *Drosophila* and mammalian circadian clocks. Their function is controlled by daily changes in synthesis and degradation, cellular localisation, phosphorylation as well as specific interactions with other clock components. In order to shed some light on these molecular mechanisms, we have solved the crystal structure of a *Drosophila* Period (dPER) fragment comprising two tandemly-organised PAS (PER-ARNT-SIM) domains (PAS-A and PAS-B) and two additional C-terminal α-helices (αE and αF). To this end, we have collected 3.5 Å SeMet-MAD data for experimental phasing at beamline **ID29** and a 3.15 Å native data set for final refinement at beamline **ID14-2.**

PAS domains represent a diverse and ubiquitous family of sensory-, signalling- and protein-protein interaction modules, which consist of a five-stranded antiparallel ß-sheet (ßA-ßE) covered on one face by several α-helices (αA-αC). The crystal structure of the dPER PAS repeat region reveals a non-crystallographic dimer stabilised by two sets of intermolecular PAS domain interactions (**Figure 79**). The dimer interfaces are mediated by interactions of PAS-A with a conserved tryptophan residue, Trp482, in the ßD'-ßE'-loop of PAS-B (PAS-A-Trp interface, **Figure 79** and **Figure 80a**) and with the helix αF located at the C-terminal to PAS-B (PAS-A-αF interface, **Figures 79, 80b**), respectively. Interestingly, a point mutation which leads to extended (29 hour) days in living flies (*per*^{L} mutation) is located in the centre of the PAS-A-αF interface. The *per*^{L} mutation, which corresponds to an exchange of Val243 to Asp

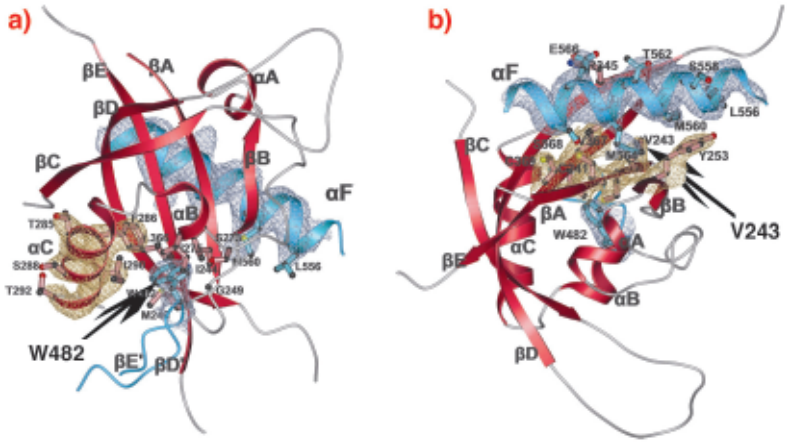

Fig. 80: PAS-A dimer interfaces of dPER. The PAS-A domain of molecule 1 is shown in red. Helix αF and the PAS-B-ßD'-ßE' loop with Trp482 of molecule 2 are shown in blue. The two PAS-A orientations provide closeup views of (a) the PAS-A-Trp482 dimer interface and (b) the PAS-A-αF dimer interface. W482 and the *per*^{L} mutation site V243 are labelled at the respective interfaces.

(V243D), dissociates the dPER dimer in gel filtration analysis, presumably by introducing a negative charge into this hydrophobic interface (**Figure 80b**). Thus we propose that the PAS-A-αF interaction plays a critical role in circadian clocks and that the 29h phenotype of *per*^{L} mutant flies is caused by a destabilisation of this interface.

Site-directed mutagenesis studies, guided by our structure, have allowed us to document the functional significance of both dPER dimer interfaces. The strong conservation of Trp482 in mammalian PER (mPER) homologues suggests, that the PAS-A-Trp interface is also present in the mPER dimers observed in the mammalian circadian clock. Additionally, our structure has led us to propose a model for dPER interaction with Timeless, the second central component of the *Drosophila* clock. Future structural analysis and structure-based biochemical experiments should improve our understanding of the molecular mechanisms underlying circadian clock regulation.

Reference

[1] N. Cermakian and P. Sassone-Corsi, *Nature Reviews*, **1,** 59-67 (2000).

Principle Publication and Authors

Ö. Yildiz (a), M. Doi (b), I. Yujnovsky (b), L. Cardone (b), A. Berndt (a), S. Hennig (a), S. Schulze (a), C. Urbanke (c), P. Sassone-Corsi (b) and E. Wolf (a), *Mol. Cell* **17**, 69-82 (2005).

(a) Max-Planck-Institute for Molecular Physiology, Department of Structural Biology, Dortmund (Germany)

(b) Institute de Génétique et de Biologie Moléculaire et Cellulaire, Strasbourg (France)

(c) Medizinische Hochschule Hannover, Biophysikalisch-Biochemische Verfahren, Hannover (Germany)

The Myosin VI Structure Reveals the Mechanism of its Reverse Directionality

Nature has evolved a number of molecular motors which accomplish motility by producing directed force along cytoskeleton filaments. The myosin superfamily regroups the motors that progress along an actin filament by conversion of chemical energy (provided by ATP hydrolysis) into mechanical energy, while transporting cargos and vesicles throughout the cell. The current view of how myosins couple ATP hydrolysis and actin binding to movement is known as the "swinging lever arm hypothesis". Briefly, the motor/ATP hydrolysis cycle is coupled to small movements within the motor domain, that are amplified and transmitted *via* the "converter" subdomain to an elongated region, called the lever arm. The lever arm (which consists of a target helix and associated light chains) further amplifies the motions of the converter into large directed movements.

Myosin VI, like myosin V, has been described as a dimeric processive motor, taking multiple steps along the actin filament before detaching. However, myosin VI, in constrast to all other characterised myosins, moves toward the minus (-) end of the actin filament [1]. Perhaps because of its reverse directionality, myosin VI has another unusual feature: it takes similarly sized steps to those of myosin V, despite having a much shorter lever arm. This property cannot be explained in the context of the "swinging lever arm" theory since its step size is not proportional to its lever arm length. In addition, myosin VI contains a specific, unique, insert of 39 residues located between the motor domain and the lever arm. Together, this evidence suggests that myosin VI produces force using a mechanism different from that of other myosins.

Electron microscopy maps of the myosin VI motor bound to actin gave the first indication that the unique 39 residue insert was involved in the myosin VI reverse directionality. These maps reveal that an ADP-mediated conformational change in the distal part of the motor occurred in the opposite direction to that observed for other myosins and that the lever arm was directed toward the (-) end of the actin filament in both states [1]. However, molecular engineering studies using myosin V/VI chimera, in which the insert was added or removed, concluded that the motor domain, and not the unique insert, determined the direction of myosin motility. Quite unexpectedly, we have later shown that this unique insert corresponds to a novel target sequence for calmodulin with calcium bound.

We have determined the structure of myosin VI in a nucleotide-free state at 2.4 Å resolution data collected on **ID14**, **ID23** and **ID29** (**Figure 81**). This structure reveals

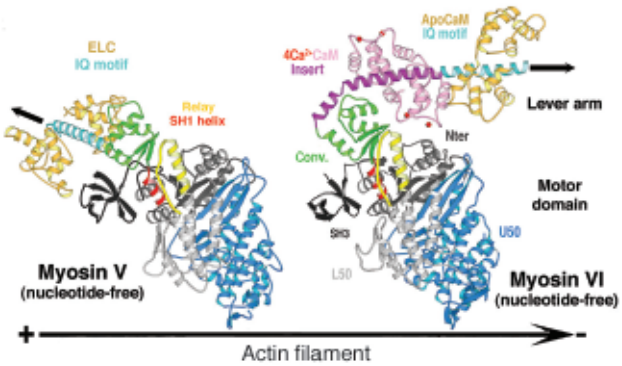

Fig. 81: The structure of nucleotide-free myosin VI compared to that of myosin V (left). Note the difference in the position of the lever arm (IQ motif, cyan) due to the unique insert (purple) and its associated-calmodulin molecule. The convertor domain is highlighted in olive.

only minor differences in the structure of the motor domain when compared to myosin V [2]. However the lever arm of myosin VI is directed in the opposite direction towards the (-) end of the actin filament and the unique amino acid insert is a helix that plays a crucial role in this reversal of direction. The proximal end of this helix wraps around the converter rather than emerging as a straight helix while the distal part of the insert forms a previously unseen calmodulin-binding motif.

Both the insert and its associated calmodulin make specific interactions with the converter domain. The net result of these interactions is that the lever arm is rotated about 120° from the position of the lever arm found for (+) end motors. This structure, which represents that at the end of the powerstroke, largely accounts for myosin VI reverse directionality. In redirecting the lever arm, the insert creates a bias for the binding of the second head towards the (-) end of actin filament. Modeling of the myosin VI conformation at the beginning of the stroke using the motor domain of myosin II in its pre-powerstroke state reveals that the stroke produced would be much smaller than that experimentally measured. In contrast, similar modeling for myosin V fully accounts for its 7 nm stroke (**Figure 82**).

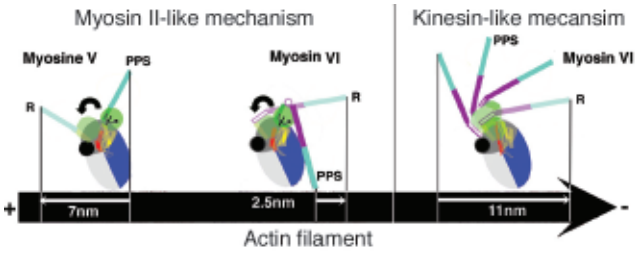

Fig. 82: Reversal of directionality mechanisms in myosins. Light chains are omitted for clarity. (R) Rigor state: a nucleotide-free high affinity state for actin filament following force production. (PPS) Pre-powerstroke state: an ADP.Pi state of weak affinity for actin filament that preceeds force production.

Myosin VI thus produces force using a different mechanism to myosin V and we propose that a kinesin-like uncoupling/docking mechanism could fully explain the movements of myosin VI. In this hypothesis, a specific region (the SH1 helix) unfolds to uncouple the lever arm from the motor domain prior to force generation. Its refolding upon force production would impose a stroke that could be as large as 11 nm (**Figure 82**). However, to further understand how myosin VI works, the structure of this motor in other conformations is needed.

References

[1] A.L. Wells, *et al*. *Nature.* **401**, 505-508 (1999).
[2] P-D. Coureux, *et al*. *Nature* **425**, 419-423 (2003).

Principal Publication and Authors

J. Ménétrey (a), A. Bahloul (a), A.L. Wells (b), C.M. Yengo (b), C.A. Morris (b), H.L. Sweeney (b), A. Houdusse (a).
Nature, **435**, 779-85 (2005).
(a) Structural Motility, Institut Curie CNRS, UMR144, Paris (France)
(b) Department of Physiology, University of Pennsylvania School of Medicine (USA)

The Structure of a Leading Malaria Vaccine Candidate: Apical Membrane Antigen 1

Malaria is a global health problem that severely hampers economic and social development in many third-world countries. It results in more than 2 million deaths each year and, along with HIV/AIDS and tuberculosis, is one of the three “diseases of poverty”. Malaria is caused by the unicellular parasite *Plasmodium*, with the two species, *P. falciparum* and *P. vivax*, being responsible for most cases of the disease in humans [1]. With the growing problem of parasite resistance to anti-malarial drugs, the search for an effective vaccine has received much attention in recent years. A number of surface proteins from *Plasmodium* show promise as vaccines and Apical Membrane Antigen 1 (AMA1) is one such candidate currently undergoing clinical trials. The precise biological function of AMA1 is not known but it is essential for invasion of the host liver and red blood cells by the parasite. Antibodies induced by AMA1 prevent invasion and provide the principal mechanism of protection against the disease when used in immunisations [2].

AMA1 is a type I membrane protein comprising an N-terminal ectoplasmic region of about 450 amino acids, a single transmembrane segment and a small C-terminal cytoplasmic domain. The crystal structure of the recombinant soluble ectoplasmic region from the species *P. vivax* has been solved by MAD using a platinum derivative (data measured on **BM14** and **ID14-4**) and refined at 1.8 Å resolution. The three-dimensional structure of this region of AMA1 is divided into three domains (**Figure 83**). Although no structural similarity to known protein folds was anticipated from the amino acid sequence of the antigen, both domains I and II were found to have a fold belonging to the PAN (Plasminogen-Apple-Nematode) motif. These two domains show negligible sequence identity between each other, but their structurally equivalent regions (a total of 83 residues) nonetheless superimpose with an r.m.s. difference of 2.7 Å between the Cα positions. Domain III does not belong to any previously identified protein fold.

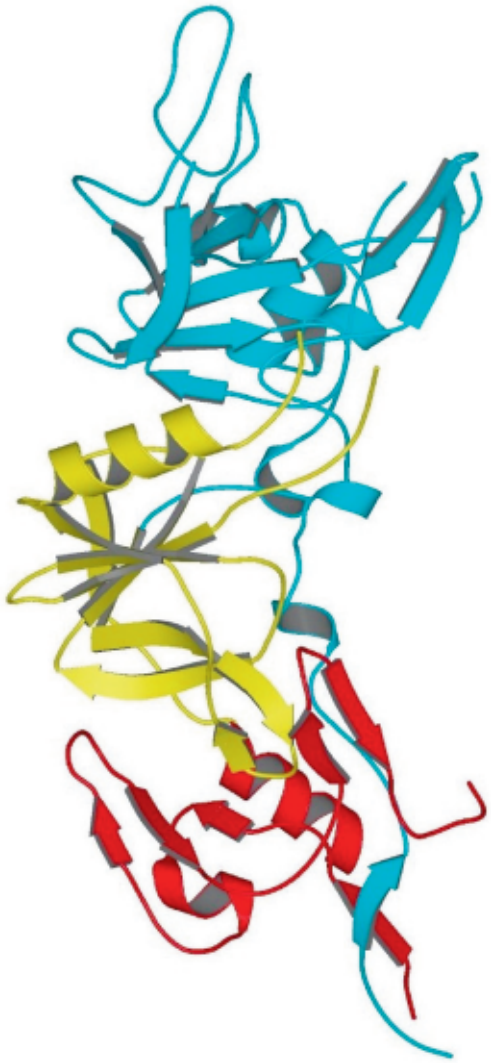

Fig. 83: Structure of the ectoplasmic region of AMA1 showing domain I (blue), domain II (yellow) and domain III (red).

Some regions of the AMA1 polypeptide chain are found as large surface-exposed insertions on the basic PAN core of domain I or domain II; these are essentially devoid of any regular secondary structure and show significant flexibility. Since AMA1 homologues are found in other members of the phylum *Apicomplexa*, to which *Plasmodium* belongs, we speculate that domains I and II derive from a gene duplication event that occurred early in the evolution of this class of unicellular organism. Little is known about general structure/function relationships of proteins bearing PAN domains, but one of their roles is the adhesion to protein or carbohydrate ligands.

Many *Plasmodium* surface antigens, including AMA1, have developed a high level of polymorphism (antigenic diversity) to escape the immune response of the host. In AMA1 from *P. falciparum*, 52 residues of the ectoplasmic region (12% of the sequence) are polymorphic. Most of this polymorphism resides in domain I, suggesting that this region plays a major role in camouflaging the parasite against the host's immune response. Curiously, however, the distribution of polymorphic sites is highly biased to one side of the molecule, implying that antigenic variation on the other side is subject to strong functional constraints. Moreover, we have pinpointed a functionally important region of AMA1 by mapping the epitope of an invasion-inhibitory monoclonal antibody through a systematic mutation study and relating these results to the three-dimensional structure. The epitope is located at the base of a flexible 40-residue loop on domain II that is devoid of any known polymorphisms. In addition, studies on the naturally acquired immunity of individuals living in malaria-endemic regions have shown that this region also carries an immunodominant T-cell epitope. Thus, the importance of the domain II loop in the immune response and its conserved sequence between different *P. falciparum* isolates suggest that it might form a basis for simpler (sub-domain) vaccine constructions.

References

[1] www.who.int/topics/malaria/en/
[2] A.W. Thomas *et al.*, *Mol. Biochem. Parasitol.*, **13**, 187-199, (1984)

Principal publication and authors

J.C. Pizarro (a), B. Vulliez-Le Normand (a), M.-L. Chesne-Seck (a), C.R. Collins (b), C. Withers-Martinez (b), F. Hackett (b), M.J. Blackman (b), B.W. Faber (c), E.J. Remarque (c), C.H.M. Kocken (c), A.W. Thomas (c), G.A. Bentley (a), *Science* **308**, 408-411 (2005).
(a) Unité d'Immunologie Structurale, CNRS URA 2185, Institut Pasteur, Paris (France)
(b) Division of Parasitology, National Institute for Medical Research, London (UK)
(c) Department of Parasitology, Biomedical Primate Research Centre, Rijswijk (The Netherlands)

X-ray Crystallography Study on Ribosome Recycling: Structural Explanation for RRF-mediated Subunit Dissociation

Ribosome recycling is commonly referred to as the fourth stage of translation as it follows the initiation, elongation and termination phases. Ribosomes entering the recycling phase contain an mRNA with a stop codon positioned at the A site, and an uncharged (deacylated) tRNA at the P site. In bacteria, this functional state is recognised by the ribosome recycling factor (RRF), which together with elongation factor G (EF-G) and initiation factor IF3, promotes both the dissociation of the ribosome into subunits and the release of the mRNA and tRNA, thus recycling the components for the next

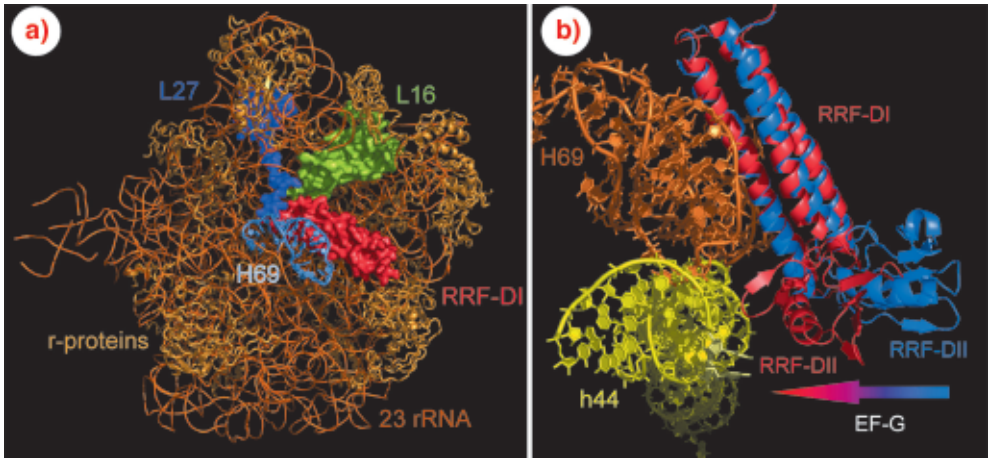

Fig. 84: (a) RRF-DI (red) interacts with helix 69 (H69) and ribosomal proteins L16 (green) and L27 (magenta) on the *D. radiodurans* 50S subunit. (b) EF-G binding induces a shift in the position (as indicated by arrow) of RRF-DII towards h44 of the 30S subunit leading to disruption of the intersubunit bridge contact between h44 (yellow) and H69 (orange).

round of translation. The importance of ribosome recycling is emphasised by the universal presence of RRF in bacteria, as well as in the mitochondria and chloroplasts, but not in the cytoplasm, of eukaryotic cells. Deletion of *frr*, the gene encoding RRF, is lethal in all the bacteria tested so far. Moreover, in *Mycoplasma* species, which have severely reduced genome sizes due to removal of nonessential genes, *frr* has been retained. The cellular importance and kingdom distribution of RRF thus make bacterial ribosome recycling an attractive target for drug design, a prerequisite of which is a high-resolution structure of the ribosomal binding site of RRF.

Using data collected on **ID29**, we have determined the X-ray structure of the ribosome binding domain of RRF (RRF-DI) bound to the large ribosomal subunit of the eubacterium *Deinococcus radiodurans* at 3.3 Å resolution (**Figure 84a**). Our study confirms the general conclusions observed in lower resolution (~12 Å) cryo-EM studies [1]. However, the position of RRF found in the cryo-EM analysis must be rotated 7° and shifted by 8 Å to be aligned with the position determined here, thus significantly altering the predicted sites of interaction. In addition, we observe multiple contacts that were not seen in the previous studies. In our study, the atomic details of the interaction of RRF with the large ribosomal subunit reveal that domain I of RRF contacts (exclusively) elements involved with tRNA binding and/or translocation (**Figure 84a**): (i) nucleotides G2252-G2254 of the P loop (H80), which play an important role for the positioning of the tRNA in the P-site, (ii) the base of A2602 present in H93, which has been suggested to guide the CCA-ends of the tRNA from the A- to the P-site during translocation, and (iii) the ribosomal proteins L16 and L27 at the peptidyl-transferase centre, which have been implicated in positioning of tRNAs at the P site.

The most extensive contacts between RRF-DI and the 50S subunit are with helices 69 and 71 (H69–H71) of domain IV of the 23S rRNA (**Figure 84a** and **b**). In the 70S ribosome, H69 and H71, make contact with h44 of the 30S subunit, to form stable inter-subunit bridges [2]. Binding of RRF-DI to the 50S induces movement of H69 away from the stalk region, to resemble more closely the position observed in the *Thermus thermophilus* 70S ribosome [2]. However, the loop of H69 in the D50S-RRF-DI structure has a different and more open conformation compared to that in the 70S, such that its tip is shifted by 20 Å towards h44 of the small subunit.

To understand how RRF and EF-G interact on the ribosome during recycling we modeled a RRF-EFG-70S complex by (i) superimposing domain I of known unbound RRF structures with the position of RRF-DI on the 50S subunit, (ii) modeling a 70S-RRF structure by combining the high resolution 30S subunit with our 50S structure on the basis of the known 70S ribosome structure [2], and (iii) docking EF-G on the ribosome on the basis of 70S-EFG cryo-EM reconstructions. The resulting model suggests that domain III and IV of EF-G predominantly make contact with domain II of RRF (RRF-DII) upon binding. Cohabitation requires RRF-DII to move towards h44 on the 30S subunit (indicated by arrow in **Figure 84b**). This leads us to suggest that splitting of the 70S ribosomes into subunits during recycling results from disruption of the universally conserved intersubunit bridges through a combination of the action of RRF-DI on H69 and the EF-G induced action of RRF-DII on h44. Support for this model has been born out by recent cryo-EM structures of EF-G and RRF on the large ribosomal subunit [3].

References

[1] R.K. Agrawal *et al., Proc. Natl Acad. Sci. USA* **101**, 8900–8905 (2004).
[2] M.M. Yusupov *et al., Science* **292**, 883–896 (2001).
[3] N. Gao *et al., Mol Cell.* **18**, 663-74 (2005).

Principle Publication and Authors

D.N. Wilson (a), F. Schluenzen (a), J.M. Harms (a), T. Yoshida (b), T. Ohkubo (b), R. Albrecht (a), J. Buerger (a), Y. Kobayashi (b), P. Fucini (a) *EMBO J.* **24**, 251-260 (2005).
(a) Max-Planck Institute for Molecular Genetics, Berlin (Germany)
(b) Graduate School of Pharmaceutical Sciences, Osaka University (Japan)

The Structure of Tryptophan 7-Halogenase (PrnA) Suggests a Mechanism for Regioselective Chlorination

Chlorinated natural products such as vancomycin and rebeccamycin are widely used in medicine. Although the chemical synthesis of these compounds is known, the agents in clinical use are actually made by fermentation of bacteria. The chlorination of these compounds has long been of interest to chemists and biochemists. This is because the enzymatic transformation which underlies the synthesis must exhibit exquisite regioselectivity. For many years the chlorination of natural products was assumed to rely on haloperoxidases. These are metal based enzymes which utilise hydrogen peroxide to generate a metal bound hypohalous ion. The metal bound intermediate is released as HOCl which then chlorinates substrate. However, this process lacks the regioselectivity seen in many important biologically active chlorinated natural products. Recently, gene sequencing has identified a new class of enzyme that displays regioselectivity and that has been shown to be responsible for the chlorination of almost all bacterial natural products. These enzymes require $FADH_2$ and molecular oxygen for activity and many laboratories have speculated on mechanisms which would explain the regioslectivity observed.

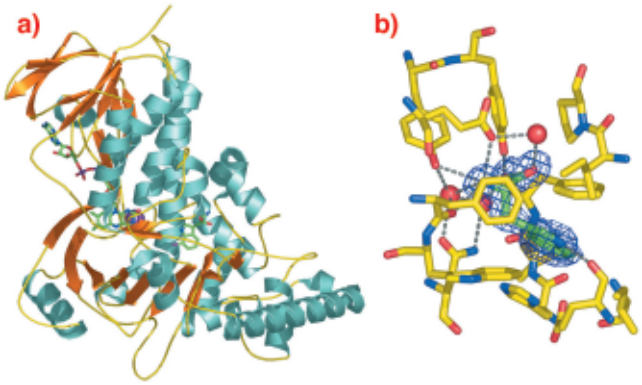

Fig. 85: a) Ribbon diagram of the PrnA-FADH and tryptophan complex. α-helices are shown in blue, β-strands in orange. The $FADH_2$ cofactor (left hand side) and tryptophan substrate are shown in ball and stick representation; b) The electron density for the substrate tryptophan molecule bound at the enzyme active site. The surrounding residues are shown.

We have determined the native structure of a tryptophan 7-halogenase (PrnA) - a member of the flavin dependent class of halogenases - using Se Met labeling of the protein and diffraction data collected on **BM14** (**Figure 85a**). Structures of PrnA complexed to substrate (tryptophan) and product (7-chloro-tryptophan) were then obtained using data collected on **ID14-1** (**Figure 85b**). The structures show that PrnA can be decomposed into two modules, a flavin binding module and a substrate binding module. The flavin binding module is similar in structure to monooxygenase enzymes and also binds the chlorine atom. The tryptophan binding module is unique. Crucially tryptophan and flavin are separated by 10 Å effectively ruling out any direct transformation of substrate to reaction product.

Using the data obtained from our structure we were able to design chemical and biochemical experiments to probe the reaction mechanism. Based on these experiments we propose that the enzyme makes HOCl in the flavin module and channels it to the tryptophan module. When at the correct position, HOCl is activated and takes part in electrophilic aromatic substitution. Halogenation using HOCl is well known in nature and organic chemistry, yet it lacks the reactivity and regioselectivity required for biosynthetic pathways. We suggest that with the halogenases described here biology has evolved a remarkable mechanism of generating, activating and controlling HOCl.

Principal Publication and Authors

C.J. Dong (a), S. Flecks (b), S. Unversucht (b), C. Haupt (b), K.-H. van Pée (b) and J.H. Naismith (a), *Science*, **309**, 2216-2219 (2005).

(a) Centre for Biomolecular Sciences, EaStchem, The University, St Andrews (UK)
(b) Institut für Biochemie, TU Dresden (Germany)

Crystal Structure of Maltooligosyltrehalose Trehalohydrolase from *D. radiodurans*

Deinococcus radiodurans is a bacterium that displays an extraordinary resistance to a wide-range of DNA-damaging agents, such as ionising radiation and desiccation [1]. Since there are no terrestrial environments that generate high doses of radiation, it has been proposed that the radioresistance of *D. radiodurans* has arisen as a by-product of selection for desiccation resistance.

The removal of water from a cell is a severe, often lethal stress. During desiccation, cell metabolism is completely arrested and subsequently needs to be fully recovered during rehydration and extensive damage is caused to DNA, proteins and lipid membranes. Certain sugars have been shown to contribute to the stability of proteins, membranes and whole cells during prolonged dehydration. In particular, trehalose appears to be the most effective stabiliser of dried proteins and membranes. Trehalose is a non-reducing α-1,1-linked disaccharide (α-D-glucopyranosyl-1,1-α-D-glucopyranose) that accumulates

in organisms under stress conditions. Evidence suggests that trehalose protects membranes and proteins by serving as a water substitute [2].

D. radiodurans uses an unusual pathway for trehalose biosynthesis. Two enzymes, maltooligosyltrehalose synthase (MTSase) and maltooligosyltrehalose trehalohydrolase (MTHase), catalyse the breakdown of maltooligosaccharides or starch into trehalose. MTHase is a member of the α-amylase family of $(\beta/\alpha)_8$ barrel glycosidases, which comprises enzymes with a wide variety of known activities. We have determined the high resolution (1.1 Å) crystal structure of *D. radiodurans* MTHase (DrMTHase) using the single-wavelength anomalous dispersion (SAD) method and data collected on beamlines **ID29** and **ID14-2**. Crystal structures were obtained for both apo- and disaccharide-bound (maltose and trehalose) forms of DrMTHase.

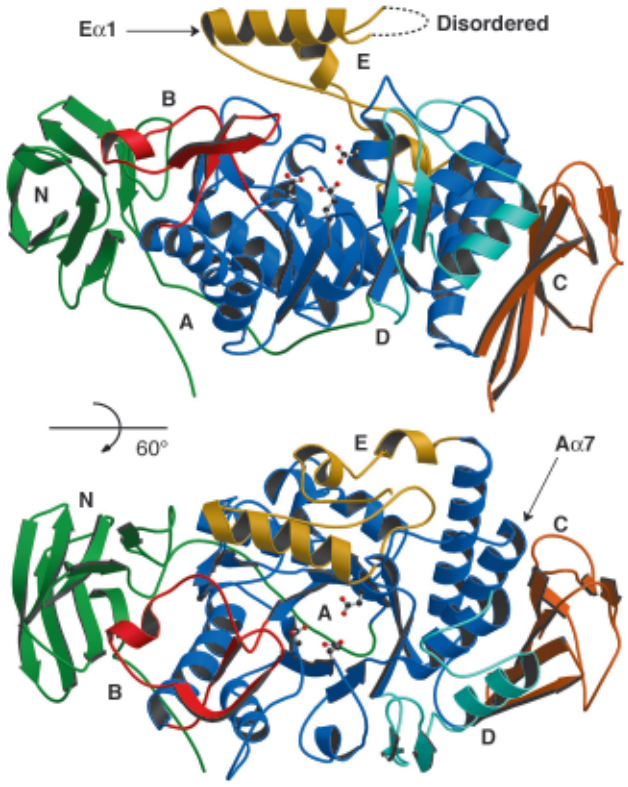

Fig. 86: Ribbon representation of the crystal structure of DrMTHase. Each domain is represented in a different colour and the catalytic residues are illustrated in ball-and-stick representation.

DrMTHase is a monomer and displays three major domains (**Figure 86**): an N-terminal domain (domain N) that consists of an eight-stranded immunoglobulin-like Greek key fold, a central catalytic $(\beta/\alpha)_8$ barrel domain (domain A) and a C-terminal domain (domain C) that consists of a six-stranded γ-crystallin-type fold. Three additional subdomains (domains B, D and E) protrude from the central domain A (**Figure 86**). The structures of DrMTHase in complex with either maltose (an α-1,4-linked disaccharide, which mimics a short portion of the substrate) or trehalose (the product of the reaction) reveal that all three inserted subdomains B, D and E are crucial for substrate binding. As shown in **Figure 87**, two channels are formed at the surface of DrMTHase to bind long sugar chains, one leading down to the active site and another guiding the sugars out again. Unlike other members of the glycosidase family, DrMTHase undergoes a significant conformational change upon substrate (maltose) binding, in order to guide the sugar chain into the active site. Subdomains B and E trap the substrate in the active site and most likely maintain the sugar chain in a strained conformation in order to lower the energy barrier of hydrolysis.

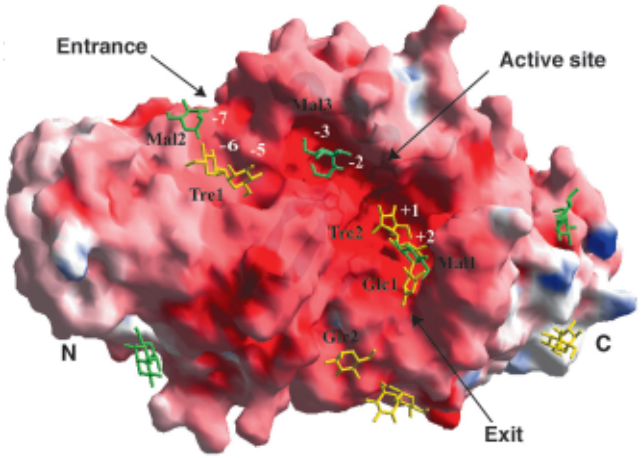

Fig. 87: Illustration of the electrostatic surface potential of DrMTHase in which red and blue represent negative and positive potentials respectively. Bound sugars are represented in green (maltose) and yellow (trehalose).

The presence of trehalose in the active site of the DrMTHase-trehalose complex has allowed the identification of the residues involved in the selective binding of the α-1,1-linked sugar, trehalose, as opposed to other maltooligosaccharides. The sugar units are specifically recognised by an extensive hydrogen bonding network, in which many water molecules are involved and are further stabilised by hydrophobic stacking interactions in between two protein aromatic side chains. Importantly, the His332 Nε2 atom hydrogen-bonds directly to the O6 atoms of the two sugar units of the bound trehalose molecule. This interaction is trehalose specific, since the presence of both O6 atoms at hydrogen-bonding distance from His332 Nε2 could only occur with a α-1,1-linked disaccharide.

This work has revealed the mode of substrate recognition of DrMTHase, which is most likely shared by other members of the subfamily of MTHase enzymes, since most of the critical residues are conserved. The presence of this unusual trehalose synthesis pathway in the extreme radiation and desiccation-resistant bacterium *D. radiodurans* suggests that this pathway may be essential to its survival, especially as the 'classical' pathway involving trehalose-phosphate synthase is missing. The rapid breakdown of the most widely available source of maltodextrins in nature, *i.e.*

soluble starch, would be an efficient mechanism to rapidly produce trehalose in response to environmental stress.

References

[1] V. Mattimore, & J. R. Battista. *J. Bacteriol.* **178**, 633-637 (1996).

[2] M. Potts. *Trends Microbiol.* **9**, 553-559 (2001).

Principal Publication and Authors

J. Timmins (a), H.-K. Leiros (a), G. Leonard (a), I. Leiros (a) and S. McSweeney (a). *J. Mol. Biol.* **347** (5), 949-963 (2005).

(a) ESRF

Phasing of Macromolecular Structures using Radiation Damage

The determination of novel macromolecular crystal structures is a critical step in the detailed understanding of many biological processes. During the course of structure determination, crystallographers must overcome the so called 'phase problem': while intensities of the X-rays diffracted by macromolecular crystals can be measured, phases cannot. The ESRF has a number of dedicated macromolecular crystallography (MX) beamlines where the energy of the incoming beam can be rapidly tuned to the absorption edge of the relevant heavy atom, thus enhancing the anomalous signal needed to solve the phase problem. These beamlines, together with fixed-energy MX stations as well as numerous other state-of-the-art and dedicated MX beamlines around the world, have made an extraordinary impact in structural biology.

Whereas these high intensity sources allow data collection at an unprecedented speed, they also painfully reveal the problem of radiation damage. Radiation damage quickly reduces the diffractive power of the cryocooled crystal, and can lead to specific changes within the structure. Heavy-atom substructures seem to be particular prone to damage, thus reducing anomalous signals, whereas small dispersive signals are easily swamped by non-isomorphism induced by the X-ray beam [1,2].

Rather than regarding radiation-damage as a problem to be avoided, we have shown that the specific nature of radiation-damage can actually be used to phase

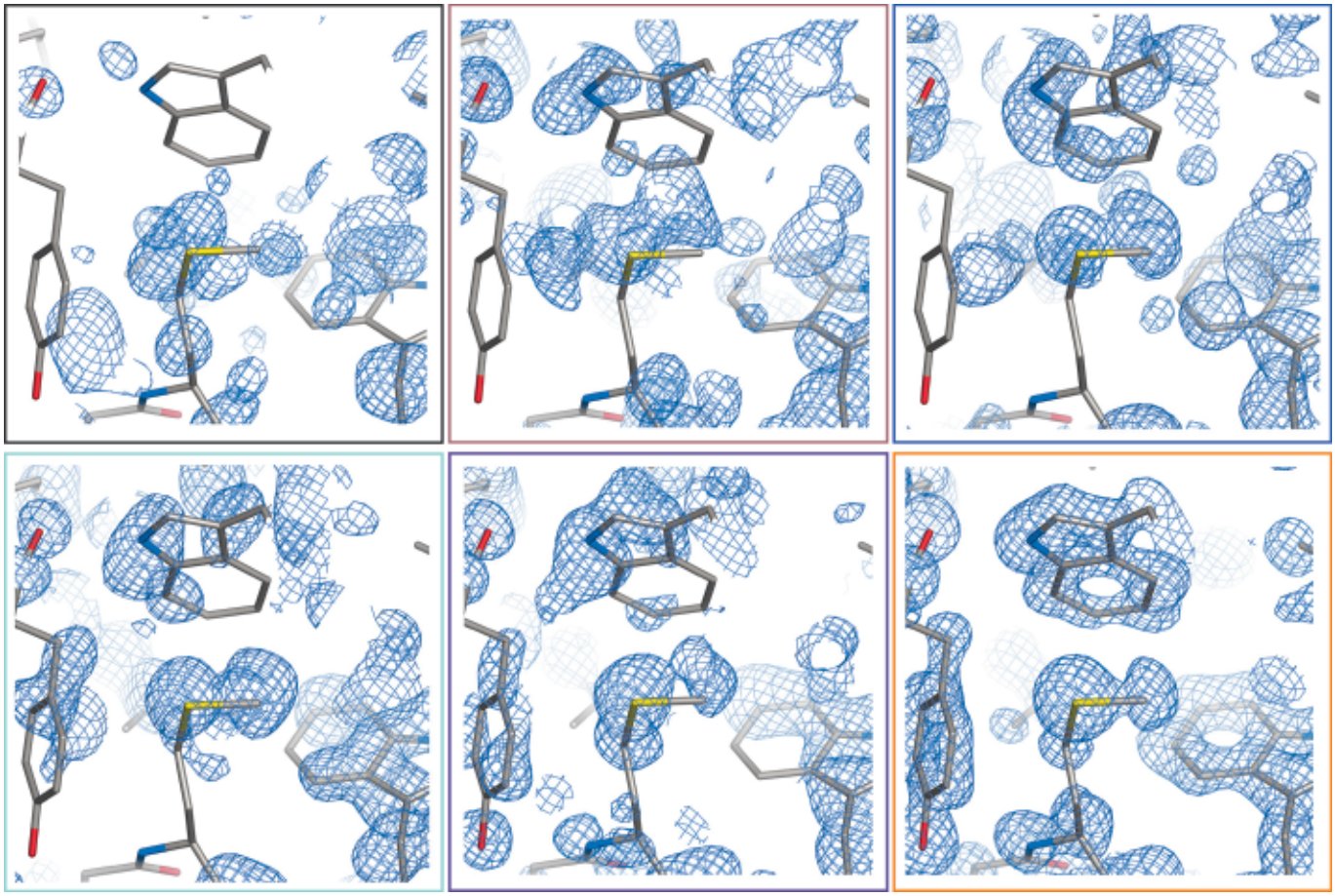

Fig. 88: Experimental RIP electron-density maps of lysozyme for different subsequent iterations in the structure determination using SHELXE. A total of 11 substructure iterations were made during which the substructure size increased from 8 to 40. Maps were drawn after iteration Nos. 1, 6, 8, 9, 10 and 11.

macromolecular structures [3]. The method has been named RIP; Radiation-damage Induced Phasing. It is tempting to compare the RIP method with the Single-Isomorphous Replacement (SIR) method, where two data sets are collected, one on a native crystal and one on a derivative. While collecting a highly redundant data set on a single crystal and splitting the data series into a number of complete, low-redundant data sets, the first data set could be seen as 'the derivative', whereas a later data set could be treated as 'the native'. Existing software can then be used for solving the phase problem in a SIR-like manner.

Six RIP data series have been collected on **ID14-4** on crystals of native proteins: most structures could be phased solely using the radiation damage signal. We have shown that RIP may also be seen as a Multiple Isomorphous Replacement (MIR) experiment, where the native data set is missing. In contrast to MIR, a RIP substructure consists of a large number of small structural changes. Special software needs to be developed to take into account the presence of both gains (positive) and losses (negative) of electron density. We have demonstrated that careful scaling is needed to take the overall decay of the crystal into account. Existing packages have been adapted to exploit the specific nature of RIP: SHELXC and SHELXD for initial substructure determination while allowing the later data set to be 'downscaled', and SHELXE to allow substructure iteration whilst accounting for negative and positive electron densities (**Figure 88**).

Unlike SIR, MIR and MAD, RIP can be performed on crystals of native proteins. The technique is complementary to sulfur-SAD: the combined use of these techniques could become a "magic bullet" - overcoming the need to derivaterise proteins. The full maturation of the RIP technique requires the development of a new generation of software packages that can accurately model and exploit radiation damage. We have presented some initial steps towards this purpose.

References

[1] L.M. Rice, T.N. Earnest and A.T. Brunger, *Acta Cryst.* **D56**, 1413-1420 (2000).
[2] R.B.G. Ravelli, M.H. Nanao, A. Lovering, S. White and S. McSweeney, *J. Synchrotron Rad.* **12**, 276-284 (2005).
[3] R.B.G. Ravelli, H.K. Leiros, B. Pan, M. Caffrey and S. McSweeney, *Structure* **11**, 217-224 (2003).

Principal Publication and Authors

M.H. Nanao (a), G.M. Sheldrick (b) and R.B.G. Ravelli (a), *Acta Cryst.* **D61**, 1227-1237 (2005).
(a) EMBL, Grenoble Outstation (France)
(b) Georg-August Universität, Göttingen (Germany)

Continuing Automation of ESRF MX Beamlines

Modern synchrotron-based macromolecular crystallography facilities must be extremely reliable, user friendly and capable of very high throughput data collection. The best means of ensuring this goal is to enable such beamlines to function automatically. Macromolecular Crystallography (MX) facilities are particularly amenable to automation as they specialise in one technique that is repeated many times a day, namely the collection of high quality single crystal diffraction data. Automation procedures for MX beamlines should address several aspects of an experiment: the provision of the X-ray beam onto the sample; the mounting and dismounting of samples onto the goniometer; the characterisation of crystal diffraction quality and subsequent data collection and processing procedures. ESRF staff in collaboration with the EMBL Grenoble out-station Instrumentation group and other European institutes have made significant contributions to all of these areas [1, 2].

On ID23-1 a new instrument control system analyses information from various instrument position monitors and detectors so that an optimal X-ray beam can be delivered to the sample. A graphical overview, shown in **Figure 89**, presents the instrument status. Now that the new control system has been thoroughly tested, it will be adopted by the other ESRF MX beamlines during 2006.

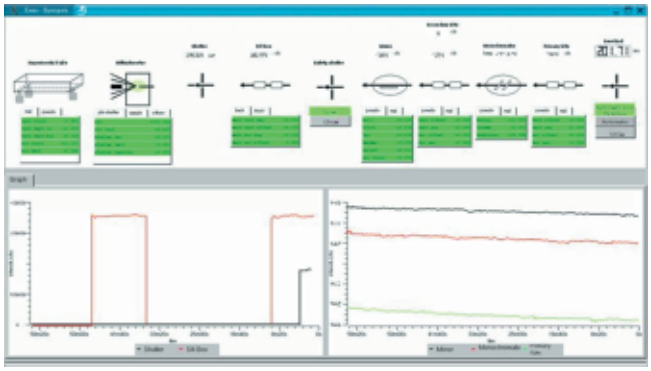

Fig. 89: Diagnostic display on ID23-1.

A new generation of robotic sample changers (SC3, **Figure 90**) that were developed and built in Grenoble are now installed on all seven of the ESRF MX beamlines [1]. These sample changers allow automation of the mundane and time consuming procedure of mounting and dismounting a crystal on the goniometer. Additionally, the SC3 robots are equipped with CCD cameras and barcode readers, together they read the SPINE standard two-dimensional datamatrix codes etched on the bases of the sample holder contained in the robot. This allows each sample to be identified and, in conjunction with the DNA software and the ISPyB Laboratory Information Management System, provides a means for sample tracking before, during and after an experimental session. These tools also provide the basis

for a data collection pipeline (DCP) developed at the ESRF [2]. The DCP allows the automatic screening of the diffraction quality of the entire contents of a sample changer and (when coupled with a Data Ranking Module implemented in DNA) allows the automatic selection of the "best" crystal from which to collect data for the project in hand.

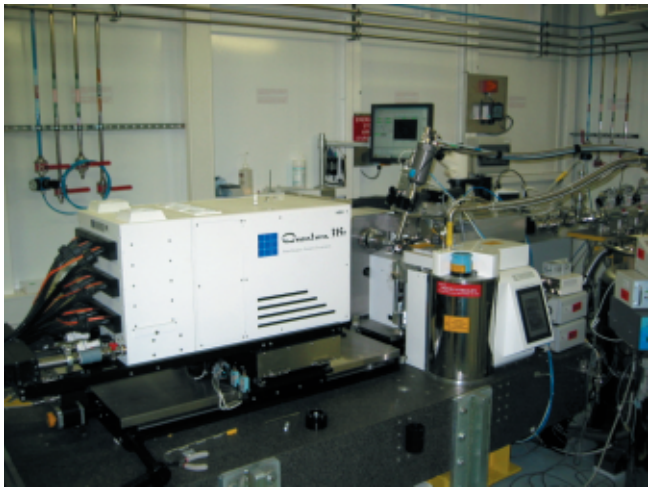

Fig. 90: ADSC Q-315r detector and sample changer (SC3).

The collaboration between ESRF and EMBL-Grenoble has been instrumental in the successful development of the mini-Kappa goniometer head (**Figure 91**). This device will improve the way diffraction data for MX is collected at the ESRF, particularly when a small anomalous signal needs to be measured accurately. When such devices are used on the beamlines (ID23-1, ID29, ID14-4) newly equipped with the ADSC Q-315 detector (**Figure 90**) they will also provide great benefit to scientists studying biomolecules with large unit cells.

Fig. 91: Mini kappa goniometer.

Taken as a whole, the recent developments at the ESRF MX beamlines mean that they now provide an outstanding framework on which MX experiments can be performed.

Principal publications

[1] F. Cipriani *et al.*, Automation Instrumentation for High Throughput Macromolecular X-ray beamlines, Submitted to *Acta Cryst D.*

[2] A. Beteva *et al.*, High throughput sample handling and data collection at synchrotrons: embedding the ESRF into the high throughput gene to structure pipeline, Submitted to *Acta Crystallographica Section D - Biological Crystallography*.

Author

X. Thibault

(on behalf of the Joint Structural Biology Group (JSBG) of the ESRF and the EMBL Grenoble Outstation)

ESRF

Highlights 2005

Surface and Interface Science

Introduction

Surface and interface preparation and characterisation have become commonplace. Ultra-high vacuum facilities and much of the associated equipment, that would have been the most important and almost exclusive tools of the surface science specialists half a century ago, are nowadays widely used in many scientific and technological disciplines. Surface science on the other hand has expanded into areas that were not too long ago considered as being too "dirty" to be associated with this discipline, such as heterogeneous catalysis, solid/liquid interfaces and friction, electrochemical plating, corrosion, batteries and fuel cells, soft condensed matter and biology. Increasingly in the limelight are *in situ* observations of surface modifications and growth as well as structure-property relationships. Surface and interface science (SIS) is also naturally an integral part of nano-science, since the surface/interface to volume ratio of atoms/molecules is increasing strongly with shrinking size of objects. At the ESRF surfaces and interfaces are studied at about 50% of all beamlines. However, the three ESRF insertion device beamlines ID01, ID03, and ID32, which comprise the SIS group, and the CRG bending magnet beamline BM32 represent the specialists in this area.

2005 had been an important year for SIS at the ESRF. Following an intensive discussion with the SIS user community, it was decided at the end of 2004 to rigorously refurbish the surface X-ray diffraction beamline ID03. In 2005 this decision had to translate into action, and the most urgent task was to replace the personnel, which had left, and devise a strategy for the refurbishment. Now the beamline is again fully staffed. Two very experienced scientists and a second postdoc, an expert in surface crystallography, have been hired. For reconstruction, ID03 had been completely dismantled, but is by now back in place again with increased space for equipment. Towards the end of spring, it is scheduled to cater again to users with much improved optics and refurbished experimental facilities.

Progress and development can also be reported from the other two SIS beamlines. At ID32, focusing with compound refractive lenses for surface diffraction and Fresnel lenses for photoelectron spectroscopy are now available. A high-resolution secondary monochromator is presently being installed and a new state of the art primary monochromator is due to arrive in March 2006. At ID01 plans are taking shape to gear the beamline up to further explore the nano world with smaller focal spot sizes and by exploiting coherent scattering.

With scientific news from ID01 and the nano-world we are also starting the 2005 SIS highlights. Malachias *et al*. (page 74) retrieve detailed quantitative information about the internal structure and the atomic ordering in Ge islands on silicon. Whereas bulk SiGe alloy is disordered, they find surprisingly ordered SiGe domains in the interior of the small islands. The way to establish order in assemblies of nano-particles, to find tricks to force inorganic matter to self organize, is in fact a big issue in current research. Leroy *et al*. (page 76) report in the next contribution about a new method to achieve this. Using the UHV growth and *in situ* X-ray scattering facilities at BM 32 they demonstrate that a two dimensional array of dislocations can be employed for forcing an assembly of tiny magnetic dots to assemble into an ordered superstructure.

Three highlights are devoted to structure-property relations. Popa *et al*. (page 77) employed surface X-ray diffraction at ID03 to shed light on the astonishingly different magnetic behaviour of ultra-thin cobalt and nickel films on a platinum surface. By solving the structure of the films they reveal the importance of magneto-elastic effects. Thiess *et al*. (page 79) utilised X-ray photoelectron spectroscopy (XPS) and X-ray standing waves (XSW) at ID32 to carry out an investigation that seems impossible at first sight. They determined the sites of origin in the unit cell for electrons in specific parts of the strontium titanate valence band. The third highlight in this category is by Lechner *et al*. (page 80). They used anomalous X-ray diffraction at ID01 to resolve the relationship between the strain and the magnetic phase diagram in thin layers of magnetic semiconductors, which are materials, which may become the workhorses of future spintronic devices.

The last two of the SIS highlights are dedicated to surface chemistry. Interfacing organic and inorganic matter is increasingly attracting interest, being of paramount importance to fields such as medicine. Hauschild *et al*. (page 81) employed XSW in combination with XPS at ID32 to resolve the minute structural changes introduced into an organic molecule when it is bound to a silver surface. The last contribution underlines, that surface scientists, in the past "addicted" to UHV, now tackle the structure and properties of "real" surfaces. Ackerman *et al*. (page 83) report about the investigation of a platinum catalyst during carbon monoxide oxidation, which is an exciting example in this respect. At ID03 they observed the associated structural changes of the surface at high temperature and close to atmospheric pressure. By monitoring the gas composition in the reaction chamber, they could intimately link the structural changes to changes in catalytic activity

J. Zegenhagen

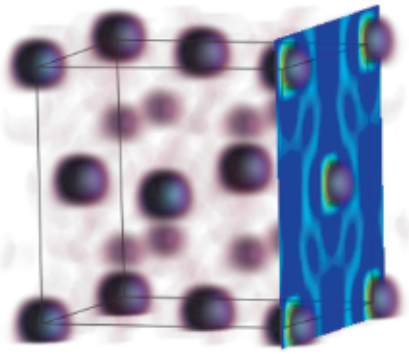

Fig. 92: Image of Mn within the cubic unit cell of GaAs. Rendering of X-ray standing wave data taken at ID32.

Nanostructures

Atomic Ordering in Self-assembled Ge Quantum Dots

The spontaneous formation of self-assembled nanostructures has become a driving force in nanoscience research during the last two decades. Semiconductor quantum dots are well-known examples of such a nanoscale system where the opto-eletronic behavior depends on the atomic-level configuration. In order to understand heteroepitaxial strained layer growth, Ge islands on Si(001) have been extensively investigated as a model system. Coherent Ge nanostructures are spontaneously formed on top of a three monolayer thick wetting-layer. Recent anomalous X-ray experiments have shown that a considerable amount of Si from the substrate is incorporated into Ge dome-shaped islands during growth [1]. However, the interdiffusion mechanism remains obscure at the atomic level. In this work basis forbidden reflections were measured in nominally pure Ge islands on Si(001). The existence of an atomically ordered alloy phase inside these islands confirm the crucial rule of surface kinetics to the final island structure and composition.

A θ-2θ radial scan in the vicinity of the in-plane Si(400) surface reflection is shown in **Figure 93a**. The broad intensity distribution along the q_r axis indicates that the lattice parameter, which was initially constrained to the Si value, relaxes continuously towards the Ge lattice parameter with increasing height inside the islands. A rather unexpected result is obtained when the scattered intensity is measured in the vicinity of the (200) reflection (**Figure 93b**), which is forbidden for pure Si and Ge crystals and also for a random alloy of the two elements. This strongly indicates that the domes consist of a SiGe alloy with a long-range atomic order.

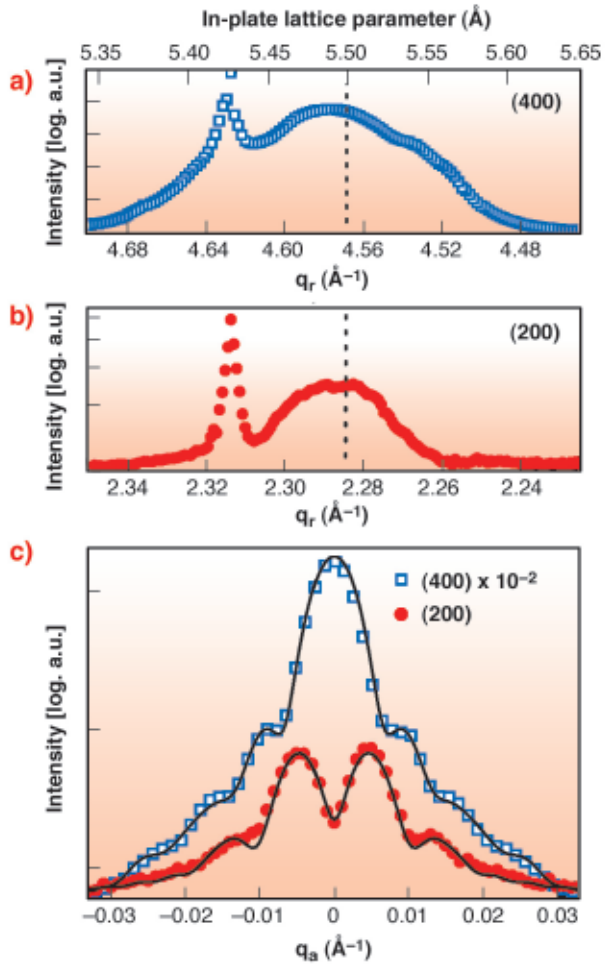

Fig. 93: Radial scans in the vicinity of (a) Si (400) reflection and (b) Si (200) reflection. The upper scale directly indicates the in-plane lattice parameter. (c) Angular scans performed at (400) and (200) reflections.

Performing a size-sensitive angular (θ) scan for a fixed 2θ, one probes the corresponding Fourier transform of a region with constant lattice parameter. One angular profile close to the (400) reflection (**Figure 93c**) exhibits a broad peak and subsidiary maxima, resulting from the finite size and narrow size distribution of constant-lattice parameter region. In contrast to the (400) reflection, an angular scan performed at the (200) reflection yields a very different profile as shown in **Figure 93c**. A pronounced minimum is observed at q_a = 0, which cannot be generated by structures that are interfering constructively. Such a profile is modeled by introducing anti-phase boundaries, which are generated by stacking faults in the in-plane atomic sequence, leading to phase inversions in the X-ray wave.

The complete q_r/q_a measured intensity map close to the Si (200) reflection is shown in **Figure 94a**. A weak narrow peak is seen exactly at the Si (200) position, indicating that the wetting-layer is partially ordered, but without establishing anti-phase boundaries. Hence, alloying and ordering begin as soon as Ge is deposited. Si atoms are incorporated into the wetting-layer in the initial phase of growth and into the islands after the beginning of their nucleation. The map shown in **Figure 94b** was obtained simulating the ordered domain size and distribution inside one island. Selected angular cuts from the

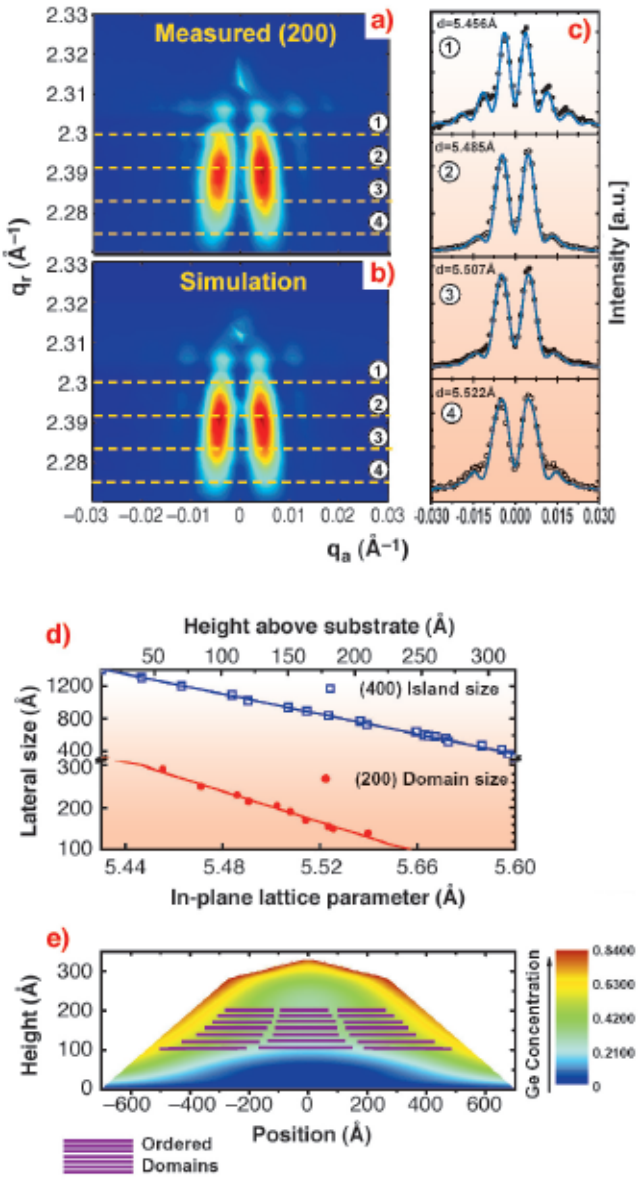

Fig. 94: Measured (a) and simulated (b) q_r-q_a intensity maps in the vicinity of the Si (200) reflection. Four numbered q_a scans (dashed lines in maps (a) and (b)) are shown in (c). (d) Size of islands and domains as a function of lattice parameter and height. (e) Ge concentration and atomic ordering map showing the location of ordered domains inside islands.

experimental and calculated maps are shown in **Figure 94c**. A comparison between island and domain size is shown in **Figure 94d**, where the size of the anti-phase domains was obtained from fits of the (200) map and the island size from fits at the (400) reflection (not shown here). For both, island and domain, there is a linear variation of size with lattice parameter and height, suggesting the existence of a stress-mediated mechanism that determines the island and domain size. A three-dimensional concentration map of the domes was obtained from anomalous scattering measurements of the (400) reflection [1]. **Figure 94e** depicts schematically the distribution of domains inside the islands. Ordered regions are present mainly in parts of the island where the Ge concentration reaches approximately 0.5.

It is worth noting that atomic ordering influences the electronic/optical properties of these islands. The presence of ordered domains results in a shift of the phonon frequency, band edge alignment and the semiconductor gap. Finally, the study of forbidden reflections can lead to a better understanding of the interdiffusion process in Si/Ge and similar Stranski-Krastanov systems.

References

[1] A. Malachias et. al., *Phys. Rev. Lett.*, **91**, 176101 (2003).

Principal Publication and authors

A. Malachias (a,b), T.U. Schülli (b,d), G. Medeiros-Ribeiro (c), L.G. Cançado (a), R. Magalhães-Paniago (a,c), M. Stoffel (e), O.G. Schmidt (e), T.H. Metzger (b), *Phys. Rev. B*, **72**, 165315 (2005).
(a) UFMG, Belo Horizonte (Brazil)
(b) ESRF (France)
(c) LNLS, Campinas (Brazil)
(d) CEA/Grenoble (France)
(e) Max-Planck-Institut für Festkörperforschung, Stuttgart (Germany)

Self-organised Growth of Nanoparticles on a Surface Patterned by a Buried Dislocation Network

The fabrication of ordered metal and semiconductor nanoparticles on solid surfaces with a uniform and controllable size and shape and with a high spatial density is an important challenge as it may find applications in nanoelectronics, ultra-high density recording materials and nanocatalysis. It has been predicted that strain patterned substrates induced by a buried dislocation network (DN) can serve as templates for growing uniform and regularly-spaced nanostructures. We present a new method based on a (001) metal surfaces nanostructured by a misfit dislocation network buried a few nanometres below the surface. We show that the trapping energy of adatoms is large enough to allow an ordering of nanostructures at room temperature. The cobalt/silver interface is chosen because it is a test bed for magnetic nanoparticles, as Co exhibits a three-dimensional (3D) growth on Ag(001) and because it does not alloy at room temperature. To modulate the surface strain field, a Ag film was grown on a MgO(001) substrate. Due to the cube on cube epitaxial relationship and the 3% lattice mismatch between Ag and MgO(001), strain relaxation occurs *via* a square misfit dislocation network with a period of $D \sim 10$ nm [1].

The experiments were carried out on the BM32 beamline, using a newly-developed setup allowing GISAXS, GIXD and X-ray Reflectivity (XR) measurements on the same sample, *in situ* [1], in Ultra High Vacuum (UHV), at different growth stages (here of Ag and Co). A 5 nm-thick 2D Ag(001) epitaxial film on MgO(001) was obtained by growing a much thicker film, annealing it, and then ion bombarding it, with *in situ* X-rays while monitoring by GISAXS, Ag(110) anti-Bragg GIXD, and XR measurements.

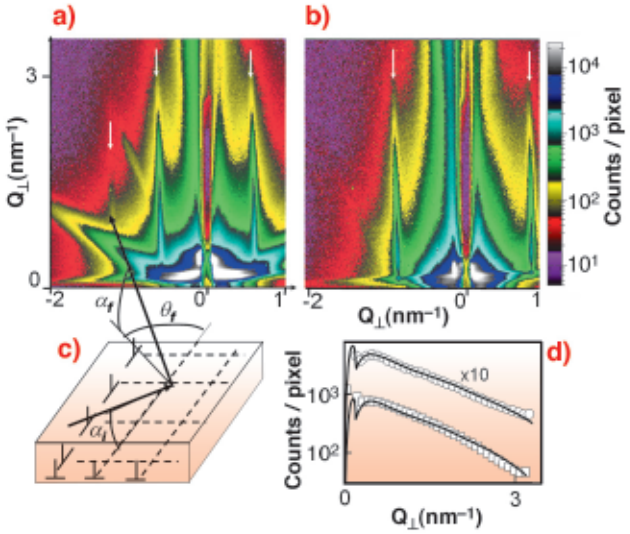

Fig. 95: (a) Experimental GISAXS pattern with the incident beam along the MgO[110] direction. (b) Same as (a), but with the incident beam along [100]. (c) Scheme of the scattering geometry of GISAXS (d) Cuts along $Q_\perp$ of the dislocation network scattering rods extracted from GISAXS patterns (a) (❑) and (b) (❍) (multiplied by 10 for clarity) and best fits.

A detailed (nano-)crystallographic study of the strain patterned substrate was first performed by GISAXS. **Figures 95a** and **b** display two GISAXS images measured on the Ag/MgO(001) film with the incident X-ray beam respectively parallel to the ⟨110⟩ and ⟨100⟩ MgO(001) crystalline axes. Sharp scattering rods in the $Q_{//}$ direction reveal a periodic nanopattern of four-fold symmetry, which were shown to be due to the buried DN. As expected [1], the in plane rod positions

correspond to dislocation lines oriented along the <110> substrate directions, with a periodicity D = 10.95 nm.

GISAXS measurements were then performed during the growth of Co on this nanostructured template for different substrate temperatures and Co growth rate. Co was finally deposited at room temperature and at a very low rate ($4x10^{-3}$ nm/min), respectively to decrease the thermal energy of the adatoms with respect to the DN nucleation trapping potential, and to increase the diffusion length of Co atoms and thus their probability to find a nucleation site. From the very beginning of the growth (0.04 nm), the subtracted GISAXS images display intensity oscillations along the DN scattering rods with a damped sinusoidal shape (**Figure 96a**). The oscillation amplitude increases with deposition time, reaches a maximum for an equivalent Co deposited thickness of 0.19 nm, and then decreases (**Figure 96b**). The period, equals to 5 nm, is a signature of the height difference between the Co clusters and the interfacial DN. Most importantly, these oscillations reveal the organised growth of Co clusters, since an interference effect can only occur if the phase shift between the waves scattered by the Co clusters and those scattered by the DN is well defined, *i.e.* if the Co clusters are well localised with respect to the dislocations positions.

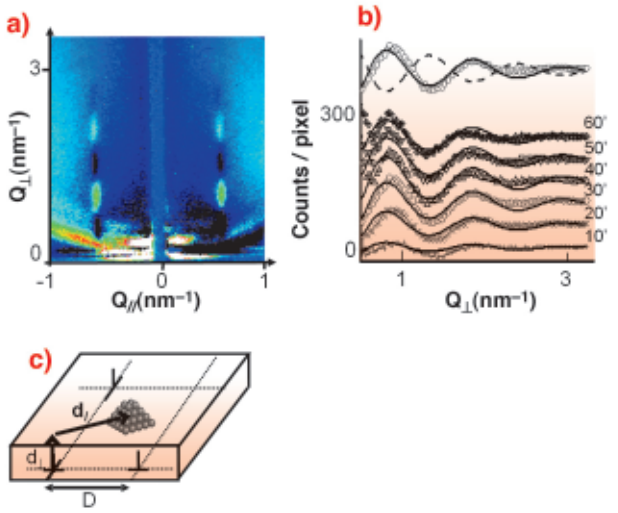

Fig. 96: (a) Experimental interference pattern with the incident beam along the [110] direction, for a 0.14 nm-thick Co deposition. The intensity is represented on a linear scale. Oscillations along the rods are clearly visible. (b) Intensity of the interference term versus $Q_\perp$, for different deposition times (symbols) with best fits. (c) Schematic representation of the Co clusters position with respect to the dislocation intersection lines.

A quantitative analysis unambiguously showed that the Co dots are located above the dislocation crossing lines, and have a height of 2 atomic layers.

To conclude, we have shown that the periodic surface strain field induced by a misfit dislocation network buried as far as 5 nm below an Ag(001) surface allows control of the growth of Co clusters at room temperature, leading to self-organised growth. We believe that this method could be used for many different systems, metal thin films being favoured with respect to semiconductor ones because of the dislocation mobility necessary to reach the equilibrium state.

References

[1] G. Renaud *et al., Science* **300**, 1416 (2003)
[2] G. Renaud, P. Guénard and A. Barbier, *Phys. Rev. B* **58**, 7310 (1998)

Principal Publication and Authors

F. Leroy (a,c), G. Renaud (a), A. Letoublon (a), R. Lazzari (b), C. Mottet (c), J. Goniakowski (a), *Physical Review Letters* **95**, 185501 (2005).
(a) CEA-Grenoble, DRFMC (France)
(b) Institut des Nanosciences de Paris (France)
(c) CRMCN-CNRS, Marseille (France)

Magnetic and Electronic Properties

Perpendicular Magnetic Anisotropy of BCC Ni Ultra-thin Films Grown on Pt(001) Surface

The magnetic anisotropy of ultra-thin films is very useful in magnetic devices where well-defined easy magnetisation axes are needed. Different ferromagnetic films on weakly magnetic substrates have been investigated in search of perpendicular magnetic anisotropy, which is of particular interest for applications in high-density magneto-optical storage. Once a system with perpendicular anisotropy is found, the goal is to understand how the magnetisation can spontaneously be oriented perpendicular to the surface, while the shape anisotropy tends to strongly orient the magnetisation in the plane of the film.

Such a system is Ni/Pt(001), which exhibits perpendicular magnetic anisotropy at room temperature for a large range of thickness. Magneto-optic Kerr effect (MOKE) measurements were performed *in situ* at the Surface Diffraction Beamline, ID03, in a geometry of the magnetic field slightly inclined with respect to the sample surface. The Ni film becomes magnetic at room temperature at 10 ML thickness, with a perpendicular easy axis. The polar MOKE cycle, which probes the perpendicular component of the magnetic field, is presented in **Figure 97a**. The coercivity increases with the film thickness and the anisotropy remains perpendicular,

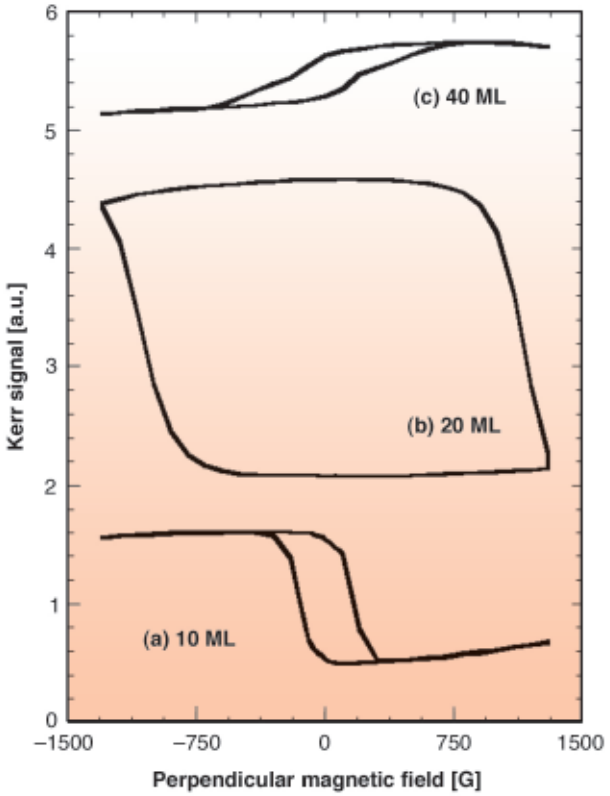

Fig. 97: Polar MOKE signal measured for Ni films deposited on Pt(001), of thickness: (a) 10 ML; (b) 20 ML; (c) 40 ML.

as showed for 20 ML in **Figure 97b**. At 40 ML, the decreasing polar MOKE signal indicates that the film is close to the point of switching toward in-plane anisotropy (**Figure 97c**).

The magnetic measurements were completed with an *in situ* crystallographic study, realised by surface diffraction at the ID03 beamline. A BCC(001) structure was identified for the Ni thin films, which arose from its very small lattice mismatch (3.7%) with the surface structure of Pt(001). Ni grows pseudomorphically on Pt(001), as proven by the similarity of the specular (00L) and non-specular (11L) rods, presented in **Figure 98** for a 10 ML Ni film. Thickness fringes are clearly visible in the low L part. The BCC (001) Ni peak was identified at L = 2.6. The vertical cell parameter was measured, showing a tetragonal distortion of the BCC Ni structure (c/a = 1.07).

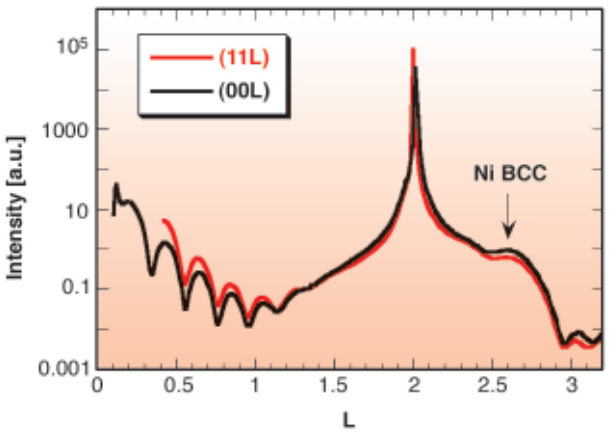

Fig. 98: (00L) and (11L) rods of a 10 ML Ni film deposited on Pt(001).

A comparison was realised with the system Co/Pt(001), previously studied at the ID03 beamline. For exactly the same crystallographic structure, the magnetic behaviour is completely different: as soon as the Co film becomes magnetic, it exhibits only in-plane anisotropy [1].

This difference can be understood on the basis of magneto-elastic effects. The bulk magnetostriction constants for FCC Co and FCC Ni are: $\lambda_{Co} = 7.5 \cdot 10^{-5}$ and $\lambda_{Ni} = -4.6 \cdot 10^{-5}$. Thus, Co and Ni behave oppositely under magnetic field: Co expands and Ni contracts in the direction of the applied magnetic film. We will presume here that the magnetostriction constants of the BCC thin films have the same signs as the bulk values.

The tetragonal distortion of the BCC structure of the Ni and Co films causes an increase of the elastic energy. Magneto-elastic effects will try then to orient the magnetisation in a way that compensates this increase. For the Co films this compensation is realised with in-plane magnetisation, while for Ni films the perpendicular magnetisation is needed.

These experimental results are in agreement with first principle calculations of uniaxial magneto-elastic anisotropy of Co and Ni ultra-thin films, realised by Burkert and co-workers [2]. They obtained a tetragonal distortion within the Bain path from FCC to BCC favors in-plane magnetic anisotropy for Co and perpendicular magnetic anisotropy for Ni.

In conclusion, BCC Ni ultra-thin films were grown pseudomorphically on the Pt(001) surface. Their perpendicular magnetic anisotropy, observed in a large range of thicknesses at room temperature, was understood on the basis of tetragonal distortion of the BCC structure and of magneto-elastic effects.

References

[1] S. M. Valvidares, T. Schroder, O. Robach, C. Quiros, T. L. Lee, S. Ferrer, *Phys. Rev. B* **70**, 224413 (2004)
[2] T. Burkert, O. Eriksson, P. James, S. I. Simak, B. Johansson, L. Nordstrom, *Phys. Rev. B*, **69**, 104426 (2004)

Principal Publication and Authors

I. Popa (a), O. Robach (b), C. Quiros (c), M.S. Valvidares (a), H. Kim (d), H. Isern (a), S. Ferrer (e), to be published
(a) ESRF
(b) CEA – DRFMC/SI3M/PCM, Grenoble (France)
(c) Depto de Fisica, Faculdad de Ciencias, Universidad de Oviedo (Spain)
(d) LG Chem. Research Park, Daejeon (Korea)
(e) CELLS – Edifici Ciencies, Bellaterra (Spain)

Site-specific Valence Band Structure of $SrTiO_3$ Determined by X-ray Standing Waves

Structure and chemical composition define the properties of materials, notably the band structure, *i.e.*, the valence band and conduction band, of solids. The band structure in turn is predominantly responsible for the optical and electronic characteristics of a material, such as the colour and the ability to reflect or absorb light or the electrical conductivity and the speed of electronic transport. Using X-ray photoelectron spectroscopy (XPS), a well-known tool for studying the chemical composition of materials, and combining it with the X-ray standing wave (XSW) technique, we can obtain electronic information on the atomic scale. It is possible to revealing how structure and chemical composition are related to the electronic structure of a solid. We used this method at ID32 to accurately determine the site within the unit cell of a $SrTiO_3$ crystal from which the electrons from a specific region of the valence band originate. $SrTiO_3$ is a wide gap (3.2 eV) semiconductor with a cubic structure where titanium occupies the centre and strontium the corners of the cube, while oxygen resides at the centre of the six faces. The unit cell, shown in **Figure 99**, has a side length of 0.3905 nm.

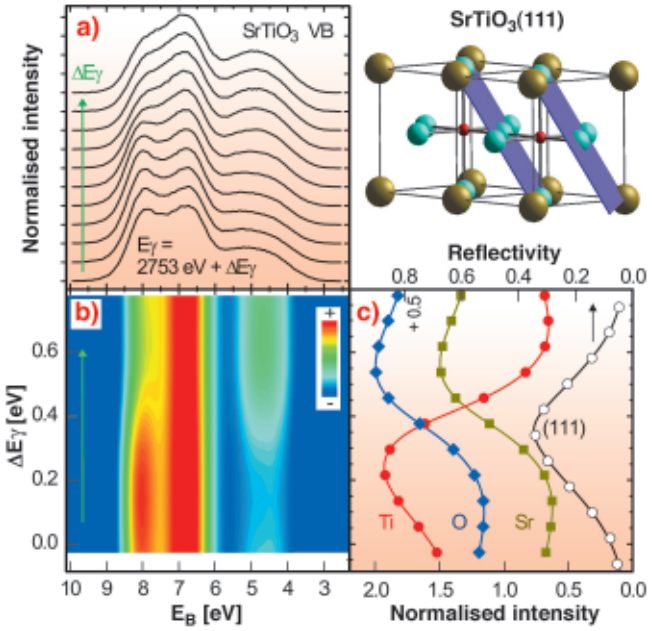

Fig. 99: Two $SrTiO_3$ unit cells, with the (111) standing wave planes indicated, are shown in the top right hand part. Oxygen atoms are in blue, titanium in red and strontium atoms in olive. a) $SrTiO_3$ valence band for different standing wave positions while crossing the (111) reflection. b) 2D colour rendering of a). c) $SrTiO_3$(111) reflection curve and simultaneously recorded Ti, O, and Sr core levels. 2.753 keV is the energy at which the (111) reflection would occur according to Braggs law.

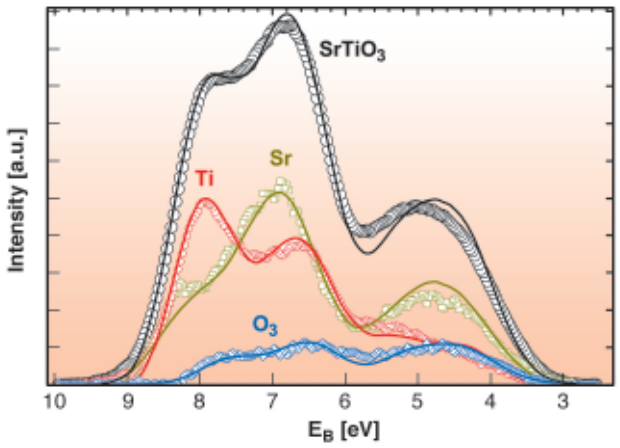

Fig. 100: $SrTiO_3$ valence band and the determined partial contribution to the valence band from the titanium, oxygen and strontium sites. The overall energy resolution is 750 meV. Symbols: experimental results; lines: DFT/LDA calculations, weighted with cross sections.

An XSW can be generated by interference via Bragg reflecting an X-ray plane wave from a single crystal. The period of this interference field reflects the spacing of the diffracting planes, which are indicated with respect to the $SrTiO_3$ unit cell for a (111) reflection in **Figure 99**. We can shift this wavefield by varying the X-ray energy within the range of the Bragg reflection, which occurs over a few 100 meV. In this way we can scan the planes of the interference field in a controlled way across the atomic positions. A maximum number of photoelectrons with a characteristic energy will be emitted when the maxima of the wavefield coincide with the centre of the atoms of a specific element in the unit cell, here Sr, Ti, and O. The emission will be strongly localised even for the largely delocalised valence band electrons, since the dipole approximation applies, meaning that photoelectron emission occurs exclusively from the centre of the atoms.

The results of an XSW/XPS measurement, using a (111) reflection from a (001) oriented $SrTiO_3$ crystal in backreflection at around 2.753 keV are shown in **Figure 99**. The valence band recorded for different positions of the standing wave within the unit cell exhibits a pronounced variation in line shape, as shown in **Figure 99a** and **99b**. **Figure 99c** shows the simultaneously recorded reflectivity curve, which allows unambiguous determination of the position of the wavefield within the unit cell of the $SrTiO_3$ crystal, and at the same time records core levels from O, Sr, and Ti. A maximum in the core emission is observed when the maxima of the wavefield are located at the position of the corresponding atoms. From a visible inspection of **Figure 99a,b** and comparison with **Figure 99c** one can conclude that the valence band at about 4.5 eV binding energy E_B is dominated by emission from Sr- and O-sites whereas at E_B = 8 eV the photoelectrons are mostly

originating from Ti-sites. With respect to the (111) reflection, Sr and Ti are located on a common plane. However, utilising another suitable Bragg reflection, the contribution from the Sr and O-sites can be disentangled.

The result of a quantitative XSW analysis is shown in **Figure 100** compared with the results of *ab initio* density functional theory (DFT) calculations in the local density approximation (LDA). The agreement is excellent. It should be noted that the density of states, which are determined by theory, must be weighted for comparison with the experimentally obtained XPS spectra. This must be carried out for the individual elements and angular momentum states. These *a priori* unknown values for the solid state, valence band cross sections are a further important result of this study.

Authors
S. Thiess (a), T-L. Lee (a), F. Bottin (b), J. Zegenhagen (a).
(a) ESRF
(b) CEA/DIF, Bruyeres-le-Chatel (France)

Strain Induced Changes in the Magnetic Phase Diagram of EuSe/PbSeTe Multilayers

Magnetic semiconductors attract a lot of interest for possible future use in spin electronics. Typical examples are Eu chalcogenide semiconductors Eu*X* (*X* = O; S; Se; Te), which are classical Heisenberg magnets due to the direct and indirect nearest (NN) and next nearest (NNN) neighbour exchange interactions between the localised magnetic moments of Eu^{2+} ions (spin 7/2). In the Eu chalcogenides, the pronounced dependence of the nearest and next-nearest neighbour exchange interactions on the interatomic distances strongly affects their magnetic properties. Hence, the biaxial lattice distortions produced in strained multilayer structures also have a major effect on the magnetic properties. EuSe is particularly interesting due to its metamagnetic behaviour caused by the near balance between the ferromagnetic NN exchange interaction J_1 and the antiferromagnetic NNN exchange interaction J_2. As a result, bulk EuSe shows several magnetic phase transitions between different antiferromagnetic, ferrimagnetic, as well as ferromagnetic phases.

We studied the growth and the magnetic properties of multilayers of strained EuSe intercalated with diamagnetic $PbSe_{1-x}Te_x$ spacers. Strained EuSe/$PbSe_{1-x}Te_x$ superlattices (SLs) were grown on top of µm-thick buffer layers in which the ternary composition was varied between x = 0 and 25% to adjust the strain state of the magnetic EuSe layers from -1.1 to +0.2%. In the SLs, the

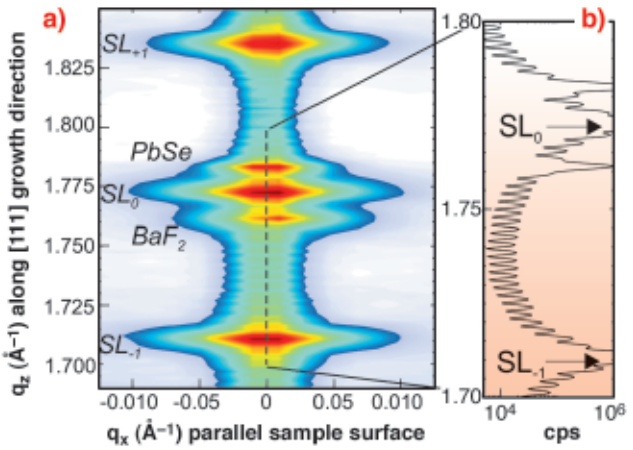

Fig. 101: (a) Anomalous XRD reciprocal space map around the (111) Bragg point of a 30 x [10 ML EuSe / 23 ML PbSe] SL. Clearly visible are the central superlattice peak SL_0, the ±1 satellites, the PbSe buffer, and the BaF_2 substrate peaks. The cross section of the RSM along q_z shown in (b) clearly reveals all 28 thickness fringes corresponding to 30 SL periods.

EuSe layer thickness was kept at 10 or 16 ML, whereas the spacer layer thickness varied from 10 to 100 ML. Thus, the final strain state in the EuSe layer is determined by the lattice constant of the spacer layers, as well as by the thickness ratio between the magnetic and nonmagnetic layers. To determine the structural quality and sharpness of the heterointerfaces, anomalous high resolution X-ray diffraction (XRD) was performed at the beamline ID01. By setting the X-ray wavelength to the Pb-M_V absorption edge around 5 Å, the chemical contrast between the EuSe and $PbSe_{1-x}Te_x$ layers can be drastically enhanced. **Figure 101a** shows the resulting reciprocal space map (RSM) recorded around the (111) reciprocal lattice point of a 30 period 10 ML EuSe/23 ML PbSe SL. Apart from the substrate, the buffer as well as central superlattice peaks, finite thickness fringes arising from the SL stack as a whole are clearly resolved between the ±1 order satellites. This is demonstrated in **Figure 101b** by the q_z cross section extracted from the RSM, where in the enlarged region all (N – 2) = 28 maxima of the interference function of the 30 bilayers are clearly observed. This proves a coherent growth of the crystal lattice throughout the complete multilayer structure. From the detailed analysis of the anomalous XRD, the precise EuSe and $PbSe_{1-x}Te_x$ layer thicknesses were obtained. To determine the in-plane lattice constant $a_{||}$ and strain of the SL structures, we have recorded reciprocal space maps around the (264) asymmetric reflection for all samples. For the strained EuSe/PbSeTe superlattices, pronounced changes of the Néel temperature T_N were observed as a function of the in-plane strain in the layers. For the smallest -1.1% compressive strain, corresponding to $a_{||}$ = 6.122 Å, T_N increases up to 6.5 K whereas for $a_{||}$ = 6.20 Å, *i.e.*, +0:2% tensile strain, a T_N value of only 3.5 K was found. Plotted versus $a_{||}$, the T_N values for the whole series of samples

show a linear behaviour with a slope $\partial T_N / \partial a_{||}$ = 37 K/Å (inset in **Figure 102a**), from which we obtain a linear change of the FM exchange constant J_1. In order to map out the whole magnetic *H-T* phase diagrams of the samples, susceptibility $\chi(T, H)$ measurements at various static magnetic fields *H* of up to 1 T were performed. The observed peaks in the $\chi(T)$ curves, indicative for the phase transitions, are compiled as *H-T* phase diagrams, which are shown in **Figure 102** for the bulk-like EuSe sample (a) and the -1.1% strained EuSe/PbSe SL (b). The *H-T* diagram of the thick EuSe epilayer (**Figure 102a**) shows similar phase boundaries as known for bulk EuSe, but with slightly increased transition temperatures and critical fields. For the -1.1% strained SL sample, the AFM phase in the *H-T* diagram of **Figure 102b** extends to significantly higher temperatures up to T_N = 6.5 K, and depicts higher critical field values for transitions from the AFM II to the FiM and from the FiM to the FM phase, respectively.

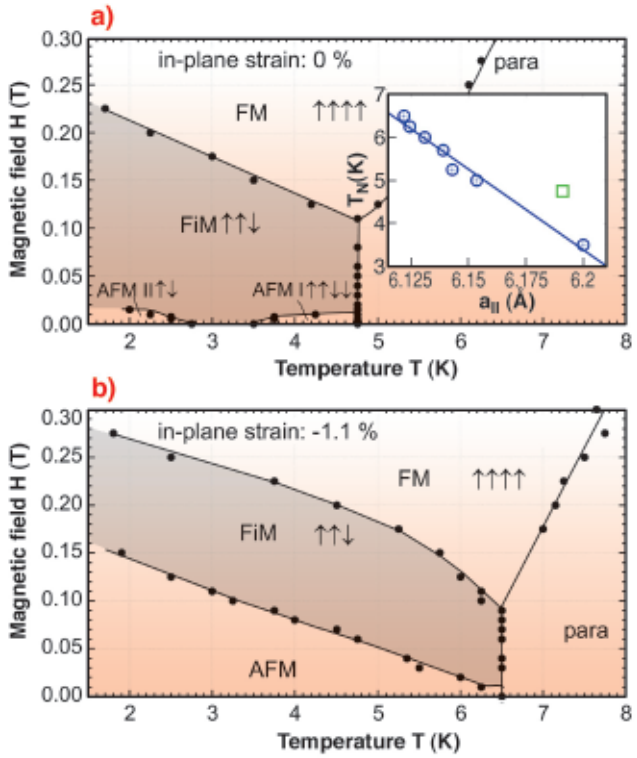

Fig. 102: *H-T* phase diagrams for unstrained (a) and -1.1% strained (b) EuSe derived from susceptibility measurements $\chi(T,H)$ (black circles) at various static magnetic fields. inset: T_N of all strained superlattices (circles) and one bulklike EuSe sample (square) plotted as a function of the in-plane EuSe lattice constant $a_{||}$.

In summary, we have demonstrated that in EuSe/$PbSe_{1-x}Te_x$ multilayers the strain imposed on the magnetic layers influences considerably the magnetic properties of the semiconductor EuSe.

Principal Publication and Authors

R.T. Lechner (a), G. Springholz (a), T.U. Schülli (b), J. Stangl (a), T. Schwarzl (a) and G. Bauer (a), *Phys. Rev. Lett.* **94**, 157201 (2005).

(a) Institut für Halbleiter- und Festkörperphysik, Johannes Kepler Universität, Linz (Austria)

(b) Commissariat à l'Energie Atomique, Grenoble (France)

Surface chemistry

Out-of-plane Distortion of a Molecule at the Interface with a Metal

When a molecule adsorbs at a surface, an obvious questions to ask is whether the internal structure of the adsorbate is changed by the interaction with the substrate. This has been studied in detail for small molecules such as CO. Yet, for the interfaces of large planar aromates with metals, which have recently become a focus of considerable research activity, very little data on the internal structure of the adsorbate is available. Even the adsorption height, *i.e.* the length of the molecule-substrate bond, has only been measured in very few cases [1]. This sparsity of experimental data contrasts with the importance of π-conjugated adsorbates in the fields of organic and molecular

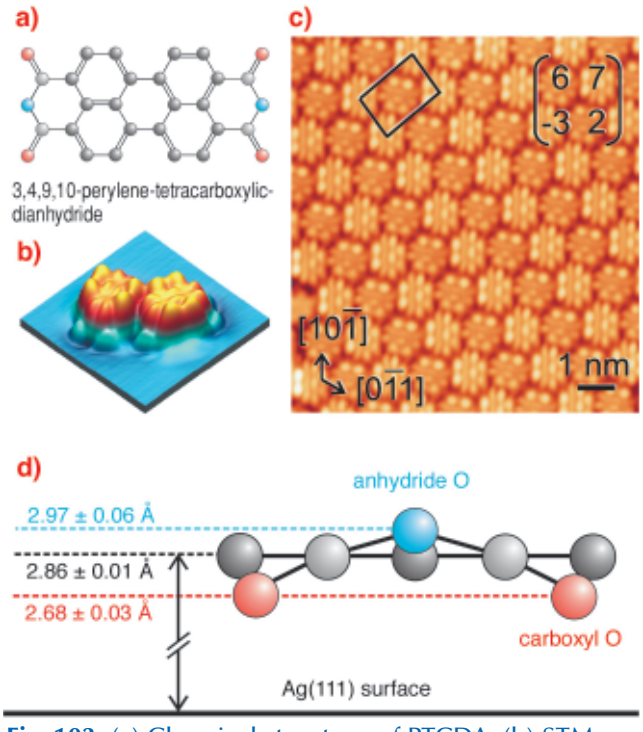

Fig. 103: (a) Chemical structure of PTCDA. (b) STM image of two individual PTCDA molecules on Ag(111). The imaged local density of states resembles the LUMO of the free molecule. (c) STM image of the PTCDA/Ag(111) interface, with superstructure unit cell and matrix, and crystallographic directions of Ag(111). (d) Side view of the molecule, showing the vertical adsorption geometry. The vertical length scale is expanded by a factor 3.

electronics, where characterisation and control of contacts between molecules and metal electrodes pose major challenges for further development.

We have carried out normal incidence X-ray standing wave (NIXSW) experiments on the PTCDA/Ag(111) interface at beamline ID32, making use of the UHV chamber facility. Perylene-tetracarboxylic-dianhydride (PTCDA), **Figure 103a-b**, is a prototypical organic semiconductor. It forms highly-ordered structures on many substrates and is therefore well suited for studies concerning fundamental interface properties. If combined with photoelectron detection, X-ray standing wave techniques unite the structural accuracy of X-ray scattering methods with the chemical sensitivity of photoemission and thus allow the element-specific determination of adsorption heights. For planar molecules containing different atomic species, the technique thus uniquely permits the precise measurement of vertical adsorbate distortions. The well-defined site-specific interaction between PTCDA and Ag(111) (**Figure 103c**) makes this system ideally suited for an exemplary study of substrate-induced distortions in a complex planar adsorbate.

The PTCDA molecule consists of a perylene core with two dianhydride groups. Since the O1s signals of the carboxylic and the anhydride oxygen are chemically shifted by ~ 2.4 eV, the position of three distinct species can be determined (**Figure 103d**). We find an average carbon-silver distance of 2.86 Å. Compared to the interlayer distance in bulk PTCDA (3.22 Å), this is a rather short bond length, indicating a sizable chemical interaction. Moreover, we observe a distortion of the molecule in which carboxylic oxygens bend down, while the anhydride oxygens move up. In fact, the height difference between the two oxygen species can already be inferred qualitatively from the observation that the two corresponding O1s peaks reach their respective maxima at slightly different X-ray energies **(Figure 104a-c)**. Quantitative analysis of the photoelectron yield curves in **Figure 104e-f** yields positions of 2.68 Å and 2.97 Å for $O_{carboxylic}$ and $O_{anhydride}$, respectively.

The observed distortion raises questions concerning the bonding mechanism of PTCDA on Ag(111). From electron spectroscopies and the submolecular scanning tunneling contrast shown in **Figure 103b-c**, we know that the bonding is chemisorptive, and that it occurs mainly on the perylene core of PTCDA. However, it was also clear that the anhydride groups must be important, too, since the bonding of perylene on Ag(111) is considerably weaker [2]. What, then, is the role played by the downward-bent carboxylic oxygen atoms? Does the buckling indicate a bonding via the carboxylic oxygens?

Analysis of the bonding confirms the dominating role of the perylene core, but also indicates the formation of

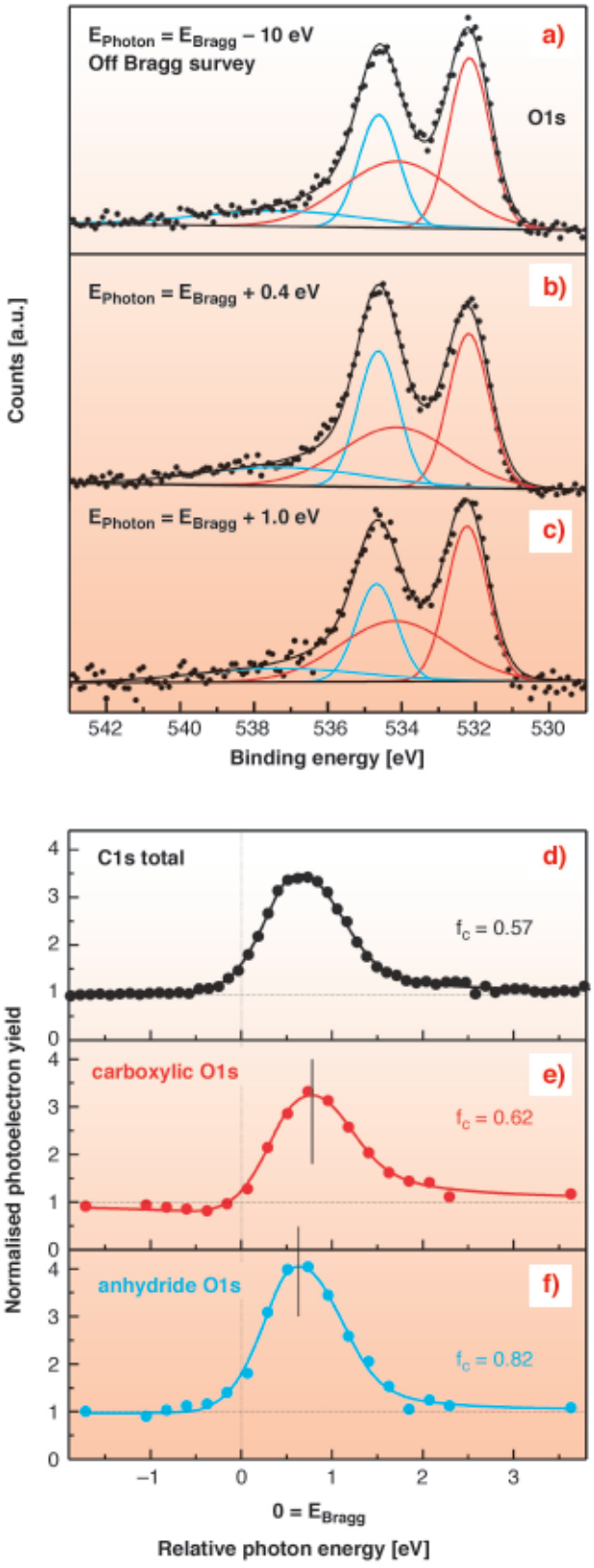

Fig. 104: (a)-(c) O1s spectra recorded at various X-ray energies close to the (111)-Bragg-energy of 2623.2 eV. (d)-(f) Photoelectron yield curves fitted in dynamic X-ray scattering theory, with corresponding coherent fractions.

weak Ag-O bonds involving carboxylic oxygen atoms. This can be understood in analogy to the established theory of CO chemisorption: For PTCDA as for CO, carbon-derived frontier orbitals participate in a strong charge exchange with the metal, and as a result, certain

intramolecular bonds are weakened. In the case of PTCDA/Ag(111) this weakening of intramolecular bonds materialises as a lowering and secondary bonding of the carboxylic oxygen to the Ag(111) surface.

In summary, our NIXSW experiments, together with the lateral structure of PTCDA/Ag(111) known from STM and LEED, yield one of the first comprehensive structural models of a complex adsorbate on a metal surface, comprising the adsorption site as well as internal adsorbate distortions. We are currently extending this work to different bonding situations and substrates, with the aim to generate a more complete structural database for the bonding of this model molecule to transition metal surfaces.

References

[1] L. Kilian *et al. Phys. Rev. B* **66**, 075412/1-9 (2002).
[2] M. Eremtchenko *et al., Nature* **425**, 602 (2003).

Principal Publication and Authors

A. Hauschild (a), K. Karki (b), B.C.C. Cowie (c), M. Rohlfing (b), F.S. Tautz (b), and M. Sokolowski (a), *Phys. Rev. Lett.* **94**, 036106 (2005) and *Phys. Rev. Lett.* **95**, 209602 (2005).
(a) Institut für Physikalische und Theoretische Chemie der Universität Bonn (Germany)
(b) School of Engineering and Science, International University Bremen (Germany)
(c) ESRF

'Live' Observation of Interplay between Structure and Chemical Activity of a Model Catalyst

Surface Science establishes a discipline within physics and chemistry that has evolved over the last 40 years to full maturity. Recently, the emphasis has been shifting away from static structures towards surface processes and dynamics. This is especially important in the light of the role that surface processes play in many practical phenomena and applications. A prominent example of such processes are chemical reactions at surfaces, *i.e.* heterogeneous catalysis.

The traditional surface-science approach to catalysis is to investigate clean, well-ordered, single-crystalline surfaces under highly idealised conditions of low temperatures and low pressures (UHV) and follow the interaction of pure gasses at low pressures with these surfaces. Much is known on regular adsorption structures and the energetics of adsorption, diffusion, reaction and desorption. The philosophy has been to extrapolate this data to high pressures and high temperatures. This requires an unrealistic leap of faith over the so-called *'pressure gap'* of typically 10 orders of magnitude, separating these laboratory experiments and practical conditions. Compared to most UHV-based techniques, X-rays are almost completely unaffected by the presence of the gas phase. Thus, Surface X-Ray Diffraction (SXRD) can resolve the structure of the active catalyst under true operating conditions without any loss of accuracy. Such experiments bring the additional advantage of introducing realistic reaction rates that bring the concentrations of reaction products to a level that can easily be measured on-line, simultaneously with the diffraction measurements. This combination provides a one-to-one correlation between the atomic-scale structure and the catalytic activity of the catalyst surface.

A favorite model reaction system is the oxidation of CO on Pt. Recent high-pressure STM observations on Pt(110) have demonstrated that at a sufficiently high O_2/CO pressure ratio this surface undergoes a structural phase transition, which has a dramatic effect on the reaction mechanism and strongly enhances the reaction rate. The STM data have been interpreted in terms of the formation of a thin platinum oxide film on the Pt(110) surface, on which the CO molecules oxidise through a Mars-Van Krevelen mechanism [1]. Other experiments as well as theory [2] strongly suggest a similar scenario on other metal surfaces.

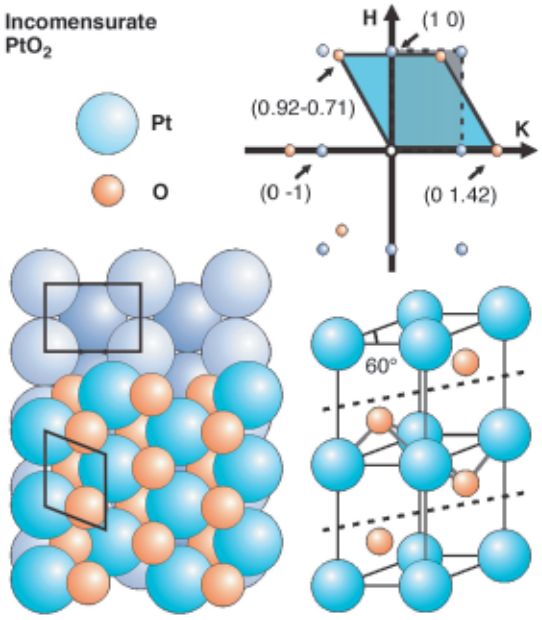

Fig. 105: *Top right:* in-plane reciprocal space map of the Pt(110) surface (blue circles) and the extra diffraction maxima due to the (PtO_2) oxide layer; *bottom:* ball model of bulk terminated and oxide covered Pt(110) (left) and ball model of bulk α-PtO_2 (right).

Here we present the first observation by high-pressure SXRD performed at the **ID03** beamline, of a correlation between the reactivity and the structure of a catalyst surface. The experiments performed during CO oxidation on Pt(110) show that the most active structure is a thin oxide film, namely PtO_2. After preparing the surface under

UHV conditions, the surface was exposed to 500 mbar of O_2. This led to new diffraction peaks at non-integer H and K positions in reciprocal space, forming a regular, slightly distorted hexagonal pattern. The unit mesh of this Pt layer was very close to that of α-PtO_2, suggesting that the overlayer was a distorted PtO_2 layer, azimuthally aligned with the substrate, and oriented with its c-axis along the surface normal (**Figure 105**). The oxide crystal truncation rods supported this interpretation and showed that the oxide was only 2 to 3 monolayers thick.

When exposed to CO, the oxide is reduced and we recover a metallic (CO covered) surface. In mixtures of CO and O_2, the surface can switch between the oxide and the bulk-terminated metallic form.

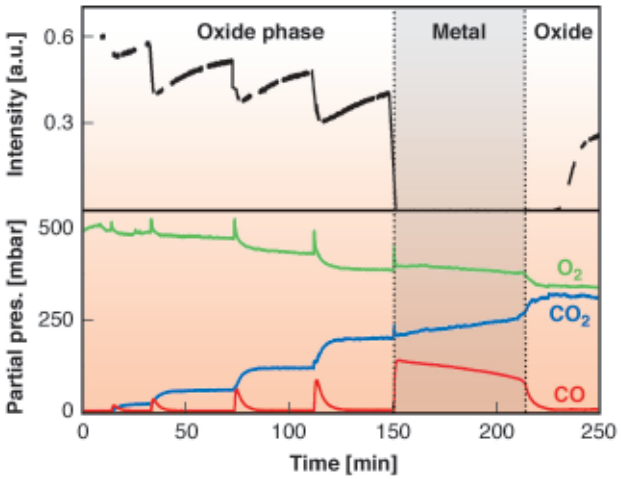

Fig. 106: Simultaneously measured X-ray diffraction intensity from the PtO_2 oxide (top panel) and partial pressures of CO, O_2, and CO_2 (bottom panel). Separate CO pulses were admitted to the reactor, which was initially filled with 500 mbar of O_2 at a temperature of 625 K.

The full power of the method becomes apparent when we combine the diffraction experiment with simultaneous measurements of the CO oxidation reactivity (**Figure 106**). Starting with the α-PtO_2 surface in 500 mbar of O_2, we admitted pulses of pure CO. The CO started reacting to CO_2 as it entered the chamber. From the increase in the CO_2 pressure, the typical turnover number can be estimated to be 3 x 10^3 molecules/site/s at 625 K in 80 mbar CO and 500 mbar O_2.

The fifth CO pulse, at t = 150 min, was so large that the oxide layer was reduced completely: the diffracted intensity from the oxide layer dropped to zero and the surface reverted to the metallic state. Simultaneously, a strong decrease was observed in the reactivity, as well as a significant change in the reaction kinetics, *i.e.* the reaction mechanism.

The combined measurements of surface structure and reaction dynamics explicitly demonstrate that a surface oxide is formed on Pt(110) that, contrary to traditional 'wisdom', exhibits a significantly higher reaction rate than the original metallic surface.

Our observations show that *in situ* measurements under actual reaction conditions are an absolute necessity for a meaningful investigation of the complex behaviour of model catalysts.

The potential of high pressure *in situ* experiments is underlined by the attention and strong support they are presently receiving, for example within the ESRF (refurbishment of ID03) and within the European community (NanO2 project).

References

[1] B.L.M. Hendriksen *et al*, *Phys. Rev. Lett.* **89**, 046101 (2002)
[2] K. Reuter, M. Scheffler, *Phys. Rev. Lett.* **90**, 046103 (2003).

Principal publication and Authors

M.D. Ackermann (a,b), T.M. Pedersen (c), B.L.M. Hendriksen (b), O. Robach (d), S.C. Bobaru (b), I. Popa (a), C. Quiros (e), H. Kim (a), B. Hammer (c), S. Ferrer (f), J.W.M. Frenken (b), *Phys. Rev. Lett.* **95**, 255505 (2005).
(a) ESRF
(b) Kamerlingh Onnes Laboratory, Leiden University (The Netherlands)
(c) Interdisciplinary Nanoscience Center (iNANO) and Department of Physics and Astronomy, University of Aarhus (Denmark)
(d) CEA-Grenoble DRFMC / SI3M / PCM17 (France)
(e) Depto. de Física, Faculdad de Ciencias, Universidad de Oviedo (Spain)
(f) CELLS - ALBA, Universita Autònoma de Barcelona (Spain)

ESRF

Highlights 2005

X-ray Absoption and Magnetic Scattering

Introduction

As in past years, the science produced in the general area of X-ray absorption and magnetic scattering covers a very wide range of subjects. The growing trends are the combination of techniques, the extension of existing methods to new applications and the development of new X-ray methods. For example, the X-ray Detected Magnetic Resonance (XDMR) article – (Goulon *et al.*, page 93).

There are also examples of measurements on the femtosecond time scale using the core-hole clock method (Braicovich *et al*., page 90) and on femtometre length scale in magnetostriction measurements (Pettifer *et al.,* page 98). Magnetic circular dichroism methods have been used as an indirect probe to study quantum diffusion (Ohresser *et al.,* page 91) and coherent diffraction has been utilised to study charge density wave dislocations (Le Bolloch *et al.* page 96). Many of the studies in the following pages push the limits of methods utilising high pressure, high magnetic fields, high and low temperature with absorption or scattering techniques to expand our knowledge in many fields (Acet *et al*. page 99, Mannix *et al.* page 86, Poloni *et al.* page 87, Wilkins *et al*. page 97). More will surely be forthcoming in the near future with facilities like the 10T magnet reaching its full potential on ID20 and the further exploitation of the XDMR technique on ID12. The impact of this later work could easily be very wide and some experiments have also been made in this general direction in the soft X-ray range [1].

Growing trends also include the use of novel *in situ* preparation techniques, an example of which is the *in situ* plasma treatment of samples (Farle *et al.,* page 94). In addition, the combination of many spectroscopic methods to address a single problem is becoming increasingly important, particularly in chemistry, as shown by the study on "metal organic frameworks" (Prestipino *et al.,* page 89). Also X-ray absorption studies have been used to address difficult biological problems such as the oxidation state of copper in complexes (D'Angelo *et al.,* page 97).

It should also be mentioned that there are many other noteworthy studies which could not be included. For example, work published in the past year has shown that additional information can be extracted by measuring the spin polarisation of emitted electrons. One paper explored the pure Fano effect in ferromagnets with an important theoretical aspect to the understanding of the phenomena [2]. Another study combined X-ray absorption measurements at the NSRRC source in Taiwan and spin

polarised measurements at the ESRF to investigate the problem of orbital liquids by studying the orbital moment and crystal field splitting in $LaTiO_3$ [3]. Again one sees that by being able to measure another experimental observable more information can be gained.

In summary, the research highlights of the past year show an evolution of the research into new and potentially very exciting directions. Old methods are being used for new problems, additional insight is being obtained by the combination of methods and new experimental tools are being developed. These trends are important today and for the future as we will see in future highlights.

N. Brookes

References

[1] Boero *et al. Appl. Phys. Lett.* **87**, 152503 (2005).
[2] Minar *et al. Phys. Rev. Lett.* **95**, 166401 (2005).
[3] Haverkort *et al. Phys. Rev. Lett.* **94**, 056401 (2005).

Unravelling Multipole Order with Resonant X-ray Scattering

Neutron and X-ray scattering techniques are established microscopic tools to reveal magnetic structure. However, the familiar dipole magnetic order of ferromagnets and antiferromagnets is not the only possible order parameter. Higher order geometric constructs, generically known as multipoles, may become the primary order parameter in some instances. A powerful new microscope of both magnetic and multipole order is provided by resonant X-ray scattering (RXS).

We have used RXS to elucidate the hitherto incomprehensible long range order occurring in phase IV of $Ce_{0.7}La_{0.3}B_6$, which condenses out of the paramagnetic phase below T_{IV} = 1.5 K. The results indicate that below T_{IV} a novel state of electronic order parameter segregation exists in which the polarisation of the 4*f* states exhibits octupole multipole order symmetry coexisting with dipole magnetic order of the 5*d* levels [1]. The success of the experiments have hinged crucially on development of a compact 1.0 Kelvin base temperature cryostat at the XMaS beamline of the ESRF [2].

Figure 107a gives the low temperature (1K) RXS polarised peak intensity, as a function of the incident photon energy at the Ce L_2 edge of the (3/2 3/2 3/2) position. The σπ (open circles) response, wherein the outgoing photon experiences a π/2 rotation of its electric field, is characterised by two peaks. The upper coincides with the white-line of the absorption edge (E = 6.167 keV) and is assigned to electric dipole transitions (E1) probing the 5*d* conduction states, while the lower, at 6.160 keV, is associated with electric quadrupole (E2) transitions probing the 4*f* states. For the σσ intensities (solid circles, no change in polarisation), only the E2 RXS peak is

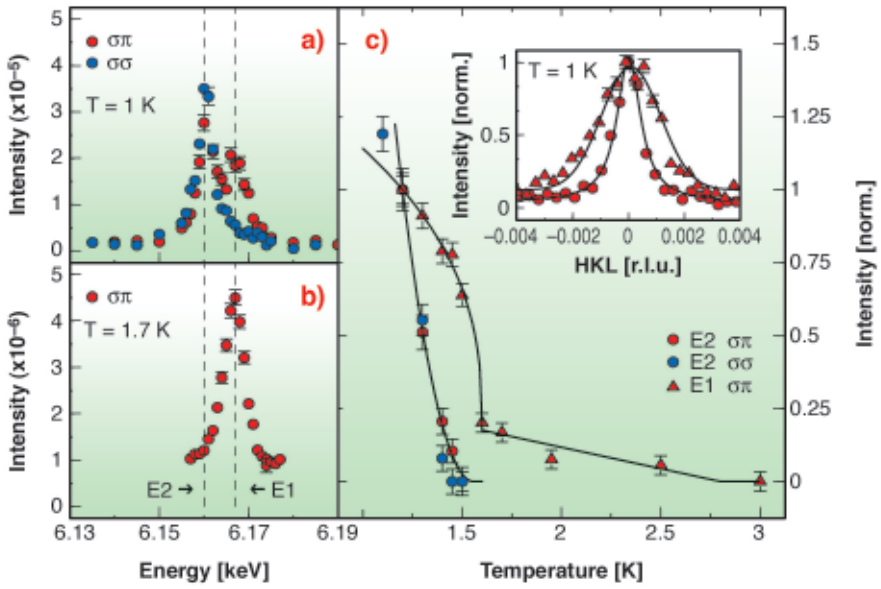

Fig. 107: (a) & (b) The RXS for the σσ (blue circles) and σπ (red circles) scattered polarisations at 1.0 K and 1.7 K, respectively. The dashed line indicates the E1 and E2 energy thresholds. (c) The temperature dependence of the E1 and E2 RXS. The inset compares the widths of longitudinal Q-scans at the E1 and E2 energies.

present. The lack of an E1 σσ component, explored over a broad range of azimuth settings, provides clear evidence of magnetic dipole order in the 5*d* shell.

A dramatic difference is observed in the temperature dependence of the polarised scattered intensities at the E1 and E2 energy thresholds, as demonstrated in **Figure 107c**. The E2 σσ and σπ intensities decrease at the same rapid rate above 1K and disappear at T_{IV} = 1.5 K. However, the E1 σπ intensity decreases only gradually with increasing temperature, suffers a discontinuity at T_{IV}, and continues up to ~ 3 K, *i.e.* well into the nominal paramagnetic phase. The effect is highlighted by comparing the energy response of the σπ intensities below, **Figure 107a**, and above, **Figure 107b**, T_{IV} where only the E1 RXS response remains. Below T_{IV} the thermal evolution of underlying sub-lattice order parameters can be described by $I = |T\text{-}T_{IV}|^{2\beta(5d,4f)}$ where β(5*d*,4*f*) are the power law exponents for the 5*d* and 4*f* responses. The solid lines for $T < T_{IV}$ in the temperature dependence of **Figure 107c** are fits with β(5d) = 0.33, β(4f) = 0.99 and T_{IV} = 1.5 K. The ratio of β coefficients is compatible with 5*d* magnetic and 4*f* octupole order.

The widths of the longitudinal scans taken at E1 and E2, given in insert of **Figure 107c**, are also markedly different. The E2 data is consistent with long-range order, while the E1 data is broad, indicating a mesoscopic order ~ 20-30 nm. The E1 intensity above T_{IV}, taken in conjunction with the radically different widths in the longitudinal scans, gives clear evidence for electronic order parameter segregation at a mesoscopic level in this compound.

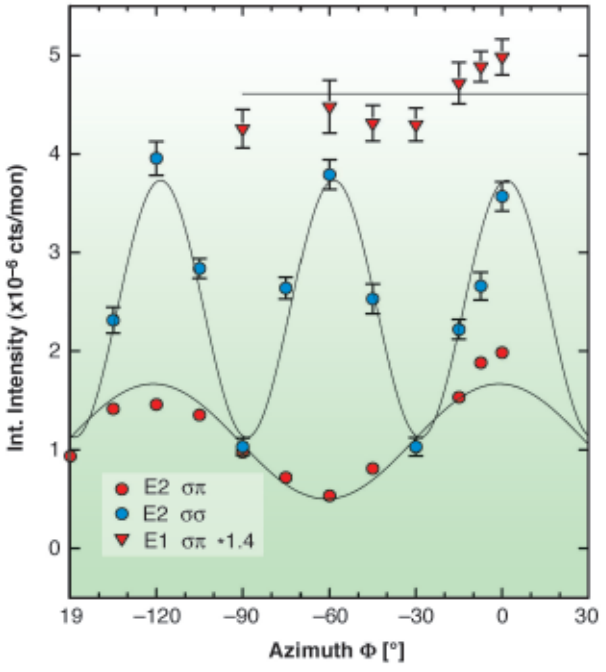

Fig. 108: The Azimuthal dependence of the RXS at the E1 and E2 energy thresholds for σσ (blue circles) and σπ (red circles/triangles) scattered polarisations.

The azimuth dependence of the (3/2 3/2 3/2) Bragg reflections for the E1 [σπ (open triangles)] and E2 [σσ (solid circles) and σπ (open circles)] resonances at 1 K are shown in **Figure 108**. The inferences drawn confirm and extend those made on the basis of **Figure 107**. Namely, the E1 σπ scattered beam is without azimuth dependence indicating 5*d* magnetic order, whilst the E2 σσ and σπ dependencies arise from a scattering amplitude of octupole symmetry. In particular, at the E2 resonance, both σσ and σπ scattering is observed with, however, different azimuth dependencies. The E2 σσ scattering has six-fold symmetry, while the E2 σπ is three-fold. The solid lines are fits which represent scattering amplitudes of octupole symmetry from the Ce 4*f* states. The model reproduces the azimuth dependencies together with their phase offset and relative intensities using only one scaling parameter [1].

The symmetry analysis of the E2 azimuth, Bragg angle and temperature dependencies determined by the RXS technique, brings to light electronic order of octupole symmetry in $Ce_{0.7}La_{0.3}B_6$. This polarisation, which exists uniquely below T_{IV} (**Figure 107**), appears to characterise the enigmatic phase IV. The long-range octupole order occurs in the presence of a pre-existing short-range order of magnetic dipole symmetry. The different thermal and spatial RXS responses from the 4*f* and 5*d* states, provide unique evidence for a novel phase of valence band order-parameter segregation in Phase IV.

References

[1] D. Mannix, Y. Tanaka, D. Carbone, N. Bernhoeft and S. Kunii, *Physical Review Letters* **97**, 117206 (2005).
[2] D. Mannix, P. Thompson, S. Brown, L. Bouchenoire and P. Canfield, *Physica B* **353**, 121 (2004).

Authors

D. Mannix (a), Y. Tanaka (b), D. Carbone (c), N. Bernhoeft (d) and S. Kunii (e).
(a) XMaS Beamline, ESRF
(b) RIKEN Harima Institute, SPRING-8 (Japan)
(c) ESRF
(d) CEA-Granoble (France)
(e) Tohoku University, Sendai (Japan)

Liquid Gallium in Confined Droplets Under High Temperature and High Pressure Conditions

The existence of liquid polymorphism is one of the most interesting and challenging problems in the domain of liquid science to emerge in the last few years. The

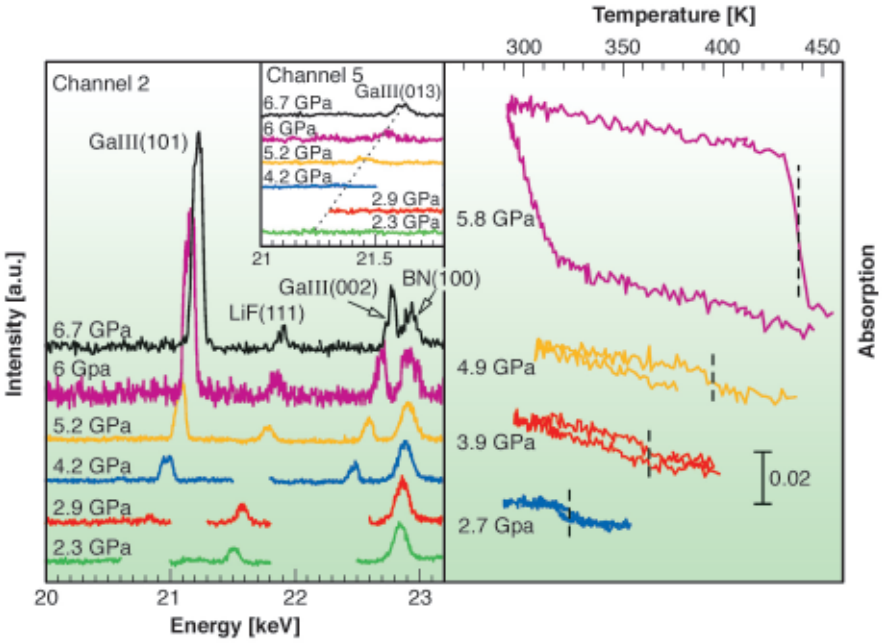

Fig. 109: *Left panel:* X-ray diffraction patterns of Ga emulsion collected at RT on channel 2 of the multichannel collimator of the ESXD setup. The trend of the Ga(III) (013) peak as detected on channel 5 for increasing pressures is shown in the inset. The peak is clearly absent below 2.9 GPa. *Right panel:* temperature scans of the absorption coefficient at constant energy (SEXAD) at various pressures. The melting temperatures are indicated as vertical dashed lines for each loop.

existence of two distinct liquids, with identical chemical composition but different physical properties, is consistent with experimental data and theoretical studies for a variety of systems. Liquid-liquid phase transitions were related to the soft-core interaction potential widely used to describe liquid metals characterised by the coexistence of metallic and covalent character in the bonding (as liquid Sn, Bi, Ga or Ge). Gallium is a good candidate for showing liquid polymorphism. This is because of its ice-type phase diagram, with a negative temperature dependence of the melting point at low pressure, and because it displays an extended polymorphism in the solid phase. Furthermore, this metal is known to show deep undercooling in the liquid phase at ambient pressure [1].

Samples consisting of a dispersion of micrometric gallium droplets (~ 4 % wt) in an inert matrix of mixed epoxy and LiF have been studied by combining Ga *K*-edge X-ray absorption spectroscopy (XAS), single-energy X-ray absorption detection (SEXAD) and energy-scanning X-ray diffraction (ESXD). The distribution of droplets was fully characterised by scanning electron microscopy (SEM). Measurements were performed at **BM29** using a Paris-Edinburgh type large volume press, in a range of pressure and temperature of 0-6.7 GPa and 298-440 K respectively. From ESXD patterns (**Figure 109**, left panel) the appearance of Ga(III) crystalline phase Bragg peaks is clearly observed above 4.2 GPa (channel 2), whereas no Ga(III) (013) peak is observed at 2.3 GPa (channel 5). The intensity increase of Ga Bragg peaks with increasing pressures indicates that the fraction of crystallised droplets increases with pressure. The appearance of Ga(III) in a region of the pressure-temperature phase diagram where Ga(II) is known to be the stable crystalline phase was previously observed by other works by mean of X-ray diffraction [2] and absorption [3]. In the same figure, right panel, temperature scans (SEXAD) recorded at different pressures present discontinuities associated with the solid-liquid phase transition. The increasing discontinuities observed as a function of pressure, starting from the scan at 2.7 GPa, confirms the occurrence of partial crystallisation of the ensemble of droplets.

In **Figure 110** we report the XAS measurements in an energy interval close to the Ga K-edge for two different thermal histories in the P-T phase diagram. By looking at these spectra and at the corresponding difference signals $\Delta\alpha(E)$, the clear change in the absorption in the liquid phase obtained between 1.6 GPa and 0 GPa may indicate that transformations involving microscopic

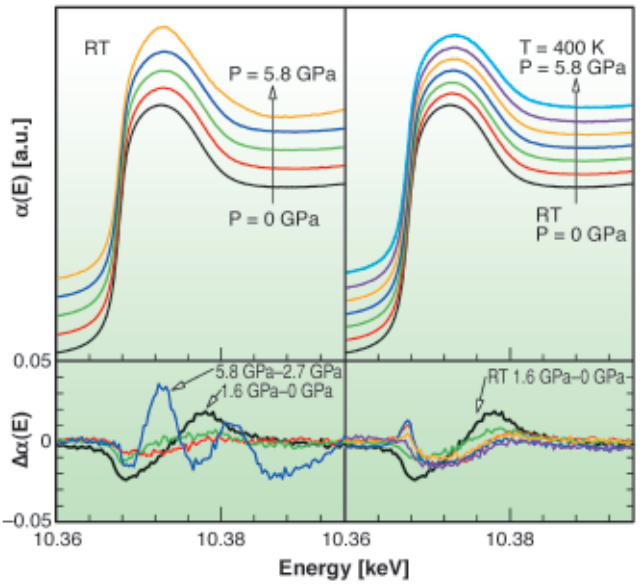

Fig 110: *Upper panels:* XAS Ga *K*-edge spectra as a function of pressure at room temperature (at ambient pressure, at P = 1.6, 1.9, 2.7 and 5.8 GPa), on the left, as a function of pressure and temperature, above the melting curve, on the right. *Lower panels:* difference signal $\Delta\alpha(E)$ of XAS spectra recorded at different pressures and temperatures.

structure and/or electronic states occur. Also, the shape of the difference signal (black curve) is remarkably different from that obtained for the spectra between 5.8 GPa and 2.7 GPa (relative to the solid and the partially crystallized samples, respectively). It is also different from a typical $\Delta\alpha(E)$ curve obtained as a difference between two equilibrium liquid Ga XAS spectra (right panel). This result may infer the existence of a different liquid phase above 1.6 GPa.

In conclusion, considering both ESXD patterns and SEXAD scans we observe that the quantity of crystallised gallium droplets increases as a function of pressure while no sign of crystallisation is observed up to 2.7 GPa, well beyond the melting point line at room temperature. The exciting hypothesis of liquid-liquid phase transitions occurring between 0 and 1.6 GPa and compatible with the result of this study stimulates further detailed investigations on this system.

References

[1] Di Cicco, *Phys. Rev. Lett.* **81**, 2942 (1998).
[2] L. Bosio, *J. Chem. Phys*. **68**, 1222 (1978).
[3] L. Comez *et al., Phys. Rev. B* **65**, 014114 (2002).

Authors

R. Poloni (a), S. De Panfilis (a), A. Di Cicco (b), G. Pratesi (b), E. Principi (b), A. Trapananti (a) and A. Filipponi (c), *Phys. Rev. B* **71**, 184111 (2005).
(a) ESRF
(b) Università di Camerino (Italy)
(c) Università dell'Aquila (Italy)

XAFS and Vibrational Characterisation of the Local Structure of Framework Cu(II) in HKUST-1 Metallorganic Framework

Metal Organic Frameworks (MOFs, also known as "Coordination Polymers") are crystalline nanoporous materials comprised of small metal-containing clusters connected three-dimensionally by poly-functional organic ligands. The ligands act as spacers, creating an open porous three-dimensional structure, with very high pore volume and surface area. This hybrid architecture opens the possibility to design and synthesise a great variety of new porous materials, which are in principle able to display novel functionalities that are potentially exploitable for a number of applications such as gas storage, non linear optics, ion-exchange and catalysis.

In the past MOFs were disavantaged by the lack of control of polymer dimensionality and poor framework stability. More recently, new MOFs have been synthesised, overcoming the above limitations in that they exhibit permanent porosity also after evacuation and template removal.

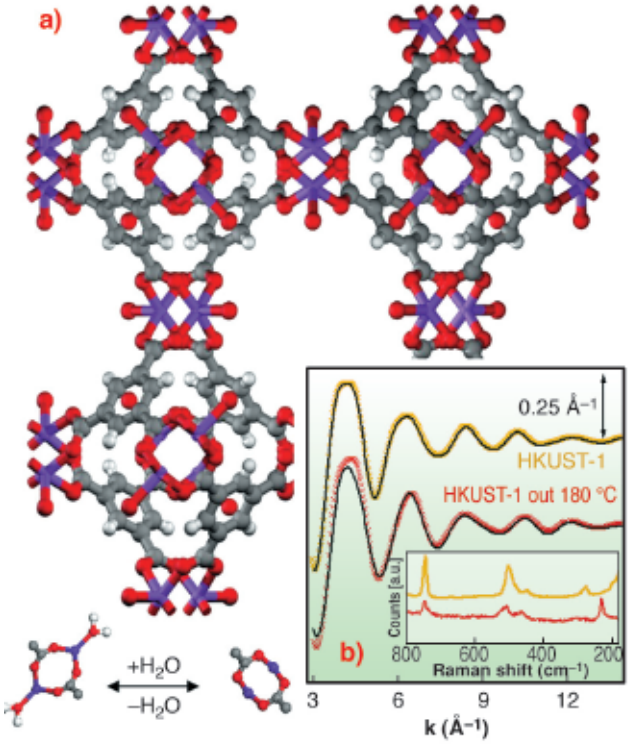

Fig. 111: (a): ball and stick representation of HKUST-1 MOF: O (red), C (gray) H (white) Cu (purple). The lower part represents the dehydration process of the $[Cu_2C_4O_8]$ cage (top view); (b): EXAFS $k\chi(k)$ signal before (yellow) and after (red) dehydration. Black curves represent the corresponding best fits. Inset: Raman spectra, collected with a $\lambda = 514$ nm laser, before (yellow) and after (red) dehydration.

This work deals with HKUST-1 [1], a copper based fcc-MOF characterised by a 3D system of large square-shaped pores (9 Å by 9 Å) (**Figure 111a**). In HKUST-1 Cu^{2+} ions form dimers, where each copper atom is coordinated by four oxygens, coming from the benzene-1,3,5 tricarboxilate linkers ($[Cu_2C_4O_8]$ cage) and one water molecule (bottom part of **Figure 111a**). We have shown that, upon an appropriate activation procedure, the water molecule can be removed from the first coordination shell of Cu^{2+} without loss of crystallinity. EXAFS (**Figure 111b**), collected on **BM29**, indicates that H_2O removal resulted in a shrinking of the $[Cu_2C_4O_8]$ cage due to water desorption, with the copper atoms that sink in the plane of carbossilic oxygens due to a shortening of the first shell Cu-O bond and to a reduction of the Cu-O-C angle, as depicted in **Figure 111a** (bottom part). This structural rearrangement has consequences on the vibrational modes of the framework as evidenced by a Raman study (inset of **Figure 1b**) and on the XANES spectrum **Figure 112**.

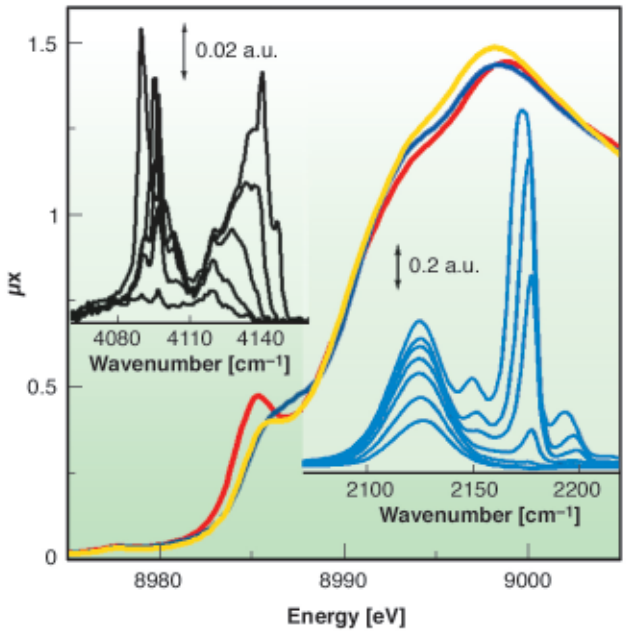

Fig. 112: XANES spectra of HKUST-1 sample collected at 77 K before (yellow) and after (red) dehydration and after CO adsorption (blue). Top and bottom insets report the IR spectra collected at increasing coverage of H_2 (at 20 K) and of CO (at 77 K), respectively.

We have proven that Cu^{2+} species in the dehydrated material are able to coordinate CO at 77 K, as evidenced by XANES (**Figure 112**) and IR data (bottom inset). This is the first direct evidence of the extensive formation of $Cu^{2+}\cdots CO$ adducts inside a porous hosting matrix, compared to the $Cu^{+}\cdots CO$ complexes largely reported in the literature [2]. As already reported for MOF-5 [3], by lowering the temperature down to 20 K also $Cu^{2+}\cdots H_2$ adducts have been observed with IR, as testified by the top inset of **Figure 112**.

References

[1] S.S.Y. Chui, S.M.F. Lo, J.P.H. Charmant, A.G. Orpen, I. D. Williams, *Science* **283** 1148-1150 (1999).

[2] C. Lamberti, G. Turnes Palomino, S. Bordiga, G. Berlier, F. D'Acapito and A. Zecchina, *Angew. Chem. Int. Ed.*, **39**, 2138-2141 (2000).

[3] S. Bordiga, J.G. Vitillo, G. Ricchiardi, L. Regli, D. Cocina, A. Zecchina, B. Arstad, M. Bjørgen, J. Hafizovic, K.P. Lillerud, *J. Phys. Chem. B*, **109**, 18237-18242 (2005).

Principal publication and Authors

C. Prestipino (a), L. Regli (a), J.G. Vitillo (a), F. Bonino (a), A. Damin (a), C. Lamberti (a), A. Zecchina (a), P.L. Solari (b), K.O. Kongshaug (c), S. Bordiga (a), *Chem. Mater.*, **18**, (2006), in press.

(a) NIS centre of excellence University of Turin, and INSTM (Italy)

(b) ESRF (France)

(c) Department of Chemistry, University of Oslo (Norway)

Femtosecond Dynamics in Ferromagnetic Metals

In electronic Resonant Raman Scattering (RRS) the sample is resonantly excited at a core threshold and a photon is emitted bringing the sample to the final state. This process sets a characteristic time scale connected to the intermediate state core-hole lifetime. If there is an evolution of the system during this time scale the effect is seen in the spectral function [1]. Consequently, this approach to study fast processes is called a core-hole clock experiment. The present work is, to our knowledge, the first implementation of the core-hole clock in the study of magnetism. This is done in the ferromagnetic metals (Fe-Co-Ni) using the scattering

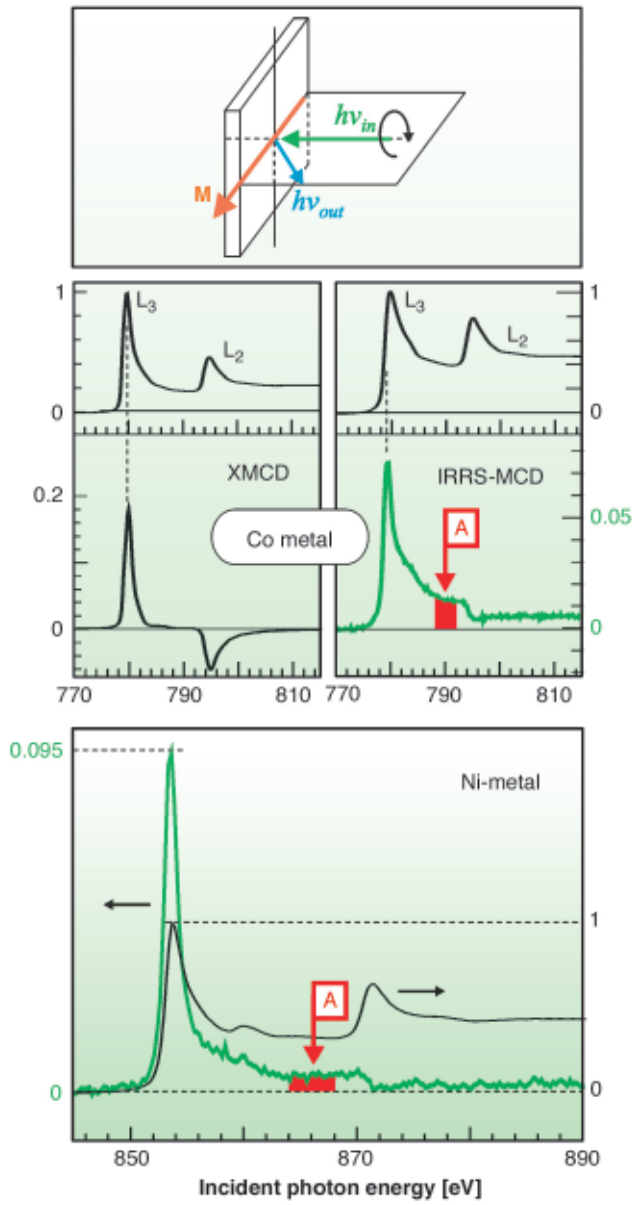

Fig. 113: Upper panel: the experimental geometry. Central panels: comparison for Co metal between the absorption XMCD (at the left) and the IRRS (at the right with the IRRS spectrum in black and dichroism in green). Lower panel: IRRS data for Ni metal.

channel $2p^63d^n + h\nu_{in} \rightarrow 2p^53d^{n+1} \rightarrow 2p^63d^{n+1}3s^1 + h\nu_{out}$, where n is the 3d occupation number in the ground state and $h\nu_{in}$ and $h\nu_{out}$ are the incident and outgoing photon energies (in this case $h\nu_{out}$ is about 100 eV lower than $h\nu_{in}$). We use the so-called Integrated Resonant Raman Scattering (IRRS) [2] where one measures as a function of $h\nu_{in}$ the integral of the scattered intensity in the scattering channel. The measurements were taken at ID08 with a special instrument built for this purpose. The geometry is shown in the upper panel of **Figure 113**. The magnetic circular dichroism (MCD) spectrum is the difference between spectra measured with left and right circularly polarised X-rays. The IRRS spectra show an effect that is absent in ferromagnetic insulators. A magnetic circular dichroism is seen in IRRS spectra also in those regions between L_3 and L_2 and above L_2 where the absorption XMCD gives no signal (see the central panels for Co in **Figure 113** where the red areas show this effect for the IRRS dichroism given in green). This effect is due to the spin dependent screening occurring in the intermediate state [3] so that the core-hole becomes polarised. In order for this to take place, this process requires a non-zero magnetic moment of the system. In the fully relaxed theoretical model of Ref. [3] the dichroism (more exactly the flipping ratio) depends on the local magnetic moment of the excited site once the core-hole is fully screened. The crucial experimental information given here is the trend of this dichroism (flipping ratio) along the sequence Fe-Co-Ni and in particular the observation, shown in the bottom panel of **Figure 113**, that Ni-metal clearly displays this effect. This is important since in a fully relaxed situation we should not have an effect because a full screening of the core-hole in Ni gives a $3d^{10}$ configuration with zero magnetic moment. Thus over the characteristic time scale of the scattering (typically 1-2 femtoseconds) Ni has no time to develop a spin dependent screening of the Fermi gas. More can be seen from **Figure 114** where the histograms give the magnetic moments of the relaxed and unrelaxed sites [3] compared to the flipping ratio of the IRRS-MCD given by red circles. The data are normalised to the case of Fe where a relaxed model accounts for the effect as seen in Auger spectroscopy [3]. The trend shows that Co is somewhere between the fully screened and unscreened situation whereas Ni is basically unrelaxed. Thus Ni is much slower in building up the screening and we attribute this behaviour to the narrow band nature of the Ni 3d holes while the Fe and Co are definitely much more itinerant. In this sense there is a connection between the correlation properties and the magnetic dynamics over short time scales. In conclusion the use of the core-hole clock in soft X-ray resonant scattering reveals a substantially slower dynamics in Ni compared to Fe and Co metal.

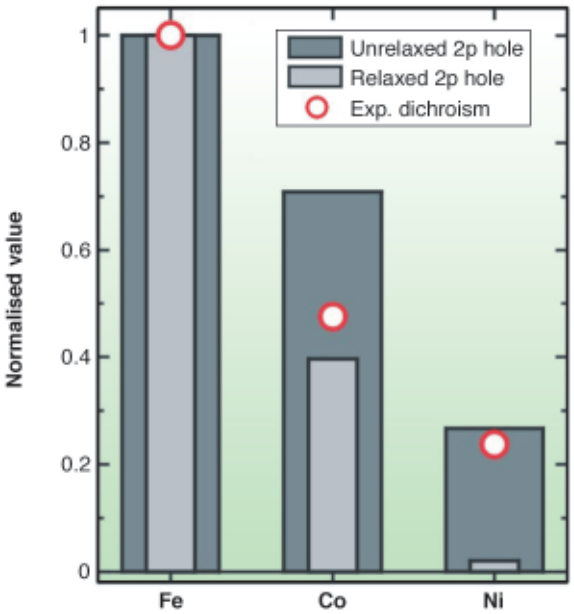

Fig. 114: Comparison between the measured IRRS dichroism (flipping ratio) in the region A (red in **Figure 113**) and the local magnetic moments with relaxed and unrelaxed 2p hole. The data are normalised to the Fe case.

References

[1] P.A. Brühwiler, O. Karis and N. Mårtensson, *Rev. Mod. Phys.* **74**, 703-740 (2002) and references quoted therein.

[2] L. Braicovich *et al., Phys. Rev. Lett.* **90**, 117401 (2003).

[3] A. Chassé *et al.*, *Phys. Rev B* **68**, 214402 (2003) and references quoted therein.

Principal Publication and Authors

L. Braicovich (a), G. Ghiringhelli (a), A. Tagliaferri (a), G. van der Laan (b), E. Annese (c) and N.B. Brookes (d), *Phys. Rev. Lett.* **95**, 267402 (2005).

(a) INFM-CNR, Dipartimento di Fisica, Politecnico di Milano (Italy)

(b) Magnetic Spectroscopy, Daresbury Laboratory, Warrington (UK)

(c) Dip. Fisica, Università di Modena e Reggio Emilia (Italy)

(d) ESRF

Quantum Tunneling Diffusion of Cr Adatoms on Au(111)

A classical particle in a potential well is trapped unless it gains enough energy to overcome the surrounding energy barrier. For adatoms adsorbed on surfaces, common temperature conditions generate lattice vibrations allowing the adatom surface diffusion. Conversely, at very low temperature, the particle motion is blocked. However, quantum mechanics allows a

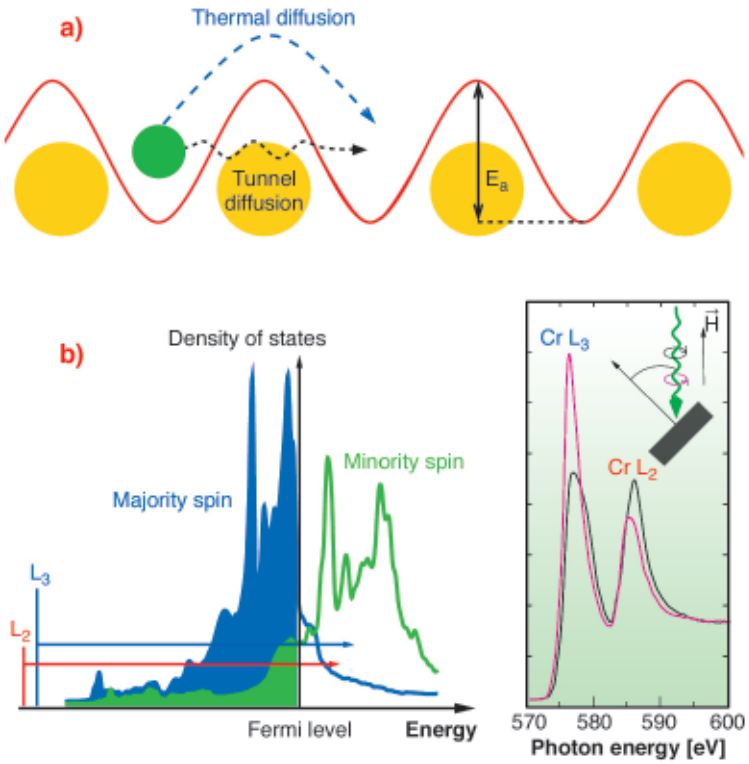

Fig. 115: (a) Adatom in a surface potential well. The particle may overcome the energy barrier either by thermal activation or by quantum tunneling. E_a is the energy barrier. (b) Electronic calculations of the density of states for a Cr monolayer on Au(111); Cr $L_{2,3}$ core-level transitions are represented (arrows) and the XAS absorption spectra are displayed for left and right circularly polarised light. A magnetic field parallel to the photon beam is applied. The XMCD signal is the difference of the two spectra.

particle to tunnel through a potential barrier (**Figure 115a**), provided its *de Broglie* wavelength is comparable to the barrier width [1]. Quantum tunneling has so far been observed for light particles such as alpha emitters or surface hydrogen adatoms [2]. For heavier particles, with a smaller *de Broglie* wavelength, drastic conditions are necessary to observe quantum tunneling. Adatom clustering at low temperature may fulfil these requirements, provided the energy activation barrier, the barrier width (adsorption site separation) and the adatom mass are chosen accordingly.

Upon clustering, charge transfer and hybridisation lead to distinct changes in the electronic structure which can be determined using X-ray Absorption Spectroscopy (XAS) or better, X-ray Magnetic Circular Dichroism (XMCD), which measures the difference between two absorption spectra recorded with opposite X-ray helicities. XMCD involves selection rule governed transitions from core levels to unoccupied states just above the Fermi level (**Figure 115b**), which are highly sensitive to the local atomic coordination. Whereas isolated *3d* adatoms exhibit multiplet peaks in the $L_{2,3}$ XMCD spectrum, coordinated atoms exhibit broader band structure features [3].

Deposition of a small amount of Cr (1% of a monolayer) on Au(111) at 10 K leads to a collection of isolated adatoms, giving a specific XMCD spectrum, different from that obtained for a Cr monolayer (**Figure 116a**). Upon diffusion, the adatoms aggregate mainly into dimers and trimers (as shown by Monte Carlo simulations) within a timescale of hours. These clusters already present an XMCD spectrum shape identical to the one obtained for a monolayer. The XMCD spectrum therefore evolves with time, and it can be decomposed in two components: atomic and "bulk-like" (**Figure 116b**). Hence, one can deduce the proportion of isolated adatoms as a function

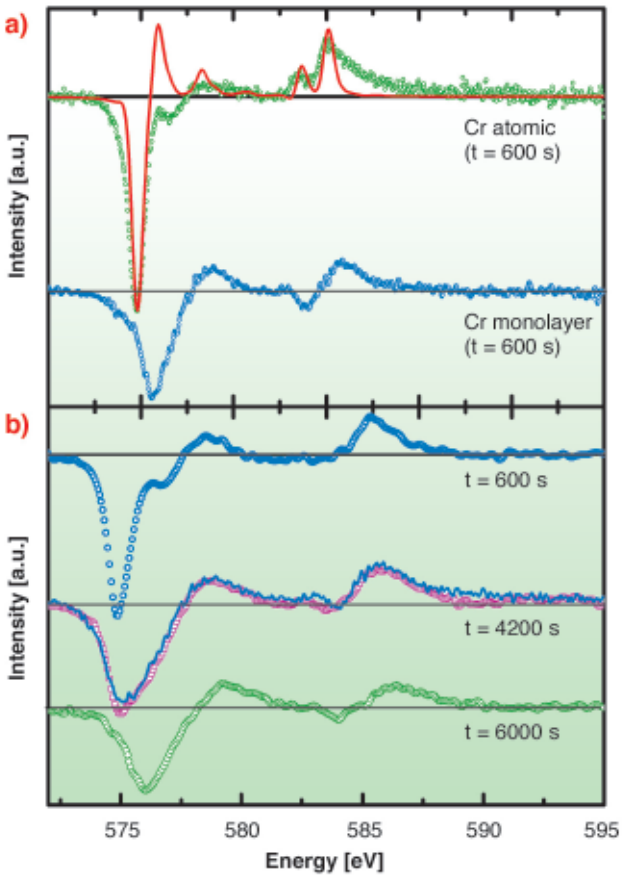

Fig. 116: (a) Cr $L_{2,3}$ XMCD spectrum for a collection of isolated atoms (top) and for a full monolayer. The red curve is a multiplet calculation for a d^5 electronic configuration. (b) Time evolution of the XMCD spectrum for a collection of initially isolated atoms.

of time, and compare it to a Monte Carlo simulated evolution. The scaling between the number of Monte Carlo steps and the experimental evolution, allows us to determine the diffusion jump rate. Above 40 K, the jump rate increases dramatically and is no longer measurable. For this system, 40 K is the onset of the thermally activated diffusion. We determine an energy barrier of ~ 100 meV, in excellent agreement with our theoretical calculation. Below 40 K, the tunnel jump rate is orders of magnitude larger than the one expected from an Arrhenius law for thermal diffusion and it is nearly temperature independent. This is a hallmark of quantum tunneling.

In summary, the sensitivity of XMCD to the atomic coordination was used to study low-temperature diffusion of Cr adatoms on Au(111). The time evolution analysis of the XMCD spectra *via* Monte Carlo simulations allowed the determination of surface diffusion jump rates. For $T < 40$ K, where the classical description of thermal diffusion forbids adatom motion, the diffusion of Cr atoms is observed over a timescale of several hours. This extremely fast diffusion, nearly temperature independent, is attributed to quantum tunneling.

These measurements were possible thanks to the fast data collection at ESRF (**ID08** beamline): an XMCD spectrum is obtained within 5 minutes, even for such low amounts of material.

In memory of Kenneth Larsson

References

[1] See *e.g.* E. Merzbacher, *Quantum Mechanics* (Wiley 1998)
[2] A. Yazdani, *Nature* **409**, 471 (2001)
[3] Gambardella *et al.*, *Phys. Rev. Lett.* **88**, 047202 (2002).

Principal Publication and Authors

P. Ohresser (a), H. Bulou (b), S.S. Dhesi (c), C. Boeglin (b), B. Lazarovits (d), E. Gaudry (e), I. Chado (f), J. Faerber (b), F. Scheurer (b), *Phys. Rev. Lett.* **95**, 195901 (2005) .
(a) Synchrotron SOLEIL, Gif-sur-Yvette (France)
(b) IPCMS – UMR7504, Strasbourg (France)
(c) Diamond Light Source (United Kingdom)
(d) Center for Computational Materials Science, Vienna (Austria)
(e) LMCP, Paris (France)
(f) Physikalisches Institut, Würzburg (Germany)

X-ray Detected Magnetic Resonance at a K-edge: First Evidence of Forced Precession of Polarised Orbital Components

X-ray Detected Magnetic Resonance (XDMR) is a novel spectroscopic method in which X-ray Magnetic Circular Dichroism (XMCD) is used to probe the resonant precession of the magnetisation caused by a strong microwave pump field h_1 orthogonal to the static bias field H_0. For the first time, XDMR was measured on exciting the Fe K-edge in a high quality thin film of Yttrium Iron Garnet (YIG: 8.9 μm thick) grown by liquid phase epitaxy along the (111) direction of a Gadolinium Gallium Garnet (GGG) substrate [1]. This experiment carried out on beamline ID12 was performed in the longitudinal geometry (see **Figure 117**), *i.e.* the wavevector $k_X(\|)$ of the incident, circularly-polarised X-rays being parallel to the static bias field H_0. The XDMR signal recorded in the X-ray fluorescence excitation mode was then proportional to the microwave power that was amplitude modulated at F_m = 35.5042 kHz. To minimize radiation damping effects, the microwave frequency (9445.0 MHz) was slightly offset with respect to the resonance of the overcoupled rectangular TE_{102} X-band cavity. Given the narrow FMR linewidth of the YIG film: ΔH_{fwhm} (β_N = 30°) = 3.64 Oe, there is no doubt that, with an incident microwave power of 30 dBm, resonant pumping occurred in a non-linear foldover regime [2] characterised by a critical precession angle which was estimated to be *ca.* θ_{crit} = 6.8° under the conditions of the XDMR experiment.

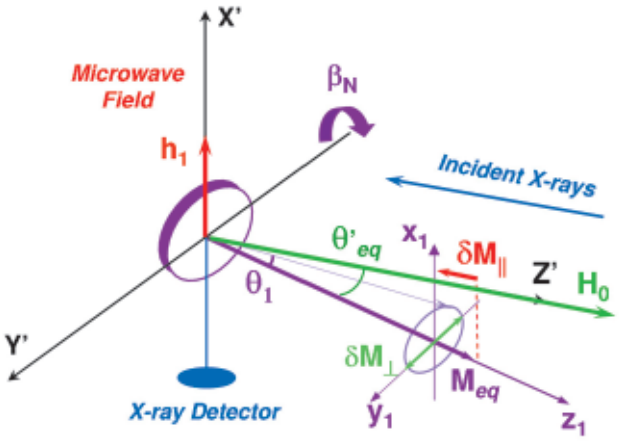

Fig. 117: XDMR in longitudinal geometry.

The resonance field was precisely scanned down to the onset of the critical foldover jump found at H_0 = 3980.6 Oe whereas the energy of the incident X-rays was tuned to 7113.74 eV, *i.e.* to the maximum of the XMCD signal in the pre-peak of the XANES spectrum. Since the ESRF

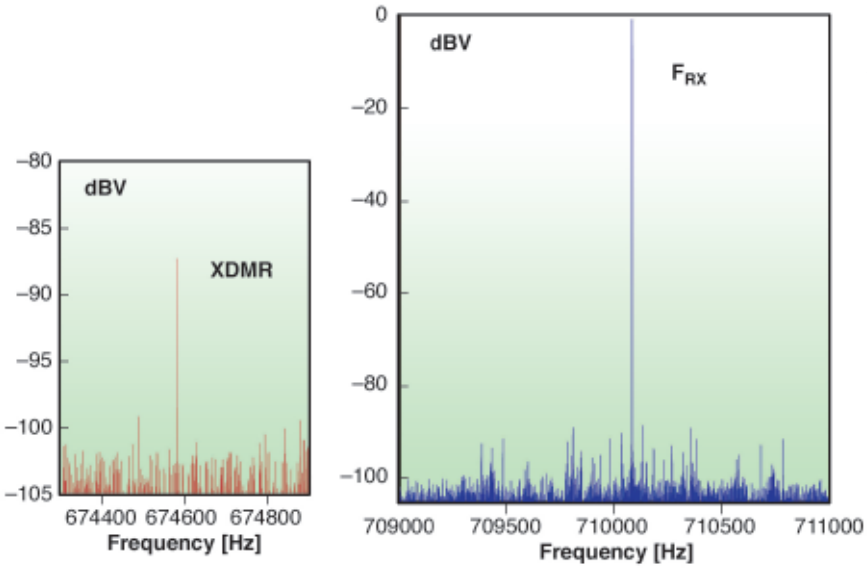

Fig. 118: XDMR signal as low-frequency side-band of F_{RX}.

storage ring was run in the 2*1/3 filling mode, the incident X-rays were modulated at the macrobunch repetition frequency F_{RX} = 710.084 kHz. The XDMR signal displayed in **Figure 118** is one of the modulation side-bands expected at 710.084 ± 35.5042 kHz whereas the signal at F_{RX} was used only for data renormalisation. The magnitude of the XDMR signal is peaking *ca.* 20 dBV above the noise floor. The real and imaginary parts of the spectrum confirmed the expected inversion of the XDMR signal when the helicity of the incident X-ray beam was changed from left to right. After proper renormalisation, the small differential cross-section: $\Delta\sigma_{XDMR} \approx 1.34 \cdot 10^{-5}$ would yield a critical precession angle of $\theta_{10} \approx 3.5°$ for the moments precessing at the Fe sites.

Since the effective operator accounting for XMCD at the Fe K-edge can be written [3]: $\partial/\partial E\ [<L_z>_{4p} + \varepsilon <L_z>_{3d}]$, the measured Fe K-edge XDMR signal thus produces clear evidence of the forced precession of orbital polarisation components.

Let us emphasise that the precession angle θ_{10} deduced from XDMR for these orbital components is only one half of the critical precession angle θ_{crit} of the effective spin moment. Since the electron gyromagnetic ratios for orbital and spin moments are precisely in a 1:2 ratio, our XDMR result proves that, in YIG, there is *no* dynamical quenching of the magnetic orbital polarisation components: spin-orbit coupling dominates orbit-lattice interactions in Kittel's picture of FMR.

References

[1] J. Goulon, A. Rogalev, F. Wilhelm, N. Jaoen, C. Goulon-Ginet, G. Goujon, J. Ben Youssef and M.V. Indenbom, *JETP Letters*, **82**, 791-796 (2005).

[2] A.G. Gurevich and G.A. Melkov: *Magnetization Oscillations and Waves*, CRC Press Boca Raton, Inc. (1996).

[3] H. Ebert, V. Popescu and D. Ahlers, *Phys. Rev. B* **60**, 7156 (1999).

Principal Publication and Authors

J. Goulon (a), A. Rogalev (a), F. Wilhelm (a), N. Jaouen (a), C. Goulon-Ginet (a), G. Goujon (a), J. Ben Youssef (b), M.V. Indenbom (b) *JETP Letters*, **82**, 791-796 (2005).

(a) ESRF

(b) Laboratoire de Magnètisme de Bretagne, CNRS FRE 2697, UFR Sciences et Techniques, Brest (France)

Plasma-assisted Magnetic Hardening of FePt Nanoparticles Investigated by X-ray Absorption

Fe_xPt_{1-x} nanoparticles are currently the subject of intense research activity due to their interesting magnetic properties [1]. Chemically-disordered $Fe_{50}Pt_{50}$ shows a high-temperature transformation to the ordered $L1_0$ phase which is associated with an enhancement of the orbital magnetic moment and a decrease of the mean distance between nearest-neighbour atoms by 2%. Therefore, on the one hand the X-ray absorption near edge structure (XANES) was analysed at the Pt $L_{3,2}$ edges to monitor structural changes, and on the other hand the X-ray magnetic circular dichroism (XMCD) was measured both at the Fe and Pt $L_{3,2}$ edges in order to investigate the orbital magnetism after thermal treatment.

The wet-chemically synthesised $Fe_{50}Pt_{50}$ particles with a mean diameter of 6 nm were self-assembled on a naturally oxidised Si substrate (total coverage: about 10%) and exposed to a soft hydrogen plasma (5 Pa for 30 min) that removes the Fe oxides and the organic ligands surrounding the particles in the as-prepared

state (**Figure 119**). Subsequently one of the samples was annealed at 600°C *in situ*. Scanning electron microscopy (SEM) images confirm the mean size, the centre-to-centre distance of 9 nm and a small agglomeration after annealing.

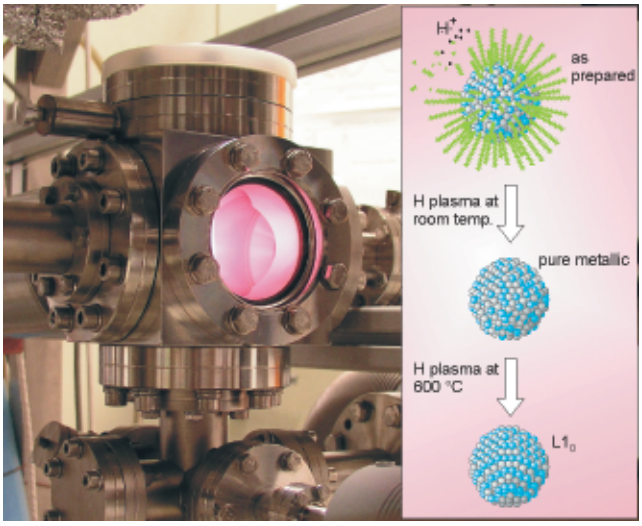

Fig. 119: Plasma chamber with ignited plasma. The inset shows schematically the removal of the organic ligands surrounding the wet-chemically synthesised Fe_xPt_{1-x}.

For measurements at the Pt $L_{3,2}$ edges, the UHV plasma chamber was attached to the experimental chamber at beamline **ID12** and the Fe oxides were removed prior to the experiments. In order to be able to record high quality XANES and XMCD spectra at the Pt $L_{3,2}$ edges on samples with such a low concentration of Pt, we have used a 35-channel silicon drift diode detector developed at the ID12 beamline in collaboration with Eurisys-Mesures (now Canberra Eurisys) [2]. During these experiments the counting rates in Pt L_α lines were *ca.* $2 \cdot 10^4$ cps per channel with a peaking time of 0.5 µs. Even though the X-ray beam was impinging on the sample with an angle of incidence of *ca.* 15°, the beam footprint was quite small: 300x30 µm^2. This is because we had to reduce the intensity of the monochromatic X-rays in order to avoid the saturation of the detector by the intense soft X-ray fluorescence signal from the substrates. The typical energy resolution of the emission spectra measured with one single SDD channel (data acquisition time: 60s; peaking time: 0.5 µs) was of the order of 132 eV for the unresolved Si $K_{\alpha\beta}$, 159 eV for the Fe K_α line and 202 eV for the Pt $L_{\alpha 1}$ line. Excellent performances of this detector allowed us to record not only the XANES spectra, but also the XMCD signals at

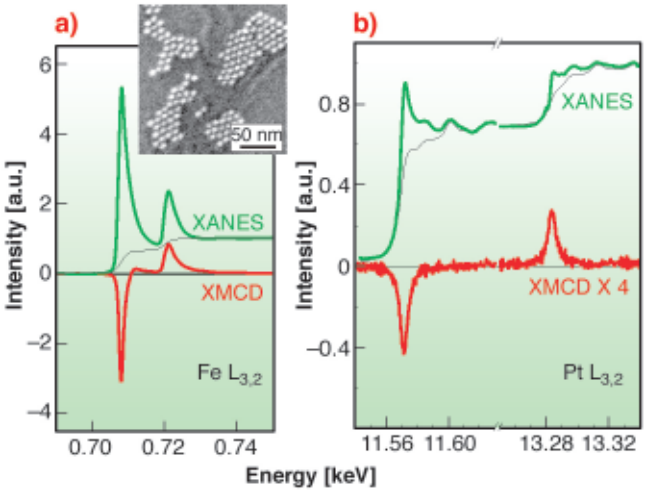

Fig. 120: XANES (green lines) and XMCD (red lines) of pure metallic $Fe_{50}Pt_{50}$ nanoparticles measured at the Fe and Pt $L_{3,2}$ edges. The dichroism spectra in (b) are scaled up by a factor of 4. The inset shows a SEM image of the sample.

the Pt $L_{3,2}$ edges in a weak magnetic field of ± 0.6 T (**Figure 120b**). The quality of the experimental data was high enough to derive the local spin and orbital magnetic moments of the Pt 5d states using the XMCD sum rules. The results of this analysis together with the analysis of the spectra recorded at BESSY, Germany, on the same samples at the Fe $L_{3,2}$ edges are given in **Table 2**.

The observed trends in μ_l / μ_S^{eff} indicate a non-cubic environment after annealing as expected for the $L1_0$ structure.

Additionally, we found that the period of the first EXAFS oscillations at the Pt $L_{3,2}$ edges decreased by (2 ± 1)% after annealing indicating a reduction of the mean distance between the atoms as known for the disorder-order transformation in the corresponding bulk material.

In conclusion, we demonstrated a method to prepare pure metallic $Fe_{50}Pt_{50}$ nanoparticles from wet-chemically synthesised particles. Evidence for the formation of the $L1_0$ phase is provided both by structural changes found in the oscillations of the XANES and by the changes in the magnetic moments.

Acknowledgement:
This work was supported by the BMBF (05 ES3XBA/5), the DFG (SFB445), the EU (MRTN-CT-2004-005566, SyntOrbMag), and the ESRF.

	Fe			Pt		
	μ_S^{eff} [μ_B]	μ_l [μ_B]	μ_l / μ_S^{eff}	μ_S^{eff} / μ_B	μ_l / μ_B	μ_l / μ_S^{eff}
disordered	2.48(7)	0.056(10)	2.2%	0.41(1)	0.054(2)	13%
annealed	2.59(8)	0.240(18)	9.3%	0.41(1)	0.042(2)	10%

Table 2: Local spin and orbital magnetic moments for Fe and Pt.

References

[1] C. Antoniak, J. Lindner, and M. Farle, *Europhys. Lett.* **70**, 205 (2005).

[2] J. Goulon, A. Rogalev, G. Goujon et. al., *J. Synch. Rad*. **12**, 57 (2005).

Principal Publication and Authors

C. Antoniak (a), J. Lindner (a), M. Spasova (a), D. Sudfeld (a), M. Acet (a), M. Farle (a), K. Fauth (b,c), U. Wiedwald (d), H.-G. Boyen (d), P. Ziemann (d), F. Wilhelm (e), A. Rogalev (e), and S. Sun (f), *submitted*.

(a) Fachbereich Physik, Universität Duisburg-Essen (Germany)

(b) MPI für Metallforschung, Stuttgart (Germany)

(c) Experimentelle Physik IV, Universität Würzburg (Germany)

(d) Abteilung Festkörperphysik, Universität Ulm (Germany)

(e) ESRF

(f) Department of Chemistry, Brown University, Providence, RI (USA)

Evidence of Topological Defects in an Electronic Crystal

Electron confinement, for example along chains of atoms, give rise to original phenomena. These effects are observed in charge-density wave (CDW) materials. Upon cooling, these materials exhibit a modulation of the electron density along the chains and become insulating. Moreover, under a large enough electric field, a strong decrease of the resistivity is observed. This phenomena, still under debate, is generally interpreted as being caused by a collective "sliding" of the CDW as a whole [1].

This CDW can be considered as an electronic crystal, ordered in the three directions of space. In particular, its wave number along the chain is equal to twice the momentum of the fastest electrons of the system: $2k_F$. Like a crystal, this electronic system is elastic and can exhibit dislocations. Predicted theoretically for 25 years [2], such topological defects are thought to play an essential role in the behaviour of the CDW under electric field. In a similar way dislocations in metals explain metal plasticity.

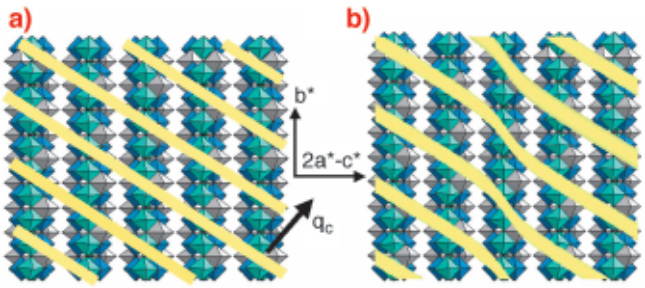

Fig. 121: Schematic representation of the Blue bronze CDW in the (2a*-c* ; b*) plane in a) a defect-free crystal and b) a crystal with a screw-like dislocation line running along b* in the middle of the figure. Only Mo octahedra are represented. Yellow lines represent the constant phase wave front of the CDW. Note that this dislocation does not introduce any dilatation or compression of the CDW along b*.

The direct observation of CDW dislocations has never been achieved. Our recent experiment on the ID20 beamline has shown that coherent X-ray diffraction measurements are very sensitive to such topological defects. In the model system called "blue bronze" (a molybdenium oxide of formula $K_{0.3}MoO_3$), the structure of a CDW dislocation imbedded in the bulk has been studied. The interference fringes of the **Figure 122b** are interpreted as originating from the presence of a screw dislocation running along the chain axis. Since the one-dimensional CDW wave vector q_c is not parallel to the chains axis, this topological defect corresponds to a mixed dislocation (between screw and edge), running along the chains direction (see in **Figure 121b**). Remarkably, this dislocation introduces no energy expensive compression or dilatation of the CDW along the chains, but involves only shears: due to the charged character of the CDW, this is expected to cost less energy than an edge dislocation.

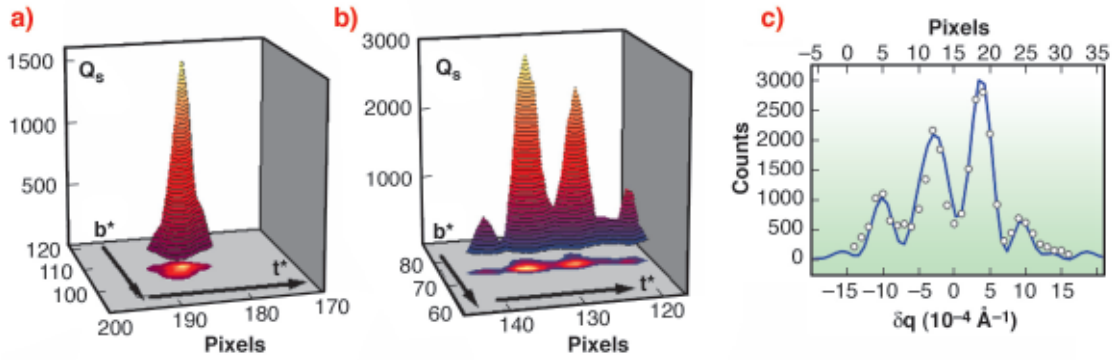

Fig. 122: 2D diffraction patterns of the $Q_s = (5,-1,-3)+q_c$ satellite reflection corresponding to a) **Figure 121a** and b) **Figure 121b**, at T = 75 K. c) Fit of the t*-scan of b) using the Fourier transform of the screw like dislocation shown in **Figure 121b**.

Beyond CDW systems, this study shows that coherent X-ray diffraction is well suited to probe any phase field deformation in the bulk, in nearly perfect lattices.

References

[1] H. Fröhlich, *Proc. Roy. Soc.* (London) **A223**, 296 (1954).

[2] P. A. Lee, T. M. Rice, *Phys. Rev. B*, **19**, 3970 (1979).

Principal Publication and Authors

D. Le Bolloc'h (a), S. Ravy (b), J. Dumas (c), J. Marcus (c), F. Livet (d), C. Detlefs (e), F. Yakhou (e), and L. Paolasini (e), *Phys. Rev. Lett.* **95,** 116401 (2005).

(a) Laboratoire de Physique des Solides, Université Paris Sud, Orsay (France)

(b) Synchrotron SOLEIL, Gif-sur-Yvette (France)

(c) LEPE/S - CNRS/25, Grenoble (France)

(d) LTPCM, Saint Martin D'Hères (France)

(e) ESRF

The Mysteries of Low-temperature Ground States of Actinide Oxides Resolved by Synchrotron Experiments

The discovery at the ESRF in 2002 [1] of quadrupole ordering in neptunium dioxide opened a new chapter in the understanding of the low-temperature ground states of actinide oxides. We concentrate in this report on the solid solutions $(U_{1-x}Np_x)O_2$, all with the simple cubic CaF_2 crystal structure and which have been studied for many years. The phenomena found at 25 K in NpO_2 (x = 1) is that the 5*f* charge distribution develops an anisotropic component that exhibits long-range ordering at T_o = 25 K. This is known as the ordering of the charge quadrupoles.

The experiments, carried out on beamline ID20, consist of tuning the photon energy to the actinide *M* absorption edge (at which photon energy core 3*d* electrons are promoted to the partially occupied 5*f* valence states), and then, once the repeat (wavevector) of the anisotropic charge distribution is known, one measures the azimuthal distribution of the scattered resonant X-ray intensity. This intensity distribution is related to the symmetry of the 5*f* anisotropic charge. The experiments were performed on single crystals prepared and mounted at the Institute of Transuranium Elements in Karlsruhe, Germany.

NpO_2 has pure quadrupole ordering, with no measurable dipole moment. In 2003 experiments were performed on a single crystal with x = 0.25 [2]. Dipole ordering was found on both the U and Np ions, and quadrupolar ordering was also found associated with both ions. However, these were different from those in pure NpO_2. Whereas a longitudinal configuration was found for x = 1 (NpO_2), the x = 0.25 sample was found to have a transverse configuration. The difference between these configurations is shown in **Figure 123**.

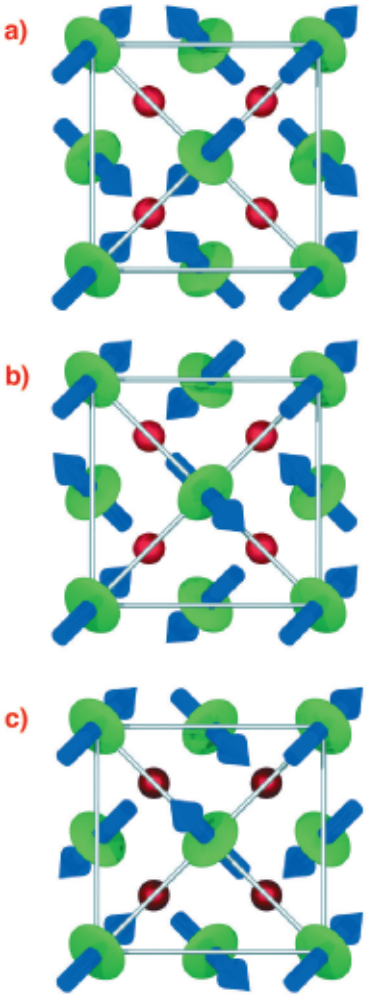

Fig. 123: Schematic representation of triple-*k* magnetic and electric-quadrupole ordering within the *a*-*b* plane for the single longitudinal (a) and two transverse (b,c) modes. The magnetic (dipole) moments are represented by blue arrows whereas the electric-quadrupole moments are shown as the green ellipsoids. The red spheres represent oxygen atoms.

The understanding of these different configurations then allowed an experiment to be performed in 2004 on a single crystal of UO_2 (x = 0). The azimuthal dependence of the intensity from the (112) reflection in UO_2 is shown in **Figure 124**, together with the predictions for a transverse configuration. Shown also in **Figure 124** is the temperature dependence of both the magnetic dipole, electric-quadrupole and the internal distortion of the oxygen cage. The complication in UO_2 is that both dipole ordering and an internal distortion of the oxygen atoms due to the quadrupole ordering are present; these have contrived to make it difficult to observe the quadrupole ordering in UO_2 directly, although such ordering was predicted almost 40 years ago [3], and the oxygen displacements reported 30 years ago [4].

These experiments also suggest a qualitative explanation of the unusual behaviour [5] of the mixed oxides with 0.40 < x < 0.80. In this region there is

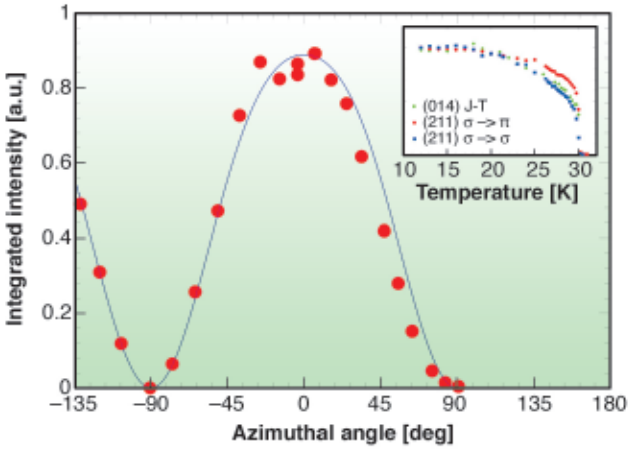

Fig. 124: UO_2. Integrated intensity as a function of azimuthal angle for the (112) superstructure reflection in the sigma–sigma polarisation channel (open circles). The line is a fit to the model for quadrupolar ordering (see text for details). In the model there is an incoherent superposition of the two transverse modes. The inset shows the temperature dependence of the integrated intensities of the (112) reflection in both the σ–π (circles) and σ–σ (diamonds) polarisation channels, and the (014) Bragg reflection (squares). These represent the magnetic dipole, electric quadrupole and Jahn-Teller internal distortion respectively.

competition between the longitudinal and transverse quadrupole ordering, resulting in quadrupolar frustration and only short-range dipole and quadrupole ordering. Experiments to detect such effects are planned.

References

[1] J.A. Paixão *et al., Phys. Rev. Lett.* **89,** 187202 (2002).
[2] S.B. Wilkins *et al., Phys. Rev. B* **70,** 214402 (2004).
[3] S.J. Allen, *Phys. Rev.* **167,** 492 (1968).
[4] J. Faber *et al., Phys. Rev. Lett.* **35,** 1770 (1975).
[5] A. Boeuf *et al., Europhys. Lett.* **3,** 221 (1987).

Principal Publication and Authors

S.B. Wilkins (a,b), J.A. Paixão (c), R. Caciuffo (a), C. Detlefs (b), J. Rebizant (a), and G.H. Lander (a), *Submitted*.
(a) European Commission, Joint Research Centre, Institute for Transuranium Elements, Karlsruhe (Germany)
(b) ESRF
(c) Physics Department, University of Coimbra (Portugal)

Measurements of Femtometre-scale Atomic Displacements by X-ray Absorption Spectroscopy

Displacements of atoms from their equilibrium distance, which are of the order of femtometres, are common in a variety of effects. For example, magnetostriction involves tiny mean atomic displacements that add up to give a macroscopically measurable quantity. Magnetostriction can be sensed as the buzz of a transformer, and used in under-water acoustic generation. We have measured the mean atomic displacement for atoms undergoing magnetostriction in an iron-cobalt alloy by employing the subtle changes observed in an X-ray absorption spectrum when the relative orientation between the photon polarisation vector and the sample magnetisation vector is changed. This technique is an advance on the widely-used EXAFS. Hitherto, displacements of atoms surrounding an absorber atom could be monitored to an accuracy of about 0.001 Å. An analysis of this limitation, lead us to conclude that two things set this limit. The first limitation was the signal to noise ratio of the measurement, and the second, the energy stability between comparative measurements. Encouraged by the success of the measurement at extreme conditions of X-ray Magnetic Circular Dichroism (XMCD) on ID24 [1], which measures the difference in absorption between two helicity states of the photon, we decided to attempt a measurement of the much weaker X-ray Magnetic Linear Dichroism (XMLD) over an extended energy range, *i.e.* the difference in EXAFS caused by magnetostrictive atom movement. ID24 provides an excellent environment for this type of measurement as it has an undulator as its source, which provides a high intensity to give a good signal to noise ratio. Also it has no moving parts, which aids the energy stability. A rough calculation of the anticipated size of the effect to be measured is ~ 10^{-4} (fractional change in normalised absorption) which requires a signal to noise ratio of about one decade better than this and also an energy stability of better than 0.01eV.

Our apparatus for performing this measurement is shown schematically in **Figure 125**. The source, S, is the

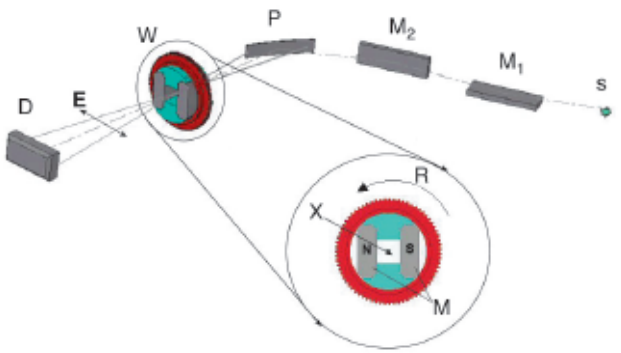

Fig. 125: A schematic of the experimental layout.

42-pole planar undulator of ID24, which is focussed vertically and horizontally by mirrors M_1 and M_2 respectively, the latter producing an image before the bent silicon crystal polychromator P. This optic selects wavelengths of the incident X-ray flux and disperses them onto a linear detector D. S, M_1, M_2, P and D are standard components of ID24. In addition the polychromator also focuses the beam onto the sample X (inset) that is held in an inert environment inside a wheel W that houses permanent magnets. The wheel rotates 90° between measurements and four measurements take approximately one second. This means that our apparently unreasonable requirement of 0.01 eV stability becomes reasonable when it is only required over a one second period.

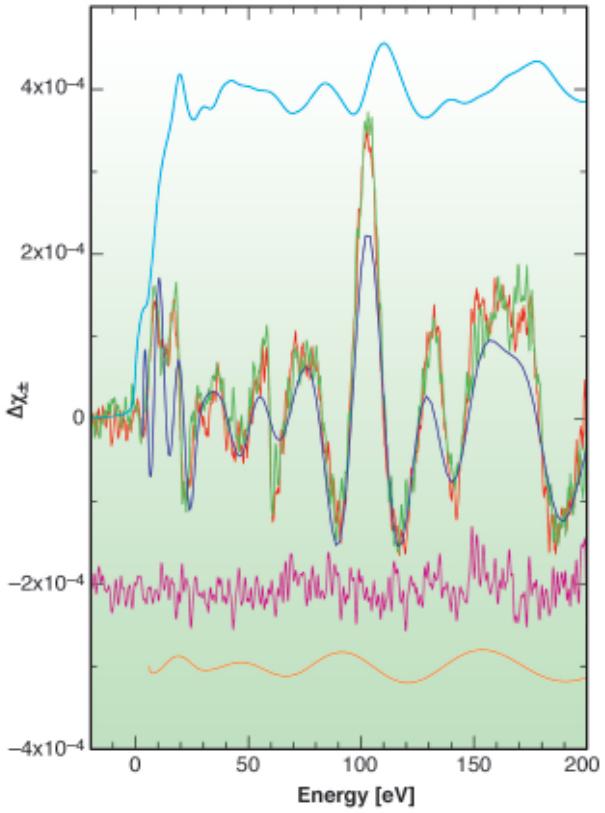

Fig. 126: The magnetostrictive differential EXAFS signal.

Some measurements are presented in **Figure 126**, which shows the differential EXAFS signal, red and green curves (these are two independent measurements with a 90° phase difference in the sequence of measurement and one curve has been inverted for comparison). The dark blue line gives a theoretical prediction of the curves, using macroscopically measured tensor coefficients. The light blue curve is a measurement of the K absorption edge of the FeCo sample on the same energy scale as the differential signal. Note that on the scale of this diagram the differences between two absorption spectra are too small to be seen. In **Figure 126**, the purple curve is a measure of the experimental noise and for comparison the brown curve is a theoretical prediction of the effect of a 1 femtometre displacement of the first shell atoms, which could be detected. These results show that EXAFS sensitivity can be extended to include atomic displacements of the order of 0.00001 Å, which is about 100 times smaller than had previously been assumed. This puts EXAFS sensitivity well within the range of thermal expansion over a temperature of one degree, piezo-effects, strictive-effects and elastic phenomena. All of these phenomena with the exception of piezo-effects are manifested in amorphous materials where the power of EXAFS as a structural technique is maximal. With advances in instrumentation we expect that the sensitivity can be improved by another decade.

Reference

[1] O. Mathon, F. Baudelet, J.P. Itié, S. Pasternak, A. Polian, S. Pascarelli, *Journal of Synchrotron Radiation* **11**, 423 (2004).

Principal Publication and Authors

R.F. Pettifer (a), O. Mathon (b), S. Pascarelli (b), M.D. Cooke (c) and M.R.J. Gibbs (c)
Nature **435** 78-81 (2005)
(a) Department of Physics, University of Warwick, Coventry (UK)
(b) ESRF
(c) Department of Engineering Materials, University of Sheffield, (UK)

Magnetic Instabilities in Fe_3C (Cementite) Particles Observed with Fe *K*-Edge X-ray Circular Dichroism under Pressure

Fe_3C is a common hardening constituent in carbon steels, and its amount in steel can be regulated by various heat treatment processes. The desired quantity depends on the particular application of the product. There is also a completely different aspect to Fe_3C in addition to it being a steel component. Fe_3C is ferromagnetic below the Curie temperature T_C of about 485 K with interesting magnetic properties featuring the invar effect, whereby the temperature dependence of its thermal expansion coefficient is nearly identical to that of the archetype Invar alloy $Fe_{0.65}Ni_{0.35}$ [1].

In the ground state of Invar type alloys, the atomic volume dependence of the binding energy exhibits a magneto-volume instability. This instability occurs between a high-spin (HS) state, which is the state of lowest energy in the vicinity of the equilibrium volume V_0, and a low-spin (LS) state. At volumes about 5% less than V_0, the LS state becomes energetically favorable

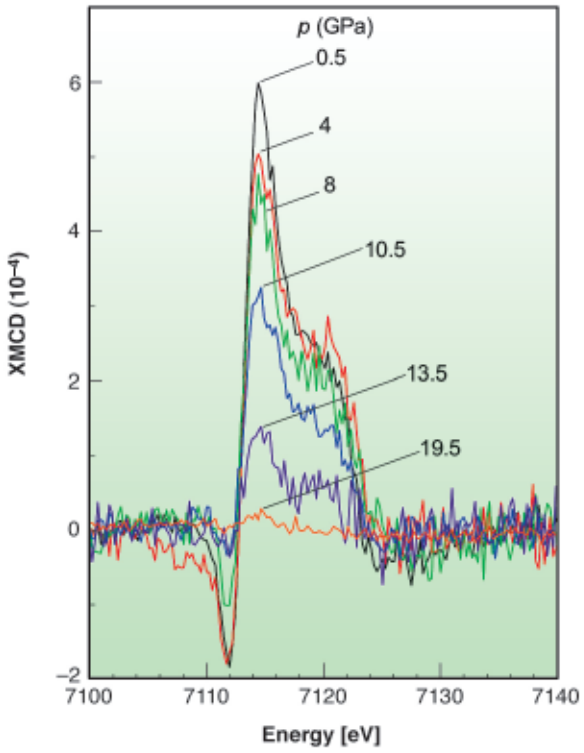

Fig. 127: The XMCD spectrum of Fe_3C around the Fe K-edge.

over the HS-state. The presence of the LS-states, therefore, provides for an enhanced anharmonicity towards volumes smaller than the equilibrium volume ("negative" anharmonicity), so that as the temperature increases, the atoms can approach one another closer than in a normal material. This results in a compensation of the normal lattice expansion, thereby leading to a vanishing thermal expansion coefficient.

Since Fe_3C shows the invar effect, its ground state binding energy is also expected to feature a magneto-volume instability. The direct method of detecting the presence of a magnetic instability that is coupled to the lattice degrees of freedom is to measure a magnetisation related parameter under applied pressure. We have, therefore, studied the pressure dependence of the X-ray magnetic circular dichroism (XMCD) of Fe_3C. The measurements were carried out on the ID24 beamline.

Figure 127 shows the XMCD spectra from ambient pressure up to about 20 GPa taken on increasing pressure. The data taken on decreasing pressure are similar. The overall intensity of the spectra diminishes as the pressure increases, and only a remanent feature remains at 19.5 GPa. The integrated XMCD is plotted as a function of applied pressure in **Figure 128a**. A clear HS-LS transition is observed starting at around 8 GPa, after which the XMCD drops rapidly and is reduced by about 80% at 13 GPa. **Figure 128b** shows the same plot as a function of reduced volume V/V_0, which is calculated using the results of equation of state studies on Fe_3C [2]. The transition occurs at a volume reduction of 4-5%; very similar to the case of $Fe_{65}Ni_{35}$.

Since the *p* electrons of the carbon atom at the interstitial sites in Fe_3C are strongly hybridised with the *d* band of Fe, the valence electron concentration *e/a* per metal atom of Fe_3C can be estimated as the concentration weighted sum of the total number of *s*, *p*, and *d* electrons, namely as [(0.75 x 8 + 0.25 x 2)/0.75] = 8.67. It is interesting to note that this value is almost exactly the same as that for $Fe_{65}Ni_{35}$, and corresponds to a valence electron concentration where invar related magnetovolume effects are largest.

In conclusion, pressure dependent XMCD spectroscopy at the Fe *K* edge proves to be a useful tool to observe volume driven magnetic instabilities in systems that incorporate Fe. By probing the magnetic degree of freedom with this method, we find direct evidence for the presence of a magnetovolume instability in Fe_3C. These instabilities are expected to be the source of the Invar-

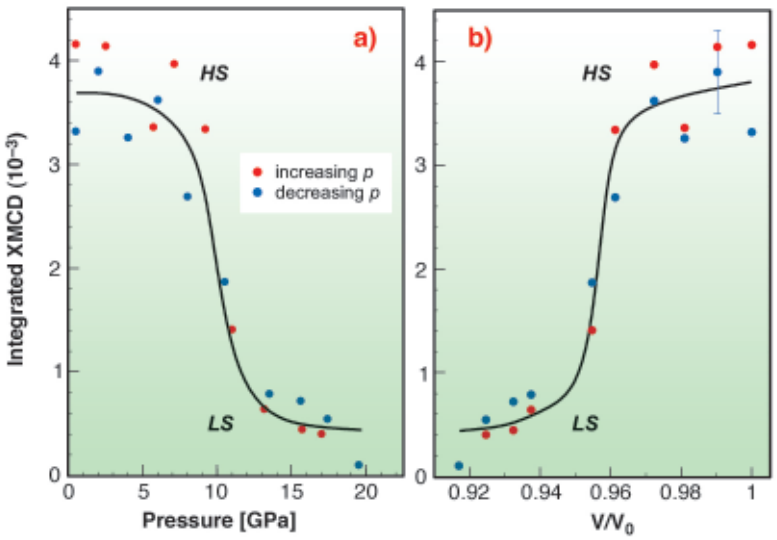

Fig. 128: The integrated XMCD plotted as a function of a) the applied pressure and b) the reduced volume.

typical features observed in the temperature dependence of the thermodynamical parameters for this material.

References

[1] W. Pepperhof and M. Acet, *Constitution and Magnetism of Iron and its Alloys* (Springer-Verlag, Berlin, Heidelberg, 2001).

[2] E. Duman, M. Acet, T. Hülser, E. F. Wassermann, B. Rellinghaus, J. P. Itié, and P. Munsch, *J. Appl. Phys.* **96**, 5668 (2004).

Principal Publication and Authors

E. Duman (a), M. Acet (a), E. F. Wassermann (a), J. P. Itié (b), F. Baudelet (c), O. Mathon (d) and S. Pascarelli (d), *Phys. Rev. Lett.* **94**, 075502 (2005).

(a) Experimentalphysik, Universität Duisburg-Essen (Germany)

(b) Physique des Milieux Condensés, CNRS-UMR 7602, Université Paris VI (France)

(c) Syncrotron Soleil (France)

(d) ESRF

X-ray Absorption Studies on the N-terminal Copper-binding Region of *Haemophilus ducreyi* Cu,Zn Superoxide Dismutase

Copper is an essential element for all aerobic organisms which incorporate this metal ion in several important enzymes. One of these enzymes is Cu,Zn superoxide dismutase (Cu,ZnSOD), which protects cells from the toxic effects of reactive oxygen intermediates by converting the superoxide radical into hydrogen peroxide and molecular oxygen. In bacteria Cu,ZnSOD is located in extracytoplasmic compartments where it plays an important role in protecting microorganisms from exogenous sources of superoxide [1]. The Cu,ZnSOD from a subset of Gram-negative pathogens possess divalent metal binding N-terminal extensions, which presumably favours the uptake of the enzyme's prosthetic metals in environments where their concentration is very low [2]. In particular, the N-terminal extension of the Cu,ZnSOD from *Haemophilus ducreyi*, the causative agent of a genital ulcerative disease known as chancroid, shows particularly interesting features (HGDHMHNHDTKMDTMSKDMMSM). The N-terminus of this motif, which contains a cluster of four histidines interspersed with other residues, is very similar to the transition metal binding regions already identified in other proteins that are able to bind Ni(II), Zn(II), or Cu(II) [2]. The second half of the domain contains an unusual methionine-rich sequence that resembles the Cu(I)-binding domains observed in several proteins involved in copper homeostasis in prokaryotic and eukaryotic cells [3,4]. These observations suggest that the N-terminal domain of *H. ducreyi* Cu,ZnSOD could allow the efficient binding of Cu(II) and Cu(I) at the histidine-rich and methionine-rich sequences, respectively.

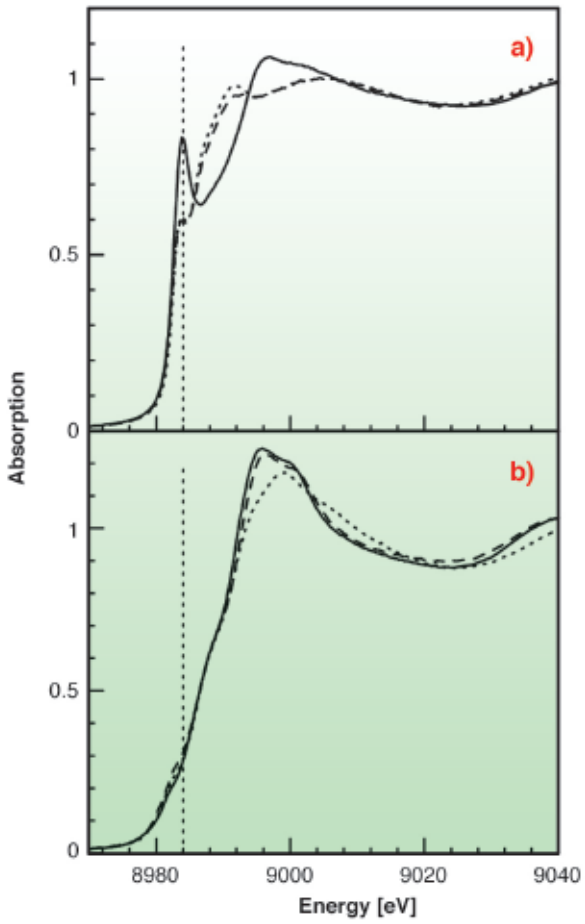

Fig. 129: (a) Cu K-edge XANES spectra for Cu(I) with Met-rich (dotted line), His-rich (solid line), and an equimolar mixture of the two peptides (dashed line) in water solution. (b) Cu K-edge XANES spectra for Cu(II) with Met-rich (dotted line), His-rich (solid line), and an equimolar mixture of the two peptides (dashed line) in water solution.

To test this hypothesis X-ray absorption spectroscopy experiments have been carried out on peptides corresponding to the two metal binding regions. Cu K-edge XAS spectra were collected in fluorescence mode at the BM30-B (FAME) beamline on samples with Cu concentrations of 2.5 and 1.25 mM. Our results indicate that both sequences can bind either Cu(II) or Cu(I) as shown in **Figure 129**. However, competition experiments demonstrate that Cu(II) is preferred by histidine residues belonging to the first half of the motif, while the methionine-rich region preferentially binds Cu(I) via the interaction with three methionine sulfur atoms as shown in **Figure 130**. These findings demonstrate that the N-terminal domain of *H. ducreyi* Cu,ZnSOD is an unusual metal trapping peptide able to bind Cu(I) or Cu(II) at

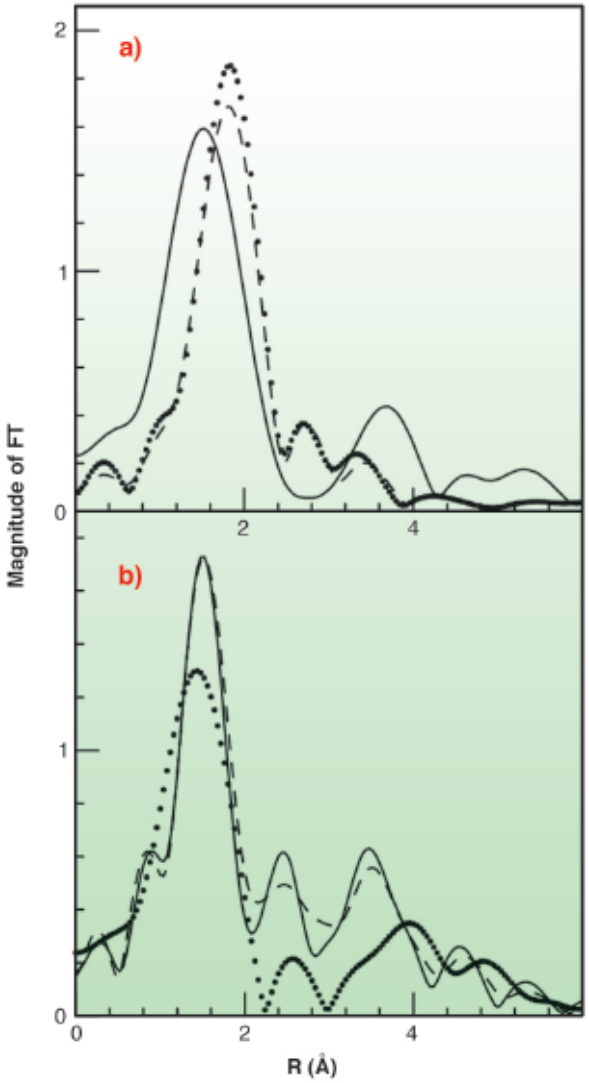

Fig. 130: Fourier Transforms of the k^2-weighted EXAFS experimental data. (A) Cu(I) complexes (B) Cu(II) complexes. Data are shown as dotted lines (Met-rich peptide), solid line (His-rich peptide), and dashed line (equimolar mixture of the two peptides).

different sites, possibly favouring an efficient copper uptake under copper starvation. Moreover, alterations in the copper coordination environment mediated by changes in the copper redox state could play a role in favoring metal transfer from the N-terminal domain to the active site.

In conclusion, we suggest that the juxtaposition of two sequence motifs potentially involved in the binding of Cu(I) and Cu(II) in the N-terminal domain of *H. ducreyi* Cu,Zn-SOD could have a double role: to facilitate copper acquisition in environments poor of this metal ion and to assist Cu(I) transfer from the high-affinity Met-rich motif to the enzyme active site.

References

[1] A. Battistoni, A. *Biochem. Soc. Trans.* **31**, 1326-1329 (2003).

[2] A. Battistoni, F. Pacello, A. P. Mazzetti, C. Capo, S. J. Kroll, P. Langford, A. Sansone, G. Donnarumma, P. Valenti, G. Rotilio *J. Biol. Chem.* **276**, 30315-30325 (2001).

[3] D.L. Huffman, J. Huyett, F.W. Outten, P.E. Doan, L.A. Finney, B.M. Hoffman, T.V. O'Halloran, *Biochemistry*, **41**, 10046-10055 (2002).

[4] K. Peariso, D.L. Huffman, J.E. Penner-Hahn, T.V. O'Halloran *J. Am. Chem. Soc.*, **125**, 342-343 (2003).

Principal Publication and Authors

P. D'Angelo (a), F. Pacello (b), G. Mancini (a), O. Proux (c), J.-L. Hazemann (d), A. Desideri (b,e), A. Battistoni (b,e) *Biochemistry* **44**, 13144-13150 (2005).

(a) Dipartimento di Chimica Università di Roma "La Sapienza" (Italy)

(b) Dipartimento di Biologia Università di Roma Tor Vergata (Italy)

(c) Laboratoire de Géophysique Interne et Tectonophysique, UMR CNRS, Université Joseph Fourier, Saint-Martin-d'Hères (France)

(d) Laboratoire de Cristallographie, CNRS, Grenoble (France)

(e) INFM, Università di Roma Tor Vergata (Italy)

ESRF

Highlights 2005

X-ray Imaging and Optics

Introduction

Synchrotron radiation based X-ray imaging and nanofocusing techniques are key elements in the preparatory document that lays out the long-term strategy of the ESRF. These techniques are promising for two reasons: firstly they are being applied to an increasingly large number of subjects including palaeontology (this Highlights cover) and environmental sciences (see **Figure 131**). Secondly, the evolution of these techniques towards quantitative measurements with high spatial and temporal resolution opens new prospects in research including the flourishing area of nano-technologies.

The development of SR-imaging and nanofocusing techniques depends on several technological improvements, particularly in the fields of mechanical and thermal stabilisation, and X-ray Optics, as shown in the first section of this chapter, X-ray Imaging Methods and Instrumentation. Two approaches are used to focus the beam to a nano-spot: the combination of an adaptive Kirkpatrick-Baez (KB) focusing optic based on elliptically-curved mirrors with X-ray waveguides, on ID22; and dynamically-bent graded multilayers, on ID19. The new sources will surely require optics elements able to withstand high heat-loads. Emphasis has therefore been put onto the collaboration with diamond producers, to obtain the highest quality diamond crystals. Some of the samples obtained to date already approach the required quality, as shown by the topographs. The two other contributions within this section describe ways to enhance the SR-based imaging techniques to offer improved opportunities for fundamental and applied science. The first involves free-space propagation and analyser-based imaging for phase contrast imaging. The second presents the results of a recently-designed laminograph, which permits three-dimensional images of flat samples that cannot be visualised using classical microtomography.

The two following sections are devoted to the application of X-ray imaging techniques to life science and medicine, on the one hand, and to the study of materials, on the other. The mechanical feasibility of a more advantageous interlaced cross-firing geometry for microbeam radiation therapy, and the validation of the use of monochromatic quantitative computed tomography for a direct measurement of the concentration of a contrast agent, are demonstrated. The application of X-ray imaging to materials is exemplified by two very different topics, the microtomographic study of a coronary stent, to reduce the risk of lesions, and results that

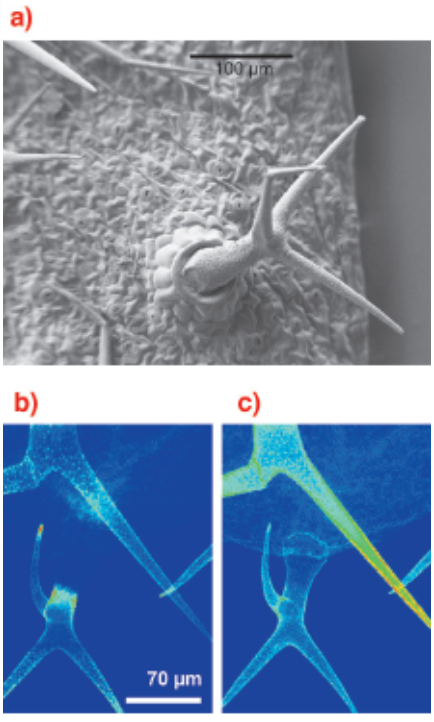

Fig.131: (a) Scanning electron microscope image of "trichomes" from the plant Arabidopsis thaliana. (b) Fluorescence image showing the cadmium content. (c) Fluorescence image showing the calcium content. Images courtesy of M.-P. Isaure, B. Fayard, G. Sarret, S. Pairis, J. Bourguignon (Publication submitted to *Environmental Science and Technology*).

shed light on an old but unresolved problem, the mechanisms of liquid metal embrittlement.

The last section, X-ray fluorescence and diffraction microscopy, shows the same wide variety of topics, which range from the conservation of Henry VIII's warship *Mary Rose*, to the critical fluctuations near a phase transition in Fe_3Al, through the investigation of extraterrestrial grains for the NASA Stardust Mission, and finally to the evidence of diffusion at room temperature in a high Tc superconductor.

We wish to illustrate this dynamically-growing area of microspectroscopy with a recent environmental science application: the chemical images of small "trichomes" on plants leaves (see **Figure 131a**). Metal accumulation occurs in these epidermial hairs covering the leaves. It is well known that cadmium is highly toxic for plants: its distribution was studied by μXRF on ID21. The metal was found to be concentrated in localised areas of the trichomes (**Figure 131b**), which were also found to be enriched with calcium (**Figure 1311c**).

J. Baruchel

X-ray Imaging Methods and Instrumentation

X-ray Waveguides Deliver Ultra-small X-ray Beams

The production of ultra-small and coherent hard X-ray nanobeams is currently an exciting field of research. Such beams would allow promising new applications such as holographic imaging and scanning X-ray probe experiments with unprecedented resolution. Among the different optics used to prepare X-ray nanobeams are Fresnel zone plates, curved mirrors, compound refractive lenses and X-ray waveguides.

We have recently combined two independent optical elements for hard X-ray nanobeams (12.5 keV) to simultaneously achieve high gain and small cross section in two dimensions. An adaptive Kirkpatrick-Baez (KB) focusing optic [1] based on elliptically-curved mirrors was used to achieve a high flux density at the ID22 undulator beamline, with a focal spot of 2.5 x 3.8 μm^2 (vert. x hor.) as measured by knife-edge fluorescence scans at the Au L-edge. This prefocused beam was coupled to the front side of a two-dimensionally confining X-ray waveguide (**Figure 132**). Depending on the lateral dimensions of the waveguide guiding core, the device allows the propagation of a defined number of modes. Owing to the filtering properties of the waveguide, the exiting beam exhibits a clean profile and it is not accompanied by any spurious reflected or transmitted beams which might present a source of complication in imaging or diffraction applications (**Figure 133**). Note that a mono-modal waveguide delivers a fully coherent beam (lateral coherence) [2].

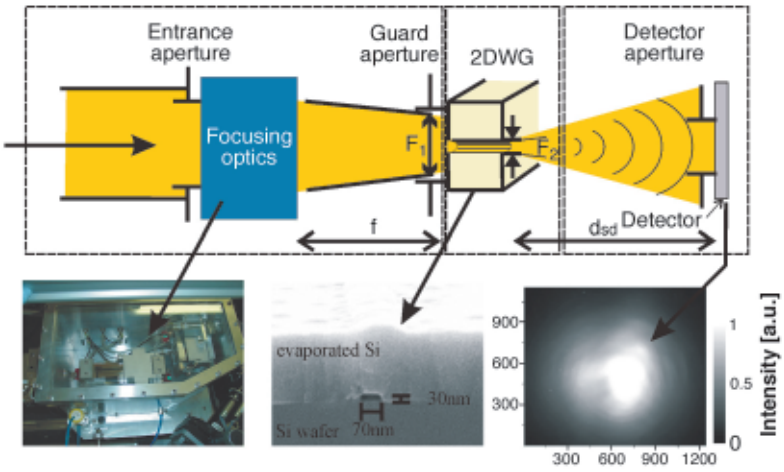

Fig. 132: Sketch of the optical system for nanobeam X-ray production. Left: The KB mirror optics is used to focus the beam. Middle: The waveguide filters the prefocused beam and further reduces its cross-section. Right: The exiting beam profile is characterised behind the waveguide.

The waveguide was prepared by e-beam lithography. It consists of a polymer (PMMA) core (30 x 70 nm^2 [vert. x hor.]) surrounded by silicon cladding on all four sides. The length of the device was 4.05 mm corresponding to an aspect ratio (length/width) of 60000. The high aspect ratio ensured negligible transmission of the primary beam through the silicon cladding (3.3 x 10^{-7}photons/s/mm^2). The farfield pattern was measured by a CCD detector (Princeton Instruments) as well as by a scintillation detector for single photon counting (Cyber Star, Oxford Instruments). The vertical and horizontal line scans in the farfield (470 mm behind the guide) are in good agreement with the simulations of beam propagation (**Figure 133**). The total flux of the exiting beam was 3.5 x 10^6 photons/s, corresponding to a waveguide efficiency of 4.7%, *i.e.* the number of photons exiting the device over number of photons impinging on the waveguide entrance. This corresponds to a overall system gain of g = 4000. Directly behind the guide, the beam has a lateral cross-section of 25 x 47 nm^2 (Full Width at Half Maximum, FWHM), which is the smallest beam size for hard X-rays published so far.

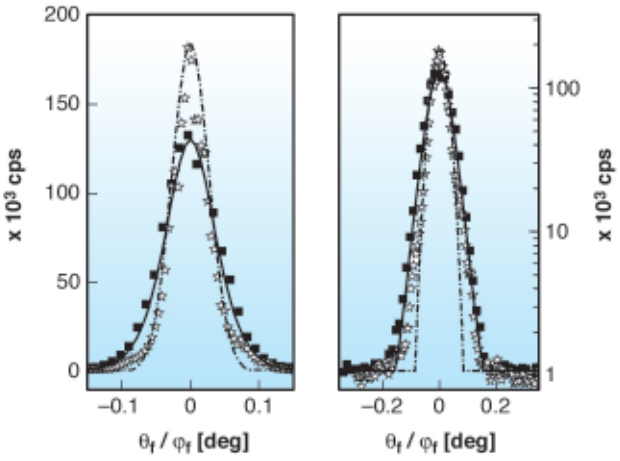

Fig. 133: The measured farfield beam profiles in the vertical (■) and horizontal (☆) directions, behind the waveguide in linear (left) and logarithmic scales (right), along with simulations based on the parabolic wave equation (lines).

Possible next steps include a better matching of the pre-focussing optics and the waveguides geometric acceptance. To this end, the KB mirrors could be placed at larger distances behind the source to further demagnify the beam. A reduction of the over-illumination at the waveguide entrance by two orders of magnitude thus seems to be feasible (thanks to the enhanced flux density). Finally, this non-dispersive optical system should allow the use of pink undulator beams, which could give an additional boost of another two orders of magnitude in coherent nanobeam flux.

References

[1] Y. Dabin, G. Rostaing, O. Hignette and A. Rommeveaux, Proc. *SPIE*, 4782, 235 (2002).

[2] C. Fuhse, A. Jarre, C. Ollinger, J. Seeger and T. Salditt., *APL* **85**, 1907 (2004).

Principal publication and Authors

A. Jarre (a), C. Fuhse (a), C. Ollinger (a), J. Seeger (a), R. Tucoulou (b) and T. Salditt (a), *Phys. Rev. Lett.* **94**, 074801 (2005).

(a) Institut für Röntgenphysik, Göttingen (Germany)

(b) ESRF

Phase-contrast X-ray Imaging Combining Free-space Propagation and Bragg Diffraction

Despite their common origin, X-ray phase contrast imaging techniques have been treated separately in the literature, both in theoretical and experimental studies. In this work, we show that by using a coherent X-ray beam and choosing an appropriate setup, two techniques, namely propagation-based imaging (PB) and analyser-based imaging (AB), can be combined together to produce images showing original features. This technique is referred to hereafter as 'Hybrid phase contrast Imaging' (HI).

The propagation-based technique consists in recording the interference pattern produced by choosing one or several sample-to-detector distances. The theoretical

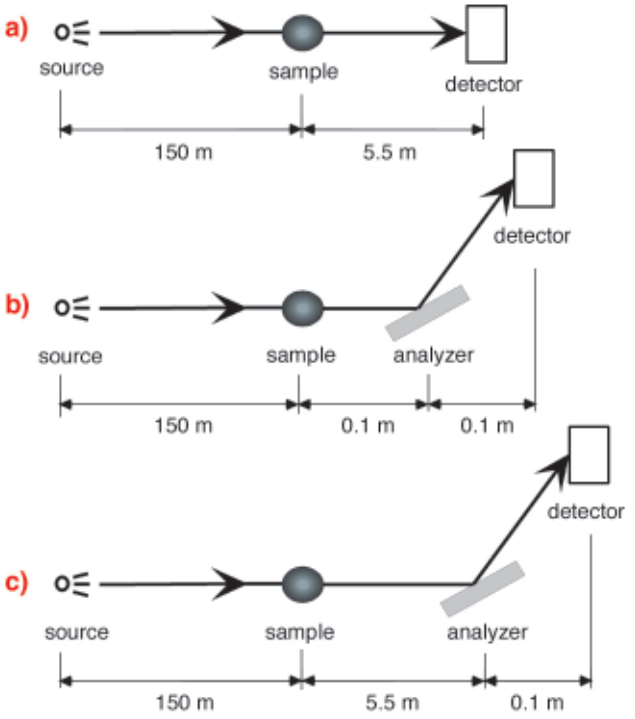

Fig. 134: Schematic representation of the configurations used for image acquisition: (a) Propagation-based Imaging; (b) Analyser-based Imaging; (c) Hybrid Imaging.

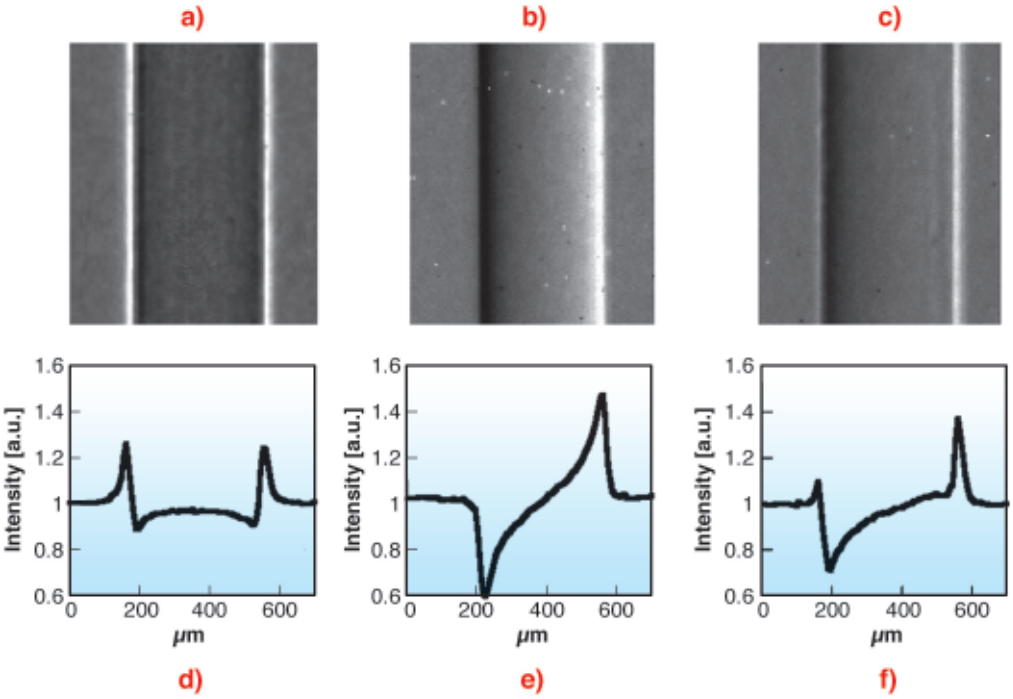

Fig. 135: Images and vertical profiles of the nylon wire: (a,d) PB; (b,e) AI; (c,f) HI.

description of the technique is based on Fresnel diffraction [1].

The analyser-based technique consists in placing a perfect crystal in Bragg or Laue geometry between the sample and the detector. The crystal acts as a filter for the radiation refracted and scattered inside the object, since it only accepts a narrow range of angles of the incident beam centred at the Bragg angle for the specific energy [2].

HI is a combination of these two techniques, performed experimentally by analysing the wave transmitted by the sample after propagation in air by means of a perfect crystal. The experimental data were acquired using 25 keV X-rays, a Si(111) analyser crystal (setups shown in **Figure 134**), and, as pure phase objects (negligible absorption), thin cylindrical polymer fibres (nylon and kevlar wires with diameters of 350 and 200 μm, respectively).

Figure 135 shows some examples of the images and the extracted intensity profiles acquired using the three techniques. The quantitative analysis has been carried out by evaluating the signal-to-noise ratio (SNR). In **Figure 136** the SNR versus the angular setting of the analyser is reported, for the two edges of the wires imaged with the AB and the HI techniques. The SNR values for the left and right edge in the PB configuration are respectively 179 ± 30 and 165 ± 12 for the nylon wire and 242 ± 30 and 207 ± 25 for the kevlar wire. The visibility of the two edges, in terms of SNR, changes substantially by varying the angle of the crystal and is mirrored with respect to the axis $\Delta\theta = 0$. In AB, this behaviour can be explained by considering the different origin of the signal for the various angular positions. In

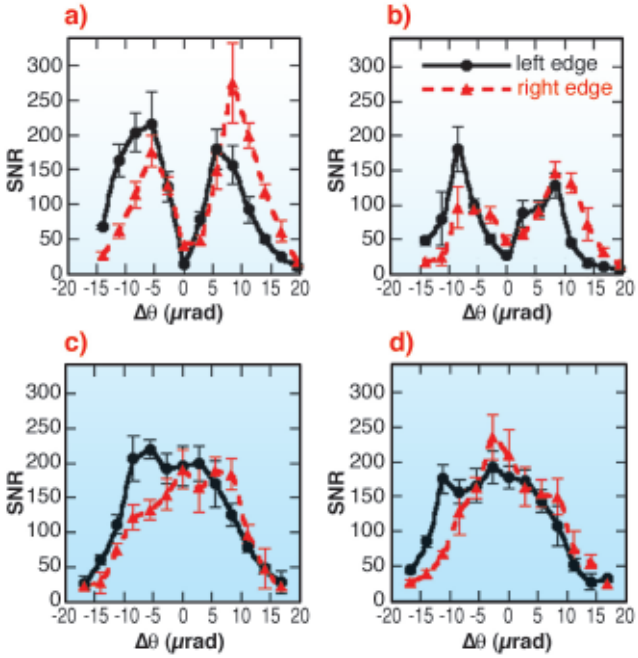

Fig. 136: Signal-to noise ratio values of the signal produced by the edges of the two wires as function of the angular position of the analyser for AB ((a) nylon wire, (b) kevlar wire) and HI ((c) nylon wire, (d) kevlar wire) configurations.

particular, while at $\Delta\theta = 0$ the signal mainly derives from refraction and the reduction of the scattering component on the image, for the other angular positions it is determined by the analyser alignment with respect to a given direction of the refracted X-rays. Therefore, by rocking the crystal, it is possible to optimise the visibility of the details. At around $\Delta\theta = 0$ there is a minimum of the derivative of the rocking curve, and then the crystal is less sensitive to X-rays refracted inside the object, determining a low SNR. On the tails of the rocking curve, the low reflectivity increases the image-noise, also reducing the SNR. In the case of the HI technique, the

main difference with respect to AB concerns the SNR values around the exact Bragg angle. In fact, while the AB signal is maximum on the shoulders of the rocking curve and it decreases towards $\Delta\theta = 0$, in HI the SNR is high even at this position where it also reaches its maximum values because of the constant presence of the PB contribution.

The HI signal combines the propagation and diffraction effects: the PB signal, determined in first approximation by the Laplacian of the phase introduced by the object and by the sample-detector distance, passes through the AB crystal acting like a band-pass filter; thus only some frequencies can reach the detector.

HI images present a weak dependence on the angular positioning of the analyser, reducing the constraints in terms of optical alignment and stability of the crystal, which are critical shortcomings of the AB technique.

In order to fully understand the peculiar characteristics of the HI signal, further theoretical and experimental investigations are required. This technique may find application in several fields already advanced by hard X-ray phase-contrast imaging, producing as high SNR as PB, while bringing the advantages of the higher refraction sensitivity of the AB technique.

References

[1] P. Cloetens, R. Barrett, J. Baruchel, J. Guigay, M. Schlenker, *J. Phys. D: Appl. Phys.*, **29**, 133-146 (1996).
[2] A. Bravin, *J. Phys. D: Appl. Phys.*, **36**, A24-A29 (2003).

Principal publication and Authors

P. Coan, E. Pagot, S. Fiedler, P. Cloetens, J. Baruchel, A. Bravin, *J. Sync. Rad.*, **12**, 241-245 (2005).
ESRF

Three-dimensional Imaging by Synchrotron Radiation Computed Laminography

Today, X-ray computed tomography – developed during the 1960s/70s for cross-sectional imaging in medicine – is an established technique at synchrotron sources for three-dimensional microimaging of materials and devices.

Computed tomography (CT) is optimised for samples whose (integral) X-ray transmission does not change significantly during rotational scanning, for example cylindrically-shaped samples undergoing rotation around their longitudinal axis. Despite the great success of CT for non-destructive imaging, it can be difficult to image the local microstructure within a limited region of interest when the sample size greatly exceeds the field of view of the detector. Indeed, inspection of devices such as flat, laterally extended microsystems on planar substrates by CT is often unsatisfactory since the strongly varying X-ray transmission during a scan is prone to generating artefacts.

This limitation has been overcome by introducing a new synchrotron imaging technique for 3D imaging of flat, laterally extended objects. This technique was stimulated by established laboratory methods from medicine (usually called digital tomosynthesis [1]) and non-destructive device testing (frequently called computed laminography [2]). These developments were carried out within an ESRF long-term project involving collaboration between the Fraunhofer IZFP, ANKA of Forschungszentrum Karlsruhe, the University of Karlsruhe and the ESRF.

Introducing a simple scanning geometry adapted to the particular experimental conditions of synchrotron imaging (such as the stationary source and parallel beam) allowed us to combine the advantages of laminography with those provided by synchrotron radiation. For instance monochromatic radiation was used to avoid beam hardening artefacts, high beam intensity permitted high spatial resolution and partial spatial coherence made it possible to exploit phase contrast.

Preliminary setups for data acquisition compatible with a stationary synchrotron source have been successfully implemented and tested at beamlines ID15 and ID19. The scanning geometry of synchrotron-radiation computed laminography (SR-CL) resembles that of SR-CT (see **Figure 137**) but the object rotation axis is inclined by an angle $\theta < 90$ degrees with respect to the quasi-monochromatic X-ray beam incident from the multilayer monochromator. Contrary to (non-local) CT the lateral extension of the sample can be larger than the field of view of the area detector system.

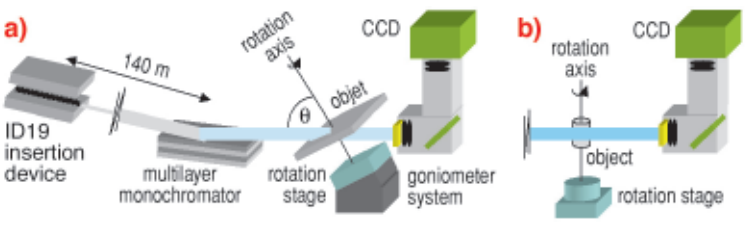

Fig. 137: (a) Experimental setup sketched for SR-CL with monochromatic beam at beamline ID19; (b) The limiting case of the axis inclination angle $\theta = 90°$ corresponds to the scanning geometry of computed tomography.

In general for all laminography methods, the 3D Fourier domain is not sampled completely. Contrary to CT and depending on the exact scanning geometry (*e.g.* axis inclination angle θ) there remain limited unsampled regions which could give rise to artefacts in the reconstructed images. The 3D reconstruction method, based on filtered backprojection adapted to the scanning geometry, minimises these artefacts.

The capability of the method for non-destructive testing in microsystem technology was demonstrated using the example of a flip-chip bonded device. Solder bumps are hidden after the bonding process and thus are not accessible by visual inspection. **Figure 138** shows two mutually perpendicular slices (a+b) through solder joints of the device, reconstructed from 900 projections with 1.4 µm pixel size taken at an X-ray energy of 35 keV. A variety of defects (small voids) which are located near the interface to the chip metallisations are related to the bonding technology and its processing parameters. In the 3D rendition (c) the chip itself is cropped by a slightly inclined plane in order to exhibit the square-shaped metallisations to the left-hand side and voids inside the bumps at the right-hand side. The large voids and solder splashes visible in the reconstructed image entail a reliability hazard of the electronic circuit.

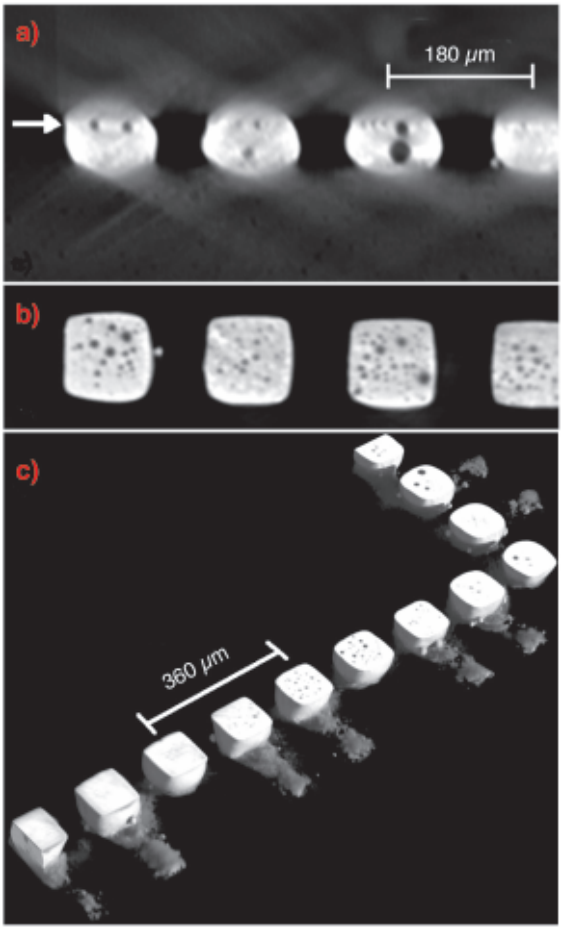

Fig. 138: Flip-chip bonded device: reconstructed cross-sections through a row of solder bumps, (a) perpendicular and (b) parallel to the device surface. The arrow in slice (a) indicates the depth position of slice (b) where many small voids are found. In the 3D rendition (c) the chip itself is cropped by a slightly inclined plane. Voxel size is 1.4 µm, X-ray energy 35 keV.

The reported results demonstrate the feasibility of synchrotron-radiation computed laminography. A dedicated setup is scheduled for installation at ID19 in March 2006. SR-CL will then be readily applicable at the ESRF for non-destructive testing of flat, laterally-extended objects such as electronic components or flat samples of microstructured materials.

References

[1] J. T. Dobbins III and D. J. Godfrey, *Phys. Med. Biol.* **48**, R65 (2003).
[2] J. Zhou, M. Maisl, H. Reiter, and W. Arnold, *Appl. Phys. Lett.* **68**, 3500 (1996).

Principal Publication and Authors

L. Helfen (a,b), T. Baumbach (b,c), D. Kiel (b), P. Pernot (b,d), P. Mikulík (a,e), P. Cloetens (d), J. Baruchel (d), *Appl. Phys. Lett.* **86**, 071915 (2005).
(a) Fraunhofer Institute for Nondestructive Testing (IZFP), Dresden (Germany)
(b) Institut für Synchrotronstrahlung (ISS/ANKA), Forschungszentrum Karlsruhe (Germany)
(c) Laboratorium zur Applikation der Synchrotronstrahlung, University of Karlsruhe (Germany)
(d) ESRF
(e) Now at: Institute of Condensed Matter Physics, Masaryk University, Brno (Czech Republic)

Focusing Below 50 nm using Dynamically-bent Graded Multilayers

Focusing hard X-rays efficiently down to spots below 100 nm is a real challenge for presently available X-ray optics. Among various alternative techniques, curved and laterally-graded multilayers are promising candidates to provide the required performance, thanks to their potentially large numerical aperture. In recent focusing experiments on beamline ID19 a focal line width below 50 nm was achieved.

The result was obtained using a dynamically-bent $[W/B_4C]_{25}$ graded multilayer in vertical reflection that was exposed to the full ID19 undulator line at 24 keV (**Figure 139**). The bending technology, the multilayer coating, and the detection setup are ESRF in-house developments.

The multilayer was placed at 150 m from the source and produced a focal line at a distance of 8 cm. The strong demagnification of 1/1875 together with the small vertical source size of 25 µm would lead to a geometrical

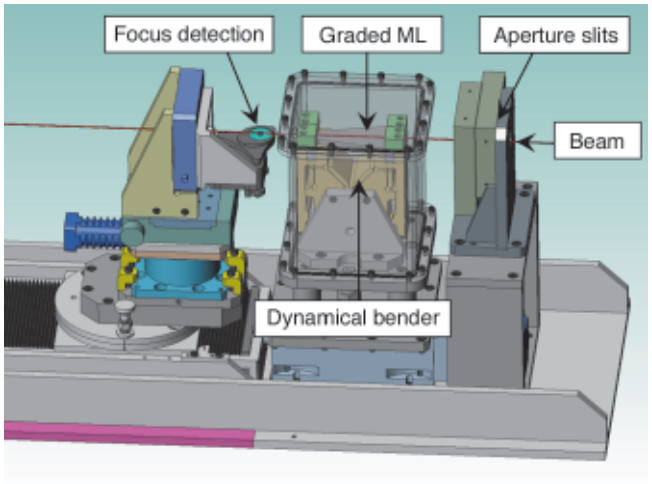

Fig. 139: Experimental focusing setup used on ID19.

line width of only 13 nm. This permits the investigation of line broadening effects due to diffraction, slope errors, and volume scattering.

The focal line was scanned using a lithographically prepared Ru nano-wire under grazing incidence while detecting the fluorescent radiation. The dimensions of the wire are known and can therefore be taken into account in the data analysis. Best values for the focal line are 45 nm FWHM for the raw data (**Figure 140**) giving 41 nm FWHM after de-convolution and with an aperture of about 130 µm. This is the smallest width ever reported using reflective multilayer optics for hard X-rays.

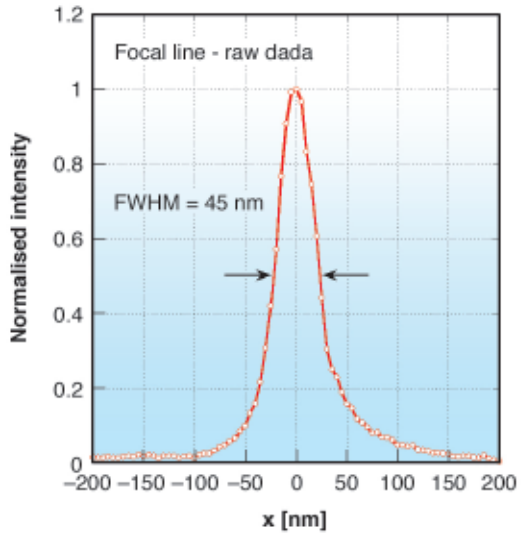

Fig. 140: Scan through the focal line (raw data).

The measured focal size is mainly limited by diffraction and mirror figure errors, which become predominant when a larger portion of the mirror is used to decrease the diffraction influence. Stability tests based on the position of the focal line indicate that mechanical vibrations remain a principle obstacle for the detection of smaller spots.

To investigate the influence of volume penetration effects in the multilayer, the photon energy of the incident beam was modified by opening the undulator gap. The wide energy bandpass of the multilayer (about 9%) allows scanning the undulator line through the first Bragg peak, leading to a strong variation of the penetration depth of the electromagnetic field into the multilayer. Unlike in the case of curved crystals, the curved and graded multilayer structure fulfils the local Bragg condition at any point along the optics. Therefore, no additional contribution to the line width has been observed.

Authors
O. Hignette, P. Cloetens, Ch. Morawe, P. Bernard, W. Ludwig.
ESRF

Diamonds for Modern Synchrotron Radiation Sources

The trend in modern X-ray sources, third (and eventually fourth) generation storage rings or free electron lasers, is towards higher brilliance, with more photons, out of smaller optical source sizes, in smaller solid angles and within shorter pulses. This may lead to high power densities, exceeding hundreds of watts per square millimetre on the first beam optical elements. These elements can be filters, windows, polarisers (phase plates), beam splitters or monochromators.

The preferred material for Bragg diffracting elements is, at present, silicon: it can be grown to a very high crystal perfection and workable size as well as rather easily processed to the required surface quality. These elements preserve the transversal coherence in the X-ray beam, which is important for phase-sensitive imaging techniques and for advanced focusing possibilities. However, in comparison to silicon, diamond has a number of advantages for X-ray optical applications. Its linear absorption coefficient, at 8 keV, is about 10 times lower, and its thermal expansion coefficient at room temperature is about 2.4 times lower than that of silicon. The thermal conductivity at room temperature is from 4 to 23 times higher, depending of the type of diamond considered. These parameters lead us to prefer diamond for many X-ray optical applications, provided that large, nearly perfect crystals are available. So far, this has not been the case.

To improve this situation a collaboration between Element Six Technologies (Johannesburg, South Africa), the University of the Witwatersrand (South Africa) and the ESRF was established to coordinate and intensify their effort to develop diamond based X-ray beam optical elements for third and fourth generation X-ray sources.

The necessary single crystalline quality may only be achieved with synthetic material. Basically two classes of growth methods are presently used, chemical vapour deposition (CVD) and high-pressure high-temperature

growth (HPHT), the last one being the most promising for X-ray optics applications.

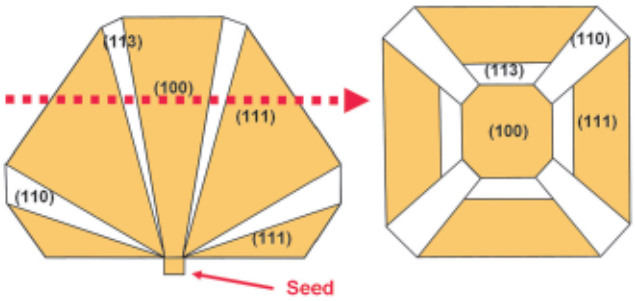

Fig. 141: Growth sectors seen most frequently in the growth of near cubo-octahedral HPHT diamond crystals of type Ib (left). The growth face orientations are indicated. View from above after a cut along the red arrow (right).

The main results may be summed up as follows:
a) The faster growing type Ib material (for many years assumed to be the best candidate for high perfection) with a nitrogen content of a few hundred parts per million and in the required size of 4 to 8 mm^2 is of too low quality. Only selected samples of that type may be used for less demanding applications like phase plates (**Figures 141** and **142**).

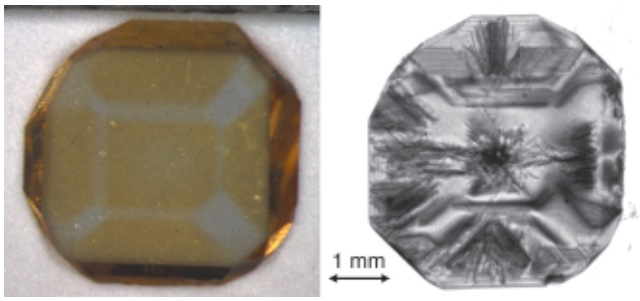

Fig. 142: Optical image (left) and X-ray white beam topograph (right) of a type Ib diamond plate, showing the inhomogeneous distribution of nitrogen and correlation with strong strain fields due to the growth sector boundaries (as sketched in **Figure 141**), as well as dislocations. The nitrogen concentration is higher in the brown sectors of the optical image.

b) Highly pure (very low nitrogen content) type IIa diamond crystals may be grown with a perfection that is approaching the quality required for the more demanding applications such as X-ray imaging and in particular X-ray imaging with coherence preservation (**Figure 143**).
c) Double crystal topography experiments (in reflection geometry) in a setup with a very low estimated detection limit for weak strains of about 10^{-7} showed no strain above that limit in the high quality crystal regions.
d) Rocking curve measurements carried out with a high-resolution setup showed negligible or only small increases (0.0" … 0.2") of local reflectivity curve widths

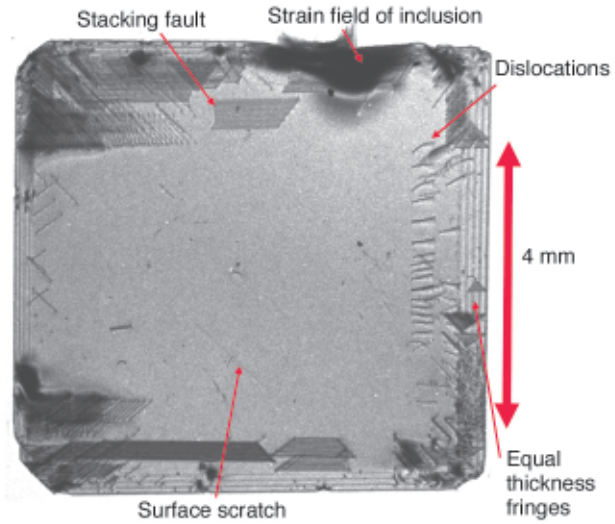

Fig. 143: X-ray white beam topograph of a type IIa diamond plate, showing a homogeneous central region and some typical defects and effects that may be present. No strain fields related to growth sector boundaries are visible.

(1") after extraction of the apparatus function (width about 0.15").
e) For a coherence preserving crystal, both the bulk and the surface quality must be sufficiently high. The material we studied so far was of high bulk quality. The current best surface finish obtained by mechanical polishing was measured on a type Ib sample, a value of 0.3 nm rms was obtained. Type IIa crystal plates have not yet been polished to that quality, the best value was 0.96 nm rms. In the best case, the effective angular source size increased by only 1.1 to 2.5 times. As soon as samples with the full surface processing (and lower micro-roughness) arrive, these measurements will be continued.

Consequently the targets for further development of the type IIa diamond are the increase of its size, a crystal perfection pushed to its limits, and a high quality surface processing.

Authors
J. Härtwig (a), P. Van Vaerenbergh (a), I. Gierz (a), J. Hoszowska (a), A. Rommeveaux (a), A. Chumakov (a), G. Carbone (a), S.H. Connell (b), M. Rebak (b), R. Setshedi (b), D. Dube (b), L. Mkhonza (b), R. Burns (c), J.O. Hansen (c).
(a) ESRF
(b) University of the Witwatersrand, (South Africa)
(c) Element Six Technologies, Johannesburg (South Africa)

X-ray Imaging in Life Science and Medicine

New Irradiation Geometry for Microbeam Radiation Therapy (MRT)

Microbeam Radiation Therapy (MRT) has the potential to treat infantile brain tumours when other kinds of radiotherapy would be excessively toxic to the developing normal brain [1, 2]. MRT uses extraordinarily high doses of X-rays but the brain provides unusual resistance to MRT's radioneurotoxicity, presumably by the migration of endothelial cells from "valleys" into "peaks", *i.e.*, into directly irradiated microslices of tissues. A novel irradiation geometry that results in an even more tolerable valley dose for the normal tissue and a decreased peak-to-valley dose ratio (PVDR) in the tumour area by applying an innovative cross-firing technique has been studied. It consists of orthogonally crossfiring two arrays of parallel, nonintersecting, mutually interspersed microbeams that produces tumouricidal doses with small PVDRs where the arrays meet and tolerable radiation doses to normal tissues between the microbeams proximal and distal to the tumour in the paths of the arrays.

A possible interlaced crossfiring geometry is shown in **Figure 144** with the microbeams at +45 degrees and –45 degrees. Before the second exposure, the target is rotated 90^0 around the axis and then displaced by 105 µm in the plane perpendicular to the direction of propagation of the microbeams, *i.e.* half the distance between two microbeams. The latter displacement was to interlace rather than intersect the orthogonally-propagated microbeam planes.

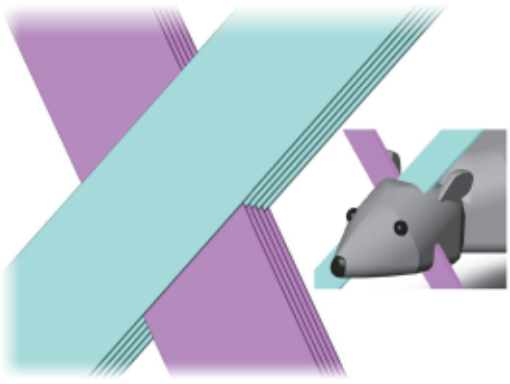

Fig. 144: interlaced cross-firing technique.

The use of microbeams as a potential alternative in radiotherapy is attractive because of the destruction of the vascularisation of the tumour and also because of the high tolerance of these microbeams by normal tissue. This dose-volume effect might therefore be used in the future in radiotherapy where crucial tissue must be spared and selectively different sensitivities of the vasculature between tumour and the surrounding tissue can be exploited. We can further enhance this effect by crossing the microbeams to selectively distribute the valley dose in the tumour to a radiotoxic value and leave the valley dose in the healthy tissue at acceptable values.

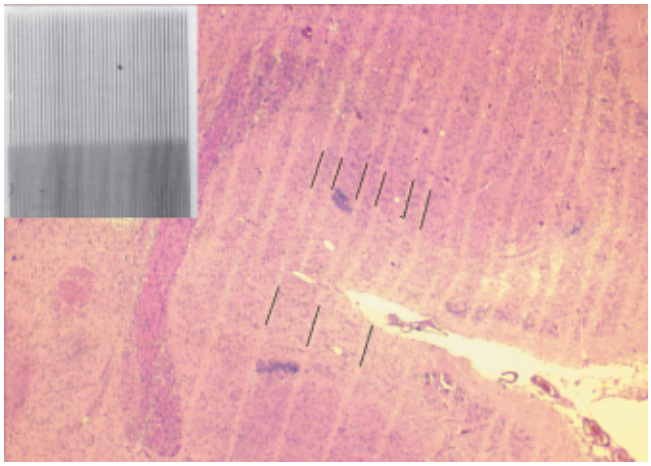

Fig. 145: the interlaced feature of our cross-fired microbeams is still preserved inside the brain of the irradiated specimen; the inserted picture showing the mechanically precise irradiation on a Gafchromic film.

The mechanical feasibility of this technique was demonstrated using Gafchromic films, but in order to answer the question of whether the interlaced feature of our cross-fired microbeams is still preserved inside the brain of the irradiated specimen, the horizontal histology cuts of such irradiated rats are shown in **Figure 145**. The parallelism of the microbeams is well preserved inside the tissue, despite the microscopic movements due to the pulsation of the heart beat and a non-ridged target like the brain. According to our Monte Carlo calculations we profit from an increase of the valley dose by about a factor of 3 (**Figure 146**).

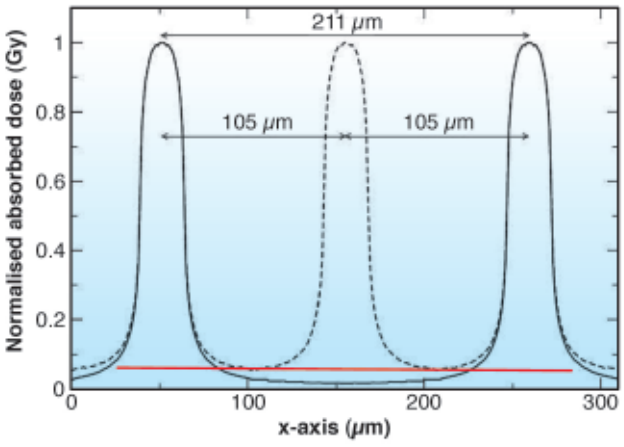

Fig. 146: Schematic illustration of PVDRs and the decrease of valley dose if the second irradiation plane is centred with its peak situated between the peaks of the first irradiation.

There are several methods for increasing the therapeutic index of MRT; first by limiting the cross-fired zone more closely to the actual tumour area. This will be the case when an adequate imaging technique is available and the densely irradiated volume can be reduced to the

actual tumour size. Additionally, a better understanding between the physical and biological correlation of parameters like microbeam planar width and centre-to-centre distances is needed to optimise the parameters which can then be selected more specifically for the healthy tissue area and the tumour region. Moreover, one can expect even better results if we move to larger volumes to be irradiated, since in this case the ratio between the total volume of the brain, the irradiated volume and the more densely crossfired tumour volume become more favourable. Additionally, we can alleviate the limitation of tumour dose, and thereby the limitation of therapeutic efficiency due to skin dose thresholds.

Conventional radiation therapy is hampered by the acceptable threshold dose of the healthy tissue. By using microbeams in an interlaced irradiation geometry, we can take advantage of healthy tissues extraordinarily good tolerance of microbeams and hence deliver a critical level of radiation only to the vicinity of the tumour. The result is a nearly homogenous distribution of high dose that is limited to the tumour area.

References

[1] J. A. Laissue, G. Geiser, P. O. Spanne, F. A. Dilmanian, J-O. Gebbers, M. Geiser, X. Y. Wu, M. S. Makar, P. L. Micca, M. M. Nawrocky, D. D. Joel, and D. N. Slatkin, *Int. J. Cancer* **78**, 654-660 (1998).

[2] J. A. Laissue, N. Lyubimova, H.-P. Wagner, D. W. Archer, D. N. Slatkin, M. Di Michiel, C. Nemoz, M. Renier, E. Brauer, P. O. Spanne, J.-O. Gebbers, K. Dixon, and H. Blattmann, *Proceedings of SPIE Vol.3770*, 38-45 (1999).

Principal publication and Authors

E. Brauer-Krisch (a), H. Requardt (a), P. Régnard (a), S. Corde (a), E. Siegbahn (a), G. LeDuc (a), T. Brochard (a), H. Blattmann (b), J. Laissue (c), A. Bravin (a), *Phys. Med. Biol.* **50**, 3103-3111 (2005).

(a) ESRF

(b) Niederwiesstrasse 13C, Untersiggenthal (Switzerland)

(c) Institute of Pathology, University of Bern (Switzerland)

Evaluation of Gd-EOB-DTPA Uptake in a Perfused and Isolated Mouse Liver Model

Gd-EOB-DTPA is a paramagnetic complex designed as a hepatotropic magnetic resonance imaging (MRI) contrast agent (CA) useful to evaluate liver functions and pathologies [1]. Even if contrast-enhanced MRI is recognised as a powerful tool for the assessment of functional parameters, the quantitative interpretation of the CA effect on image intensity is not straightforward because the MR signal is a complex function of CA characteristics and image acquisition parameters. Depending on its concentration and imaging sequences, a given CA can indeed induce an opposite effect on contrast. For these reasons, CA concentration is difficult to obtain from image intensity measurements. Among computed X-ray tomography methods, monochromatic quantitative computed tomography (MQCT) has been implemented at ESRF (medical beamline, ID17) and highlighted as a complementary tool to other imaging techniques in the field of preclinical research [2]. As a result of the monochromaticity of the synchrotron beam, this technique allows for nondestructive, real-time, and absolute quantitative *in vivo* measurement of Gd concentration. The aim of this study was to evaluate the pharmacokinetic pattern of Gd-EOB-DTPA in a model of isolated and perfused mouse livers by both MRI and MQCT techniques.

Hepatic perfusion consists of the administration to the liver of a blood substituting solution. Three protocols of mice liver perfusion were carried out for MRI experiments (gallbladder spared, severed or clamped) whereas the gallbladder was always spared for MQCT experiments. Gd-EOB-DTPA solution was directly administered through the perfusion medium as follows: for MQCT imaging at a final concentration of 0.26 and 0.52 mM of perfusion medium, and for MRI imaging at the optimal case obtained in MQCT, *i.e.*, 0.52 mM. Mice livers were perfused during 1 hour, with the first 30 minutes in recirculating mode (accumulation of CA) and the following 30 minutes in open circuit (washout period). MRI and MQCT images were acquired during the one-hour perfusion period.

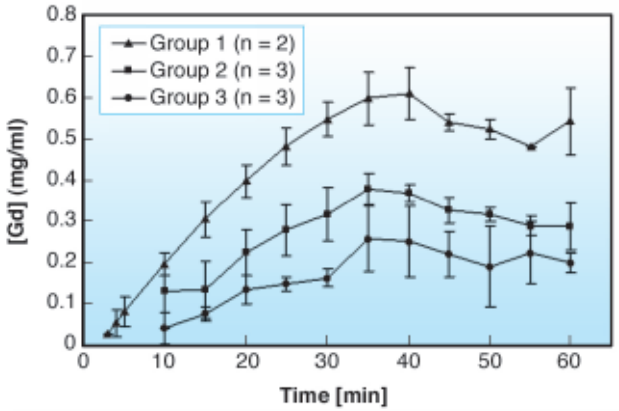

Fig. 147: Pharmacokinetic curves obtained by MQCT.

Figure 147 presents the quantitative results obtained in MQCT after image analysis. At the highest dose, two groups of mice are distinguishable according to the accumulation kinetics of Gd-EOB-DTPA (represented by ▲ and ■). As expected, the curve obtained at the lowest dose exhibits the smallest evolution (represented by ●). At both doses, the kinetic curve of Gd-EOB-DTPA shows the same characteristic: a phase of uptake (increase of liver intensity that reaches a plateau) followed by the clearance of the CA (decrease of the intensity). As in MQCT, two clear trends were also observed in MRI with regard to the accumulation and elimination of Gd-EOB-DTPA when the gallbladder

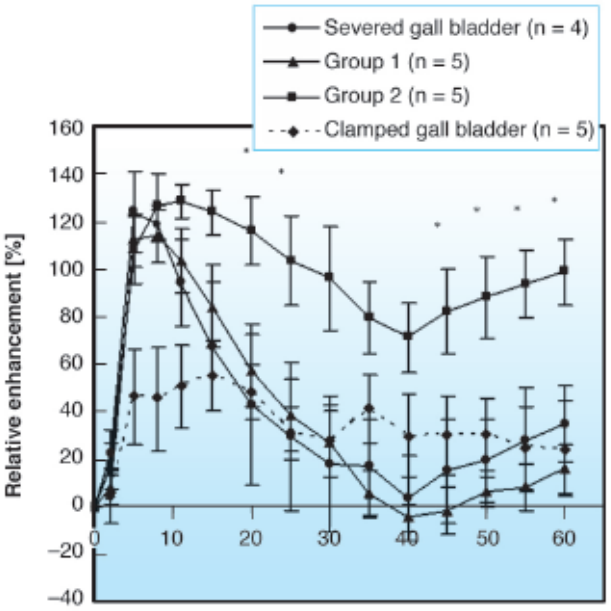

Fig. 148: Relative enhancement expressed in percentage (RE%) as a function of time obtained on MRI images.

was spared (**Figure 148**). The first group exhibited a larger contrast evolution than the second one, in which signal intensities decreased later and less rapidly. Although quantitatively different, these two behaviours have a similar signature characterised by three distinct phases. The first phase is a significant contrast uptake. The increase of signal intensity is caused by a T_1 effect resulting from the accumulation of the CA. The subsequent phase (from the 8th to the 40th minute of perfusion) is characterised by a decrease of intensity, slower in the second group than in the first one. This decrease of intensity is caused by the well-known T_2 effect resulting from a too high concentration of CA accumulated by the liver. Finally, the clearance of the contrast agent is characterised by a restoring of the signal intensity; this is the return to a T_1 effect resulting from the progressive elimination of Gd-EOB-DTPA. Two complementary experiments were performed with MRI to understand the behaviours described here (**Figur 148**). Livers with severed gallbladder follow the same behaviour as livers of the first group while contrast agent accumulation is impaired in livers with clamped gallbladder (low increase of signal intensity).

In conclusion, this pilot study has confirmed the validity of both approaches for evaluating the uptake of a hepatotropic contrast agent by the mouse liver. MRI is an ideal technique for diagnosis, but the complex relationship between the CA concentration and signal intensity makes it difficult to quantitatively follow pharmacokinetic patterns. Although less conveniently accessible, MQCT is the most direct approach to the quantitative measurement of the concentration of the CA. This study has additionally demonstrated the peculiarity of the model of the isolated and perfused mouse liver, which appears unstable, leading to an abnormal behaviour characterised by an impaired uptake function.

References

[1] H.J. Weinmann, W. Ebert, B. Misselwitz and H. Schmitt-Willich, *Eur. J. Radiol.* **46**, 33-44 (2003).

[2] G. Le Duc, S. Corde, H. Elleaume, F. Esteve, A.M. Charvet, T. Brochard, S. Fiedler, A. Collomb and J.F. Le Bas, *Eur. Radiol.* **9**, 1487-1492 (2000).

Principal Publication and Authors

J. Segers (a), G. Le Duc (b), C. Laumonier (a), I. Troprès (c), L. Vander Elst (a) and R.N. Muller (a), *Invest. Radiol.* **40**, 574-582 (2005).

(a) University of Mons-Hainaut, Mons (Belgium)

(b) Biomedical beamline, ESRF

(c) 3T MRI unit, CHU, Grenoble (France)

X-ray Imaging in the Study of Materials

X-ray Microtomography of a Coronary Stent

Coronary stents are small, metallic scaffolds implanted to re-open coronary arteries which have become seriously narrowed or blocked as a result of heart disease. Re-opening the artery restores blood flow to the heart muscle, reducing the risk of a “heart attack”. A stent is implanted by making a small incision, usually in the femoral artery, through which a guidewire and catheter are inserted, enabling the use of small surgical tools at the blockage site. The stent is crimped onto a special balloon catheter. Once in position, the balloon is inflated with saline, expanding the stent and opening up the blocked artery. The balloon is then deflated and the catheter removed, leaving the stent permanently in place as a support for the artery. Wherever possible, stent implantation is used instead of bypass surgery, because it is much less invasive and the patient can often go home from hospital the same day.

Sometimes, stent implantation is compromised by re-blockage of the artery. This is due to an over-active inflammatory response, triggered by injury to the artery wall during surgery. To prevent re-blockage, the latest stents have a drug coating which suppresses inflammation. Despite the introduction of these drug-coated stents, there is still scope for improving stent design and implantation techniques to reduce vessel injury.

While it is known that stent deployment can injure the vessel wall, it is hard to observe how a stent interacts with the artery during implantation. Detailed observation inside a patient is not yet possible. Imaging in engineering laboratory tests is difficult, because of the small stent size (expanded diameter 3.0 mm; strut width

70-100 µm). The challenge is to find a technique that can image stent deployment, in three dimensions, with a resolution of 10 µm or better so that the interaction of individual struts with the artery can be observed.

Fortunately, a candidate technique exists: X-ray microtomography. This is a development of the computed tomography (CT) technique used in hospitals. The operating principles are the same, except that the resolution attainable is higher. Using the coherent synchrotron X-ray source at the ESRF, volume element (voxel) sizes as small as 0.3 µm are possible and phase contrast techniques can be used to enhance imaging.

An experiment was designed to prove the concept of using X-ray microtomography to study a coronary stent. The stents selected for this study were stainless steel coronary R-stents (Orbus Medical Technologies, Inc.). The experimental setup was kept as simple as possible. Each stent was deployed inside a model artery made from latex rubber and silicone foam, which have similar mechanical properties to natural arterial tissue. **Figure 149** shows a stent implanted in a model artery and an X-ray projection taken at the ESRF. Tomography scans were taken before, during and after stent deployment, using beamline BM05. Using 25 keV X-rays, the voxel size was 5.3 µm, with a vertical field of view of 4.5 mm. To image whole stents, which were 13 – 25 mm long, multiple scans were taken, translating the sample vertically between scans until the whole stent was imaged.

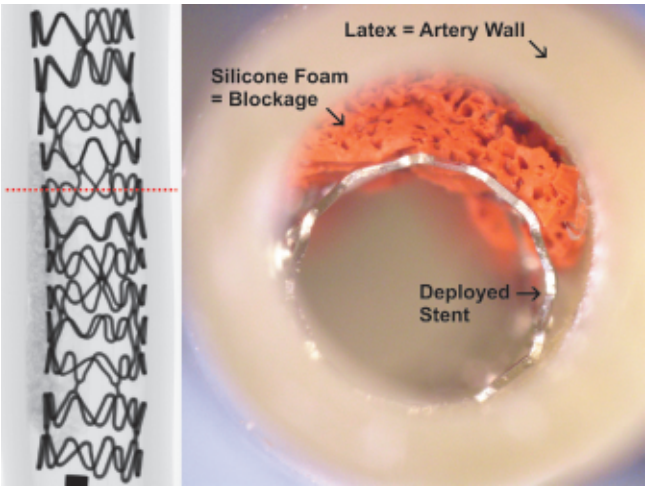

Fig. 149: Photograph of a stent implanted in a model artery. The inset on the left is an X-ray projection of the implanted stent, which is 13 mm long. The dashed line shows the position of the tomography slice shown in **Figure 150**.

The tomography data can be observed in a number of ways, such as cross-sections (slices) through the sample, or rendered images. It is also possible to export the data to computer aided design and mechanical modelling software. **Figure 150** is an example slice, showing the latex tubing representing the artery wall, the stent struts and the silicone foam representing the blockage. Phase contrast makes it possible to see the

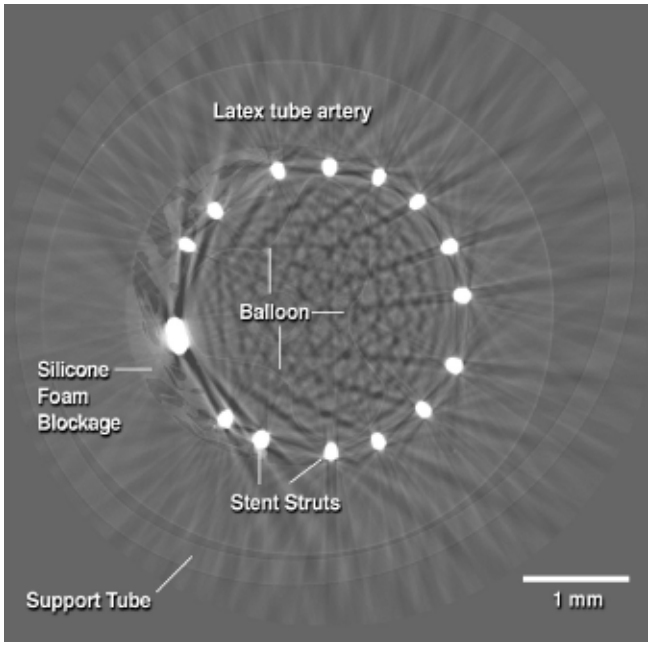

Fig. 150: Example slice from the tomography scan of the stent in **Figure 149**.

foam and the deflated balloon, which was left in place for the scan. The streaks in the image are attenuation artefacts associated with the stent struts. There is a complete set of slices, taken every 5.3 µm, enabling very detailed observation and measurements of stent-artery interactions. Further analysis is in progress.

To conclude, the feasibility of using high-resolution X-ray microtomography to image a coronary stent in a model artery was demonstrated. The stent and artificial artery materials were imaged satisfactorily, though with some attenuation artifacts arising from the metallic stent struts. There is considerable scope to develop the technique further, including observation of real tissue samples or excised stents.

Principal Publication and Authors

T. Connolley (a), D. Nash (a), J-Y. Buffière (b), F. Sharif (a), P.E. McHugh (a), Submitted to *Ann. Biomed. Engng.*

(a) NCBES, National University of Ireland, Galway (Ireland)
(b) GEMPPM, INSA de Lyon, Villeurbanne (France)

New Insight into the Mechanisms of Liquid Metal Embrittlement by X-ray Projection Microscopy

The penetration of liquid gallium into the grain boundaries of aluminium alloys is known to be at the origin of severe intergranular embrittlement of aluminum alloys. However, despite decades of research, no consistent picture of the physical mechanisms leading to the rapid formation of microscopic intergranular liquid layer has evolved so far. For instance, we still do not know whether Grain Boundary Penetration (GBP)

involves the replacement of solid metal atoms by liquid metal atoms (through dissolution for instance) or if it proceeds by an invasion like process involving deformation and separation of the grains by an amplitude equal to the liquid layer thickness.

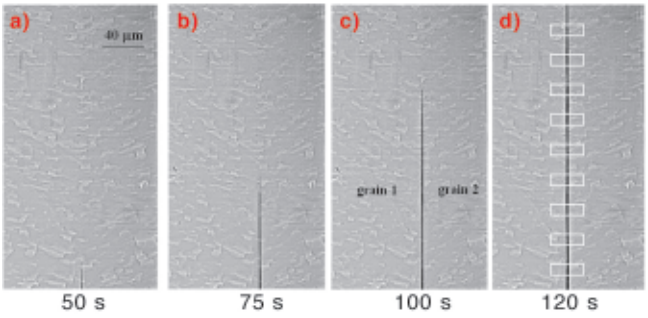

Fig. 151: Microradiographs showing liquid Ga penetration along an Al bicrystal grain boundary. The field of view is situated approximately in the centre of the 4 mm long grain boundary. The last image shows the regions of interest used to analyse the penetration rate.

The use of the novel ESRF X-ray projection microscope, based on Kirkpatrick-Baez optics [1], has now provided an answer to this ongoing controversy: the unique combination of high resolution, bulk and *in situ* observation capabilities provided by this instrument has allowed us to simultaneously characterise the liquid film thickness (deduced from X-ray attenuation measurements) and any associated grain deformation (determined via image correlation techniques) during the penetration process. The experiments have been performed at a X-ray energy of 20.5 keV using pure Al bicrystal slices (10 x 4 0 x 0.8 mm^3) which were imaged in close to edge-on configuration. In this acquisition geometry the detection limit for liquid Ga films can be as low as 5 nm [2]. **Figure 151** shows four out of a series of several hundred projection images acquired during the penetration process of the bicrystal sample. The restricted field of view of about 150 x 250 µm was situated approximately in the middle of the 4 mm long grain boundary and the *in situ* observation was started with the initiation of penetration process at the lower extremity of the grain boundary and was continued until arrival of the penetration front at the other extremity of the bicrystal. The four images were chosen from the restricted time interval of about 70 seconds during which the penetration front has crossed the field of view. The analysis of the penetration kinetics from the images acquired in this time window reveals a linear penetration rate of 3.4 µm per second (**Figure 152**), in good agreement with previous measurements [2].

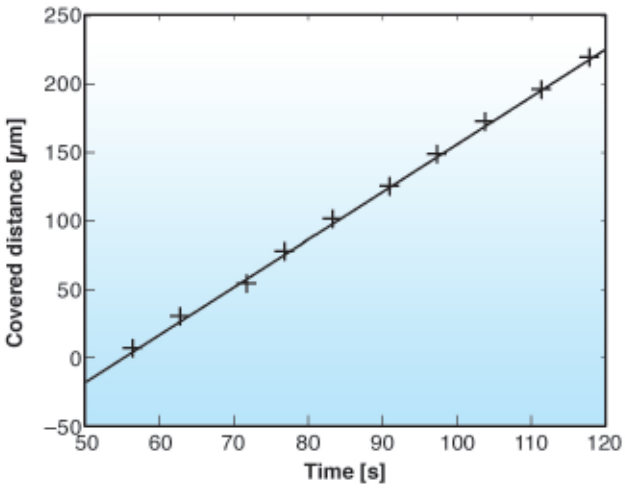

Fig. 152: Plot of the penetration distance versus time.

The simultaneous measurement of the grain deformation during the penetration process was based on image correlation of surface stains, left over from the chemical etching and subsequent polishing of the sample surface. **Figure 153a** depicts the three regions of interest, the relative displacements of which was analysed during the entire period of the penetration process. As can be seen from the plot in **Figure 153b**, the final amplitude of the

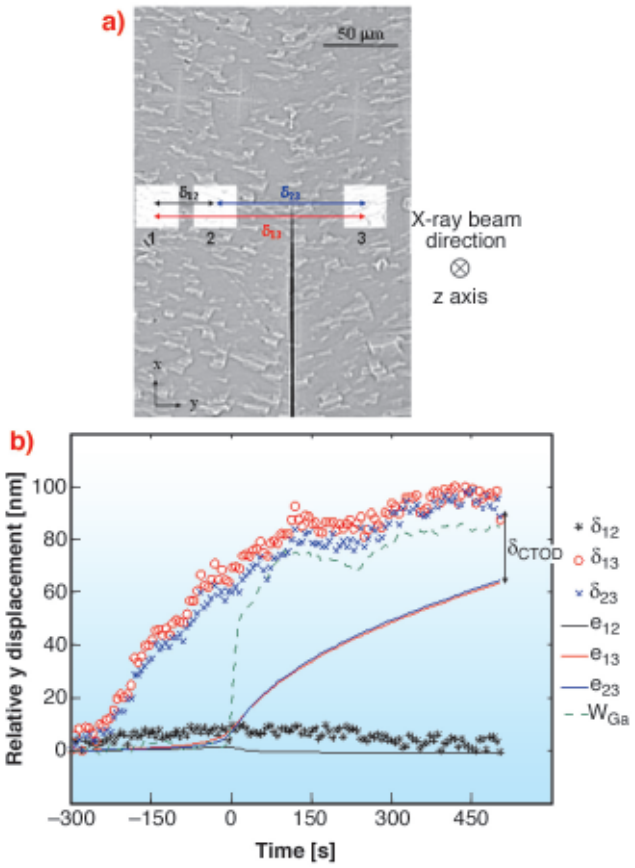

Fig. 153: (a) The three ROIs and their relative distances (δ_{12}, δ_{23}, δ_{13}) analysed during the penetration process. (b) Evolution of the relative grain displacement with time, giving clear evidence for grain deformation during penetration. The measured film thickness w_{Ga} and the displacement that would be provoked by a purely elastic crack propagation (solid lines e_{12}, e_{13}, e_{23}) with a constant stress intensity factor K_I = 0.045 MPa.$m^{0.5}$ are also presented. The difference between the simulated and the experimental displacement, as well as the time lag of about 200 s between onset of displacement and attenuation contrast, can be attributed to the accompanying plastic deformation process.

relative displacements between the regions of interest situated on opposite sides of the grain boundary is close to the thickness of the liquid Ga film as estimated from the absorption measurements, whereas the relative displacement of the regions of interest situated on the same grain is close to zero. Note, however, that the onset of the relative grain displacement occurs about 200 s before the arrival of the Ga penetration front. This time lag can be explained in a consistent way, if one assumes that the penetration of the microscopic Ga layer can be assimilated to the propagation of a crack along the grain boundary. The experimentally observed displacement amplitudes as well as the time shift can be rationalised with fracture mechanics by assuming the existence of a very weak (0.045 MPa.m$^{0.5}$) but constant stress intensity factor during the propagation of the liquid film. This rather surprising finding would suggest the existence of some kind of local crack driving force at the tip of the penetration front.

The answer to the initial question about the formation mechanism of the microscopic penetration layers, has given rise to a new question concerning the origin of the driving force: is it residual stresses in the bicrystal sample or some more fundamental physico-chemical mechanisms at the propagation front which maintain the crack propagation in the case of Al-Ga?

References

[1] O. Hignette, P. Cloetens, G. Rostaing, P. Bernard, C. Morawe, *Rev. Sci. Instrum*. **76**, 063709 (2005)
[2] W. Ludwig, E. Pereiro-Lopez, D. Bellet, *Acta Mater.* **53**, 151 (2005)

Principal Publication and Authors

E. Pereiro-Lopez (a,b), W. Ludwig (c), D. Bellet (a,b), P. Cloetens (b), C. Lemaignan (a,d), PRL **95**, 215501 (2005).
(a) ENSPG, INPG, Saint Martin d'Hères (France)
(b) ESRF
(c) INSA de Lyon (France)
(d) CEA Grenoble (France)

X-ray Fluorescence and Diffraction Microscopy

Microspectroscopy of Sulfur Helps Conservation of Henry VIII's Warship Mary Rose

The *Mary Rose* served successfully for 35 years in Henry VIII's navy. In 1545, when preparing for battle with a French fleet, she suddenly capsised and sank outside Portsmouth, U.K. The starboard side of the hull, salvaged in 1982, has been sprayed with an aqueous solution of polyethylene glycol (PEG) for the last 10 years, to prevent the waterlogged wood from cracking in the final drying stage of conservation (**Figure 154**). The report of tons of reduced sulfur compounds slowly forming acid in the almost intact hull of the 17th century Swedish warship *Vasa* gave rise to new concerns [1], and core samples taken from the *Mary Rose's* hull revealed about 1 mass% sulfur throughout the oak timbers (~ 280 tons). When atmospheric oxygen gains access to the moist wood in the presence of catalytically-active iron ions, this starts the acid-producing oxidation of the reduced sulfur compounds.

Fig. 154: Hull timbers of the *Mary Rose* being sprayed with PEG solution *(photo F. Jalilehvand)*.

The total sulfur and iron concentrations were determined by several methods in cores (0.4 x 15 cm) sampled from the *Mary Rose* hull timbers [2]. Sulfur K-edge X-ray absorption near edge structure (XANES) spectra of segments along the cores were measured at Stanford Synchrotron Radiation Laboratory. They permitted the relative amounts of sulfur in different functional groups to be evaluated by curve fitting with normalised XANES spectra of known standard compounds. Often several types of reduced sulfur species contribute to a major XANES peak at ~ 2473 eV: thiols (R-SH), disulfides (R-SS-R), elemental sulfur (S_8), occasionally pyrite (FeS_2) and other iron sulfides. Magazine stored timber and core surfaces show minor amounts of sulfonates ($R\text{-}SO_3^-$) and sulfate (SO_4^{2-}) at 2483 eV, while hull timber under spray treatment has almost no sulfate. Sulfoxides (R(SO)R),

absorbing at 2476 eV, are intermediate organosulfur oxidation products occurring in a few % in all XANES spectra.

Thin wood slices were examined using scanning X-ray absorption microspectroscopy (SXM) at ESRF beamline **ID21**. Raster scanning with focused X-rays at characteristic sulfur XANES resonance energies were used to create SXM images, revealing that reduced sulfur species (at 2473 eV) are concentrated in the lignin-rich middle lamella between the wood cells, and also in a distinct double layer in the lignin-reinforced walls of a vessel, which is a transport channel in oak wood. Focused micro-XANES spectra confirmed that the organosulfur consists of thiols and disulfides, and occasionally iron sulfides in separate particles (**Figure 155**).

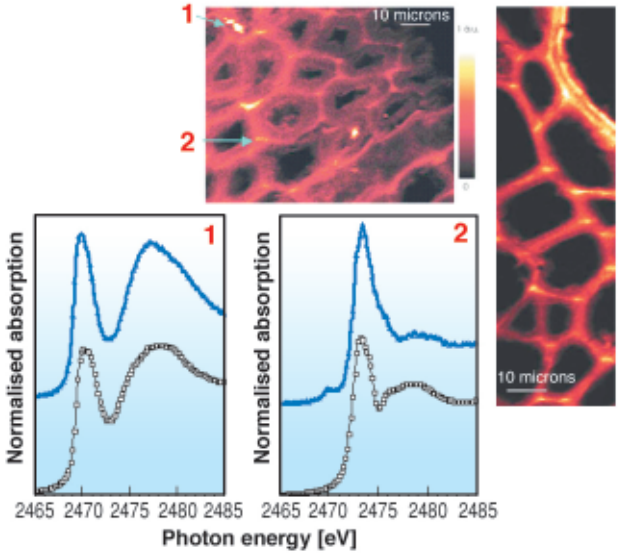

Fig. 155: Scanning X-ray microspectroscopy images at 2473 eV of reduced sulfur (brighter color → higher concentration): (top) oak core, sampled from *Mary Rose* hull timber. (below) Micro-XANES curves (blue: sample spots, black: standard spectra) indicating 1 iron sulfide particle (standard: pyrrhotite $Fe_{1-x}S$, peak at 2471 eV); 2 thiols (R-SH) in the middle lamella (standard: cysteine 2473 eV). (right) Freshly salvaged oak wood from the *Mary Rose* shows two distinct layers of thiols in the lignin-reinforced wall of a vessel (top right); the dark patches surrounded by cell walls are the lumina.

Dissolved hydrogen sulfide (or HS^-), produced by bacteria reducing sulfate ions in anoxic seawater, converts in the waterlogged wood to solid sulfur compounds in amounts depending on the state of wood degradation, the concentration of hydrogen sulphide, and of iron(II) ions. The microcrystalline iron sulfides formed in the presence of corroding iron, are known to be unstable toward oxidation in a humid environment, and are probably the primary source of acid.

For the *Mary Rose* the spraying washes out the acid, and the recirculated PEG solution is monitored to assess when strongly acid-forming sulfur species are exhausted. Antioxidants are being evaluated for subsequent stabilisation of the lignin-bonded organosulfur compounds and also to prevent PEG degradation. In the international "Preserve the *Vasa*" project, tests are being carried out to remove iron with efficient chelates [2], or in other ways retard the oxidation processes. The sulfuric acid accumulated in the *Vasa's* hull timbers after the spray treatment was stopped in 1979, is estimated to be about 2 tons. Neutralising that acid with an ammonia gas treatment, followed by storage in stable and low (~ 55%) relative humidity, may be sufficient to hold back the production of new acid and possible wood degradation effects. Synchrotron-based analyses will continue to play an important role for the development of conservation methods for historical shipwrecks and marine-archaeological artefacts.

References

[1] M. Sandström, F. Jalilehvand, I. Persson, U. Gelius, P. Frank, I. Hall-Roth, *Nature* **415,** 893-897 (2002); see also Feb. 2002 SSRL Science Highlights: *http://www-ssrl.slac.stanford.edu/research/highlights_archive/vasa.html.*
[2] M. Sandström, Y. Fors, F. Jalilehvand, E. Damian, U. Gelius, in *Proceedings of the 9th ICOM Group on Wet Organic Archaeological Materials Conference, Copenhagen 2004,* P. Hoffmann *et al.* (Eds.), Deutsches Schiffahrtsmuseum, Bremerhaven, 2005, pp. 181-199; see also: *http://www.fos.su.se/~magnuss/*.

Principal Publication and Authors

M. Sandström (a), F. Jalilehvand (b), E. Damian (a), Y. Fors (a), U. Gelius (c), M. Jones (d) and M. Salomé (e), *PNAS 40*, 14165-14170 (2005).
(a) Structural Chemistry, Stockholm University (Sweden)
(b) Department of Chemistry, University of Calgary (Canada)
(c) Department of Physics, Uppsala University (Sweden)
(d) The Mary Rose Trust, HM Naval Base, Portsmouth (U.K.)
(e) ESRF

In situ Fe XANES on Extraterrestrial Grains Trapped in an Aerogel for the Stardust Mission

In January 2006, the NASA Stardust mission will bring aerogel collectors back to Earth in which grains of the comet Wild-2 as well as interstellar grains have been trapped. In order to develop an analytical protocol, micrometre-sized grains trapped inside pieces of aerogel were analysed. The pieces of aerogel, called keystones, were a few hundreds of micrometres large. They originate either from the NASA Orbital Debris Collection Experiment (ODCE) exposed outside the Mir station for 18 months from 1997 to 1998 (samples LC01B2, 2D0403

and 2D0401), or from gas gun shots in Stardust's aerogel of grains from the Allende meteorite (sample 8JUN05B). Micro-fluorescence mappings and XANES spectra at the iron K-edge have been performed on these samples using the X-ray Microscopy beamline ID21.

From the micro-fluorescence mappings performed on the ODCE samples, both the final grain and the penetration track were identified (**Figure 156**). It can be concluded from the Fe "hot spots" found along the track that the incident grain broke up into many fragments while entering and slowing down in the aerogel in spite of its low density (0.02 g.cm^{-3}). For the other sample 8JUN05B, the only material found along the track is in the form of iron beads coming from the barrel of the dust gun, confirming that Stardust's aerogel, characterised by a gradient of density, is suitable for slowing down hypervelocity particles. The efficiency of a new technique consisting in cutting the keystone along the penetration track was verified on the sample 2D0401 by imaging the track and the final grain both exposed to the air by this preparation. This allows coupling X-ray analyses with other analytical techniques like Raman and IR microspectroscopies since the beam no longer needs to pass through the aerogel.

In a previous experiment, we showed with LC01B2 that the redox state of iron varies from the entrance of the track (Fe^{3+}) to its end and the final grain (Fe^{2+}) [1]. In order to confirm this, XANES spectra at the Fe K edge were acquired in hotspot regions of each sample using a Si(220) monochromator with an incident energy ranging from 7.1 to 7.28 keV in steps of 0.25 eV. The synchrotron X-ray source was demagnified using Fresnel zone-plate lenses and the beam size at the sample was 0.5 x 0.5 μm^2. For each spectrum, the energy of the absorption edge and the centroid energy of the pre-edge (intensity-weighted average of each component energy) were used to determine the Fe redox states, following [2]. Results are summarised in **Table 3**. The edge and the pre-edge centroid (**Figure 157**) evolve towards a reduced form (Fe^{2+}) from the track entrance to the end of the track and the final grain. Beam-induced photo-reduction was checked for by acquiring several spectra on the same points and seeing no shift towards lower energies.

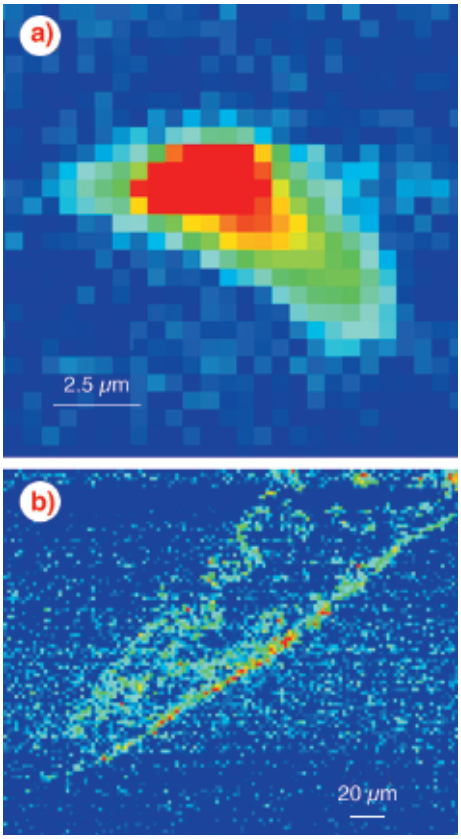

Fig. 156: Fe distribution in 2D0401: (a) The final grain 4 μm in size. (b) The penetration track, about 250 μm long, with a spatial resolution of 2 μm.

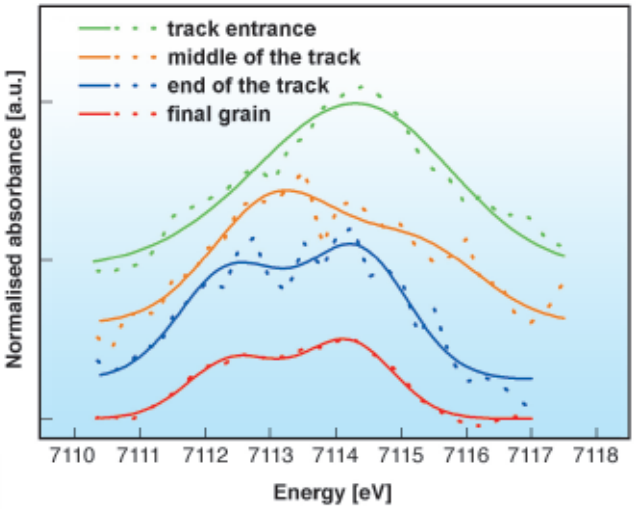

Fig. 157: Normalised pre-edge features of absorption spectra in different region of 2D0401. The data are represented by a dotted line and the fit of the pre-edge by a solid line.

Sample	Region	Edge energy (eV)	Pre-edge centroid (eV)
	(a)	7123.7	7114.2
2D0401	(c)	7119.9	7113.4
	final grain	7119.5	7113.4
	(b)	7119.2	7114.0
2D0403	(c)	7118.3	7113.4
	final grain	7119.7	7113.5
	(a)	7123.2	7114.6
LC01B2	(c)	7119.6	7113.6
	final grain	7119.7	7113.1
8JUN05B	final grain	7119.5	7113.5

Table 3: Edge and pre-edge characteristics of Fe-XANES spectra.

(a) track entrance, (b) middle of the track, (c) end of the track.

Given the observed Fe redox state of the particles in the aerogel, several mechanisms can be inferred. Most probably, incident grains of 2+ oxidation state undergo rapid oxidation to 3+ at the entrance of the track, due to high temperature slowing down from the initial velocity of a few km.s^{-1} in the presence of the aerogel oxygen. The shell of oxidised iron is lost at the track entrance by the grain that remains in the 2+ oxidation state at the end of the track.

In conclusion, fluorescence imaging using the ID21 SXM was succesful in locating the residual impacted grain and the substantial fraction of matter spread along the penetration track. Furthermore, Fe K-edge XANES allows precise studies of the redox reactions associated with the grain slowing down in the oxygen-rich aerogel.

References

[1] J. Borg, Z. Djouadi, F. Grossemy, D. Eichert, G. Martinez-Criado, A.J. Westphal, D. Deboffle, C.J. Snead and A. Somogyi, *Advances in Space Research, in press* (2005)

[2] M. Wilke, F. Farges, P-E. Petit, GE. Brown Jr and F. Martin, *Amer. Min.,* **86**, 714-730 (2001)

Authors

F. Grossemy (a), J. Borg (a), Z. Djouadi (a), A. Simionovici (b), L. Lemelle (b), D. Eichert (c), D. Deboffle (a).

(a) Institut d'Astrophysique Spatiale (IAS), Université Paris-Sud 11 and CNRS, Orsay (France)

(b) Laboratoire des Sciences de la Terre (LST), ENS Lyon (France)

(c) ESRF

Evidence of Ion Diffusion at Room Temperature in Microcrystals of the $Bi_2Sr_2CaCu_2O_{8+\delta}$ Superconductor

Single crystals of the $Bi_2Sr_2CaCu_2O_{8+\delta}$ (Bi-2212) high-*T*c superconductor can be grown in samples whose length (≥ 500 µm) is much greater than both their width and their thickness (whiskers). These kinds of samples have recently attracted remarkable interest from the point of view of both basic and applied physics. In fact, they have proved to be suitable systems for the study of the excess conductivity above T_c and of the transport properties along the *c* axis because of their high quality and small sizes [1].

Bi-2212 whiskers undergo a significant increase in the in-plane resistivity when aged at room temperature, most likely because of the oxygen loss [2]. Variations in the O non-stoichiometry of Bi-2212 whiskers must be accompanied by a change of the Cu oxidation state to guarantee the electrostatic neutrality. To verify whether the variation of the local Cu oxidation state, induced by O diffusion, is accompanied by a cation migration or not, we have combined µ-XANES and µ-XRF experiments at beamline ID22. Also the *c*-axis value has been monitored by µ-XRD. A laboratory AFM study supports the ID22 data.

Figure 158 presents the Cu K edge fluorescence µ-XANES spectra. Moving from the central position (green spectrum) to the crystal edge (red spectrum), we observe an increase in the white line intensity of ≈ 10% and a red shift of the edge of 2.5 eV. This indicates an important gradient of local structure and in the oxidation state of Cu along the *b* direction. At the crystal edges a significant Cu^+ enrichment is observed (**Figure 158**). This is where the atomic O^{2-} anions are supposed to recombine to give O_2 molecules, which then leave the crystal (leaving behind their 4 electrons). According to previous XANES studies we evaluated that a fraction of about 30% of Cu^+ is estimated at the edges [3]. This suggests that the rate-determining step of the O loss process is the O^{2-} migration to the crystal surface and not the O_2 recombination at the surface. From the µ-XRF study (**Figure 158** inset) a Cu enrichment at the crystal edges along the *b* direction is found.

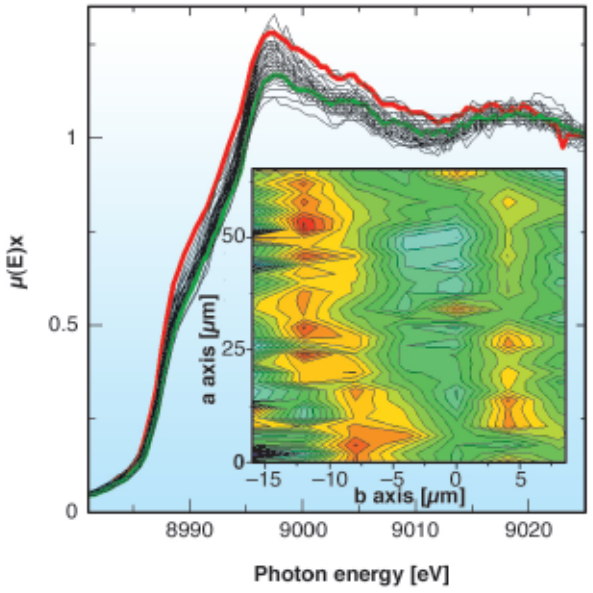

Fig. 158: Normalised XANES spectra collected on different positions of the Bi-2212 whisker. A shift of the edge up to 2.5 eV, accompanied by a modification of the white line intensity, which clearly displays an important modification of both the oxidation and the coordination state of Cu along the crystal. Bold curves represent spectra collected in central (green) and in near-edge (red) positions along the b direction, the others representing intermediate positions.
The inset shows the map (resolution 1 x 4 µm) reporting the ratio between the Cu(Kα) and Bi(Lβ) XRF counts on the same portion of the Bi-2212 sample used for the XANES study (color scale: red = 0.24; green = 0.22; blue = 0.20). The red regions correspond to the edge of the crystal, where a Cu enrichment has been observed. Beam energy = 17.3 keV).

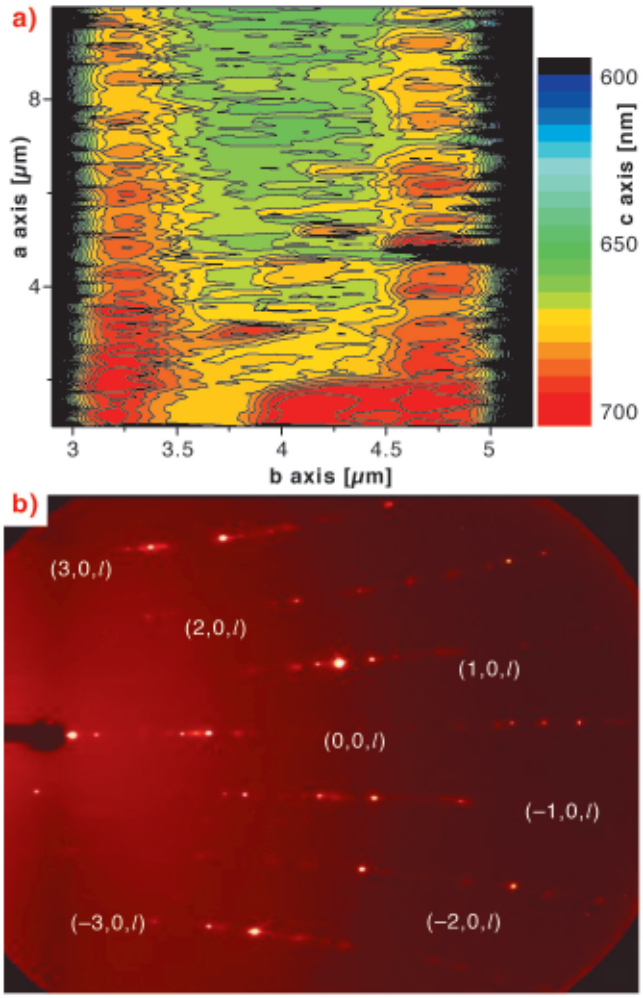

Fig. 159: (a) Colour scale AFM map of the Bi-2212 sample. The red regions correspond to the edge of the crystal, where a higher thickness has been observed. (b) (h, 0, l) reflections (h = -3, -2, -1, 0, 1, 2 and 3) collected at ID22 in transmission mode with an image plate sampling a point in the border region along the b axis. Beam energy = 17.3 keV.

The crystal, exhibiting an almost flat *a*-*b* surface in the as-grown condition, clearly shows an increased thickness Δz at the borders along the *b* direction, as determined by AFM (**Figure 159a**). This is the consequence of the O depletion, which is known to induce an increase of the *c* axis lattice parameter whose average over the crystal size along the *c*-axis direction (≈ 200 unit cells) has been clearly detected by AFM. The *c*-axis increase, located at the border of the crystal along the *b* direction, well correlates with the higher fraction of Cu^{+} singled out in the same region by μ-XANES (**Figure 158**). These independent pieces of evidence agree with the anisotropy in the in-plane O diffusion coefficients for Bi-2212 that indicates a slower migration process along the *b* direction. Therefore, the possibility of identifying a compositional gradient is enhanced. Quantitatively, the measured $\Delta z/z$ (corresponding to $\Delta c/c$) is 4%, indicating that the average *c* value on the *b* borders is around 32 Å. μ-XRD measurements, collected at ID22 in transmission mode with an image plate, resulted in *c* = 32.2 Å for the *b* border region (**Figure 159b**).

References

[1] Y.I. Latyshev, T. Yamashita, L.N. Bulaevskii, M.J. Graf, A.V. Balatsky, and M. P. Maley, *Phys. Rev. Lett*. **82**, 5345-5348 (1999).

[2] M. Truccato, G. Rinaudo, C. Manfredotti, A. Agostino, P. Benzi, P. Volpe, C. Paolini, and P. Olivero, *Supercond. Sci. Technol*. **15**, 1304-1310 (2002).

[3] C. Lamberti, G. Turnes Palomino, S. Bordiga, G. Berlier, F. D'Acapito and A. Zecchina, *Angew. Chem. Int. Ed*., **39** 2138-2141 (2000).

Principal publication and Authors

M. Truccato, C. Lamberti, C. Prestipino, A. Agostino, *Appl. Phys. Lett.*, **86**, 213116 (2005).

NIS centre of Excellence University of Turin, and INSTM (Italy)

Scaling in the Time Domain - Universal Dynamics of Order Fluctuations in Fe_3Al

Solid state theory predicts that a material should respond ultra-sensitively to external perturbations (temperature, pressure, magnetic or electric fields), when it is close to a phase transition. This response is governed by microscopic fluctuations in the system: quantities like volume, entropy or sub-lattice order are strongly fluctuating for temperatures near the critical temperature T_C. For continuous phase transitions, the correlation length (ξ) in the system is diverging [1] when T_C is approached. The mesoscopic size of fluctuating domains leads to universal macroscopic response functions – power laws involving critical exponents that depend only on the dimensionality and symmetry of the system. X-ray and neutron scattering experiments have led to a consistent picture of the static critical behaviour. However, since fluctuations exhibit a time structure, our picture of phase transformations is incomplete without understanding the microscopic fluctuations in the time domain.

Recently the technique of X-ray intensity fluctuation spectroscopy has been developed, using coherent synchrotron X-ray beams: the diffracted intensity is a time-dependent "speckle pattern", uniquely related to the spatial arrangement of the ordered domains in the sample [2]. This approach is strongly limited today by the low intensity in the coherent beam. In order to observe dynamic fluctuations on a microscopic scale we used a partially coherent focused X-ray beam (**Figure 160**) illuminating the sample which is kept close to T_C. We record in real time intensity fluctuations of the diffracted beam, which are associated with the order fluctuations in the sample. Since a fully coherent beam is not required in this approach, the whole X-ray beam can be focused

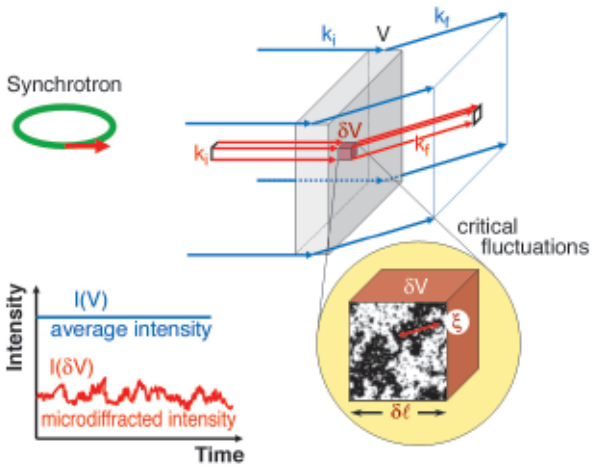

Fig. 160: Principle for a diffraction "microscope": In a conventional diffraction experiment (large probed volume compared to ξ) an ensamble average is performed, the diffracted intensity is constant (blue curve). When the probed volume in the sample δV is small enough to contain only a few fluctuating domains (each of size ξ), the diffraction experiment no longer performs an ensamble average; the diffracted intensity fluctuates and directly reflects the dynamics of thermal fluctuations (red curve).

to a micrometre spot on the micrometre-thick sample. Thus, we reduce the probed volume to a few μm^3 and also preserve the high number of incident photons.

The experiment was carried out at the ID22 beamline using a focused beam slightly smaller than 2 x 2 μm^2. The sample was a Fe_3Al single crystal, in which the Fe and Al atoms order on a cubic lattice (chemical order). Upon increasing the temperature, the atoms are mobile enough to jump between sites, reducing the chemical order (crystalline order still preserved). We investigated the B2-A2 order-disorder transition in Fe_3Al

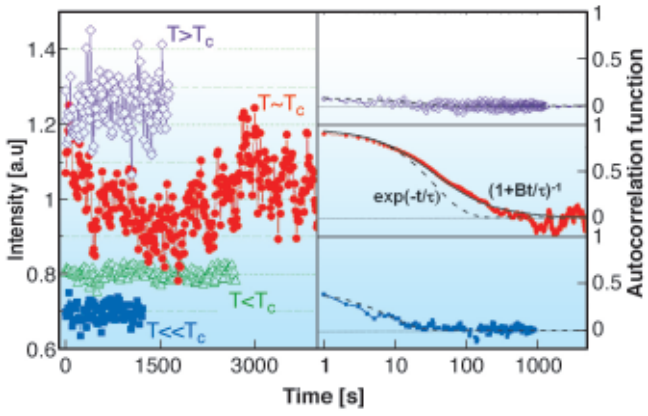

Fig. 161: (left) Time-resolved diffraction intensities at temperatures near T_C. The series are normalised to 1 then shifted vertically for the sake of clarity. (right) Correlation functions for different temperatures. Black lines are the fits using the algebraic forms: exponential decay (dotted line) and power law decay (continuous line).

by recording (near Tc) the intensity of superstructure peaks. Upon increasing the temperature, the atoms are mobile enough to change sites and reduce the chemical order whereas the crystalline order is still preserved. Consequently the intensity of superstructure peaks diminishes and ultimately vanishes in the disordered state. Moreover, in the vicinity of T_C the X-ray intensity exhibits fluctuations in time, fluctuations which are diverging at T_C (shown in **Figure 161** (left)). We have recorded in real time the X-ray intensity fluctuations close to T_C, where both ordered and disordered domains exist. The associated fluctuating domain size is expected to diverge.

The autocorrelation functions of the measured intensities (**Figure 161** (left)) are 4-point correlation functions. The theoretical analysis showed that the autocorrelation functions can be very well described in a simple form: an exponential decay at temperatures far from T_C and a power law decay for $T \approx T_C$ (**Figure 161** (left)). The associated critical exponent is deduced and found to be in good agreement with the theoretical value ($z \sim 2$), demonstrating the universal character of the fluctuations in Fe_3Al. The dynamics of the ordered domains was slow enough to be accessed in a time-frame of the order of a few seconds. The associated correlation times are surprisingly large (up to 70 seconds at $T \approx T_C$), many orders of magnitude larger than the characteristic microscopic time-scale (~10^{-7} seconds for the single jump of a Fe atom). The decay of the correlation function with a power law confirms scaling in the time domain.

Our results clearly indicate that incoherent focused microbeams can be used to study 4-point correlation functions and the dynamics of critical fluctuations in crystalline materials. The experimental results demonstrate directly the crossover from non-critical ($T < T_C$) to critical ($T \sim T_C$) dynamics in solid binary alloys. With the development of high brilliance micro- and nanobeams at synchrotron radiation and free electron laser facilities, such experiments will give access to other type of fluctuations, particularly for systems in confined geometries as they appear in thin films and nanosystems.

References

[1] M. E. Fisher, in Critical Phenomena, M. S. Green, Ed. (Academic Press, London, 1971).
[2] M. Sutton *et al.*, *Nature* **352**, 608 (1991).

Principal Publication and Authors

C. Mocuta (a,b), H. Reichert (a), K. Mecke (a), H. Dosch (a) and M. Drakopoulos (b), *Science* **308,** 1287 (2005).
(a) Max-Planck-Institut für Metallforschung, Stuttgart (Germany)
(b) ESRF

ESRF

Highlights 2005

The X-ray Source

Introduction

Throughout 2005, the Machine Division continued its efforts to improve performance whilst carrying out a number of developments, which are described hereunder.

Machine Parameters

Table 4 presents a summary of the characteristics of the storage ring's electron beam:
Table 5 gives the main optics functions, electron beam sizes and divergences at the various source points. For insertion device source points, the beta functions, dispersion, sizes and divergences are computed in the middle of the straight section. Two representative source points of bending magnet radiation have been selected, corresponding to observation angles of 3 mrad and 9 mrad from the exit, which correspond to different magnetic fields. Electron beam profiles are Gaussian and the size and divergence are presented in terms of rms quantities. The associated full width half maximum sizes and divergences are 2.35 times larger. Horizontal electron beam sizes and divergences are given for the uniform filling modes and apply to almost all filling patterns except for the single bunch, for which a slightly larger size and divergence is attained due to the increased energy spread of the electron beam. Vertical electron beam sizes and divergences apply to the Uniform, 2 x 1/3 and Hybrid filling modes only. To increase the lifetime of the stored beam, the vertical beam sizes and divergences are increased typically by 50% in the 16 and 4 bunch filling patterns.

The lifetime, bunch length and energy spread depend, to a large extent, on the filling pattern. These are given in **Table 6** for a few representative patterns. Note that in both the 16 bunch and 4 bunch filling patterns, the energy spread and bunch length decay with the current (the value indicated in the table corresponds to the maximum current). The bunch lengths are given for the usual RF accelerating voltage of 8 MV.

Energy	[GeV]	6.03
Maximum current	[mA]	200
Horizontal emittance	[nm]	4
Vertical emittance (minimum achieved)	[nm]	0.03
Revolution frequency	[kHz]	355
Number of bunches		1 to 992
Time between bunches	[ns]	2816 to 2.82

Table 4: Principal characteristics of the electron beam.

		Even ID Section (ID2,ID6…)	Odd ID Section (ID1,ID3 …)	Bending Magnet 3 mrad	Bending Magnet 9 mrad
Field	[T]	Depends on ID	Depends on ID	0.4	0.85
Horiz. Beta Functions	[m]	35.2	0.5	1.41	0.99
Horiz. Dispersion	[m]	0.137	0.037	0.061	0.045
Horiz. rms e- beam size	[µm]	402	59	100	77
Horiz rms e- divergence	[µrad]	10.7	90	116	111
Vert. Beta Functions	[m]	2.52	2.73	34.9	34.9
Vert. rms e- beam size	[µm]	7.9	8.3	29.5	29.5
Vert. rms e- divergence	[µrad]	3.2	3	0.85	0.85

Table 5: Beta functions, dispersion, rms beam sizes and divergences for the various source points of the ESRF.

Filling pattern		Uniform	Hybrid	16-b	4-b
Number of bunches		992	24x8+1	16	4
Maximum current	[mA]	200	200	90	40
Lifetime	[h]	75	30	11	6
Rms energy spread	[%]	0.11	0.11	0.12	0.16
Rms bunch length	[ps]	20	25	48	55

Table 6: Current, lifetime, bunch length and energy spread in various representative filling modes.

RUN NUMBER	TOTAL 2004	2005-01	2005-02	2005-03	2005-04	2004-05	TOTAL 2005
Start		21/01/05	08/04/05	03/06/05	19/08/05	21/10/05	
End		25/03/05	25/05/05	27/07/05	17/10/05	19/12/05	
Total number of shifts	843	189	141	162	177	177	846
Number of USM shifts	681	149	114	131	146.1	143.1	683.250
Beam available for users (h)	5295.2	1162.6	871.1	1015	1127.5	1119.8	5296
Availability	97.95%	97.8%	96.6%	97.6%	97.6%	98.3%	97.6%
Dead time for failures	2.05%	2.2%	3.4%	2.4%	2.4%	1.7%	2.4%
Dead time for refills	0.75%	0.3%	1.1%	0.7%	1.1%	0.5%	0.7%
Average intensity (mA)	151	185	120	149	123	181	153.4
Number of failures	111	28	30	24	21	20	123
Mean time between failures (h)	49.1	42.6	30.4	43.7	55.7	57.3	44.4
Mean duration of a failure (h)	1.0	0.9	1	1.1	1.4	1	1.06

Table 7: Summary of the Machine Operation in 2005.

Summary of Machine Operation

In 2005, 683.25 shifts (5466 hours) of beam were scheduled, of which 5296 hours of beam were effectively delivered (including 39.4 hours of refills). This represents a beam availability of 97.6%. Dead time due to failures accounts for the remaining 2.4% (see **Table 7**). In March there was a serious failure originating from a water leak into the ring vacuum on the cell-15 crotch absorber (see below); this resulted in the loss of five days. In order to return this lost time to the users of the ESRF, the October shutdown was shortened and five days of USM added with proper advanced re-scheduling. The figure of beam availability has been modified retroactively. The Mean Time Between Failures (MTBF) reached 44.4 hours.

Due to a number of water leaks (see below), the beam availability and the MTBF are slightly below the 2004 figure (namely 97.95% and 49 h). The beam losses were rather uniformly distributed over the year. In July 2005, the beam was delivered in 16 bunch mode for 7 days in a row without interruption (see **Figure 162**).

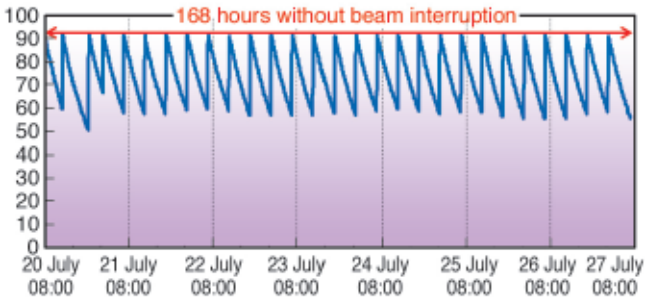

Fig. 162: 168 hours of beam delivery without interruption.

Filling Patterns

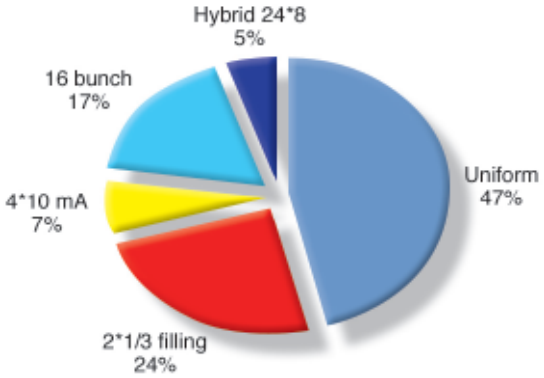

Fig. 163: Distribution of the various filling modes used in 2005.

No significant changes in the distribution of the modes are to be noted compared to the 2004 period (**Figure 163**). The multi-bunch modes with the largest current and the longest lifetime remain dominant, making up 76 % of the shifts. Following the regular installation of additional small aperture ID chambers, the single bunch mode (15 mA) was replaced in 2004 by the 4-bunch mode (4*10 mA), which generate a higher average current while avoiding the difficult machine tuning required to raise the single bunch current beyond 10 mA in a stable and repeatable manner. In 2005, we observed a stabilisation of the effect and no difficulties are anticipated for the delivery of the timing modes with similar performance in 2006.

Water Leaks and Crotches

Contrary to previous years, 2005 was marked by a number of water leaks. A water leak-to-air developed on the photon beam movable absorbers of a number of bending magnet and insertion device beamlines. These leaks affected only the oldest units in operation since 1992-1993. Remedies were found to limit the impact on user operation. A number of spare absorbers were ordered and delivered, enabling the replacement and

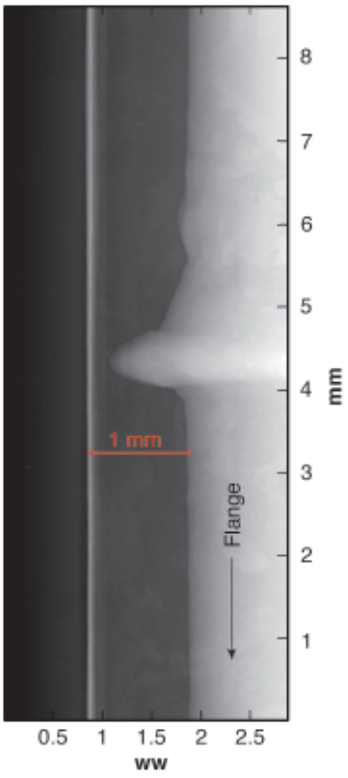

Fig. 164: Radiography of the cell-6 crotch absorber observed on the ID15 beamline. The water flows from bottom to top. The white trace is the water channel in the tube while the grey part is the copper wall surrounding the tube It shows that a cavity has developed and propagated through the 1 mm thick copper tube.

repairs of the defective absorbers during the machine shutdowns. The process leading to this leak has been understood and is linked to the high pressure water flow which generates cavitation followed by erosion of the wall material in some sharp edge elbows made of copper. The replacement or repair of all defective ID absorbers is expected to be by the end of 2006. For the bending magnet absorbers, a repair is being made to save time and a new design of absorber has been produced and will soon be tested before purchasing a series.

The most severe failure, given its impact on user operation, was the water leak-to-vacuum of the cell-15 crotch absorber, which resulted in the venting of two cells of the ring in March 2005. Altogether 5 days of USM had to be cancelled and were rescheduled in October. The investigation showed that a flat cavity with narrow vertical height (~ 0.5 mm) had developed in the wall of the first tubes of the crotch. The cavity formed in the plane of the bending magnet radiation and is deeper in places where the copper was the thinnest. The leak occurred when the cavity breached the copper wall of the tube, originally a minimum of 1mm thick. The chemistry involved in this process can be qualitatively explained as follows. The hard X-ray beam from the bending magnet, having traversed 5 mm of copper, is still sufficiently intense to produce a high number of radicals or oxidant species with a short lifetime, which corrode the tube in the vicinity of the place where they are produced. This process is slow since it took 10 years to traverse the 1mm thickness of the copper tube. The question was raised concerning the state of all the other machine absorbers and in particular all 64 crotch absorbers located immediately after each bending magnet along the ring circumference. These crotches are built to the same design as the cell-15 crotch absorber. A normal crotch absorber from cell-6 was exchanged during summer and further investigated by non destructive radiography on the ID-15 beamline

The radiography presented a similar cavity in the water tube but with a reduced penetration corresponding to an 0.25 mm residual wall thickness (see **Figure 164**). The reduced penetration of the cell-6 crotch absorber (compared to the cell-15 crotch) is understood from the 15% higher power density on the cell-15 crotch combined with a 9% lower effective copper thickness. A simple model based on the scaling of the power density and the X-ray transmission through the copper predicts that all 64 crotches should fail in a similar manner in the few years to come. To slow down the process, all crotches have been displaced vertically by 2 mm in such a way that the X-ray beam falls outside the existing cavities. Meanwhile, an order has been placed to replace all crotches with a modified design that would extend the lifetime beyond 50 years.

Hybrid in-Vacuum Undulators

The development of in-vacuum undulators started at the ESRF in 1999. In December 2005, eight devices were in user operation and two units were in preparation (**Table 8**).

Beamline	Name	Period [mm]	Peak field [T] @ gap 6 mm	Technology	Magnet Material
ID11	U23	23	0.96	Hybrid	Sm_2Co_{17}
ID22	U23	23	0.76	PPM	Sm_2Co_{17}
ID9	U17	17	0.57	PPM	Sm_2Co_{17}
ID29	U21	21	0.7	PPM	Sm_2Co_{17}
ID13	U18	18	0.6	PPM	Sm_2Co_{17}
ID11	U22	22	0.93	Hybrid	Sm_2Co_{17}
ID27	U23	23	0.76	PPM	Sm_2Co_{17}
ID27	U23	23	0.76	PPM	Sm_2Co_{17}
ID9	U20	20	0.92	Hybrid	NdFeB
ID15	U22	22	0.93	Hybrid	Sm_2Co_{17}

Table 8: Main Parameters of the in-vacuum undulators. All undulators are presently in operation except the last two devices, U20 for ID9 and U22 for ID15, which are scheduled for installation in January 2006 and July 2007. Note that both ID11 and ID27 are equipped with two in-vacuum undulator segments.

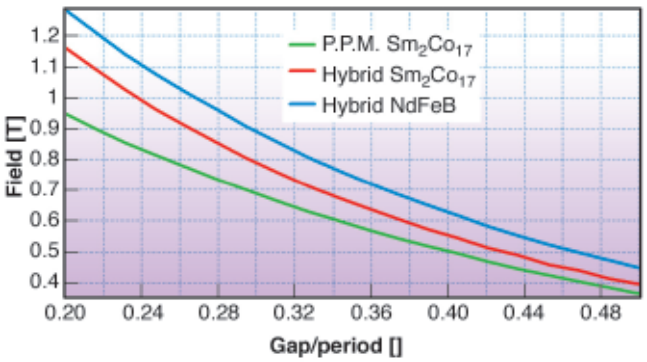

Fig. 165: Peak field versus the ratio of gap/period for three different type of in-vacuum undulators. The ones with the best performance are indeed the hybrid undulators made of NdFeB material but they are also the most sensitive to radiation damage.

As for any type of permanent magnet undulator, the assembly can either be based on a Pure Permanent Magnet (PPM) assembly with 4 magnet blocks per period, each block having a magnetisation rotated by 90 degrees, or can based on the Hybrid technology in which the period is constituted from two magnet blocks separated by a soft iron pole. The hybrid technology produces a higher peak field for the same magnetic gap and period. However the magnetic field corrections (field integral, integrated multipole and phase shimming) are much easier to perform with the PPM technology. The ID11 U23 mm undulator, the first in-vacuum undulator installed in 1999, was already built with the hybrid technology, but its phase errors and residual field integrals were rather poor as a result of a lack of time for the shimming process as well as a inadequate mechanical design of the magnet holders. To avoid these difficulties, subsequent in-vacuum undulators were built with the PPM technology and indeed achieved an adequate phase error around 2 degrees. Once the process of producing high field quality PPM in-vacuum undulators was mastered, the question was then reinvestigated for the ID11 U22 and the ID9 U20 for which it was decided to return to the hybrid technology in order to boost the peak field. The rms phase error reached 2.5 degrees for the U22. The phase error of the U20 is 4 degrees but was not corrected since being used on the fundamental or third harmonics it was considered as adequate. Another important modification was introduced in the newly built ID9 U20, namely the replacement of the Sm_2Co_{17} magnet material (originally selected for its high resistance to radiation damage) by a special grade of NdFeB magnet with high coercivity. The question of radiation damage is a sensitive issue for in-vacuum undulators, which aim at the smallest gap possible and constitute the places in the ring circumference where the electrons are most likely to be lost. The showers produced by electrons in the magnetic material results in a partial demagnetisation. The risk of using NdFeB material for the ID9 U20 was accepted considering that such an undulator is only used on harmonics one and three. **Figure 165** presents the peak field vs the ratio of gap over period. These curves clearly show a 30% field increase reached by the hybrid NdFeB compared to the PPM Sm_2Co_{17} for a 6 mm gap undulator with a 20 mm period.

Vacuum Chambers and NEG Coating

In the past, as the magnetic gap of the Insertion Devices (IDs) was reduced from 20 to 10 mm, the vertical aperture of the ID vacuum chambers had to be reduced accordingly. As a consequence, excessive Bremsstrahlung has been observed downstream in the beamlines. This Bremsstrahlung is created by the collision of the electron beam with the residual gas inside the ID vacuum chambers and becomes a serious problem for small aperture chambers in which the small conductance results in high pressure. The Bremsstrahlung is scattered off-axis by the optical component in the beamline (monochromator, mirror,…) and can be detected in the air outside the lead hutch. Even though more shielding can be added to the beamline hutches, this is not desirable or practical for a number of beamlines. Two solutions have been explored at the ESRF to alleviate the problem. One consists in placing the magnet assemblies in the vacuum (see above). Another solution consists in sputtering a Non Evaporable Getter (NEG) thin film (0.5-1.0 micrometres) on the wall of the vacuum chamber. Such a technique has been pioneered at CERN and has been extensively used at the ESRF on both stainless steel and aluminium narrow aperture IDs. Following activation of the NEG material (made of titanium, zirconium and vanadium) at 180 °C, the NEG coated surface provides pumping and the photo-induced desorption is largely reduced, thereby accelerating the vacuum conditioning time under beam. For this reason, a newly prepared 8 mm aperture 5 m long constant cross-section NEG coated Aluminium chamber has been installed in the ID6 straight section during every machine shutdown, for the past few years. The chamber is conditioned for 6-8 weeks until the following shutdown when it is moved to the final ID beamline destination. The chamber then only needs a few days of re-conditioning allowing the user operation to start almost immediately after the shutdown. This refurbishment process, while somewhat slow since it only allows a maximum of 5 beamlines to be upgraded per year, presents a number of advantages. It allows a smooth transition for the beamline with no beam interruption of the user program. It allows the quantitative measurement of the Bremsstrahlung vs. dose using the same monitors installed in the ID6 hutch and quantifies in term of Bremsstrahlung any change

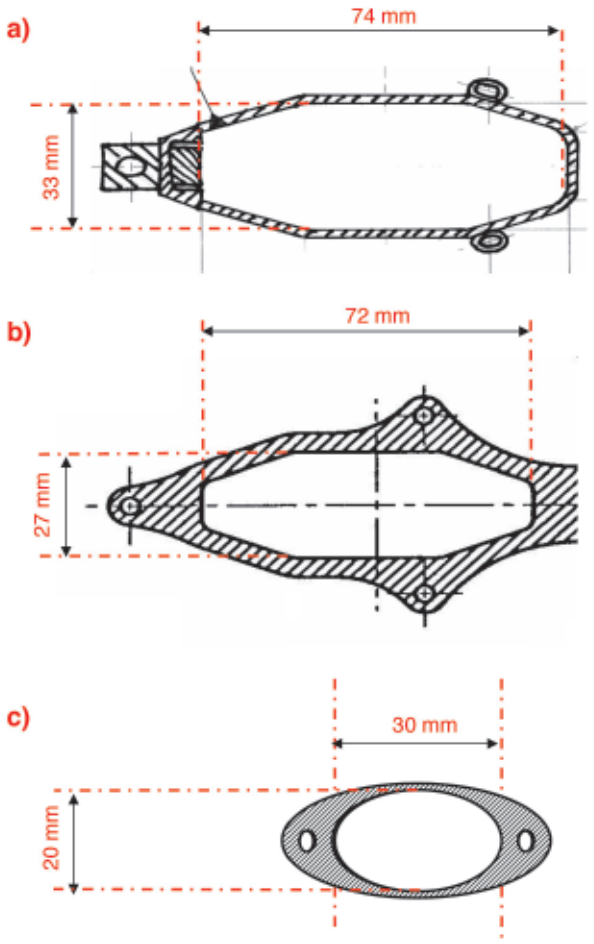

Fig 166: Cross sections of 3.5 m long quadrupole chambers tested at the ESRF in 2005. a) ESRF standard profile that is made of stainless steel and presents 3 pumping ports welded laterally to the profile. It is pumped with 2 NEG cartridges (2 x 200 l/s) and 1 ion pump (45 l/s). b) The SOLEIL profile, which is a constant cross-section with no pumping ports that relies exclusively on the pumping by the NEG coating. c) Narrow profile, which corresponds to the smallest aperture compatible with a 100% injection efficiency. It is also NEG coated and made of aluminium with a constant cross-section and no pumping port. Both aluminium profiles were tested in the cell-6 straight section in 2005 and showed a very rapid conditioning time and low Bremsstrahlung.

applied in the coating or cleaning sequence . At the end of 2005 nineteen NEG coated ID chambers were in operation in the beamline. Most of them are made of extruded aluminium 5 m long with a constant elliptical cross-section and an internal aperture of 57 x 8 mm^2. A NEG coating facility has been built at ESRF. At the end of 2005 two coating benches were operated simultaneously each processing a 5 m long chamber. A number of labs have expressed their interest in this technology and ID chambers have been NEG coated for SLS and SOLEIL.

As a new development, during 2005, was two 3.5 metre-long “quadrupole” type chambers that were coated and installed in cell 6, one using the Soleil aluminium extrusion profile, the other using a new profile, characterised by an elliptical cross-section of only 30 x 20 mm^2 (See **Figure 166**).

The aluminium vessels have performed extremely well in the storage ring, in terms of prompt vacuum conditioning times and low Bremsstrahlung levels. It has become clear that a “pump-free” solution for light source vacuum chambers is now possible, when a sufficiently low pressure is obtained by using NEG-coated chambers, with only few lumped pumps being necessary at high-desorption locations, such as crotch absorbers. In addition, narrow aperture chambers can be used which allow the use of stronger gradient quadrupoles and sextupoles which in turn allow a reduction of the quadrupole and sextupole size as well as their cost. This has generated considerable interest by many laboratories at a recent, dedicated vacuum workshop.

One possible drawback of this NEG technology is the requirement of *in situ* baking in order to activate the pumping. Conventional baking jackets take some space that increase the effective size of the chamber. In this respect we have used a recently developed technique of interlaced baking tape and insulation developed by CERN for the LHC warm chambers which is shown in **Figure 167**. Such tapes allow the full baking at 180 deg C and have a total thickness of 0.3 mm only.

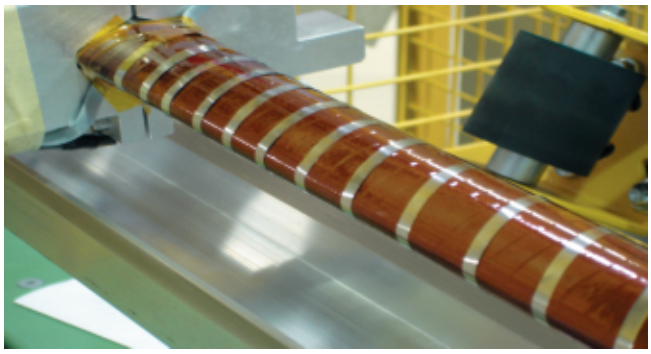

Fig. 167: Narrow profile 30 x 20 mm quadrupole chamber shown with its baking tape and insulation.


ESRF
Highlights 2005
Facts
and Figures

Member and Associate Countries

(as of January 2006)

Members' share in contribution to the annual budget:

27.5%	France
25.5%	Germany
15%	Italy
14%	United Kingdom
4%	Spain
4%	Switzerland
6%	Benesync (Belgium, The Netherlands)
4%	Nordsync (Denmark, Finland, Norway, Sweden)

Additional contributions
(percentages refer to Members' total contribution):

1%	Portugal
1%	Israel
1%	Austria
0.6%	Poland
0.44%	Czech Republic
0.2%	Hungary

The Beamlines

Details of the thirty-one public ESRF beamlines are given in **Table 9**. Three of these beamlines possess two end-stations, so there are thirty-four end-stations in total, which can be run independently. An additional sixteen beamline branches, situated on bending magnets, are devoted to Collaborating Research Groups (CRG). **Figure 168** shows the location of the beamlines in the experimental hall; a list of the CRG beamlines is presented in **Table 10**.

The Partnership for Structural Biology (PSB) initiated the construction of a new beamline complex at ID23. The first (multi-wavelength) branch has been operational since June 2004, the second (single wavelength microfocus) branch has been operational since October 2005.

The High Pressure beamline has been moved from ID30 to a new location, ID27, that was previously used for an industrial beamline. The refurbished High Pressure beamline has been operational since February 2005.

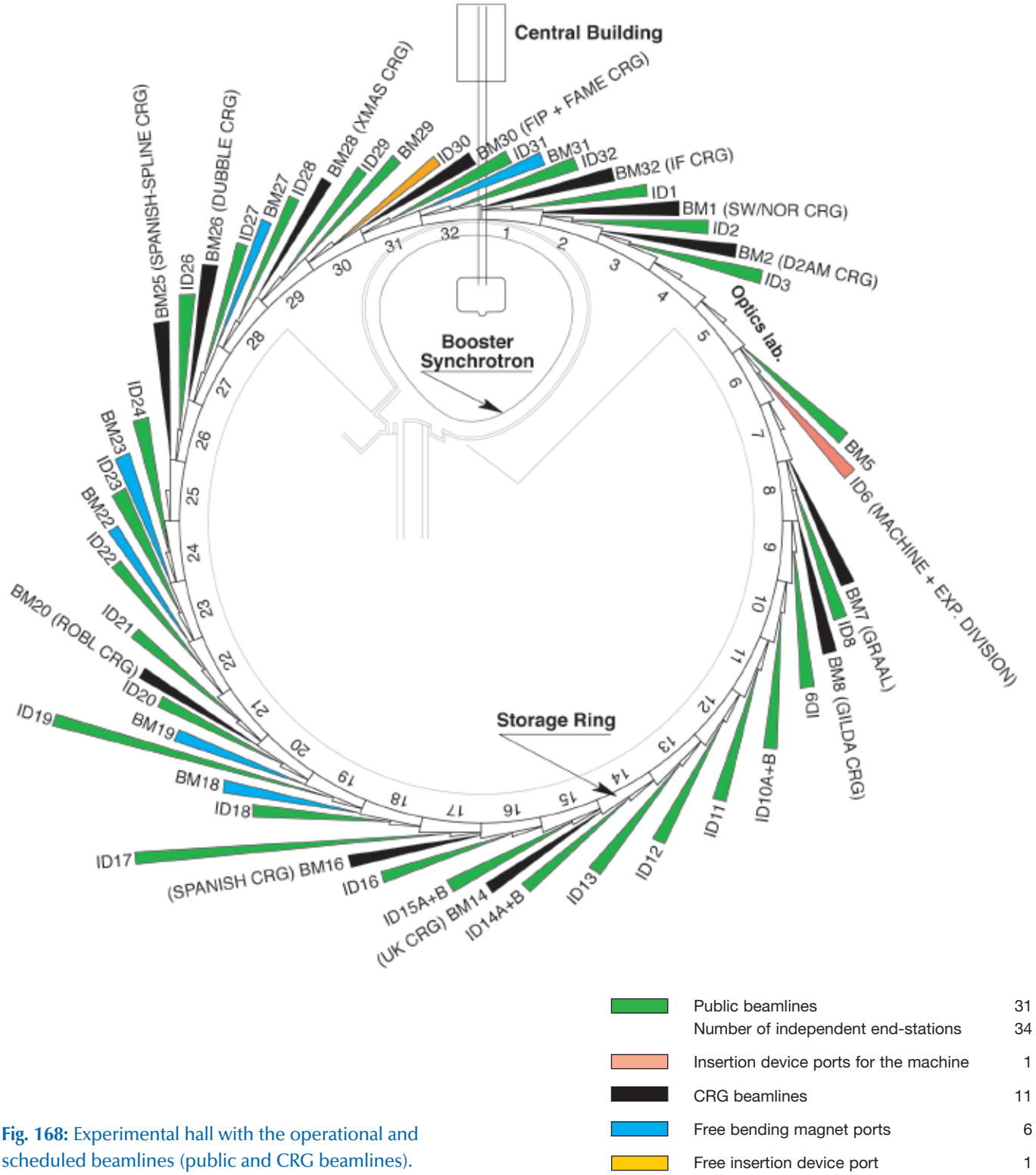

Fig. 168: Experimental hall with the operational and scheduled beamlines (public and CRG beamlines).

SOURCE POSITION	NUMBER OF INDEPENDENT END-STATIONS	BEAMLINE NAME	STATUS
ID1	1	Anomalous scattering	Operational since 07/97
ID2	1	High brilliance	Operational since 09/94
ID3	1	Surface diffraction	Under refurbishment until 06/06
ID6	1	50% Machine; 50% High magnetic fields	Operational in 2007
ID8	1	Dragon	Operational since 02/00
ID9	1	White beam	Operational since 09/94
ID10A	1	Troika I + III	Operational since 09/94
ID10B	1	Troika II	Operational since 04/98
ID11	1	Materials science	Operational since 09/94
ID12	1	Circular polarisation	Operational since 01/95
ID13	1	Microfocus	Operational since 09/94
ID14A	2	Protein crystallography EH 1	Operational since 07/99
		Protein crystallography EH 2	Operational since 12/97
ID14B	2	Protein crystallography EH 3	Operational since 12/98
		Protein crystallography EH 4	Operational since 07/99
ID15A	1	High energy diffraction	Operational since 09/94
ID15B	1	High energy inelastic scattering	Operational since 09/94
ID16	1	Inelastic scattering I	Operational since 09/95
ID17	1	Medical	Operational since 05/97
ID18	1	Nuclear scattering	Operational since 01/96
ID19	1	Topography	Operational since 06/96
ID20	1	Magnetic scattering	Operational since 05/96
ID21	1	X-ray microscopy	Operational since 12/97
ID22	1	Microfluorescence	Operational since 12/97
ID23	2	Macromolecular crystallography MAD	Operational since 06/04
		Macromolecular crystallography microfocus	Operational since 09/05
ID24	1	Dispersive EXAFS	Operational since 02/96
ID26	1	X-ray absorption and emission	Under refurbishment until 09/06
ID27	1	High pressure	Operational since 02/05
ID28	1	Inelastic scattering II	Operational since 12/98
ID29	1	Multiwavelength anomalous diffraction	Operational since 01/00
ID31	1	Powder diffraction	Operational since 05/96
ID32	1	SEXAFS	Operational since 11/95
BM5	1	Optics - Open Bending Magnet	Operational since 09/95
BM29	1	X-ray absorption spectroscopy	Operational since 12/95

Table 9: List of the ESRF public beamlines in operation and under construction.

SOURCE POSITION	NUMBER OF INDEPENDENT END-STATIONS	BEAMLINE NAME	FIELD OF RESEARCH	STATUS
BM1	2	Swiss-Norwegian BL	X-ray absorption & diffraction	Operational since 01/95
BM2	1	D2AM (French)	Materials science	Operational since 09/94
BM7	1	GRAAL (Italian / French)	Gamma ray spectroscopy	Operational since 06/95
BM8	1	Gilda (Italian)	X-ray absorption & diffraction	Operational since 09/94
BM14	1	UK CRG	Macromolecular crystallography (MAD)	Operational since 01/01
BM16	1	SPANISH CRG	Structural biology (MAD, SAX)	Operational since 01/03
BM20	1	ROBL (German)	Radiochemistry & ion beam physics	Operational since 09/98
BM25	2	SPLINE (Spanish)	X-ray absorption & diffraction	Operational since 04/05
BM26	2	DUBBLE (Dutch/Belgian)	Small-angle scattering & interface diffraction Protein crystallography + EXAFS	Operational since 12/98 Operational since 06/01
BM28	1	XMAS (British)	Magnetic scattering	Operational since 04/98
BM30	2	FIP (French) FAME (French)	Protein crystallography EXAFS	Operational since 02/99 Operational since 08/02
BM32	1	IF (French)	Interfaces	Operational since 09/94

Table 10: List of the Collaborating Research Group beamlines in operation and under construction.

User Operation

After 10 years of successful operation of the facility for scientific Users, the year 2005 again saw the full complement of 31 public beamlines, together with 10 additional beamlines operated by Collaborating Research Groups (CRGs) available for experiments by visiting user teams. **Figure 169** shows the increase in the number of applications for beam time since 1998, and confirms that although the main beamline construction effort was complete by 1999, the number of applications for beam time continues to increase steadily.

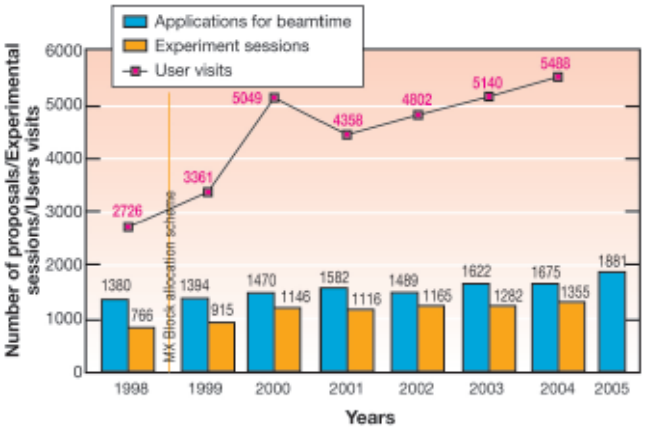

Fig. 169: Numbers of applications for beam time, experimental sessions and user visits, 1998 to 2005. N.B. Final numbers of experiments and user visits for 2005 were not available at the time of going to press.

Proposals for experiments are selected and beam time allocations are made through peer review. Review Committees of specialists for the most part from European countries and Israel, have been set up in the following scientific areas:

- chemistry
- hard condensed matter: electronic and magnetic properties
- hard condensed matter: structures
- materials, engineering and environmental matters
- macromolecular crystallography
- medicine
- methods and instrumentation
- soft condensed matter
- surfaces and interfaces.

The Review Committees met twice during the year, some six weeks after the deadlines for submission of proposals (1 March and 1 September). They reviewed a record number of 1881 applications for beam time, and selected 781 (41.5%), which were then scheduled for experiments.

Features of this period include:

- increasing numbers of projects concerned more with applied than basic research in materials science, engineering, environmental and cultural heritage matters. As shown in **Figure 170**, experiments in these areas accounted for 15% of the total number of experiments carried out in the first half of 2005, an increase from 10% in 2002.
- the continued successful operation of the Block Allocation Group (BAG) scheme for macromolecular crystallography users. This scheme, designed to encourage groups of users to block together their multiple requests for beam time, and the scheduling of their experiments, encompassed 41 groups from Europe and Israel in 2005.

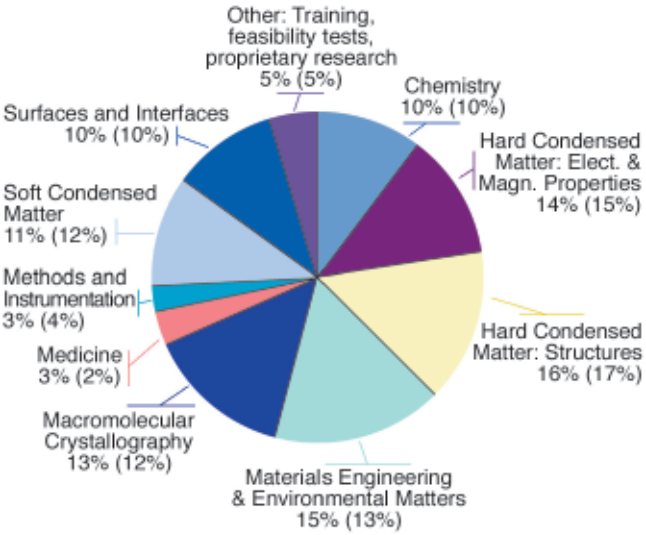

Fig. 170: Shifts scheduled for experiments, March to July 2005, by scientific area *(Percentages for 2004 in parentheses)*.

Requests for beam time, which is scheduled in shifts of 8 hours, totalled 30 311 shifts or 242 488 hours in 2005, of which 12 894 shifts or 103 152 hours (42.5 %) were allocated. The distribution of shifts requested and allocated, by scientific area, is shown in **Table 11**.

Scientific field	Total shifts requested	Total shifts allocated
Chemistry	3 894	1 351
Hard condensed matter:		
• Electronic and magnetic prop.	4 073	1 835
• Structures	5 710	2 037
Materials engineering & environmental matters	4 606	2 168
Macromolecular crystallography	2 913	2 116
Medicine	1 229	462
Methods & instrumentation	985	408
Soft condensed matter	3 690	1 296
Surfaces & interfaces	3 211	1 221
Totals	**30 311**	**12 894**

Table 11: Number of shifts of beam time requested and allocated for user experiments, year 2005.

The first half of 2005 saw 2761 visits by scientists to the ESRF under the user programme, to carry out 652 experiments. **Figure 169** shows the rapid rise in the number of user visits since 1998, the higher numbers in recent years reflecting in part the multiple visits made by

macromolecular crystallography BAG teams. The peak in 2000 is due to a somewhat longer scheduling period, and correspondingly higher overall number of experimental sessions, and visits by users.

Overall, the number of users in each experimental team averaged 4 persons, and they stayed for some 4 days. Users responding to questionnaires indicate that they particularly appreciate the assistance they receive from scientists and support staff on beamlines, and smooth administrative arrangements, in addition to the quality both of the beam and of the experimental stations. Facilities on site, such as preparation laboratories, a canteen open 7 days a week, and the Guesthouse, also make an important contribution to the quality of user support.

Administration and Finance

Revised expenditure and income budget for 2004

Expenditure	kEuro	kEuro	Income	kEuro
Machine			2004 Members' contributions	65 358.4
Personnel		4 796.5	Funds carried forward from 2003	13.0
Recurrent		2 350.5		
Operating costs	*1 951.2*		Other income	
Other recurrent costs	*399.3*		Scientific Associates	3 424.8
Capital		3 523.8	Sale of beamtime	2 640.2
Machine developments	*3 523.8*		Other sales	1 090.8
Beamlines, experiments and in-house research			Compensatory funds	1 159.0
			Scientific collaboration and Special projects	885.9
Personnel		21 791.0	Other	973.91
Recurrent		6 659.9		
Operating costs	*3 667.1*			
Other Recurrent costs	*2 992.8*			
Capital		7 299.7		
Beamline developments	*4 077.8*			
Beamline refurbishment	*3 221.9*			
Technical and administrative supports				
Personnel		15 595.7		
Recurrent		9 053.1		
Capital		2 759.0		
Personnel costs provision		1 711.2		
Unexpended committed funds				
Funds carried forward to 2005		5.6		
Total		**75 546.0**	**Total**	**75 546.0**

Revised expenditure and income budget for 2005

Expenditure	kEuro	kEuro	Income	kEuro
Machine			2005 Members' contributions	67 081
Personnel		4 745	Funds carried forward from 2004	6
Recurrent		2 175		
Operating costs	*1 801*		Other income	
Other recurrent costs	*374*		Scientific Associates	3 740
Capital		3 845	Sale of beamtime	2 375
Machine developments	*3 845*		Other sales	405
Beamlines, experiments and in-house research			Compensatory funds	1 157
Personnel		22 505	Scientific collaboration and Special projects	1 505
Recurrent		3 366	Other	1 570
Operating costs	*3 290*			
Other Recurrent costs	*3 076*			
Capital		6 743		
Beamline developments	*4 283*			
Beamline refurbishment	*2 460*			
Technical and administrative supports				
Personnel		15 470		
Recurrent		9 145		
Capital		4 775		
Industrial and commercial activity				
Personnel		535		
Recurrent		210		
Personnel costs provision		1 325		
Total		**77 839**	**Total**	**77 839**

Expenditure 2004 by nature of expenditure

	kEuro
PERSONNEL	
ESRF staff	40 561.9
External temporary staff	13.3
Other personnel costs	1 607.9
RECURRENT	
Consumables	6 759.5
Services	9 060.2
Other recurrent costs	2 243.8
CAPITAL	
Buildings, infrastructure	1 069.4
Lab. and Workshops	389.6
Machine incl. ID's and Fes	3 523.8
Beamlines, Experiments	7 299.7
Computing Infrastructure	1 164.4
Other Capital costs	135.7
Personnel costs provision	1 711.2
Unexpended committed funds	
Funds carried forward to 2005	5.6
Total	**75 546.0**

Revised budget for 2005 by nature of expenditure

	kEuro
PERSONNEL	
ESRF staff	41 470
External temporary staff	85
Other personnel costs	1 700
RECURRENT	
Consumables	6 280
Services	9 351
Other recurrent costs	2 265
CAPITAL	
Buildings, infrastructure	3 290
Lab. and Workshops	260
Machine incl. ID's and Fes	3 845
Beamlines, Experiments	6 743
Computing Infrastructure	835
Other Capital costs	390
Personnel costs provision	1 325
Total	**77 839**

2005 manpower
(posts filled on 31/12/2005)

	Scientists, Engineers, Senior Administrators	Technicians and Administrative Staff	PhD students	Total
Staff on regular positions				
Machine	25	38	2	65
Beamlines, instruments and experiments*	192	63.2	27	282.2
General technical services	51.6	66.6		118.2
Directorate, administration and central services	31.3	52.6		83.9
Sub-total	*299.9*	*220.4*	*29*	*549.3*
Other positions				
Short term contracts	2	13.8		15.8
Scientific collaborators	6			6
Staff under "contrats de qualification" (apprentices)		14		14
European Union grants	7.8	3		10.8
Total	**315.7**	**251.2**	**29**	**595.9**
Absences of staff (equivalent full time posts)				24.5
Total with absences				*571.4*
External funded research fellows				*22*

** Including scientific staff on time limited contract.*

Financial resources in 2003, 2004, 2005 and 2006, by major programme
(current prices in MEuro for the respective years)

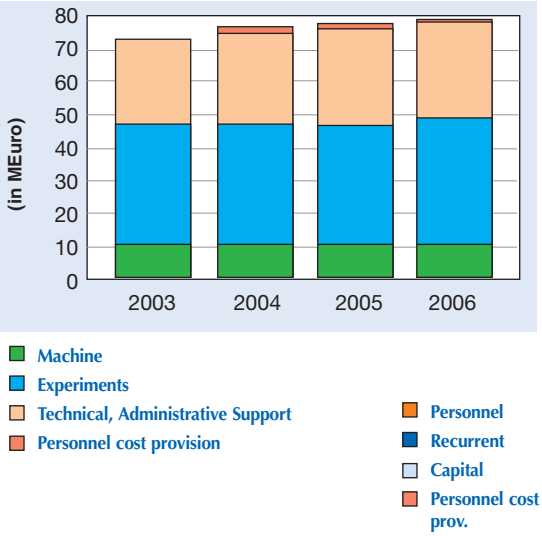

Financial resources in 2003, 2004, 2005 and 2006, by nature of expenditure
(current prices in MEuro for the respective years)

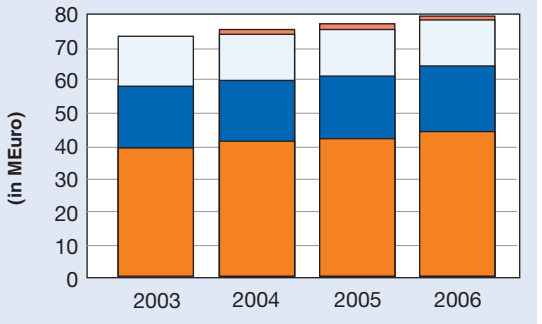

Organisation Chart of the ESRF (as of January 2006)

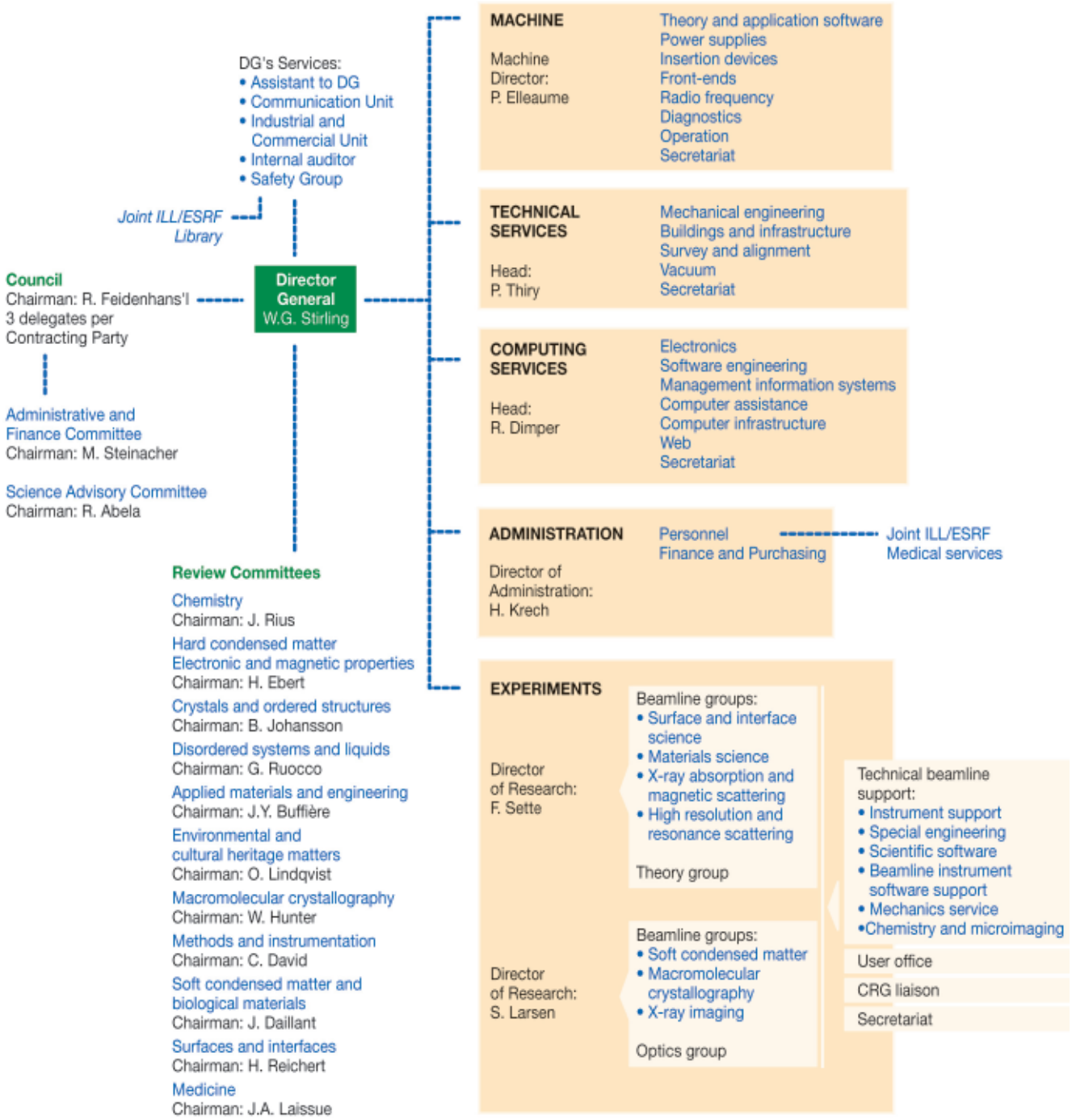

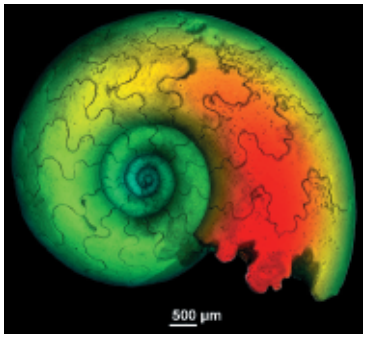

Cover image: 3D rendering of a Jurassic juvenile ammonite (about 155 million years old) from France. The shell was removed digitally to reveal the internal structures. The superimposed colours correspond to the 3D topology of this internal shell surface. Microtomographic data were collected on the beamline ID19, with a 7.5 µm pixel size, using a 60 keV monochromatic beam. Image courtesy of Paul Tafforeau, ESRF.

Back cover photo: Peter Ginter

We gratefully acknowledge the help of:
C. Argoud, J. Baruchel, N. Brookes, P. Elleaume, A. Kaprolat, Å. Kvick, S. Larsen, G. Leonard, R. Mason, C. Riekel, R. Rüffer, F. Sette, W.G. Stirling, S. McSweeney, K. Witte, J. Zegenhagen, and all the users and staff who have contributed to this edition of the Highlights.

Editor
G. Admans
Layout
Pixel Project
Printing
Imprimerie du Pont de Claix

© ESRF • February 2006

Communication Unit
ESRF
BP220 • 38043 Grenoble • France
Tel. (33) 4 76 88 20 56 • Fax. (33) 4 76 88 25 42
http://www.esrf.fr